



Stylianou, Panagiotis (2022) *Collider phenomenology of new physics Beyond the Standard Model*. PhD thesis.

<https://theses.gla.ac.uk/83162/>

Copyright and moral rights for this work are retained by the author

A copy can be downloaded for personal non-commercial research or study, without prior permission or charge

This work cannot be reproduced or quoted extensively from without first obtaining permission from the author

The content must not be changed in any way or sold commercially in any format or medium without the formal permission of the author

When referring to this work, full bibliographic details including the author, title, awarding institution and date of the thesis must be given

Enlighten: Theses

<https://theses.gla.ac.uk/>
research-enlighten@glasgow.ac.uk

Collider phenomenology of new physics Beyond the Standard Model

Panagiotis Stylianou



*Submitted in fulfillment of the requirements for the degree of
Doctor of Philosophy*

School of Physics and Astronomy
College of Science and Engineering
University of Glasgow

Abstract

On the one hand, the Standard Model has been established as the best description of the fundamental laws of nature. On the other hand, various phenomena remain unaddressed, motivating the study of Beyond the Standard Model theories along with future experimental concepts that can pinpoint the right direction forward.

Looking into new physics from multiple perspectives, this thesis presents different phenomenological studies utilising both model-dependent and -independent approaches. A comparison of future experiments is presented within a simplified dark matter model, allowing the assessment of the constraints on the parameter space. In theories with extended scalar sectors, the capacity of cascade scalar decays in the potential discovery of new physics is showcased, taking advantage of the discriminative power of Neural Networks. The applicability of such Machine Learning techniques also extends to effective field theories leading to critically improved bounds on Wilson Coefficients attainable in the top sector. Finally, particular measurements from experiments related to CP violation in the gauge-Higgs sector and the muon's anomalous magnetic moment are scrutinised within the Standard Model Effective Field Theory framework.

Acknowledgements

First of all, I can not express my gratitude enough to my supervisor, Christoph Englert. His encouragement, endless patience and continuous guidance made this work possible, while his humour and friendliness kept the journey enjoyable. I am exceptionally fortunate to have had such an enthusiastic, inspirational and knowledgeable supervisor.

I would like to express my deepest appreciation to every single one of my collaborators whom I had the pleasure of working during my studies, with a special thank you to Joydeep Chakraborty and Michael Spannowsky, with whom I collaborated in most of my projects.

I would like to thank Christine Davies for leading a great group to do physics, as well as Chris Bouchard and David Miller for making PPT a unique and wonderful place. I also want to thank Dan and Dan for their warm welcome and advice in the early months, Stephen, Esther and Oliver for making the group a friendly environment, Will for the countless hilarious and unforgettable moments and Akanksha and Anisha for their friendship during my last months in the group.

I additionally acknowledge support from the Science and Technology Facilities Council (STFC).

Είμαι επίσης ευγνώμων στους γονείς μου, Κωνσταντίνα και Στέλιο για την οικονομική και ηθική στήριξη που μου παρείχαν σε όλη μου τη ζωή και που με παρότρυναν πάντοτε να κυνηγώ τα προσωπικά μου ενδιαφέροντα και προσδοκίες. Ευχαριστώ επίσης την αδερφή μου Ελένη, απλά επειδή κάνει τη ζωή μου πιο χαρούμενη.

Καταλήγοντας θα ήθελα να ευχαριστήσω την Μαρία για την ανυπολόγιστη στήριξη στις δύσκολες περιστάσεις, τις πολλές ευτυχισμένες στιγμές και για την υπομονή της όταν μιλούσα ασταμάτητα για την φυσική.

Declaration of originality

The content of this thesis is my own work except where explicit attribution to others is made. Chapter 2 introduces the topic. Chapters 3, 4, 5, 6 and 7 based on the following publications:

- Chapter 3:
“Power meets Precision to explore the Symmetric Higgs Portal” [1], written in collaboration with Dr. Christoph Englert, Dr. Joerg Jaeckel and Dr. Michael Spannowsky.
- Chapter 4:
“Sensing Higgs boson cascade decays through memory” [2], written in collaboration with Dr. Christoph Englert, Dr. Malcolm Fairbairn, Dr. Michael Spannowsky and Dr. Sreedevi Varma, and
“On interference effects in top-philic decay chains” [3], written in collaboration with Mr. Oliver Atkinson and Dr. Christoph Englert.
- Chapter 5:
“Improved constraints on effective top quark interactions using edge convolution networks” [4], written in collaboration with Mr. Oliver Atkinson, Dr. Akanksha Bhardwaj, Mr. Stephen Brown, Dr. Christoph Englert and Dr. David J. Miller.
- Chapter 6:
“CP violation at ATLAS in effective field theory” [5], written in collaboration with Dr. Supratim Das Bakshi, Dr. Joydeep Chakraborty, Dr. Christoph Englert and Dr. Michael Spannowsky, and
“Landscaping CP-violating BSM scenarios” [6] written in collaboration with Dr. Supratim Das Bakshi, Dr. Joydeep Chakraborty, Dr. Christoph Englert and Dr. Michael Spannowsky.

- Chapter 7:
“Implications of the muon anomalous magnetic moment for the LHC and MUonE” (preprint) [7],
written in collaboration with Dr. Akanksha Bhardwaj and Dr. Christoph Englert.

All results in these chapters are my own except the following which were either collaborative efforts including myself or solely work of others as stated:

- In Chapter 3, the sensitivity for indirect modes was conducted by myself along with Dr. Christoph Englert adjusting code implemented from collaborators in previous works.
- In Chapter 4, the implementation and performance assessment of the network was done by both myself and Dr. Sreedevi Varma. The work on the model-dependent part was conducted by myself along with Mr. Oliver Atkinson and Dr. Christoph Englert.
- In Chapter 5, Mr. Stephen Brown generated the data, obtained individual and profiled intervals on Wilson Coefficients with the baseline analysis, and utilised the network scores provided by myself to obtain the improved bounds (including Tabs. 5.1, 5.2, 5.3). The exploration of different ways to utilise the network scores in the simple case of two effective operators was conducted jointly by myself and Mr. Oliver Atkinson.
- In Chapter 6, the calculations and derivations in Sec. 6.3 were done by Dr. Supratim Das Bakshi (including Tabs. 6.1, 6.2, 6.3).
- In Chapter 7, the data for $h \rightarrow \mu\mu\gamma$ were generated by Dr. Akanksha Bhardwaj.

Figures are my own except Figs. 3.15, 3.16, 3.17 and 3.18 which were created by Dr. Christoph Englert, Fig. 5.7 which was created by Mr. Oliver Atkinson, Fig. 5.9 created by Mr. Stephen Brown and Figs. 6.3 and 6.4 which were created by Dr. Supratim Das Bakshi.

Contents

List of Figures	x
List of Tables	xviii
1 Introduction	1
2 The Standard Model of particle physics	4
2.1 Standard Model Lagrangian in the unbroken phase	5
2.1.1 The Yang-Mills part	5
2.1.2 Fermionic part	6
2.1.3 Higgs part	8
2.2 Standard Model Lagrangian in the physical basis	9
2.2.1 Higgs sector after SSB	9
2.2.2 Fermion sector after SSB	11
2.3 Path Integral quantisation	12
2.4 Renormalisation	15
2.5 Aspects of the Standard Model	17
2.5.1 Perturbative unitarity	17

2.5.2	Higgs physics at the LHC	20
2.6	Shortcomings of the Standard Model	25
2.7	Beyond the Standard Model	28
2.7.1	Standard Model Effective Field Theory	28
2.8	Summary	33
3	Power meets precision to explore the symmetric Higgs portal	34
3.1	Introduction	34
3.2	Direct Detection	36
3.2.1	Hadron Colliders	37
3.2.2	Lepton Colliders	40
3.3	Indirect Sensitivity: Virtual S imprints	45
3.3.1	Higgs coupling modifications	46
3.3.2	Off-Shell Higgs boson probes	47
3.3.3	Higgs Pair Production	48
3.3.4	Oblique Corrections	49
3.4	Power meets Precision: Expected Collider Sensitivity	52
3.4.1	Expected collider sensitivity for direct detection	52
3.4.2	Expected collider sensitivity for indirect detection	53
3.5	Discussion and Conclusions	56
4	Asymmetric Cascade decays in models with rich scalar phenomenology	59
4.1	Introduction	59
4.2	Models	61
4.2.1	N2HDM	63

4.2.2	Two-singlet extended SM	64
4.3	Sensitivity improvements through neural network memory	66
4.3.1	Remarks on Neural Networks with memory	66
4.3.2	Signature	68
4.3.3	Event generation and selection	69
4.3.4	Network Architectures	71
4.3.5	Model-independent performance tests	71
4.3.6	Sensitivity for a benchmark N2HDM point	72
4.4	Interference effects in multi-Higgs cascade decays	76
4.4.1	Signal-Background Interference	76
4.4.2	Cascade interference in the two-singlet extended SM	79
4.4.3	Conclusions	81
5	Improving constraints on Wilson Coefficients with Graph Neural Networks	84
5.1	Introduction	84
5.2	Effective interactions	85
5.2.1	Analysis Setup and Fit Methodology	86
5.3	Graph representation of events	88
5.3.1	Graph Neural Networks with Edge Convolution	89
5.3.2	Network Architecture and Training	91
5.4	GNN-improved Wilson coefficient constraints	92
5.4.1	A minimal example	92
5.4.2	Fit constraints with GNN selections	98
5.5	Conclusions	100

6	CP violation in gauge-Higgs interactions	102
6.1	Introduction	102
6.2	Scrutinizing CP violating $\mathcal{O}_{\phi\widetilde{W}B}$ operator with diboson data	104
6.2.1	Analysis of the CP sensitive $\Delta\phi$ distribution	104
6.2.2	Diboson analyses	105
6.2.3	Diboson Results	107
6.3	Scenarios with low energy CP violation	108
6.3.1	Doublet-Triplet VLL	110
6.4	Minimal Fit of CP violation	114
6.4.1	WBF selection and cuts	114
6.4.2	Combined WBF & Diboson Results	115
6.5	Conclusions	116
7	Implications of the muon anomalous magnetic moment for the LHC and MUonE	118
7.1	Introduction	118
7.2	Δa_μ in SMEFT	119
7.2.1	UV divergent operators: a_μ as input parameter	124
7.2.2	a_μ as a radiative SMEFT effect	128
7.3	Tensioning the dipole operators	129
7.3.1	Z decay	129
7.3.2	$gg \rightarrow h \rightarrow \mu\mu\gamma$ channel	130
7.3.3	MUonE	133
7.4	Conclusions	135

CONTENTS

ix

8 Conclusions

137

Bibliography

139

List of Figures

2.1	Feynman diagrams relevant for the $WZ \rightarrow WZ$ scattering in the SM.	20
2.2	Partial wave of $W_L Z_L \rightarrow W_L Z_L$ at different centre-of-mass energies \sqrt{s} with and without the scalar sector. The scenario of a Higgs boson with mass $m_h = 2.5$ TeV is also shown, which also violates perturbative unitarity.	21
2.3	Feynman diagrams for decays of the scalar Higgs boson.	22
2.4	Figure (a) shows the Higgs branching ratios for different values of the Higgs mass, and (b) displays the value of the total decay width as a function of the mass. Both figures are taken from Ref. [89] (see also [90]).	23
2.5	Example Feynman diagrams for the production of the scalar Higgs boson.	24
2.6	The cross section of Higgs production at different energies is shown in (a), while (b) shows their dependence on the Higgs mass. Both figures are from Ref. [105].	25
3.1	Figure showing the total cross section for producing an SS pair along with two jets through WBF (red) and the mono-jet production from gluon fusion (blue). Compared to WBF, the associated $(h \rightarrow SS)V$ production is three orders of magnitude lower and therefore is not taken into consideration.	37
3.2	Feynman diagram for the WBF case at hadron colliders. This Higgs production channel with the subsequent production of S particles can be identified with the final state signature of two jets and missing energy.	38

3.3	Normalised \cancel{E}_T distributions at 100 TeV FCC after the baseline cuts given in Tab. 3.1. The signal is for a mass $m_S = 100$ GeV and a coupling $\lambda = 1$ at 100 TeV FCC and both QCD and electroweak backgrounds are shown.	39
3.4	Example diagram for mono-jet case, where gluon fusion at next-to-leading-order yields a Higgs recoiled against QCD radiation. Pair production of S is then feasible.	39
3.5	\cancel{E}_T distribution (normalised) for mono-jet production of the signal with mass $m_S = 100$ GeV and $\lambda = 1$ at 100 TeV FCC along with the distribution for the combined background. Only the baseline cuts of Tab. 3.2 have been applied for this plot.	41
3.6	Cross section distributions against centre-of-mass energies for WBF and associate pair production of S and two leptons.	42
3.7	Feynman diagram for associate production of the S pair. Although this channel is subdominant at hadron colliders with respect to the WBF, it is still relevant for future lepton collider experiments at relatively low energies, such as ILC.	42
3.8	Associate production MIM distributions for an S particle with mass $m_S = 100$ GeV and a Higgs portal coupling $\lambda = 1$. Results for both 500 GeV ILC and 3 TeV CLIC are shown, where in the former case, associate production is more pertinent for the analysis than in the latter.	43
3.9	Distributions for MIM for signal with mass $m_S = 100$ GeV and $\lambda = 1$ at 500 GeV and 3 TeV lepton colliders produced through WBF, as well as the background contamination arising from the SM.	45
3.10	Differential cross sections for the channel $gg \rightarrow ZZ$ at 100 TeV FCC implying that corrections from S to the Higgs channel of $pp \rightarrow 4\ell$ are negligible.	48
3.11	Representative Feynman diagrams for the polarisation functions of the boson V at two-loops. Such diagrams result in modifications of the Peskin-Takeuchi parameters S, T, U . Φ, Φ' indicate the possible Higgs and Goldstone boson insertions, while $V, V', V'' = W, Z, A$ are the allowed vector bosons.	49

3.12	Example counterterm topologies required for renormalisation of two-loop polarisation function diagrams shown in Fig. 3.11. The first diagram indicates two-loop renormalisation constants that do not appear at one-loop level. Note that the $\Phi\Phi V''$ vertex counterterms are suppressed.	50
3.13	Values for the oblique parameters using $\lambda = 1$ at different masses.	51
3.14	(a) 68% exclusion regions for FCC at integrated luminosities of 3 ab^{-1} and 30 ab^{-1} . 30% increment of the background for the 3 ab^{-1} and 30 ab^{-1} luminosities are shown as loosely dotted and dotted, respectively. (b) Exclusion regions at 68% for ILC at 2 ab^{-1} integrated luminosity and 3 TeV CLIC at 3 ab^{-1}	53
3.15	Limits from uncertainties quoted in Eqs. (3.27a)-(3.27e) for the parameter space of the Higgs portal model.	54
3.16	Sensitivity obtained from di-Higgs production at FCC-hh with an integrated luminosity of 30/ab. The different lines indicate the expected accuracies of κ_λ , and 3% corresponds to the 68% confidence level reported in Ref. [206]. Results for CLIC are shown in Fig. 3.18(b).	55
3.17	S, T constraints at 68% and 95% confidence levels are shown with solid and dashed lines, respectively. Red (blue) indicates the results for LHC 300/fb (ILC/GigaZ) obtained with the confidence intervals provided by GFITTER [200] for $U = 0$. . .	55
3.18	Best case sensitivities for (a) FCC-hh and (b) CLIC (3 TeV). The dashed blue line for S pair production refers to WBF, the green line denotes the expected constraints from Higgs signal strengths, and the GigaZ extrapolation of the sensitivity obtained from oblique corrections is shown as a black dashed line. Results from di-Higgs are reflected by the red lines and for 3 TeV CLIC both 5%- and 10%-level accuracies are included as dash-dotted and solid lines, respectively. The Higgs signal strength results are obtained with the 3 TeV value $\delta\mu/\mu = 0.39\%$ from Ref. [205]. Assuming no additional heavy states other than the singlet scalar, the stability constraints are shown as shaded regions [202].	57
4.1	Gluon fusion diagrams for an H_3 resonance that decays to $H_3 \rightarrow t\bar{t}$ or $H_3 \rightarrow H_2 h$.	61
4.2	Signal only and destructive signal-background interference. The figure is from Ref. [233].	61

4.3	A Dense Neural Network.	67
4.4	An RNN of a single unit and how it can be unfolded for each entry in the sequence. a_t denotes the node's output for the entry t in the sequence. Examples of input components are often words in a sentence.	68
4.5	Background rejection values for different $M_{H_{2,3}}$ values for the LSTM and dense networks. These rejections are calculated at signal efficiencies of 10% and 30%, and the width of H_3 is always fixed to 10% of its mass. Using a width of 30% of M_{H_3} produces comparable results. This is anticipated since, while the width of the heavy resonance will influence the normalisation rate, cross section is not a feature used as input in the network. Therefore the efficiency of the network is unaffected by rescaling the total rate and sensitive only to kinematical features of the final states.	70
4.6	Final signal cross sections after all selection criteria required to achieve $N_S/\sqrt{N_B} = 2$ (95% CL) in the $M_{H_3} - M_{H_2}$ plane. For this scan the requirement $M_{H_3} > M_{H_2} + 125$ GeV is imposed and branching ratios are fixed to $\text{BR}(H_3 \rightarrow H_2 h) = 0.5$ and $\text{BR}(H_2 \rightarrow t\bar{t}) = 1$	72
4.7	The loss function during training is shown for all networks in 4.7(a). 4.7(b) shows the ROC curves used to identify an optimal RNN (DNN) score cut-off, with the score also shown in 4.7(c) (4.7(d)).	73
4.8	Example histograms for the reconstructed mass $M_{H_{3,2}}$ before (after) running the network selection are shown on the left (right) for the generated events. Masses were set to $M_{H_3} = 722$ GeV, $M_{H_2} = 480$ GeV and widths were set to 45 GeV and 4.9 GeV for H_3 and H_2 , respectively.	74
4.9	Triangle (a) and box (b) Feynman diagrams producing the $H_2 h$ state.	77
4.10	Effect of varying masses and widths for different ggH_i couplings is shown in 4.10(a) and 4.10(b), respectively. Figs. 4.10(c) and 4.10(d) compare interference and signal-squared contributions for $m_{t\bar{t}}$ and $m_{t\bar{t}b\bar{b}}$ while the effect of odd Yukawa couplings is shown in 4.10(e) and 4.10(f). It is highlighted that the plotted curves contribute to the differential cross section but only the sum of all contributions is physical (i.e. interference does not include the signal-squared terms and hence it can be negative).	78

4.11	The effect of signal-signal interference as a ratio of the cross section close to the scalar's mass with interference divided by the cross section without interference for the channels $H_i \rightarrow t\bar{t}, hh$ at 13 TeV. It is particularly important that such effects are included for the decay to $t\bar{t}$	81
4.12	Effects from including signal-background (signal-signal) interference for the asymmetric cascade decay $H_3 \rightarrow H_2 h \rightarrow t\bar{t}b\bar{b}$ at 13 TeV are shown on the left (right).	82
4.13	Figures show the importance of signal-background (left) and signal-signal (right) interference for the FCC-hh operating at energies of 100 TeV.	82
5.1	Feynman diagram that can receive corrections from dimension-six operators for the considered process.	87
5.2	Diagram indicating the workflow. An event with final states passes through selection and reconstruction before being embedded in a graph structure. A representative diagram is shown for a created graph. The W bosons indicated with red may be missing if the W mass is not reconstructed, and then the final states will be connected directly to the top quarks. The event is then fed into the network of the indicated architecture, which supplies the scores for each class.	90
5.3	Loss and accuracy curves that show convergence for the minimal setup of Sec. 5.4.1 with only three classes. The choice of network architecture avoids overtraining, and this is generalised to the complete setup with all operators of Sec. 5.4.2.	92
5.4	Distribution of generated events according to the SMEFT network scores is shown on the left while ROC curves are on the right. The latter are calculated in a one-vs-rest scheme for each class.	93
5.5	Same as Fig. 5.4 but for fully connected graphs.	93
5.6	Two-dimensional differential distribution histograms for each class.	95

5.7	Exclusion contours on WCs at the 95% CL from the constructed χ^2 . The baseline results with the network selection of Sec. 5.2 are shown in black. On the left, contours are obtained by imposing cuts on the NN scores at optimal values and performing the analysis using $p_T(b_1)$ distributions. On the right, the result with the NN score is again shown in comparison with the contour from the analysis on the 2D score histograms (without cuts on the NN score). The contours from the analysis with the 1D BSM score histogram are also shown.	96
5.8	ROC curves for multi-class classification performed on all the thirteen SMEFT operators and the SM.	97
5.9	Decrease in the 2σ WC interval for individual (orange) and profiled (blue) bounds of Tab. 5.3, when utilising the NN score. The integrated luminosity used is 3/ab.	97
6.1	The $\Delta\phi_{\gamma\ell}$ distribution has two well-separated peaks at LO (left) but this behaviour changes when an extra jet is emitted (right).	107
6.2	95% CL contours for different diboson processes at 139/fb are shown on the left, including the Zjj contour. The best fit lines from the observations of Ref. [329] are also included. On the right, the plot is reproduced for 3/ab.	108
6.3	Field strengths are represented by $X (= B, W, G)$. Assuming $X_1 = X_2$, the relevant dimension-six operators are $\mathcal{O}_{\phi W}$, $\mathcal{O}_{\phi B}$, $\mathcal{O}_{\phi G}$, $\mathcal{O}_{\phi\tilde{W}}$, $\mathcal{O}_{\phi\tilde{B}}$ and $\mathcal{O}_{\phi\tilde{G}}$, while if $X_1 \neq X_2$, the relevant operators are $\mathcal{O}_{\phi WB}$ and $\mathcal{O}_{\phi\tilde{W}B}$. Whether the diagram constructed by the field insertions results in a CP even or CP odd operator depends on the number of γ_5 matrices in the vertices; an even (odd) number of γ_5 s results in a CP even (odd) diagram.	110
6.4	Diagrams to produce the operators \mathcal{O}_W and $\mathcal{O}_{\tilde{W}}$ after integrating out the heavy VLL (see Eq. (6.15)). While the \mathcal{O}_W operator can be produced at one-loop, the CP violating $\mathcal{O}_{\tilde{W}}$ can only be generated at two-loop processes. CP even and odd couplings in the diagram correspond to $a = \alpha_\chi$ and $b = \beta_\chi$ for the model of Eq. (6.18).	111

6.5	Scan over points in the $\text{Re}(y_{\chi_L} y_{\chi_R}^*) - \text{Im}(y_{\chi_L} y_{\chi_R}^*)$ plane for three distinct VLL masses by sampling random values of y_{χ_L} and y_{χ_R} . The absolute values of the ratios in Tab. 6.3 are required to remain less than unity in order to indicate the regions where the leading contributions are sourced by dimension-six operators. The region shaded with gray indicates $ y_{\chi_{L,R}} > 4\pi$	113
6.6	Example histogram for the WBF process showing the SM contribution and the effect of introducing further operators.	115
6.7	Contours for the combined WBF and diboson analyses at $3/\text{ab}$. On the left, $C_{\widetilde{W}}$ and $C_{\phi\widetilde{B}}$ are fixed to zero, while on the right, only $C_{\widetilde{W}} = 0$ is fixed, and profiling is performed over $C_{\phi\widetilde{B}}$	116
7.1	Contours for consistency with Fermilab/BNL in the $C_{eW} - C_{eB}$ plane with $\mu = m_\mu$. The remaining WCs are fixed to zero.	125
7.2	Individual intervals allowed by Fermilab/BNL for C_{eB} , C_{eW} as the dimensional regularisation scale μ is varied.	125
7.3	The filled interval denotes the individual bound on $C_{e\gamma}$ for consistency with the Fermilab/BNL measurement, including one-loop corrections, as a function of μ . The dashed lines indicate the corresponding interval for only tree level contributions.	126
7.4	Plot showing the shift of the $C_{e\gamma}$ K-factor from the additional presence of C_{eZ} , with the scale fixed at $\mu = m_\mu$. The one-loop corrections can be rendered negligible with small values of C_{eZ}	127
7.5	Plots showing the minimum possible K-factor for $C_{e\gamma}$ (at $\mu = m_\mu$), keeping the anomalous magnetic moment in agreement with Fermilab/BNL for different values of the additional WC.	128
7.6	Vertex generated by the presence of the operators in Eq. (7.5) and contributing to the decay of the Higgs.	131
7.7	Normalised histogram for the reconstructed Higgs mass M_{reco} indicating the different shapes between the pure SM contributions and the interference with effective interactions.	131
7.8	Exclusion intervals in the $C_{eW} - C_{eB}$ plane obtained from the $h \rightarrow \mu\mu\gamma$ process.	132

- 7.9 Electroweak (a) and hadronic (b) diagrams for different SM t -channel processes contributing to the differential cross section measured by the MUonE experiment. 134
- 7.10 Contributions to the $d\sigma/dt$ differential distribution from Λ^{-2} terms when different WCs contribute and for the SM. The dimension-six contributions arise from interference with the SM and only a single WC is included for each case with its value set to +1. The histograms are normalised such that the area under the curve corresponds to ± 1 depending on whether the interference is positive or negative. For the SM, the bin adjacent to zero is ~ 0.9 . Additionally, $C_{\phi\ell}^{(1)}$ and $C_{\phi\ell}^{(3)}$ overlap. 135

List of Tables

2.1	Dimension-six operators other than the four-fermion ones from Ref. [139].	31
2.2	Four fermion operators from Ref. [139] conserving the baryon number.	32
2.3	Four fermion operators from Ref. [139] violating the baryon number. C denotes the charge conjugation matrix.	32
3.1	Cross sections in units of pb for SS pair production from WBF and contributing SM background at 100 TeV FCC. The Higgs portal parameters are set to $m_S = 100$ GeV and $\lambda = 1$, and baseline cuts correspond to the cuts in Sec. 3.2.1, that have the relaxed restrictions $\Delta\eta_{jj} > 4.0$, $\cancel{E}_T > 100$ GeV and $m_{jj} > 800$ GeV. Corrections from higher order QCD do not affect the calculated estimates, as shown in Ref. [173].	40
3.2	Cross sections for S pair production through gluon fusion with a radiated jet at 100 TeV FCC. The S field parameters are set to $m_S = 100$ GeV and $\lambda = 1$. Cross sections for the background processes are also shown for the baseline cuts without any \cancel{E}_T cut and $p_T(j_1) > 30$ GeV. Subsequent cuts of $p_T(j_1) > 100$ GeV and $\cancel{E}_T > 150$ GeV reduce the background significantly. It should be noted that subdominant $t\bar{t}j$ contamination has not been taken into account and all the background cross sections are corrected with a K-factor of $K \simeq 1.6$ [173] to accommodate NLO effects.	41
3.3	Cross sections before and after the applied cuts for the pair production of SS along with a Z through a virtual Higgs. The values are for $\sqrt{s} = 500$ GeV with model parameters set to $m_S = 100$ GeV and $\lambda = 1$	43

3.4	The effect of the applied cuts on the cross sections for the S pair produced through WBF and background at 3 TeV CLIC. Parameters of the model are set to $m_S = 100$ GeV and $\lambda = 1$, while cuts $\cancel{E}_T' > 70$ GeV and $M_{ee} > 1500$ GeV are enforced at generation level.	44
4.1	SM contributions with identical final state as the signature of process (4.23) at the 13 TeV LHC. It should be noted that the rates of $t\bar{t}b\bar{b}$, $t\bar{t}h$ and $t\bar{t}Z$ have been scaled with K-factors 1.8 [253], 1.17 [105] and 1.2 [254], respectively. The selection criteria used are discussed in Sec. 4.3.3.	69
5.1	Distributions used for the fit in this Chapter, from Ref. [311].	86
5.2	2σ bounds on WCs with the baseline analysis for different luminosities.	98
5.3	Optimal improvements on the 2σ constraints by using a cut on the NN score. . .	99
6.1	Operators of the X^3 and $\phi^2 X^2$ classes, along with their matched WCs obtained by integrating out the heavy VLL of Eq. (6.15). For simpler expressions, the WCs (\mathcal{C}_i) do not include the $(16\pi^2 m^2)^{-1}$ factor.	112
6.2	Dimension-eight CP violating operators of the $\phi^4 X^2$ class and their WCs. The operator structures are from Ref. [345].	112
6.3	Ratio of dimension-eight and -six WCs.	113
7.1	Intervals on WCs (units of TeV^{-2}) for Δa_μ lying within the Fermilab/BNL measurement and for remaining within the errors of the SM prediction given in Ref. [136], using $\mu = m_\mu$. Only bounds with values $\lesssim 4\pi/\text{TeV}^2$ are shown.	123
7.2	68% bounds on WCs in units of TeV^{-2} from the Z boson decay. Perturbatively meaningful constraints for the dipole operators could not be obtained.	129
7.3	68% CL individual intervals on WCs from MUonE. When reexpressed, these correspond to $ C_{e\gamma} \leq 0.18$ and $ C_{eZ} < 12.75$, and MUonE can not obtain perturbatively meaningful constraints for operators of the $\psi^2 \phi^2 D$ class.	135

Chapter 1

Introduction

The Standard Model of particle physics addresses the elementary constituents of the Universe along with their fundamental interactions, and it does so with a tremendous amount of success, unveiling many of the microscopic world's enigmas.

Its accomplishments are the result of many years of theoretical developments and an immense amount of measurements gathered by experiments with great effort. The epitome of achievements was the discovery of the Higgs boson in 2012 [8, 9] as theorised by the Standard Model but finding the particle was not a surprise. The Large Hadron Collider, smashing the previous records of centre-of-mass energies, was guaranteed to either discover the long-awaited boson or some new mechanism to supply masses for the elementary particles. Nevertheless, the theory is no panacea; phenomena such as dark matter, gravity, baryogenesis and more remain unaddressed, and the hopes were high that the Large Hadron Collider would be able to discover or deliver evidence of new physics.

As the Large Hadron Collider enters the third operational round, hopes still remain that, in the near future, evidence of beyond the Standard Model physics might be observed. With efforts focusing on the question “What’s beyond the Standard Model?” the particle physics community has proven to be extremely resourceful. Studies range from exploring concrete theories of the ultraviolet regime in order to assess their applicability in resolving the puzzling flaws of the Standard Model, to model-independent reinterpretations of experimental results within effective field theories. New creative techniques have been demonstrated to be, beyond doubt, valuable in searching for new physics, such as applications of Machine Learning which can provide

state-of-the-art results unachievable through the mainstream methodology. In the meantime, new experimental collider concepts have been proposed either for the (relatively) recent or faraway future, including upgrades of the Large Hadron Collider, precise linear lepton colliders and circular hadron colliders reaching unprecedented energies of even 100 TeV.

This thesis aims to explore a variety of paths forward utilising many of the methods of the wide community, with emphasis on the caveats of the Standard Model. In Chapter 2, the Standard Model is introduced before and after the electroweak symmetry breaking, giving rise to massive particles. The anticipation of the discovery of the Higgs is detailed by requiring compliance with perturbative unitarity, and the most critical processes of the Higgs sector at the Large Hadron Collider are enumerated. The rest of the thesis is devoted to the remaining mysteries unexplainable by the Standard Model, which motivate the search for new physics, either with concrete models or the Standard Model Effective Field Theory.

With attention centred on dark matter, the Higgs portal model is thoroughly investigated in Chapter 3. The relevant direct and indirect modes are identified for both lepton and hadron collider concepts of the future, and a detailed comparison of the constrained parameter space is conducted. The study includes direct production of dark matter, measurements of the Higgs strength and di-Higgs production, and also a two-loop calculation of the affected Peskin-Takeuchi parameters.

In Chapter 4, scalar cascade decays are shown to be an excellent probe of models with extended scalar sectors when Machine Learning techniques are employed. Recurrent Neural Networks exploiting the phenomenology of the events can separate efficiently the signal from background leading to discovery, in contrast with standard cut-and-count techniques. The effects of both signal-background and signal-signal interference are also evaluated, as destructive interference could compromise sensitivity.

Shifting the perspective to model-independent approaches in Chapter 5, Graph Neural Networks are shown to be a powerful paradigm of how Neural Networks benefit from the underlying structure of the events when embedded into physics-inspired graphs. The unparallel signal-background discrimination leads to favourable constraints on Wilson Coefficients in the top sector compared with a baseline differential distribution analysis.

In Chapter 6, CP violation in the gauge-Higgs sector is explored in a model-independent fashion, showing that diboson processes are instrumental in placing bounds on the relevant interactions. Motivated by top-down approaches, the space of Wilson Coefficients can be reduced in motivated

scenarios and a minimal fit of CP violation in the gauge-Higgs sector is obtainable by the inclusion of Higgs data. Chapter 7 reinterprets the anomalous magnetic moment within the Standard Model Effective Theory framework and explores avenues to scrutinise the dipole operators which could explain the Fermilab/BNL measurements.

Finally, Chapter 8 summarises this thesis.

Chapter 2

The Standard Model of particle physics

The best current description of elementary particles and their interactions is given by the Standard Model of Particle Physics (SM), which combines quantum chromodynamics (QCD) [10–12] with the Glashow-Salam-Weinberg model [13–15] under the internal gauge symmetry group $SU(3)_C \times SU(2)_L \times U(1)_Y$. Quarks are colour charged and strong interactions are mediated by gluons, which are related to the generators of the $SU(3)_C$ group. Both leptons and quarks are charged under the weak isospin and hypercharge groups, denoted by $SU(2)_L$ and $U(1)_Y$, respectively, where C, L, Y are the quantum numbers of the relevant group. The electroweak part of the symmetry group, $SU(2)_L \times U(1)_Y$, unifies the electromagnetic and weak interactions in the unbroken phase.

In the Lagrangian formalism, the invariance under the symmetry group manifests the conserved quantities present in nature, and as in any relativistic theory, the construction of the Lagrangian must additionally satisfy invariance under transformations of the external Poincaré group, consisting of translations and Lorentz transformations. Restricting the Lorentz group to only elements connected to the identity and preserving the direction of time, one is left with the special orthochronous group $SO_+^\uparrow(1,3) = SL(2, \mathbb{C})/\mathbb{Z}_2$, where the right-hand-side denotes its universal cover group and \mathbb{Z}_2 identifies which elements are connected to $\mathbb{1}_2$ or $-\mathbb{1}_2$. The Lie algebra of the universal cover group splits upon complexification into two distinct $su(2)$ algebras. Lorentz representations can be thus identified from representations of $su(2) \oplus su(2)$ and are given in

the (\cdot, \cdot) notation. Building blocks of the SM Lagrangian are then fields in the scalar, left- and right-handed Weyl and vector representations of the Lorentz group, denoted as $(\mathbf{0}, \mathbf{0})$, $(\mathbf{1}/\mathbf{2}, \mathbf{0})$, $(\mathbf{0}, \mathbf{1}/\mathbf{2})$ and $(\mathbf{1}/\mathbf{2}, \mathbf{1}/\mathbf{2})$, respectively.¹

The Lagrangian can be separated into a Yang-Mills component describing the dynamics of the three gauge bosons, as well as a Higgs and a fermion part,

$$\mathcal{L}_{\text{SM}} = \mathcal{L}_{\text{gauge}} + \mathcal{L}_H + \mathcal{L}_F . \quad (2.1)$$

The spontaneous symmetry breaking (SSB) of the electroweak group to the Quantum Electrodynamics (QED) group $SU(2)_L \times U(1)_Y \rightarrow U(1)_{\text{QED}}$ occurs by the presence of a complex scalar doublet, known as the Higgs field, which acquires a non-zero vacuum expectation value (VEV) in the broken phase. While the gluon and photon remain massless after SSB, the weak bosons and the fermions acquire masses, with the exception of the neutrinos (although extensions to accommodate this are viable). The SM Lagrangian before and after SSB is renormalisable at all orders of the perturbative expansion [17–19], with ultraviolet (UV) divergences commonly removed by the introduction of counterterms. The following sections will describe each of the Lagrangian parts by introducing the relevant fields and discussing the physical implications following SSB.²

2.1 Standard Model Lagrangian in the unbroken phase

2.1.1 The Yang-Mills part

The gauge dynamics of the theory are included in the Yang-Mills part of Eq. (2.1) and are associated with the internal symmetries of the theory. For a local non-abelian gauge group $SU(N)$, the gauge field is defined in terms of the generators of the Lie Algebra in the fundamental representation as $A_\mu = A_\mu^a t^a$, where the generators t^a satisfy the commutation relation

$$[t^a, t^b] = i f^{abc} t^c . \quad (2.2)$$

¹It should be noted that as the Poincaré group has no finite-dimensional unitary representations, an infinite-dimensional representation can be constructed by having the basis of the fields depend on momentum p^μ , following Wigner’s classification [16].

²The interested reader can find thorough introductions in Refs. [20–22].

The coefficients f^{abc} are the antisymmetric structure constants of the Lie algebra. The antisymmetric field strength tensor defined as

$$F_{\mu\nu}^a = \partial_\mu A_\nu^a - \partial_\nu A_\mu^a + gf^{abc} A_\mu^b A_\nu^c, \quad (2.3)$$

can be then used to write down a Lagrangian term that is locally invariant under the $SU(N)$ transformations [23],

$$\mathcal{L}_{\text{gauge}} = -\frac{1}{4} F^{a\mu\nu} F_{\mu\nu}^a, \quad (2.4)$$

and induces the propagation of the gauge boson A . The introduction of interactions between the gauge bosons and additional fields is attainable by acting on the fields with the covariant derivative $D_\mu = \partial_\mu - igA_\mu^a t^a$.

It should be noted that for the abelian $U(1)$, the structure constant terms disappear, and one is left with the usual electromagnetic tensor. Therefore for the SM symmetry, the three field strength tensors for $SU(3)_C$, $SU(2)_L$ and $U(1)_Y$ are

$$G_{\mu\nu}^a = \partial_\mu G_\nu^a - \partial_\nu G_\mu^a + g_s f^{abc} G_\mu^b G_\nu^c, \quad \text{with } \{a, b, c\} \in \{1, \dots, 8\}, \quad (2.5)$$

$$W_{\mu\nu}^I = \partial_\mu W_\nu^I - \partial_\nu W_\mu^I + g_2 \epsilon^{IJK} W_\mu^J W_\nu^K, \quad \text{with } \{I, J, K\} \in \{1, 2, 3\}, \quad (2.6)$$

$$B_{\mu\nu} = \partial_\mu B_\nu - \partial_\nu B_\mu, \quad (2.7)$$

respectively, where the structure constants of the $SU(2)_L$ group are given by the three-dimensional Levi-Civita tensor ϵ^{IJK} . For each group, a Yang-Mills term (2.4) built from the field tensors is added in the classical SM Lagrangian to describe the dynamics of the (massless) three gauge fields. The covariant derivative of the SM gauge group subsequently reads as

$$D_\mu = \partial_\mu - ig_1 B_\mu Y - ig_2 W_\mu^I T^I - ig_s G_\mu^a t^a, \quad (2.8)$$

where Y (g_1), T^I (g_2) and t^a (g_s) are the generators (gauge couplings) of $U(1)_Y$, $SU(2)_L$ and $SU(3)_C$ respectively, and allows the construction of gauge-invariant currents when fermion and scalar matter fields are introduced later on.

2.1.2 Fermionic part

Fermionic matter in the SM includes leptons and quarks, both interacting with the electromagnetic force, with the distinction between them being that only the quarks are charged under the colour

group³. In terms of the isospin group, the left-handed fermion Weyl fields are grouped into doublets, and their representations under the SM group are

$$Q_i^{\prime L} = (u_i^{\prime L}, d_i^{\prime L}) : (\mathbf{3}, \mathbf{2}, +\frac{1}{6}), \quad (2.9)$$

$$L_i^{\prime L} = (\nu_i^{\prime L}, \ell_i^{\prime L}) : (\mathbf{1}, \mathbf{2}, -\frac{1}{2}), \quad (2.10)$$

where the $i = 1, 2, 3$ indexes the generation. The unprimed notation for fermions is reserved for the fields in the physical basis. Each of the right-handed fields transforms as a singlet of $SU(2)_L$

$$u_i^{\prime R} : (\mathbf{3}, \mathbf{1}, +\frac{2}{3}), \quad (2.11)$$

$$d_i^{\prime R} : (\mathbf{3}, \mathbf{1}, -\frac{1}{3}), \quad (2.12)$$

$$\ell_i^{\prime R} : (\mathbf{1}, \mathbf{1}, -1), \quad (2.13)$$

and $SU(2)_L$ generators do not act on $u_i^{\prime R}$, $d_i^{\prime R}$ and $\ell_i^{\prime R}$ when the covariant derivative of the SM is applied. Right-handed neutrinos are not included in the minimal SM, although it is feasible to do so in order to take into account the neutrino oscillations that are supported by experimental evidence [27–35]. The fermionic part of the Lagrangian takes the form

$$\mathcal{L}_f = \sum_i (\bar{L}_i^{\prime L} i \not{D} L_i^{\prime L} + \bar{Q}_i^{\prime L} i \not{D} Q_i^{\prime L}) + \sum_i (\bar{\ell}_i^{\prime R} i \not{D} \ell_i^{\prime R} + \bar{u}_i^{\prime R} i \not{D} u_i^{\prime R} + \bar{d}_i^{\prime R} i \not{D} d_i^{\prime R}), \quad (2.14)$$

where the Dirac-slashed notation has been adopted when gamma matrices are contracted with Lorentz vectors ($\gamma_\mu k^\mu = \not{k}$ for a Lorentz vector k^μ). Any of the aforementioned left- and right-handed fermionic fields can be grouped in Dirac bispinors of the $(\mathbf{1}/\mathbf{2}, \mathbf{0}) \oplus (\mathbf{0}, \mathbf{1}/\mathbf{2})$ Lorentz representation

$$f' = \begin{pmatrix} f^{\prime L} \\ f^{\prime R} \end{pmatrix}, \quad (2.15)$$

and the Weyl fields are recovered using the projectors $\mathbb{P}^{L,R} = (1 \mp \gamma_5)/2$ with $f^{\prime L,R} = \mathbb{P}^{L,R} f'$.

³Quarks were initially introduced in Refs. [24, 25] in order to categorise and provide relations for baryons. Later developments led to the concept of colour with quarks interacting via the gluon octet [12, 26].

2.1.3 Higgs part

While constructing the SM Lagrangian, one quickly realises that masses for the fermion fields are impossible to introduce. While mass terms such as $-m(\bar{f}'^L f'^R + \bar{f}'^R f'^L)$ are allowed in QED, the chiral $SU(2)_L$ transformation does not leave the term invariant and such term is consequently forbidden when invariance under the SM group is required. The problem also extends to mass terms for gauge bosons since, after an infinitesimal gauge transformation, one realises that terms such as $-m^2 W_\mu^a W^{\mu,a}$ are not gauge-invariant and the mediators have to remain massless. A viable way around this is to spontaneously break the $SU(2)_L \times U(1)_Y$ symmetry with the inclusion of a scalar field that acquires a finite VEV and leaves the QED $U(1)_{\text{QED}}$ as the remaining symmetry of the theory [36–40]. To achieve this, a complex scalar field, called the Higgs field, is introduced with representation under the SM gauge group as

$$\Phi = \begin{pmatrix} \Phi^+ \\ \Phi^0 \end{pmatrix} : (\mathbf{1}, \mathbf{2}, +\frac{1}{2}) . \quad (2.16)$$

The hypercharge is chosen as $+1/2$ by convention, although it is necessary to have a hypercharge $\pm 1/2$ to allow for Yukawa couplings. The Higgs potential reads

$$V(\Phi) = \frac{\lambda_{\text{SM}}}{4} (\Phi^\dagger \Phi)^2 - \mu^2 \Phi^\dagger \Phi , \quad (2.17)$$

where $\lambda_{\text{SM}} > 0$ otherwise, the potential is unbounded from below and $\mu^2 > 0$ since the relative sign of the two terms must be opposite in order to have a non-vanishing VEV.⁴ The Higgs part of the SM Lagrangian is then given by

$$\mathcal{L}_H = (D_\mu \Phi)^\dagger (D^\mu \Phi) - V(\Phi) - \sum_{i,j} \left(\bar{L}_i'^L Y_{ij}^\ell \ell_j'^R \Phi + \bar{Q}_i'^L Y_{ij}^u u_j'^R \Phi^c + \bar{Q}_i'^L Y_{ij}^d d_j'^R \Phi + \text{h.c.} \right) , \quad (2.18)$$

where the charge conjugated Higgs field is $\Phi^c = i\tau^2 \Phi^* = (\phi^{0*}, -\phi^-)$ and Y^ℓ, Y^u, Y^d are the Yukawa coupling matrices⁵, which will be responsible for the masses of fermions after SSB.

⁴It should be noted that the potential receives corrections from higher orders leading to the effective Coleman-Weinberg potential [41]. Higher orders can imply instability. There can exist a deeper stable vacuum, and it would be possible for the current vacuum to decay to it through quantum tunneling [42–44]. Current results indicate that the SM is metastable (see Ref. [45] and for a pedagogical review see Ref. [46]).

⁵These lead to the Yukawa potential proposed in Ref. [47].

2.2 Standard Model Lagrangian in the physical basis

The classical scalar potential $V(\Phi)$ has a non-zero minimum at

$$|\langle\Phi\rangle| = \frac{2\mu^2}{\lambda_{\text{SM}}} \equiv \frac{v^2}{2} \neq 0. \quad (2.19)$$

Without loss of generality, we can then expand the Higgs field around the VEV as

$$\Phi = \begin{pmatrix} \pi^+ \\ \frac{1}{\sqrt{2}}(v + h + i\pi^0) \end{pmatrix}, \quad (2.20)$$

which introduces two charged and one neutral Goldstone bosons (π^\pm, π^0), as well as a real physical field h .

The high-energy electroweak symmetry is then broken to the low-energy $U(1)_{\text{QED}}$ whose mediator is the massless physical photon given as a linear combination of the W_μ^3 generator of $SU(2)_L$ and the hypercharge boson B_μ . The hypercharges have been thus defined in such a way that after SSB the couplings of fermionic fields to the photon reproduce the QED results (up to conventions). The following sections explore the implications of SSB, mainly how the two weak bosons, the leptons and the quarks acquire masses, as well as the interactions between the physical states.

2.2.1 Higgs sector after SSB

In order to identify the mass eigenstates for the weak vector bosons, one needs to expand the kinetic part of the Higgs Lagrangian and identify bilinear terms coupled due to the presence of the VEV. For simplicity the unitary gauge (see Sec. 2.3) will be used, where the Goldstone fields decouple and $\pi^a = 0$ ($a \in \{+, -, 0\}$) eliminates any unphysical degrees of freedom. The eigenstates of the QED charge and mass will then be the physical content of the SM after SSB. Due to the fact that the hypercharge of the gauge bosons vanishes, one concludes that the eigenstates of the charge operator Q are found from the generator T^3 which is equal to $-i\epsilon^{3ab}$ in the adjoint representation of $SU(2)_L$. Identifying the eigenvalues and eigenvectors of the Levi-Civita tensors manifests that the physical states must be combinations of the uncharged W_μ^3, B_μ and the charged $W_\mu^\pm = (W_\mu^1 \mp iW_\mu^2)/\sqrt{2}$. The expanded Lagrangian of the Higgs sector

with the gauge field redefinitions includes the bilinear terms

$$\begin{aligned} \mathcal{L}_H \supset & \frac{1}{4}v^2g_2^2W_\mu^-W^{+\mu} + \frac{1}{8}v^2(g_2W_\mu^3 + g_1B_\mu)(g_2W^{3\mu} + g_1B^\mu) \\ & + \frac{1}{2}(\partial_\mu h)^2 - \mu^2h^2 - \frac{1}{\sqrt{2}}(v+h) \sum_{f \in \{\ell, u, d\}} \sum_{i,j} \left(\bar{f}_i^L Y_{ij}^\ell f_j^R + \text{h.c.} \right), \end{aligned} \quad (2.21)$$

where the second line contains the dynamics of the physical scalar h and the masses of the fermionic fields.

The mass of the charged gauge boson is, therefore, $M_W = g_2v/2$, and it is necessary to diagonalise the term corresponding to the neutral bosons B_μ, W_μ^3 . To keep the bosons canonically normalised, they should only be orthogonally rotated with

$$\begin{pmatrix} B_\mu \\ W_\mu^3 \end{pmatrix} = \begin{pmatrix} c_w & -s_w \\ s_w & c_w \end{pmatrix} \begin{pmatrix} A_\mu \\ Z_\mu \end{pmatrix} \implies \begin{pmatrix} A_\mu \\ Z_\mu \end{pmatrix} = \begin{pmatrix} c_w & s_w \\ -s_w & c_w \end{pmatrix} \begin{pmatrix} B_\mu \\ W_\mu^3 \end{pmatrix}, \quad (2.22)$$

where $c_W = \cos \theta_W$ and $s_W = \sin \theta_W$ stand for the cosine and sine of the Weinberg angle, defined with $\tan \theta_W = g_1/g_2$. After the rotation, the covariant derivative part related to the photon is rewritten as

$$\begin{aligned} -D_\mu \supset & ig_1B_\mu Y + ig_2W_\mu^I T^I, \\ & \supset ieA_\mu(T^3 + Y), \end{aligned} \quad (2.23)$$

and denoting the electric charge as Q the relation between the third isospin generator and the hypercharge, it can be read off as

$$Q = Y + T^3. \quad (2.24)$$

This is the Gell-Mann-Nishijima relation [48, 49] which measures the electric charge of particles. The mass of the heavy weak boson can be then identified from Eq. (2.21) as $M_Z = v\sqrt{g_1^2 + g_2^2}/2$ while A_μ remains massless as required for the photon field. For the discovery of the W and Z bosons see Refs. [50–53].

Eq. (2.21) also predicts the existence of a physical scalar h that is neutral and has a mass $M_h = \sqrt{2}\mu$. In addition, the Yukawa terms indicate that all fermions, with the exception of

neutrinos, acquire masses after diagonalisation of the matrices

$$M_{ij}^f = \frac{1}{\sqrt{2}} Y_{ij}^f v, \quad f = \ell, u, d. \quad (2.25)$$

which is performed by using a bi-unitary transformation acting differently on the left- and right-handed fermion fields. Using $f_i^L = \sum_k U_{ik}^{f,L} f_k^{\prime L}$ and $f_i^R = \sum_k U_{ik}^{f,R} f_k^{\prime R}$ allows the identification of the fermion masses as

$$m_{f,i} = \frac{v}{\sqrt{2}} \sum_{k,m} U_{ik}^{f,L} Y_{km}^f (U_{mi}^{f,R})^\dagger. \quad (2.26)$$

It should also be mentioned that the interactions of Higgs field h with the fermions are also diagonalised after the bi-unitary transformations, and the couplings will be proportional to the fermion masses.

2.2.2 Fermion sector after SSB

As already stated, the hypercharges were defined in such a manner that after SSB the couplings of the fermions to the photons match the couplings of the well-tested theory of QED, given by the currents

$$e Q_f \bar{f}_i \not{A} f_i. \quad (2.27)$$

Q_f denotes the charge of the corresponding fermion under $U(1)$ and in the SM is given by Eq. (2.24). The fermionic Lagrangian of Eq. (2.14) can be rewritten in terms of the physical fermions and it includes the term

$$\mathcal{L}_F \supset \sum_i g_2 s_w Q_f \bar{f}_i \not{A} f_i. \quad (2.28)$$

Matching the two terms allows the determination of the relation between the gauge coupling constants and the elementary charge

$$e = g_2 s_w = g_1 c_w = \frac{g_1 g_2}{\sqrt{g_1^2 + g_2^2}}. \quad (2.29)$$

The rest of the terms in the fermion part of the Lagrangian quantify the interactions of the

fermions with Z_μ and W_μ^\pm which after the rotation to the physical basis read as

$$\begin{aligned} \mathcal{L}_F \supset & \sum_i \frac{e}{c_w s_w} (\bar{f}_i^L \gamma^\mu T^3 f_i^L - s_w^2 Q_f \bar{f}_i^L \gamma^\mu f_i) Z_\mu \\ & + \sum_{i,j} \frac{e}{\sqrt{2} s_w} \left(\bar{u}_i^L \gamma^\mu [U^{u,L}(U^{d,L})^\dagger]_{ij} d_j^L W_\mu^+ + \bar{d}_i^L \gamma^\mu [U^{d,L}(U^{u,L})^\dagger]_{ij} u_j^L W_\mu^- \right) \\ & + \sum_{i,j} \frac{e}{\sqrt{2} s_w} \left(\bar{\nu}_i^L \gamma^\mu [U^{\nu,L}(U^{\ell,L})^\dagger]_{ij} \ell_j^L W_\mu^+ + \bar{\ell}_i^L \gamma^\mu [U^{\ell,L}(U^{\nu,L})^\dagger]_{ij} \nu_j^L W_\mu^- \right). \end{aligned} \quad (2.30)$$

The current coupled to the Z boson is not dependent on the bi-unitary matrices $U_{ij}^{f,L}$ and $U_{ij}^{f,R}$ and hence there are no neutral flavour-changing currents in the classical Lagrangian of the SM. This is not the case for the current coupled to the W^\pm bosons where the matrix $V = U^{u,L}(U^{d,L})^\dagger$ induces mixing between the up and down flavours in the quark sector. The matrix is known as the Cabibbo-Kobayashi-Maskawa (CKM) matrix [54, 55] which, as a 3×3 complex unitary matrix, has nine real degrees of freedom. Five degrees of freedom can be absorbed into phase transformations of the fields that leave the masses invariant, resulting in three degrees of freedom, corresponding to rotation angles and one phase, which can induce CP violation in the SM.

Since massless neutrinos were assumed, there is freedom in choosing $U_{ik}^{\nu,L}$ such that the physical neutrino states $\nu_i^L = \sum_j U_{ij}^{\ell,L} \nu_j^{\prime L}$ induce no mixing between leptons and neutrinos through interactions with the charged W boson.

This concludes the discussion of the classical SM Lagrangian. As in any quantum field theory, the Lagrangian must be quantised, and this will be performed with the path integral formalism.

2.3 Path Integral quantisation

The classical Lagrangian of the SM given by Eq. (2.1) after the rotation to the mass basis can be quantised by defining the generating functional (or partition function) [20]

$$\mathcal{Z}[J_V, J_\phi, J_\psi] = \int \mathcal{D}V \mathcal{D}\phi \mathcal{D}\bar{\psi} \mathcal{D}\psi e^{i\mathcal{S}}, \quad (2.31)$$

$$\text{for the action } \mathcal{S} = \int d^4x \mathcal{L} + \sum_V J_V V_\mu + \sum_\phi J_\phi + \sum_\psi (J_\psi \psi - \bar{\psi} J_{\bar{\psi}}), \quad (2.32)$$

where V , ϕ and ψ denote any vector boson, scalar or fermion present, respectively, and $J_{V,\phi,\psi,\bar{\psi}}$ are the sources. The integration is performed over all field configurations, and for fermionic fields, the integration is over Grassmann numbers to capture the anticommuting behaviour. Matrix elements (or Green's functions) can then be calculated as

$$G_n(x_1, \dots, x_n) = \langle T\{\phi x_1 \dots \phi x_n\} \rangle = \frac{1}{\mathcal{Z}[0, 0, 0]} \int \mathcal{D}V \mathcal{D}\phi \mathcal{D}\bar{\psi} \mathcal{D}\psi e^{iS} \phi(x_1) \dots \phi(x_n) \quad (2.33)$$

with similar equations for the rest of the fields. An expansion of the exponential results in a perturbative treatment, which can also be used to derive the Feynman rules for the theory. Green's functions are the basis of calculations in perturbation theory, as in the momentum space after truncation, they result in the S -matrix element

$$\langle i|S|f \rangle = (2\pi)^4 \delta^4(p_i - p_f) G_n^{\text{trunc}}(p_1, \dots, p_n), \quad (2.34)$$

describing the transition from the initial state to the final. Truncation is performed by associating propagators only to internal lines, as the propagators of external lines are cancelled by the Lehman-Symanzik-Zimmermann (LSZ) reduction formula relating Green's functions to $\langle i|S|f \rangle$ [56]. The LSZ formula for m incoming and n outgoing scalar particles of masses m_j (where j runs from unity to $k+n$) is given by

$$\begin{aligned} \langle i|S|f \rangle &= \langle -p_{k+1}, \dots, p_{n+k} | S | p_1, \dots, p_k \rangle \\ &\propto (2\pi)^4 \delta^4(p_i - p_f) (p_1^2 - m_1^2) \dots (p_{n+k}^2 - m_{n+k}^2) G(p_1, \dots, p_{n+k}) \Big|_{p_j^2 = m_j^2}. \end{aligned} \quad (2.35)$$

Therefore, calculating a process proceeds by identifying the appropriate Feynman rules and then summing over all the connected Feynman diagrams in momentum space with the appropriate external lines.

The first step would be to derive the propagators of the free fields, which can be achieved by manipulating the Lagrangian in the action to appear in the form of a Gaussian integral and then performing the integration over the configuration space. The fields whose matrix element is being evaluated are subsequently replaced with derivatives with respect to the respective source, and evaluating the derivatives would result in the propagator. N -point Green's functions proceed in a similar manner.

However, a complication arises for the vector bosons due to the fact that performing the Gaussian

integral over the configurations requires the inversion of $K^{\mu\nu} = g^{\mu\nu}\partial^2 - \partial^\mu\partial^\nu$ which appears in the Lagrangian from the gauge term and is singular. The issue can be understood to arise due to the integration over two unphysical degrees of freedom and is resolved with gauge fixing through the Faddeev-Popov procedure [57]. This requires the appearance of the unphysical ghost and anti-ghost fields for each of the gauge bosons, denoted as u^a and \bar{u}^a , for $a \in \{+, -, A, Z, G\}$. It should also be noted that SSB will induce bilinear terms coupling a gauge vector boson with a Goldstone when not using the unitary gauge, and it is hence convenient to formulate gauge fixing in such a way that these terms cancel in the Lagrangian up to total derivatives. In particular, one has

$$\begin{aligned} C_G^a &= \frac{1}{\sqrt{\xi_G}} \partial^\mu G_\mu^a, \\ C_A &= \frac{1}{\sqrt{\xi_A}} \partial^\mu A_\mu, \\ C_Z &= \frac{1}{\sqrt{\xi_Z}} \partial^\mu Z_\mu - M_Z \sqrt{\xi_Z} \pi^0, \\ C_\pm &= \frac{1}{\sqrt{\xi_W}} \partial^\mu W_\mu^\pm \mp i M_W \sqrt{\xi_W} \pi^\pm, \end{aligned} \tag{2.36}$$

which results in an effective Lagrangian term

$$\mathcal{L}_{\text{fix}} = -\frac{1}{2} [(C_A)^2 + (C_Z)^2 + C_+ C_- + C_G^a C_G^a]. \tag{2.37}$$

To maintain the consistency of the path integral after the introduction of the gauge-fixing Lagrangian and to compensate for its effects the ghost Lagrangian

$$\mathcal{L}_{\text{ghost}} = \bar{u}^a \frac{\delta C^a}{\delta \theta^b} u^b, \text{ where } \{a, b\} \in \{+, -, A, Z, G\}, \tag{2.38}$$

must be introduced, which involves the variations of Eq. (2.36) with respect to gauge transformation of a vector boson θ^V . The quantised SM Lagrangian after SSB is then effectively written as the sum of the classical Lagrangian, the gauge fixing term and the ghost part (for more details, see [20]). The generating functional is also modified to include integrations over the ghost and anti-ghost configurations. The vector boson propagators are given by

$$\Delta_{VV}^{\mu\nu}(q) = \frac{-i}{q^2 - M_V^2} \left[g^{\mu\nu} + (\xi_V - 1) \frac{q^\mu q^\nu}{q^2 - \xi_V M_V^2} \right], \tag{2.39}$$

while for the Goldstone bosons, they read as

$$\Delta_{\pi^i \pi^i}(q^2) = \frac{i}{q^2 - \xi_V M_V^2} \quad (2.40)$$

where $i \in +, -, 0$ and V indicates the associated vector boson that becomes massive. Commonly $\xi_V \rightarrow \infty$ for tree level calculations, which corresponds to the unitary gauge, while for loop calculations, the Feynman gauge $\xi_V = 1$ is often preferred since the Goldstone propagators cancel a term in the vector propagators. The unitary gauge $\xi_V \rightarrow \infty$ is preferred for tree level calculations as the Goldstones decouple. It should be emphasised that physical quantities remain the same irrespective of the gauge choice as the theory is gauge invariant.

Expressions for all the propagators and Feynman rules in the R_ξ gauge can be found in Ref. [20]. Nowadays their calculation from an implemented Lagrangian proceeds practically by utilising automated packages such as FEYNRULES [58, 59] and SARAH [60]. Amplitudes are then calculated by drawing suitable diagrams involving the desired external states. Diagrams with loops, however, can result in divergences; this is remedied in the next section.

2.4 Renormalisation

At tree level in the unitary gauge, the free parameters of the Lagrangian intuitively have a physical meaning and are related to physical quantities. For example, the masses appearing in bilinear terms correspond to the actual physical masses of the particles. In contrast with the classical theory, though, the quantisation allows Feynman diagrams with closed loops (see Ref. [61]) where higher orders contribute to the values of the parameters, breaking the direct relation to physical observables. More importantly, these ‘bare parameters’ of the Lagrangian can be infinite, resulting in divergent expressions when calculating loops. The solution to this difficulty is to first regularise the theory to make the divergent expressions well-defined. This can be done with the Pauli-Villars regularisation by introducing a cut-off Λ when integrating over the loop momenta and then taking the appropriate limit to recover the original theory. Subsequently, bare parameters of the regularised theory are redefined in terms of physical parameters. Considering as an example the Coulomb potential, loops with electrons result in higher order corrections involving the bare parameter e , but result in UV divergences. A possible renormalisation procedure could proceed by defining the renormalised electric charge e_R as the Coulomb potential at some particular momentum scale, up to a fixed order at perturbation theory. The bare parameter can then be

substituted for the renormalised, and the theory is predictive with results for physical observables dependent on the chosen scale.

It is not necessary to renormalise the theory in terms of observables; in fact, it is more common to renormalise Green's functions of subgraphs used to construct the matrix elements. For some renormalisation scale μ , the bare parameters are reparametrised by inserting renormalisation coefficients. Such coefficients can also be introduced for the fields since the normalisation of the states is also modified. In perturbation theory, for a bare parameter g_0 , and a field ϕ_0 , these can be expanded as

$$\begin{aligned} g_0 &= Z(\mu)g_R = (1 + \delta Z_g(\mu)) g_R, \\ \phi_0 &= Z_\phi^{1/2}(\mu)\phi_R = \left(1 + \frac{1}{2}\delta Z_\phi(\mu)\right) \phi_R. \end{aligned} \quad (2.41)$$

The Lagrangian of the theory then reads

$$\mathcal{L}(\phi_0, g_0) = \mathcal{L}(\phi_R, g_R) + \mathcal{L}_{\text{ct}}(\phi_R, g_R, \delta Z_\phi, \delta Z_g), \quad (2.42)$$

and the counterterm Lagrangian \mathcal{L}_{ct} induces the Feynman rules for the counterterms. By imposing renormalisation conditions on Green's functions, the theory can be renormalised order by order with infinite quantities absorbed in the counterterms. It should be highlighted that only superficially divergent diagrams require renormalisation. Considering for example (see e.g. [20, 21])

$$\begin{array}{c} \text{Diagram: a circle loop with two wavy external lines. The top arc has a clockwise arrow and is labeled 'k'. The bottom arc has a counter-clockwise arrow and is labeled 'k-p'.$$

$$\propto \int d^4k \frac{\text{Tr} [\gamma_\mu(\not{k} + m)\gamma_\nu(\not{k} - \not{p} + m)]}{[k^2 - m^2][(k-p)^2 - m^2]}, \quad (2.43)$$

in the SM, and defining the superficial degree of divergence D as the overall power of the loop momenta, including the integral measure, the diagram has $D = 2$ and needs to be regulated and renormalised. Interestingly some integrals are divergent for dimensions $d \geq 4$ which is the basis of the dimensional regularisation scheme [62], where diagrams are reformulated in $d = 4 - 2\epsilon$ dimensions and then the original theory is recovered by the $\epsilon \rightarrow 0$ limit. Any UV divergence at one loop appears then as a pole in ϵ^{-1} with the form

$$\Delta = \frac{\Gamma(1 + \epsilon)}{\epsilon} = \frac{1}{\epsilon} + \log(4\pi) - \gamma_E, \quad (2.44)$$

where γ_E is the Euler-Mascheroni constant. The renormalisation condition will then determine how the pole is subtracted. Absorbing only the ϵ^{-1} pole in the suitable counterterm would result in the minimal-subtraction scheme (MS), while absorbing Δ defines the $\overline{\text{MS}}$ scheme. An alternative is the on-shell scheme where renormalisation conditions enforce that the renormalised propagator has a pole at the physical mass with residue i .

A theory is then renormalisable when only a finite number of diagrams are UV divergent, and the divergences can be cancelled by introducing a finite number of counterterms. From a finite number of measurements that define the renormalised parameters, one can obtain any prediction from the theory, and the Standard Model is renormalisable. However, not every theory is renormalisable. Apart from momenta, the scales appearing in the loop integral can also be from dimensionful couplings (like masses). Noting that the mass dimension of a Lagrangian is $[\mathcal{L}] = 4$, it is feasible to determine that Dirac, scalar and vector fields have dimensions $3/2$, 1 and 1 , respectively, and it is then viable to calculate the dimension of couplings. By power counting, one can determine the superficial degree of divergence in terms of the possible vertex insertions and internal momenta of fields. These can be related to the number of external fields (E_ϕ , E_f and E_V for scalars, fermions and bosons) and the dimension of the vertices appearing $[g_v]$ as⁶

$$D = 4 - \frac{3}{2}E_f - E_\phi - E_V - \sum_v [g_v]. \quad (2.45)$$

The significant consequence of this equation is that if $[g_v] < 0$, then an infinite number of superficially divergent integrals can be constructed, and any such theory is non-renormalisable. One such interaction is the four-fermion interaction that appears in the 4-Fermi theory or in the Standard Model Effective Field Theory (SMEFT) which will be discussed later on. Such theories formally require an infinite amount of counterterms to be renormalised but are still predictive.

2.5 Aspects of the Standard Model

2.5.1 Perturbative unitarity

In quantum field theory, the S -matrix relates the initial and final states in a scattering process, and like any operator in quantum mechanics, it has to be unitary. Considering only the interacting

⁶Assuming that a propagator of a vector boson is $\sim k^{-2}$, no massive vector bosons and no derivatives acting on external lines (for more details, see Ref. [20]).

part of the S -matrix $S = 1 + iT$, the relevant matrix element \mathcal{M}_{fi} is given by (see for example Ref. [21])

$$\langle f|T|i\rangle = (2\pi)^4 \delta^4(p_i - p_f) \mathcal{M}_{fi} . \quad (2.46)$$

and by imposing the unitarity requirement, one arrives at the optical theorem, which relates the imaginary part of an elastic scattering process to the total cross section through the relation⁷

$$(\mathcal{M}_{fi} - \mathcal{M}_{if}^\dagger) = i \sum_X \int d\Pi_X (2\pi)^4 \delta^4(p_i - p_X) \mathcal{M}_{iX} \mathcal{M}_{Xf}^\dagger . \quad (2.47)$$

The sum is over single- and multi-particle states that can appear in the process $i \rightarrow X \rightarrow f$ and $d\Pi_X$ denotes integration over the phase space. Focusing on two-by-two scattering, the matrix element can be decomposed to partial waves by writing

$$\mathcal{M}_{if} = 16\pi \sum_J (2J+1) a_{fi}^J (D_{\lambda,\lambda'}^J(\theta, \phi))^* , \quad (2.48)$$

where λ (λ') is the difference between helicities in the initial (final) state of angular momentum J and $D_{\lambda,\lambda'}^J$ is the Wigner-D function⁸ appearing in the Jacob-Wick expansion [63]. The optical theorem can be rewritten in terms of the partial waves, and the fact that the RHS of Eq. (2.47) will be a sum over only two-particle states implies that it will be less or equal to the LHS. The equation simplifies when considering large centre-of-mass energies $\sqrt{s} \rightarrow \infty$ for $|i\rangle = |f\rangle$ and reads

$$\text{Im}(a_{ii}^J) \geq |a_{ii}^J|^2 , \quad (2.49)$$

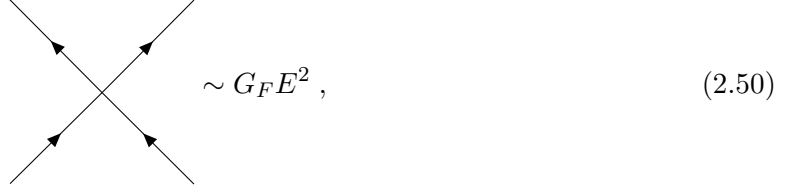
which is the equation of a circle of radius 1/2 in the complex plane. The implication is that $|\text{Re}(a_{ii}^J)| \leq 1/2$ defines an upper bound providing important limitations on the allowed behaviour of scattering amplitudes.

Any amplitude violating the bound hints at perturbativity being lost, and the effect of loop diagrams can not be neglected. The solution is to find a UV completion that explains physics in the region where perturbation theory is no longer trusted or to introduce a new particle that causes cancellations and restores perturbative unitarity. The 4-Fermi interaction [64] was a

⁷This relation also gives an alternative intuition on the requirement of ghosts in gauge theories discussed in Sec. 2.3. For loop diagrams with longitudinal modes of gauge bosons as virtual particles, the optical theorem implies that there should be tree level diagrams with such unphysical degrees of freedom appearing as external states, and this necessitates the introduction of ghosts (for more details see also Ref. [22]).

⁸For $\lambda = \lambda' = 0$ it simplifies to the Legendre Polynomials.

noteworthy example of such a scenario where the scattering amplitude grows with energy,



$$\sim G_F E^2, \quad (2.50)$$

and eventually crosses the upper limit of the bound unless there exists some intermediate vector boson [65–70] which is now known to be the W boson. History repeated itself later on when the $bW \rightarrow bW$ process before the top quark was discovered⁹ had a similar behaviour, and the partial wave analysis could allow placing upper limits on the allowed mass of the top quark that would appear as a propagator (see for example Ref. [73]). This idea implied that if a collider was operating at energies where perturbation theory was not to be trusted, it would be guaranteed that new physics would be observed, either in the form of new particles or some alternative UV completion of the theory. These upper bounds were accordingly often referred to as ‘No-Lose theorems’, and the implications for the SM before the discovery of the Higgs will be discussed in the following section.

Unitarity in scattering of W, Z bosons

The implications of the partial wave analysis in the SM become apparent in scattering processes with massive gauge bosons. Focusing on $WZ \rightarrow WZ$ scattering, there are six diagrams contributing to the matrix element, shown in Fig. 2.1, with three of them involving the scalar Goldstone bosons and the Higgs. By considering the $J = 0$ state and focusing only on the longitudinal degrees of freedom ($W_L Z_L \rightarrow W_L Z_L$), the partial wave can be projected as [74, 75]

$$a_{ii}^0 = \frac{\beta^{1/2}(s, M_Z^2, M_W^2)}{32\pi s} \int_{-1}^1 d(\cos\theta) \mathcal{M}(W_L Z_L \rightarrow W_L Z_L), \quad (2.51)$$

where $\beta(x, y, z) = x^2 + y^2 + z^2 - 2xy - 2yz - 2zx$. The resulting partial wave with and without the Higgs particle is shown in Fig. 2.2 and while for the former case the bound $|Re(a_{ii}^0)| \leq 1/2$ is violated, perturbative unitarity is restored by including a ‘light-enough’ physical Higgs particle h .¹⁰ A more detailed study, including all the scattering processes, resulted in an upper bound on the mass of the Higgs $m_h \leq 1$ TeV, known as the Lee-Quigg-Thacker bound [77] and the LHC,

⁹For the discovery of the top quark see Refs. [71, 72].

¹⁰Calculation was performed with FORMCALC [76].

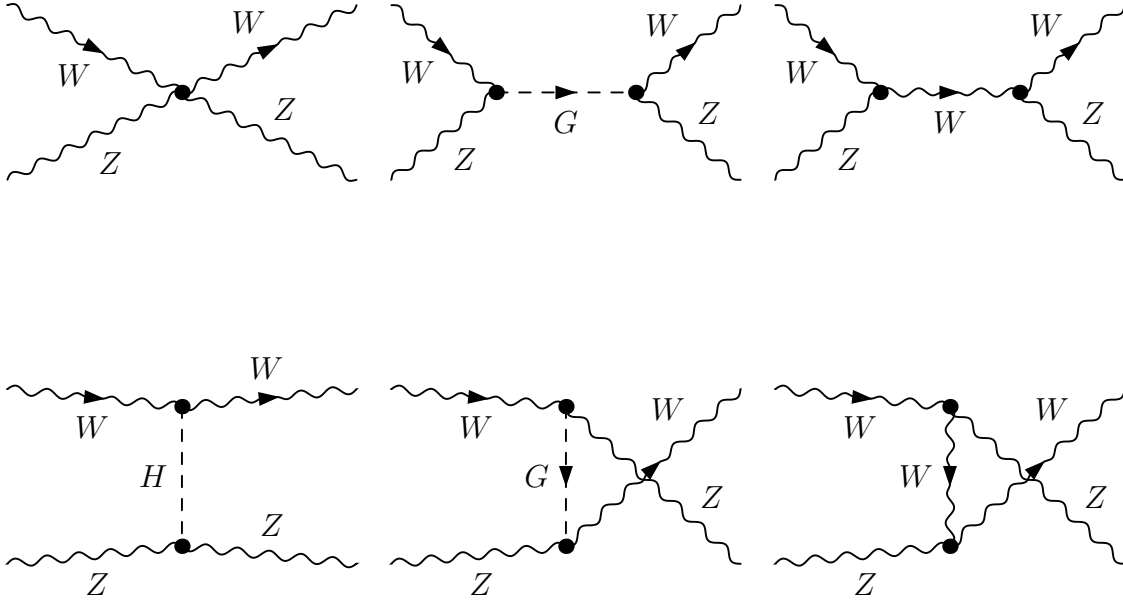


Figure 2.1: Feynman diagrams relevant for the $WZ \rightarrow WZ$ scattering in the SM.

designed to operate at energies up to 14 TeV, was guaranteed a new physics observation. Nature's choice was indeed the existence of the Higgs particle, discovered by ATLAS and CMS [8, 9]. The question that arises though, is whether the discovered Higgs at the LHC is indeed the SM Higgs.

2.5.2 Higgs physics at the LHC

Higgs decays

Performing the phase space integration in the optical theorem of Eq. (2.47) for the special one-particle case where $|i\rangle = |f\rangle = |h\rangle$ results in $\text{Im}(\Sigma_{hh}) = m\Gamma$, where Γ (m) is the total decay rate (mass) of the particle h and Σ is the $1 \rightarrow 1$ matrix element. The propagator receives corrections from an infinite number of diagrams and, after summing the geometric series, reads as

$$\text{---} \text{---} \text{---} \text{---} + \text{---} \text{---} \text{---} \text{---} \text{---} + \dots = \frac{i}{p^2 - m^2 + \Sigma(p^2)} = \frac{i}{p^2 - m_{\text{pole}}^2 + im_{\text{pole}}\Gamma}. \quad (2.52)$$

with the shaded circles denoting the one-particle irreducible insertions. Squaring the corrected propagator results in the Breit-Wigner distribution [78], which is the characteristic shape that an

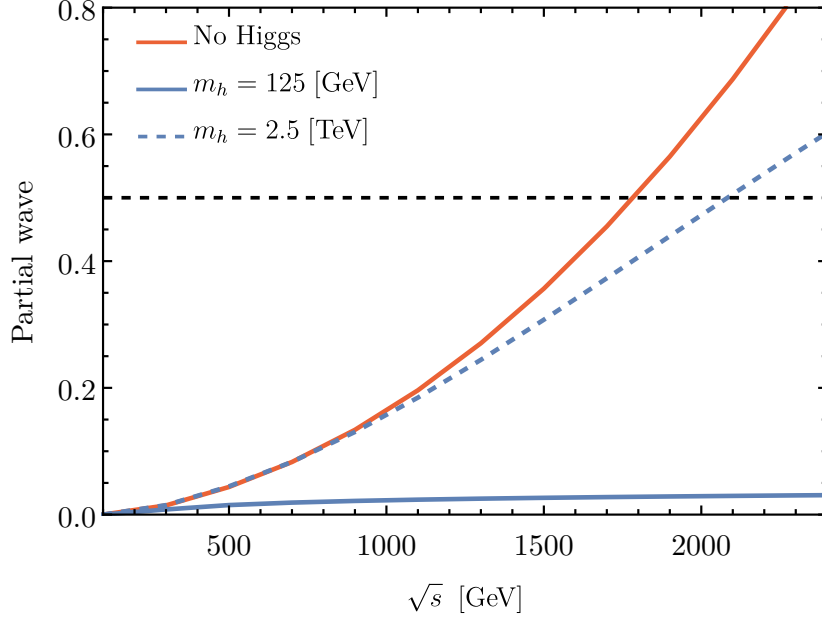


Figure 2.2: Partial wave of $W_L Z_L \rightarrow W_L Z_L$ at different centre-of-mass energies \sqrt{s} with and without the scalar sector. The scenario of a Higgs boson with mass $m_h = 2.5$ TeV is also shown, which also violates perturbative unitarity.

on-shell resonance follows.

Focusing on the decays of the Higgs particle, the partial decay widths can be calculated from the suitable Feynman diagrams shown in Fig. 2.3. For the SM Higgs with mass at $m_h = 125$ GeV, the dominant decay mode is to a pair of bottom quarks. The size of the partial widths for fermionic decays is given by [79]

$$\Gamma(h \rightarrow f\bar{f}) = \frac{G_\mu m_f^2 N_c}{4\sqrt{2}\pi} m_h \sqrt{1 - \frac{4m_f^2}{m_h^2}}, \quad (2.53)$$

and is proportional to the squared mass of the fermion m_f^2 . Since the mass of the top is kinematically inaccessible, the dominant decay of the Higgs is to bottom quarks. N_c is equal to three (one) for quarks (leptons). The decay to two massive vector bosons requires the calculation of final states arising from virtual vector bosons and has been calculated in Refs. [80, 81]. For massless gauge bosons, there is no tree level contribution, and one needs to evaluate the one-loop triangle diagrams, which result in a C_0 Passarino-Veltman function [82]. These were evaluated including the full top mass dependence [83, 84] and the results for all the Higgs decays can be

reviewed in Ref. [79]. The behaviour of the partial decay widths of the Higgs as well as the total decay width can be seen in Fig. 2.4 for various values of the Higgs mass. It is now known that $m_h = 125$ GeV and decays of the discovered scalar resonance indicate that it is indeed the SM Higgs, or at least a SM-like resonance [85–88]. Nonetheless, the decay widths for arbitrary masses can still be of interest in the case of additional scalar bosons. One would expect the decay to a top pair to dominate, however, this is not the case as the Higgs for larger masses decays predominantly to two vector bosons. In fact, the growth of the total decay width at larger energies is actually driven by the $h \rightarrow VV$ branching ratios, which can be understood in terms of perturbative unitarity: as the scattering of longitudinal vector bosons grows with energy, the coupling of the Higgs to the massive vector bosons must also grow in order to produce the essential cancellations.

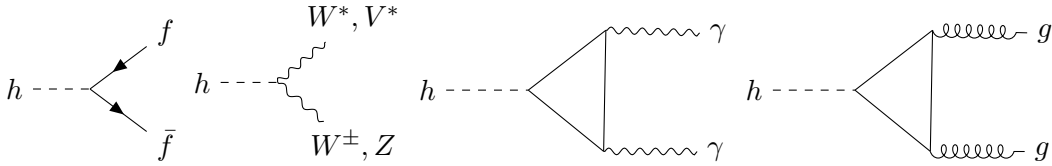


Figure 2.3: Feynman diagrams for decays of the scalar Higgs boson.

Higgs production at hadron colliders

In hadron colliders cross sections are computed assuming that they factorise to $\sigma = f \otimes \sigma_H$ [91], where f denotes the Parton Distribution Functions (PDFs).¹¹ The cross section is obtained from the convolution of the PDFs with the hard scattering cross section σ_H , which considers partons extracted from the proton (e.g. quarks or gluons) interacting between them to produce the observed final state. While the latter is a perturbative calculation, the former are probabilities of a particular parton inside the proton to carry a fraction of its momentum, which are governed by non-perturbative physics and are obtained by matching to data (for a review, see Ref. [93]). In practice, the convolution is automated nowadays through the use of Monte Carlo packages such as MADEVENT [94–96] that are used for simulating events at the LHC and other colliders.

The dominant production process of the Higgs boson at the LHC is gluon fusion shown in Fig. 2.5 which is calculated in the same manner as the decay width. Its evaluation with the full mass

¹¹Ref. [92] provides a didactic overview on the effects of QCD on LHC physics.

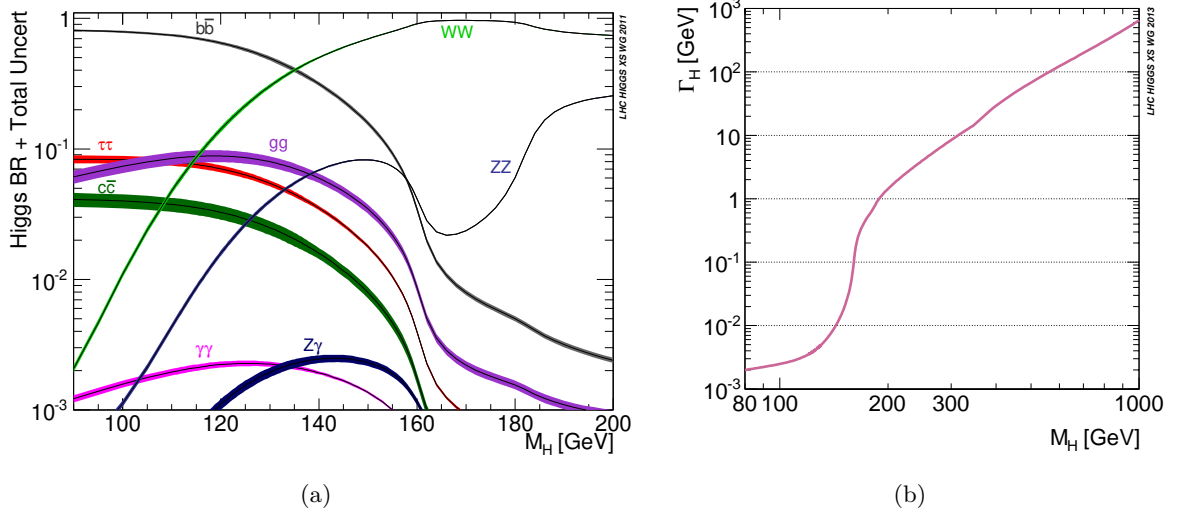


Figure 2.4: Figure (a) shows the Higgs branching ratios for different values of the Higgs mass, and (b) displays the value of the total decay width as a function of the mass. Both figures are taken from Ref. [89] (see also [90]).

dependence will be revisited later on in Chapter 4, however, it should be mentioned that for certain scenarios, it is useful to use the effective interaction

$$\mathcal{L}_{\text{LEFT}} = \frac{\alpha_s}{12\pi} G^{a\mu\nu} G_{\mu\nu}^a \log\left(1 + \frac{h}{v}\right), \quad (2.54)$$

which can be derived in the heavy top limit using low energy theorems (for more details, see Ref. [97]). In gluon fusion, the main channels are the decay of the produced Higgs to a pair of photons or $ZZ \rightarrow 4\ell$, despite other branching ratios being larger. The problem for $H \rightarrow b\bar{b}$ arises from the large QCD background from $gg \rightarrow b\bar{b}$. Decays to taus or W bosons result in neutrinos in the final states that appear as missing energy in the detector, and thus, reconstruction of the Higgs mass is difficult.

The next channel of significant importance is the Higgs production in association with two jets¹² through weak boson fusion (WBF) [100–102], as seen in Fig. 2.6. The incoming partons emit the

¹²Due to confinement, quarks and gluons can not be observed as isolated states. Instead the produced quarks and gluons can hadronise or undergo soft QCD radiation producing collimated sprays of hadrons, i.e. jets, that can be detected by experiments. Jet algorithms have to be employed in order to cluster particles into jets, and in this thesis the anti- k_t clustering algorithm [98] is always used. The interested reader can see the pedagogical review of Ref. [99] for more information.

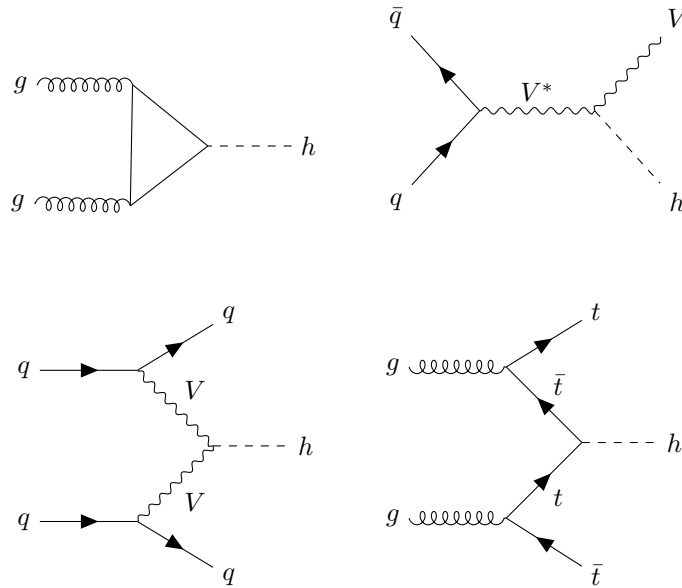


Figure 2.5: Example Feynman diagrams for the production of the scalar Higgs boson.

intermediate weak bosons (see Fig. 2.5), leading to a Higgs boson produced in the centre of the detector. In order for the Higgs to be produced, the incoming quarks must have relatively large momenta and continue in the forward part of the detector with relatively low transverse momenta but large rapidities. The back-to-back geometry of the two jets in the final state allows the efficient removal of background arising from QCD [100, 101, 103, 104]. It should be noted that the decay of the Higgs to bottom quarks is still troublesome to detect due to the QCD background, in contrast with the decays to $\gamma\gamma$ or ZZ . Additionally, the decay to $\tau^+\tau^-$ becomes attainable since, although they decay to neutrinos, they can be assumed collinear due to the sizeable transverse momentum of the Higgs. Thus, the tau pair momentum reconstruction can be approximated by the sum of the final lepton momenta and the missing transverse momentum.

Moving to associated production, the process $pp \rightarrow Vh$ with the subsequent leptonic decay of the vector boson has a lower cross section but is still phenomenologically important. The system of Vh is central due to the large mass, and the two bosons are boosted. Probing a boosted Higgs is possible through a cut on the transverse momentum of the V boson. Therefore, their decay products possess sizeable transverse momentum, which allows easier tagging. Due to the smaller

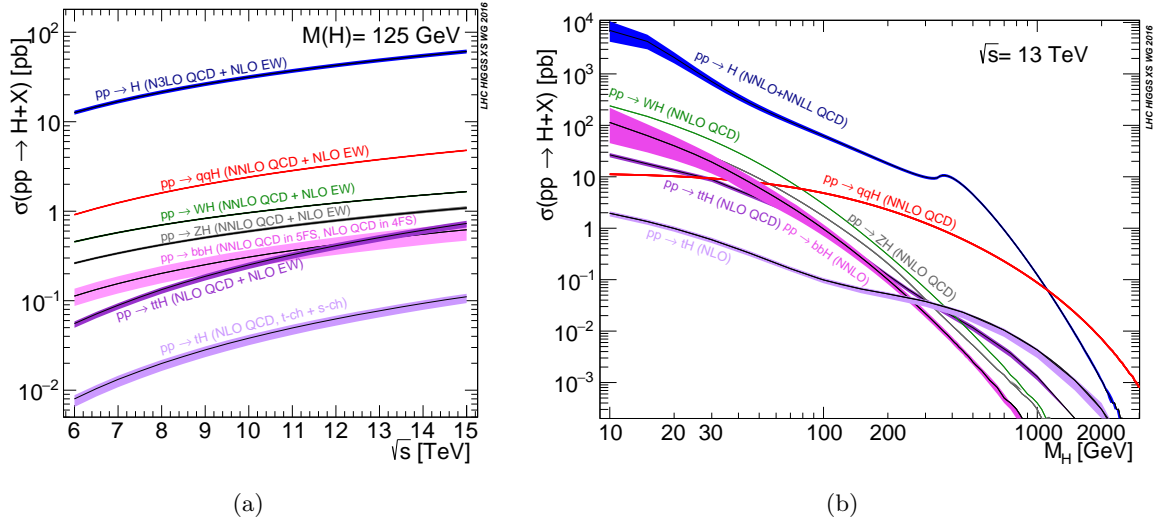


Figure 2.6: The cross section of Higgs production at different energies is shown in (a), while (b) shows their dependence on the Higgs mass. Both figures are from Ref. [105].

cross section, the channels can be probed with $h \rightarrow b\bar{b}$ which requires the use of jet substructure techniques [106].

Additional channels include the associated production with a top/bottom pair or the production with a single top. Nevertheless, these channels are subdominant and much more challenging to detect (e.g. observation of $t\bar{t}h$ at ATLAS required advanced Machine Learning techniques to separate the background [107]) and will not be discussed further.

2.6 Shortcomings of the Standard Model

Despite the SM's tremendous success, it is far from a final theory. Perhaps the most obvious weak point of the SM is that gravity, one of the four fundamental forces, is not incorporated in the theory at all. The weakness of the gravitational interaction at the atomic level, however, implies that quantum effects are not expected to be relevant at scales lower than the Planck mass. There is also no explanation of dark energy, theorised due to the universe's accelerated expansion as observed in astronomical probes. Solutions to these two drawbacks are not easily addressed with particle physics experiments at current energies and will not be discussed further. In spite of that, several shortcomings such as the hierarchy problem or the absence of dark matter and

sufficient CP violation have the potential to be studied at colliders.¹³

Hierarchy problem The hierarchy problem is essentially the question ‘Why is the Higgs mass so small when it receives corrections from heavier scales?’. If the SM is considered an effective theory that breaks down at some scale Λ (e.g. the Planck scale at $\sim 1.2 \times 10^{19}$ GeV), then the radiative correction from a fermion loop to the mass of the Higgs is quadratically divergent, i.e.

$$\text{---} \circlearrowleft \text{---} \sim -\frac{C}{16\pi^2}\Lambda^2, \quad (2.55)$$

where C is a constant related to parameters of the SM. From Eq. (2.52) it is conceivable to deduce that the corrected pole mass of the Higgs will then be given by

$$m_{pole}^2 \approx 2\mu^2 - \frac{C}{16\pi^2}\Lambda^2, \quad (2.56)$$

which should result in 125 GeV. If the SM is the correct description of nature for energies up to the Planck scale where quantum gravity becomes important, then the parameters of the SM in C and μ must be incredibly fine-tuned in order to result in such a small value. This would be in violation of the concept of naturalness, where parameters in a fundamental theory are expected to be of order one, and in fact scales $\Lambda \gg \text{TeV}$ would require fine-tuning. Grand Unified theories and supersymmetry often provide natural ways to keep the scalar boson mass small from symmetry arguments, while composite Higgs models resolve this troubling situation by speculating that the Higgs boson is a bound state arising from a new strong interaction. Models of supersymmetry and compositeness can lead to simplified low-energy theories extending the SM with additional scalars, such as the 2HDM [109].

Dark matter The existence of dark matter is evident from its effect on gravitationally collapsed structures such as galaxy rotation curves [110–112]. Both macroscopic and microscopic hypotheses about the nature of dark matter exist, characterised by not emitting electromagnetic radiation. Addressing dark matter within extensions of the SM is commonly done by the inclusion of additional fields that do not couple to the photon. Therefore, dark matter will not leave any signal on the detector rendering such theories challenging to observe at the LHC. A particular extension in which a scalar dark matter field is coupled only to the Higgs will be explored in Chapter 3.

¹³Massive neutrinos are also not discussed since the SM can be modified to include these (e.g. see Ref. [108]).

CP violation A necessity for the dominance of matter over antimatter in our universe requires baryon anti-baryon asymmetry, which can be achieved by fulfilling the Sakharov conditions [113]. For baryogenesis to occur, there must exist a sufficient source of CP violation that will cause matter to be produced at different rates than antimatter. CP violation in the SM is sourced mainly from the CKM matrix¹⁴ but is not sufficient to lead to baryon dominance. Therefore, this motivates the introduction of additional sources of CP violation in new physics scenarios, which can also appear in the Higgs sector. Chapter 6 studies operators that lead to these effects in the electroweak gauge-Higgs sector.

Muon anomalous magnetic moment Immersing a Dirac particle of spin 1/2 such as the muon in an external magnetic field leads to a potential energy dependent on its magnetic moment

$$\vec{\mu} = \frac{e}{2m} g \vec{S}, \quad (2.57)$$

where the Dirac equation implies $g = 2$. Even though the Dirac equation stands at tree level, higher orders can contribute to the g -factor and its deviation from two can be captured with the muon anomalous magnetic moment

$$a_\mu = \frac{g - 2}{2}. \quad (2.58)$$

Polarised muons injected in a storage ring with a homogeneous magnetic field B and specific momenta have an anomalous recession frequency $\omega = a_\mu eB/m_\mu$ ¹⁵ which can be measured.

However, the most precise measurement performed at Fermilab [114] which also confirmed the previous results of BNL E821 [115] indicated an anomaly of

$$\Delta a_\mu = a_\mu(\text{exp}) - a_\mu(\text{SM}) = (25.1 \pm 5.9) \times 10^{-10}, \quad (2.59)$$

which leads to a $\sim 4\sigma$ tension [116–135] (see also [136]) compared to the SM theoretical prediction. If new physics indeed source the deviation, this raises the question of whether it can arise from, which motivates studying flaws of the SM in a model-independent fashion. This will be explored in Chapter 7.

¹⁴CP violation is also plausible from the QCD sector but will not be examined.

¹⁵A proper choice for the velocity of the muon and the electromagnetic fields cancels relativistic effects.

2.7 Beyond the Standard Model

A plethora of BSM scenarios have been formulated, each attempting to demystify one or more of the SM's drawbacks. Varying in complexity from simple extensions introducing new fields to warped extra dimensions, the detailed discussion of UV completions is beyond the scope of this thesis. Instead, the centre of attention will be on addressing phenomena of simple extensions of the SM's Higgs sector, with suitable models introduced in Chapters 3 and 4.

In the rest of the Chapters, attention is shifted away from concrete models and towards the SMEFT framework, which allows studying flaws of the SM in a model-independent fashion. SMEFT is introduced in the following subsection.

2.7.1 Standard Model Effective Field Theory

Looking at renormalisation from Wilson's viewpoint [137], for any theory there can be some high-energy cut-off Λ_H . An effective theory can be defined by splitting the fields into low- and high-energy parts and then integrating over the latter, resulting in an effective action. As an example, let the Lagrangian of a generic theory with a scalar ϕ be given with $\mathcal{L} = \sum g_i^{(r)} \mathcal{O}_i^{(r)}$, where $g_i^{(r)}$ are dimensionful couplings for operators $\mathcal{O}_i^{(r)}$. The operators have mass scale r . By splitting the scalar field as $\phi = \phi' + \chi$, where ϕ' and χ correspond to momentum shells of $|p| < \Lambda$ and $\Lambda < |p| \leq \Lambda_H$, the effective action can be written as

$$S_{\text{eff}}[\phi'] = -\log \int \mathcal{D}\chi e^{-S[\phi'+\chi]} . \quad (2.60)$$

The partition function that captures the physics of the theory remains invariant, irrespective of the choice of Λ . This defines the Renormalisation Group Evolution (RGE)¹⁶ for the partition function

$$\Lambda \frac{d\mathcal{Z}}{d\Lambda} = 0 , \quad (2.61)$$

which implies that the couplings of the theory vary according to a RGE equation

$$\Lambda \frac{d}{d\Lambda} g_i^{(r)} = \frac{1}{\Lambda^{r-4}} \beta(\{g_i^{(r)} \Lambda^{r-4}\}) , \quad (2.62)$$

¹⁶RGE effects can also be derived from the viewpoint of renormalisation introduced in Sec. 2.4 by requiring the bare Lagrangian to remain invariant under changes of the dimensional regularisation scale μ .

to accommodate the effect of integrating modes out. Solving such differential equations allows the determination of how the couplings at some low scale depend on the high-energy scale Λ_H appearing from the boundary conditions. In general, three behaviours are possible for the operators, which depend on r by dimensional analysis arguments (for detailed discussions, see Refs. [21, 22]):

Relevant: Such operators have that couplings diverge when the limit $\Lambda_H \rightarrow \infty$ is taken. For four-dimensions they are those with $r < 4$. Couplings of such operators are often UV sensitive unless protected by some symmetry, with the Higgs mass a prime example, leading to the hierarchy problem.

Marginal: Operators with $r = 4$ are marginal, and they can be either marginally relevant or marginally irrelevant. Higher order corrections are required to understand whether its coupling grows as $\Lambda_H \rightarrow \infty$.

Irrelevant: For these $r > 4$ operators the couplings remain finite, and their effects are minor at large distances.

A theory with $r \leq 4$ will be renormalisable, in line with what has been discussed in Sec. 2.4.

This point of view provides an intuitive description of why the SM is renormalisable: for a UV completion with high-scale $\Lambda_H \rightarrow \infty$, there exists an effective description after integrating out the heavy degrees of freedom at a lower scale Λ . This effective theory is the SM along with additional irrelevant operators. Then the fact that there is no experimental evidence suggesting the existence of new physics just indicates that there is a mass gap between the electroweak scale and the mass scales of the BSM scenario. Due to the size of the mass gap, the effects from the $r > 4$ operators are suppressed. The additional irrelevant terms are introduced either through a ‘top-down’ or a ‘bottom-up’ approach.

Top-down approach

In the top-down approach, effective Lagrangians [138] can be constructed capturing the full theory’s infrared effects by taking a UV concrete scenario and integrating out the heavy BSM states. Their interactions afterwards can be matched on $r > 4$ operators. An infamous example of this is the 4-Fermi theory, where the W boson is integrated out and matched to a four-fermion operator. To demonstrate this, consider the $\mu\nu_\mu \rightarrow e\nu_e$ interaction given by

$$\propto \frac{g_2^2}{8} \frac{1}{p^2 - M_W^2} \sim \frac{g_2^2}{8M_W^2}. \quad (2.63)$$

The same Lorentz structure as the above amplitude can be obtained by an effective Lagrangian that includes $(G_F/\sqrt{2})(\bar{L}_1\gamma_\mu L_2)(\bar{L}_2\gamma^\mu L_1) + \text{h.c.}$ generating

$$\propto \frac{G_F}{\sqrt{2}}. \quad (2.64)$$

Requiring that the two diagrams match in the limit $M_W^2 \gg p^2$ results in $G_F = g_2^2\sqrt{2}/(8M_W^2)$ and the same procedure is, of course, suitable for BSM theories with heavy degrees of freedom.

Bottom-up approach

Instead, of depending on some new physics model to identify which operators to include, it is viable to agnostically include all the deformations possible constructed from SM fields, truncating at some particular order of Λ^{-1} . This allows reinterpreting the LHC results as interval bounds on the coefficients of the operators in a model-independent fashion, searching for indirect effects of new physics. In this bottom-down approach, the Lagrangian is a series of operators of order Λ^{-2} and dimension-six¹⁷, the SMEFT Lagrangian is [139, 141–145]

$$\mathcal{L} = \mathcal{L}_{\text{SM}} + \sum_i \frac{C_i}{\Lambda^2} \mathcal{O}_i, \quad (2.65)$$

where C_i represents the Wilson Coefficient (WC) of the operator \mathcal{O}_i . In the Warsaw basis [139] the operators are independent and are given in Tabs. 2.1, 2.2 and 2.3. SMEFT has been widely studied by the community (e.g. [146–148] and see also [149] for a recent review).

The Lagrangian is often truncated at dimension-six, allowing to obtain any differential cross

¹⁷In principle, the first higher-order operator is the Weinberg operator [140] appearing at dimension-five. However, this operators only concerns physics of neutrino masses.

X^3		ϕ^6 and $\phi^4 D^2$		$\psi^2 \phi^3$	
\mathcal{O}_G	$f^{abc} G_\mu^{a\nu} G_\nu^{b\rho} G_\rho^{c\mu}$	\mathcal{O}_ϕ	$(\Phi^\dagger \Phi)^3$	$\mathcal{O}_{e\phi}$	$(\Phi^\dagger \Phi)(\bar{L}_p \ell_r \Phi)$
$\mathcal{O}_{\tilde{G}}$	$f^{abc} \tilde{G}_\mu^{a\nu} G_\nu^{b\rho} G_\rho^{c\mu}$	$\mathcal{O}_{\phi\Box}$	$(\Phi^\dagger \Phi)\Box(\Phi^\dagger \Phi)$	$\mathcal{O}_{u\phi}$	$(\Phi^\dagger \Phi)(\bar{Q}_p u_r \Phi^c)$
\mathcal{O}_W	$\epsilon^{IJK} W_\mu^{I\nu} W_\nu^{J\rho} W_\rho^{K\mu}$	$\mathcal{O}_{\phi D}$	$(\Phi^\dagger D^\mu \Phi)^* (\Phi^\dagger D_\mu \Phi)$	$\mathcal{O}_{d\phi}$	$(\Phi^\dagger \Phi)(\bar{Q}_p d_r \Phi)$
$\mathcal{O}_{\tilde{W}}$	$\epsilon^{IJK} \tilde{W}_\mu^{I\nu} W_\nu^{J\rho} W_\rho^{K\mu}$				
$X^2 \phi^2$		$\psi^2 X \phi$		$\psi^2 \phi^2 D$	
$\mathcal{O}_{\phi G}$	$\Phi^\dagger \Phi G_{\mu\nu}^a G^{a\mu\nu}$	\mathcal{O}_{eW}	$(\bar{L}_p \sigma^{\mu\nu} \ell_r) \tau^I \Phi W_{\mu\nu}^I$	$\mathcal{O}_{\phi l}^{(1)}$	$(\Phi^\dagger i \overleftrightarrow{D}_\mu \Phi)(\bar{L}_p \gamma^\mu L_r)$
$\mathcal{O}_{\phi \tilde{G}}$	$\Phi^\dagger \Phi \tilde{G}_{\mu\nu}^a G^{a\mu\nu}$	\mathcal{O}_{eB}	$(\bar{L}_p \sigma^{\mu\nu} \ell_r) \Phi B_{\mu\nu}$	$\mathcal{O}_{\phi l}^{(3)}$	$(\Phi^\dagger i \overleftrightarrow{D}_\mu^I \Phi)(\bar{L}_p \tau^I \gamma^\mu L_r)$
$\mathcal{O}_{\phi W}$	$\Phi^\dagger \Phi W_{\mu\nu}^I W^{I\mu\nu}$	\mathcal{O}_{uG}	$(\bar{Q}_p \sigma^{\mu\nu} t^a u_r) \Phi^c G_{\mu\nu}^a$	$\mathcal{O}_{\phi e}$	$(\Phi^\dagger i \overleftrightarrow{D}_\mu \Phi)(\bar{\ell}_p \gamma^\mu \ell_r)$
$\mathcal{O}_{\phi \tilde{W}}$	$\Phi^\dagger \Phi \tilde{W}_{\mu\nu}^I W^{I\mu\nu}$	\mathcal{O}_{uW}	$(\bar{Q}_p \sigma^{\mu\nu} u_r) \tau^I \Phi^c W_{\mu\nu}^I$	$\mathcal{O}_{\phi q}^{(1)}$	$(\Phi^\dagger i \overleftrightarrow{D}_\mu \Phi)(\bar{Q}_p \gamma^\mu Q_r)$
$\mathcal{O}_{\phi B}$	$\Phi^\dagger \Phi B_{\mu\nu} B^{\mu\nu}$	\mathcal{O}_{uB}	$(\bar{Q}_p \sigma^{\mu\nu} u_r) \Phi^c B_{\mu\nu}$	$\mathcal{O}_{\phi q}^{(3)}$	$(\Phi^\dagger i \overleftrightarrow{D}_\mu^I \Phi)(\bar{Q}_p \tau^I \gamma^\mu Q_r)$
$\mathcal{O}_{\phi \tilde{B}}$	$\Phi^\dagger \Phi \tilde{B}_{\mu\nu} B^{\mu\nu}$	\mathcal{O}_{dG}	$(\bar{Q}_p \sigma^{\mu\nu} t^a d_r) \Phi G_{\mu\nu}^a$	$\mathcal{O}_{\phi u}$	$(\Phi^\dagger i \overleftrightarrow{D}_\mu \Phi)(\bar{u}_p \gamma^\mu u_r)$
$\mathcal{O}_{\phi WB}$	$\Phi^\dagger \tau^I \Phi W_{\mu\nu}^I B^{\mu\nu}$	\mathcal{O}_{dW}	$(\bar{Q}_p \sigma^{\mu\nu} d_r) \tau^I \Phi W_{\mu\nu}^I$	$\mathcal{O}_{\phi d}$	$(\Phi^\dagger i \overleftrightarrow{D}_\mu \Phi)(\bar{d}_p \gamma^\mu d_r)$
$\mathcal{O}_{\phi \tilde{W}B}$	$\Phi^\dagger \tau^I \Phi \tilde{W}_{\mu\nu}^I B^{\mu\nu}$	\mathcal{O}_{dB}	$(\bar{Q}_p \sigma^{\mu\nu} d_r) \Phi B_{\mu\nu}$	$\mathcal{O}_{\phi ud}$	$i(\Phi^c \dagger D_\mu \Phi)(\bar{u}_p \gamma^\mu d_r)$

Table 2.1: Dimension-six operators other than the four-fermion ones from Ref. [139].

section distribution through

$$d\sigma = d\sigma_{\text{SM}} + \frac{C_i}{\Lambda^2} d\sigma_i^{(1)} + \frac{C_i C_j}{\Lambda^4} d\sigma_{ij}^{(2)}, \quad (2.66)$$

where $d\sigma_{\text{SM}}$ denotes the purely-SM contributions and $d\sigma_i^{(1)}$ captures the interference of operator \mathcal{O}_i with the SM. The Feynman rules for SMEFT at dimension-six are provided by Ref. [145]. The last term represents contributions that arise from cross-terms between two effective interactions and thus are Λ^4 suppressed. This term is of the same order as dimension-eight interference with the SM, and $d\sigma$ is often also truncated, keeping only contributions up to Λ^{-2} .

$(\bar{L}L)(\bar{L}L)$		$(\bar{L}R)(\bar{R}L)$ and $(\bar{L}R)(\bar{L}R)$	
\mathcal{O}_{ll}	$(\bar{L}_p\gamma_\mu L_r)(\bar{L}_s\gamma^\mu L_t)$	\mathcal{O}_{ledq}	$(\bar{L}_p^j\ell_r)(\bar{d}_s Q_t^j)$
$\mathcal{O}_{qq}^{(1)}$	$(\bar{Q}_p\gamma_\mu Q_r)(\bar{Q}_s\gamma^\mu Q_t)$	$\mathcal{O}_{quqd}^{(1)}$	$(\bar{Q}_p^j u_r)\epsilon_{jk}(\bar{Q}_s^k d_t)$
$\mathcal{O}_{qq}^{(3)}$	$(\bar{Q}_p\gamma_\mu\tau^I Q_r)(\bar{Q}_s\gamma^\mu\tau^I Q_t)$	$\mathcal{O}_{quqd}^{(8)}$	$(\bar{Q}_p^j t^a u_r)\epsilon_{jk}(\bar{Q}_s^k t^a d_t)$
$\mathcal{O}_{lq}^{(1)}$	$(\bar{L}_p\gamma_\mu L_r)(\bar{Q}_s\gamma^\mu Q_t)$	$\mathcal{O}_{lequ}^{(1)}$	$(\bar{L}_p^j\ell_r)\epsilon_{jk}(\bar{Q}_s^k u_t)$
$\mathcal{O}_{lq}^{(3)}$	$(\bar{L}_p\gamma_\mu\tau^I L_r)(\bar{Q}_s\gamma^\mu\tau^I Q_t)$	$\mathcal{O}_{lequ}^{(3)}$	$(\bar{L}_p^j\sigma_{\mu\nu}\ell_r)\epsilon_{jk}(\bar{Q}_s^k\sigma^{\mu\nu}u_t)$
$(\bar{R}R)(\bar{R}R)$		$(\bar{L}L)(\bar{R}R)$	
\mathcal{O}_{ee}	$(\bar{\ell}_p\gamma_\mu\ell_r)(\bar{\ell}_s\gamma^\mu\ell_t)$	\mathcal{O}_{te}	$(\bar{L}_p\gamma_\mu L_r)(\bar{\ell}_s\gamma^\mu\ell_t)$
\mathcal{O}_{uu}	$(\bar{u}_p\gamma_\mu u_r)(\bar{u}_s\gamma^\mu u_t)$	\mathcal{O}_{lu}	$(\bar{L}_p\gamma_\mu L_r)(\bar{u}_s\gamma^\mu u_t)$
\mathcal{O}_{dd}	$(\bar{d}_p\gamma_\mu d_r)(\bar{d}_s\gamma^\mu d_t)$	\mathcal{O}_{ld}	$(\bar{L}_p\gamma_\mu L_r)(\bar{d}_s\gamma^\mu d_t)$
\mathcal{O}_{eu}	$(\bar{\ell}_p\gamma_\mu\ell_r)(\bar{u}_s\gamma^\mu u_t)$	\mathcal{O}_{qe}	$(\bar{Q}_p\gamma_\mu Q_r)(\bar{\ell}_s\gamma^\mu\ell_t)$
\mathcal{O}_{ed}	$(\bar{\ell}_p\gamma_\mu\ell_r)(\bar{d}_s\gamma^\mu d_t)$	$\mathcal{O}_{qu}^{(1)}$	$(\bar{Q}_p\gamma_\mu Q_r)(\bar{u}_s\gamma^\mu u_t)$
$\mathcal{O}_{ud}^{(1)}$	$(\bar{u}_p\gamma_\mu u_r)(\bar{d}_s\gamma^\mu d_t)$	$\mathcal{O}_{qu}^{(8)}$	$(\bar{Q}_p\gamma_\mu t^a Q_r)(\bar{u}_s\gamma^\mu t^a u_t)$
$\mathcal{O}_{ud}^{(8)}$	$(\bar{u}_p\gamma_\mu t^a u_r)(\bar{d}_s\gamma^\mu t^a d_t)$	$\mathcal{O}_{qd}^{(1)}$	$(\bar{Q}_p\gamma_\mu Q_r)(\bar{d}_s\gamma^\mu d_t)$
		$\mathcal{O}_{qd}^{(8)}$	$(\bar{Q}_p\gamma_\mu t^a Q_r)(\bar{d}_s\gamma^\mu t^a d_t)$

Table 2.2: Four fermion operators from Ref. [139] conserving the baryon number.

B -violating	
\mathcal{O}_{duq}	$\epsilon^{\alpha\beta\gamma}\epsilon_{jk}\left[(d_p^\alpha)^T C u_r^\beta\right]\left[(Q_s^{\gamma j})^T C L_t^k\right]$
\mathcal{O}_{qqu}	$\epsilon^{\alpha\beta\gamma}\epsilon_{jk}\left[(Q_p^{\alpha j})^T C Q_r^{\beta k}\right]\left[(u_s^\gamma)^T C e_t\right]$
\mathcal{O}_{qqq}	$\epsilon^{\alpha\beta\gamma}\epsilon_{jn}\epsilon_{km}\left[(Q_p^{\alpha j})^T C Q_r^{\beta k}\right]\left[(Q_s^{\gamma m})^T C L_t^n\right]$
\mathcal{O}_{duu}	$\epsilon^{\alpha\beta\gamma}\left[(d_p^\alpha)^T C u_r^\beta\right]\left[(u_s^\gamma)^T C e_t\right]$

Table 2.3: Four fermion operators from Ref. [139] violating the baryon number. C denotes the charge conjugation matrix.

2.8 Summary

In this Chapter, the Lagrangian of the SM in the unbroken phase and the implications of electroweak SSB have been introduced, as well as quantisation through the path integral formalism and the necessity of renormalisation. The anticipation of the Higgs boson's existence was elaborated through perturbative unitarity, which served as a stepping stone through the identification of a No-Lose theorem, as in the past. The LHC successfully produced the Higgs through multiple production and decay channels resulting in its discovery by both CMS and ATLAS, bringing many years of theoretical and experimental efforts to a fruitful end. The SM, however, was never meant to be the complete description of particle physics, and in the following chapters, its defects will be used as motivation to explore avenues that could lead to the discovery of the next prevalent model.

Chapter 3

Power meets precision to explore the symmetric Higgs portal

3.1 Introduction

The limitations of the SM in explaining the aforesaid phenomena stipulate the essential existence of new physics. The pattern of identifying a No-Lose theorem that hints at the energy scales at which experimentalists can perform studies to find discoveries is, however, impossible due to the renormalisable nature of the SM. Unlike the guaranteed discovery of either the Higgs or alternative new physics curing the unitarity of longitudinal vector boson scattering, there is no clear path forward for future experiments.

Even though the current situation may seem grim, it is actually an excellent opportunity for particle physicists to investigate different models resolving the SM deficiencies and how they can be favoured or disfavoured when studied at future experiments. As the LHC programme collects more data and performs additional measurements, there is an active debate regarding what experiment should follow. A new Future Circular Collider colliding hadrons (FCC-hh) [150–152] can push the energy frontier to a centre-of-mass energy of 100 TeV. Such a discovery machine should be able to directly probe the existence of heavier particles that can be theorised from BSM theories. However, as with the LHC, such machines suffer from large backgrounds and require considerably more work to bring the systematic and statistical uncertainties under control. In contrast, in the proposed experiments of the Compact Linear Collider (CLIC) [153] and

FCC-ee [150], colliding leptons at smaller energies can lead to precision measurements benefitting from highly controlled processes. An alternative option is the GigaZ experiment [154–156] which can be anticipated to deliver unparalleled precision in Z boson physics.

Such future experiments will enable us to search for new physics causing deviations from the SM in various processes, and due to their fundamentally diverse approaches, they can be complementary; a signature that could be promising for one may be completely inaccessible in the other. The relevant processes for a particular BSM theory of interest that can be induced at one of these experiments need to be identified in order to assess their significance, which can be particularly strenuous as new effects can arise from higher orders in the perturbative expansion of the theory. This Chapter will focus on pinpointing significant effects with loop calculations in a concrete renormalisable model that provides a dark matter candidate.

A simple extension to the SM is the \mathbb{Z}_2 -symmetric Higgs portal [157–162], which introduces a scalar field S , uncharged under the SM and only coupled to the Higgs sector. It can be characterised by the Lagrangian

$$\mathcal{L} = \mathcal{L}_{\text{SM}} + \mathcal{L}_{\text{portal}} = \mathcal{L}_{\text{SM}} + \frac{1}{2}(\partial_\mu S)^2 - \frac{m_S^2}{2}S^2 - \lambda S^2(\Phi^\dagger\Phi - v^2/2), \quad (3.1)$$

where the term $\lambda S^2\Phi^\dagger\Phi$ describes the interaction between the SM Higgs doublet Φ and the new scalar, characterised by the Higgs portal coupling λ . The Lagrangian respects the \mathbb{Z}_2 symmetry $S \rightarrow -S$, while the SM fields remain themselves invariant. Assuming that the scalar does not acquire a VEV, this symmetry remains unbroken. In contrast, the doublet develops a VEV, which, in the usual manner, breaks the electroweak symmetry and allows SM particles to acquire the necessary mass terms. Expansion of the doublet around its VEV, as in the SM, gives rise to terms included in the interaction Lagrangian of the form

$$\lambda\Phi^\dagger\Phi S^2 \supset \lambda\frac{v^2}{2}S^2 + \lambda v h S^2 + \frac{\lambda}{2}h^2 S^2, \quad (3.2)$$

that couple a pair of S scalar particles to either one Higgs boson or a pair. The unbroken symmetry implies that S is stable and a dark matter candidate that can only be pair-produced through the physical Higgs and would appear as missing energy in detectors, similar to neutrinos. The case of spontaneously broken \mathbb{Z}_2 has also been explored in the past but has a dissimilar phenomenology [163] and will not be discussed here.

Electroweak measurements can be used as input parameters of the theory. The SM vacuum

expectation value can be written as

$$v = \frac{2M_W s_w}{e}, \quad (3.3)$$

in terms of the elementary charge which is related to the fine structure constant via $e = \sqrt{4\pi\alpha}$. The latter is then determined in terms of the Fermi constant G_F and reads

$$\alpha = \frac{\sqrt{2}}{\pi} G_F M_W^2 s_w^2 = \frac{\sqrt{2}}{\pi} G_F M_W^2 \left(1 - \frac{M_W^2}{M_Z^2}\right). \quad (3.4)$$

In this Chapter, direct and indirect detection probes to search for evidence of the presence of S will be explored in Secs. 3.2 and 3.3, respectively, before discussing the expected collider sensitivity in Sec. 3.4. Conclusions from comparing the different future experimental concepts are presented in Sec. 3.5.

3.2 Direct Detection

If the scalar S is light compared to the Higgs, then an on-shell Higgs can decay invisibly to an SS pair and can be probed through Higgs partial width measurements [164, 165]. In contrast, when S is relatively heavy with respect to the Higgs, i.e. $m_S > m/2$, the two-body decay is kinematically inaccessible, and S pair production can only occur via an off-shell Higgs, rendering detection substantially more troublesome and less constrained. The scalar particle is produced through channels similar to Higgs production; nonetheless, because S appears as missing energy, direct detection of such signal necessitates the production along with visible signatures. This occurs through WBF $ff \rightarrow SSff$ (f denotes a SM fermion), boson-associated Higgs production $f\bar{f} \rightarrow VSS$, where V is either a W or Z boson and through gluon fusion $gq \rightarrow SSj$ or $gg \rightarrow SSj$. The latter will be referred to as mono-jet since it requires at least one jet in order to be able to identify the final state. Other processes, such as the production of Higgs along a pair of heavy quarks, do not provide such a strong signal as the modes mentioned above due to the lower production cross section of the Higgs (e.g. see Fig. 2.6). Signal cross sections depend primarily on the mass of the scalar particle, with larger masses being considerably harder to constrain. Future lepton and hadron colliders are considered in order to identify the mass range that can be excluded from searches of future experimental concepts such as FCC-hh, ILC and CLIC.

Events for the analysis are generated using a FEYNRULES [58, 59] model, along with NLOCT [166], MADEVENT [94–96] and PYTHIA8 [167] for showering. Resulting events are stored in the HEPMC

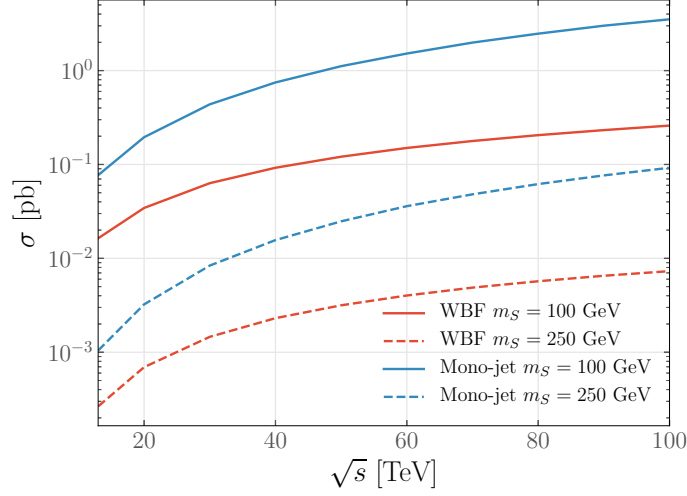


Figure 3.1: Figure showing the total cross section for producing an SS pair along with two jets through WBF (red) and the mono-jet production from gluon fusion (blue). Compared to WBF, the associated $(h \rightarrow SS)V$ production is three orders of magnitude lower and therefore is not taken into consideration.

format [168] and a cut-and-count analysis can be implemented using RIVET [169].

3.2.1 Hadron Colliders

For hadron colliders, the suitable channels are WBF, associated production and mono-jet production, resulting in an off-shell Higgs that subsequently decays to an S pair. The study follows CMS and ATLAS searches that have been performed in the past, as well as other studies of the Higgs portal, such as Refs. [170, 171]. To understand the particular importance of each channel for the BSM theory as well as its dependence on m_S , cross sections for S pair production against the centre-of-mass energy \sqrt{s} of the colliding proton beams are shown in Fig. 3.1. For each channel, the appropriate background is considered, along with appropriate cuts to enhance the channel's significance.

Associate production: Associate Higgs production, followed by S pair production, has a significantly smaller cross section compared to the other channels. At FCC, colliding protons with energies of 100 TeV, the signal cross section is of order $\mathcal{O}(10^{-2})$ fb before any cuts and using a relatively light $m_S = 100$ GeV with a Higgs portal coupling $\lambda = 1$. The process $pp \rightarrow (h \rightarrow SS)(V \rightarrow jj)$ has the same signature as WBF, but the latter has a larger cross

section and is anticipated to be phenomenologically more relevant. Since the two channels are contaminated from the same SM background, one can expect that any beyond the SM evidence would arise solely from WBF for the case of hadron colliders. Therefore, associate production will not be considered further.

Figure 3.2: Feynman diagram for the WBF case at hadron colliders. This Higgs production channel with the subsequent production of S particles can be identified with the final state signature of two jets and missing energy.

Weak Boson Fusion:

Turning to WBF $pp \rightarrow hjj$ (Fig. 3.2), the dominant backgrounds contributing from SM processes are $(Z \rightarrow \nu\bar{\nu}) + \text{jets}$ and $(W \rightarrow \ell\nu) + \text{jets}$ with any jet in the final state arising from either the weak force or the strong force. The jets are reconstructed in the analysis with the anti-kT algorithm [98] of radius 0.4 as in Ref. [172] with a transverse momentum of $p_T(j) > 20$ GeV and within an absolute pseudorapidity region of $|\eta| < 4.9$. Subsequently, any event without at least two leading jets satisfying $p_T(j) > 50$ GeV within $|\eta(j)| < 4.7$ is vetoed. The jets produced by WBF in the signal are expected to have large pseudorapidity η separation and to be back-to-back. Therefore, the signal region is further constrained by requiring $|\Delta\eta(jj)| > 4.0$ and $\eta(j_1)\eta(j_2) < 0$. The latter requirement ensures that the two jets are within opposite hemispheres of the detector, as predicted from the WBF topology. Subsequently, jets that lie between the two leading jets are scanned, and if any of them has a transverse momentum of $p_T > 30$ GeV, the event is vetoed, which allows the suppression of background and signal processes produced by QCD instead of the desired electroweak interaction.

In addition, since the $(W \rightarrow \ell\nu) + \text{jets}$ background process has a lepton in the final state, any event with an isolated lepton is rejected with isolation criteria imposed separately on electrons and muons. Isolation is defined as the sum of transverse momenta of all particle candidates within radius $R = \sqrt{(\Delta\eta)^2 + (\Delta\phi)^2} = 0.3$ (0.4) for electrons (muons). If the isolation is smaller than 16% (25%) of the electron (muon) transverse momentum, then it is defined as isolated. The search region is further restricted with a cut on missing transverse energy $\cancel{E}_T > 100$ GeV and on the invariant mass of the two leading jets $m_{jj} > 800$ GeV.

These cuts are the analysis's baseline cuts, and additional cuts are subsequently applied to study the cut flow of events. For example, the missing energy \cancel{E}_T event distribution plot displayed in Fig. 3.3 shows that the QCD background can be reduced by restricting the search region to

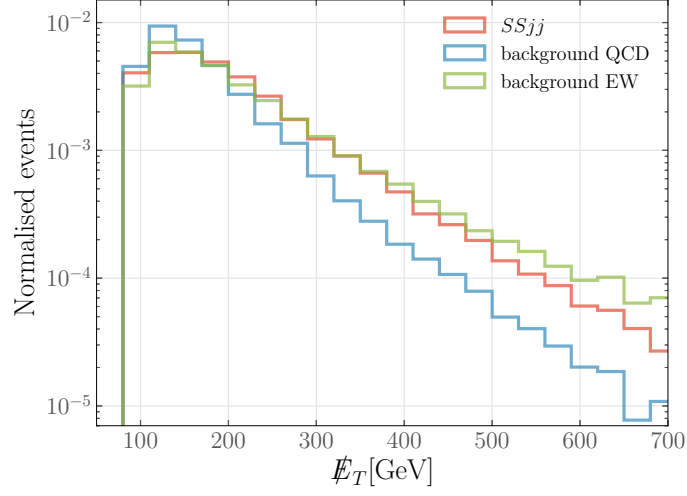


Figure 3.3: Normalised \cancel{E}_T distributions at 100 TeV FCC after the baseline cuts given in Tab. 3.1. The signal is for a mass $m_S = 100$ GeV and a coupling $\lambda = 1$ at 100 TeV FCC and both QCD and electroweak backgrounds are shown.

$\cancel{E}_T > 200$ GeV. The electroweak background though follows a distribution closer to the signal even at higher missing energies. Additional restrictions are also imposed on the pseudorapidity difference between the jets $\Delta\eta > 4.2$ and on their invariant mass $m_{jj} > 2300$ GeV. The result of these stricter requirements can be seen in Tab. 3.1 and the analysis is particularly efficient in restricting the QCD background. It should be noted that only tree level processes have been included, although next-to-leading order (NLO) corrections reported in Ref. [173] will not be critically important to affect the results of this investigation.

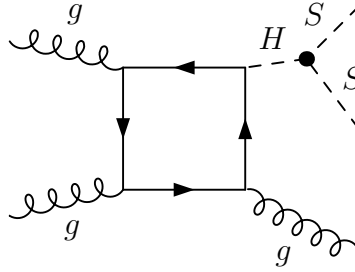


Figure 3.4: Example diagram for mono-jet case, where gluon fusion at next-to-leading-order yields a Higgs recoiled against QCD radiation. Pair production of S is then feasible.

Cuts	$SSjj$	Zjj	W^+jj	W^-jj	Zjj EW	W^+jj EW	W^-jj EW
Baseline	0.0238	10.103	6.6287	3.0501	0.9386	0.5897	0.3833
$\Delta\eta > 4.2$	0.0217	6.6052	4.4727	1.9775	0.8325	0.5232	0.3384
$\cancel{E}_T > 200$ GeV	0.0080	1.5842	0.7633	0.2666	0.3952	0.1668	0.0940
$m_{jj} > 2300$ GeV	0.0041	0.3637	0.2409	0.0637	0.2256	0.1071	0.0594

Table 3.1: Cross sections in units of pb for SS pair production from WBF and contributing SM background at 100 TeV FCC. The Higgs portal parameters are set to $m_S = 100$ GeV and $\lambda = 1$, and baseline cuts correspond to the cuts in Sec. 3.2.1, that have the relaxed restrictions $\Delta\eta_{jj} > 4.0$, $\cancel{E}_T > 100$ GeV and $m_{jj} > 800$ GeV. Corrections from higher order QCD do not affect the calculated estimates, as shown in Ref. [173].

Mono-jet production:

The gluon fusion channel is unique to hadron colliders and requires one-loop processes such as triangle or box Feynman diagrams shown in Fig. 3.4. An off-shell Higgs is produced, along with a single jet, with the S pair production occurring virtually through the Higgs. Background contribution for this channel includes processes with $(Z \rightarrow \nu\bar{\nu}) + \text{jet}$ or $(W \rightarrow \ell\nu) + \text{jet}$ final states as well as $t\bar{t}j$. However, the latter is substantially smaller, in agreement with [170, 174], and hence it has not been included in the full analysis. The accepted events in the analysis must contain a leading jet with transverse momentum $p_T > 30$ GeV and pseudorapidity $|\eta| < 2.4$. A second jet with p_T larger than 30 GeV is allowed in the accepted final state, but its azimuthal separation with the leading jet must satisfy $|\Delta\phi(j_1, j_2)| < 2.5$. This ensures the suppression of possible dijet events. Using the above requirements as baseline cuts, the search region is further restricted with a cut on the missing energy $\cancel{E}_T > 150$ as well as the leading jet transverse momentum $p_T > 100$ GeV. The cut flow from the final two cuts is shown in Tab. 3.2 and the effect of both is important for background reduction. The background has considerable contributions from higher orders in this channel, and thus cross sections are rescaled by a global K-factor $K \simeq 1.6$ as reported in Ref. [173]. The event distributions of signal and background against missing energy \cancel{E}_T are shown in Fig. 3.5.

3.2.2 Lepton Colliders

The same procedure as for the hadron colliders is followed for the lepton collision experiments. Scalar pair production through a virtual Higgs occurs mainly via the associate production with a

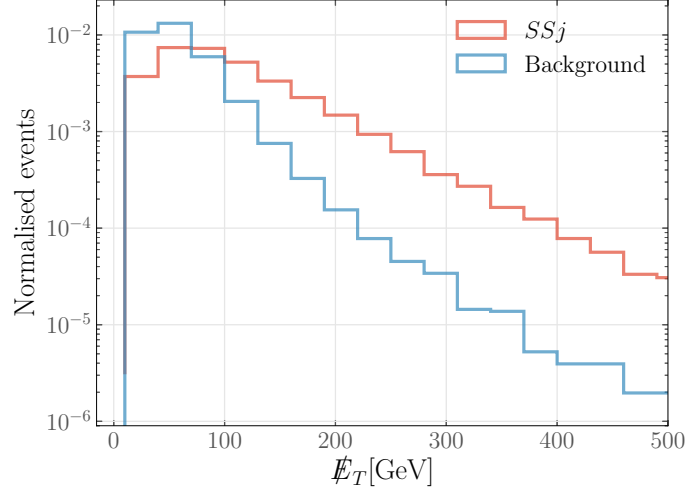


Figure 3.5: \cancel{E}_T distribution (normalised) for mono-jet production of the signal with mass $m_S = 100$ GeV and $\lambda = 1$ at 100 TeV FCC along with the distribution for the combined background. Only the baseline cuts of Tab. 3.2 have been applied for this plot.

Cuts	SSj [pb]	Zj [pb]	W^-j [pb]	W^+j [pb]
Baseline	0.9322	15283	17495	19799
$p_T(j_1) > 100$ GeV	0.2858	820.54	553.20	670.02
$\cancel{E}_T > 150$ GeV	0.1810	298.28	87.381	138.12

Table 3.2: Cross sections for S pair production through gluon fusion with a radiated jet at 100 TeV FCC. The S field parameters are set to $m_S = 100$ GeV and $\lambda = 1$. Cross sections for the background processes are also shown for the baseline cuts without any \cancel{E}_T cut and $p_T(j_1) > 30$ GeV. Subsequent cuts of $p_T(j_1) > 100$ GeV and $\cancel{E}_T > 150$ GeV reduce the background significantly. It should be noted that subdominant $t\bar{t}j$ contamination has not been taken into account and all the background cross sections are corrected with a K-factor of $K \simeq 1.6$ [173] to accommodate NLO effects.

vector boson and via WBF; however no mono-jet channel is available since this requires gluon interactions. To see the effect of the scalar mass m_S , cross sections for various centre-of-mass energies have been calculated for two distinct masses, as shown in Fig. 3.6. In contrast to hadron colliders, the associate production case is considerable, especially for lower energies such as 500 GeV, where the future ILC collider will possibly operate. All events for lepton collisions are generated with cuts $p_T(\ell) > 10$ GeV, $|\eta(\ell)| < 5$ and $\Delta R_{\ell\ell} > 0.4$ applied on the final state light

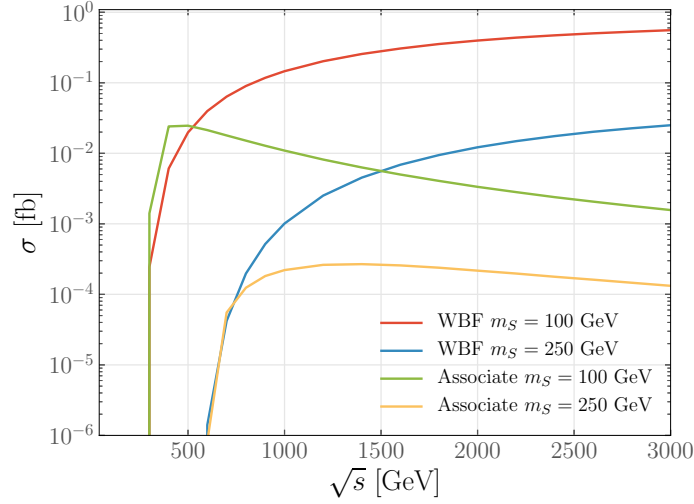


Figure 3.6: Cross section distributions against centre-of-mass energies for WBF and associate pair production of S and two leptons.

leptons ℓ . The analysis for WBF closely follows the one found in Ref. [171].

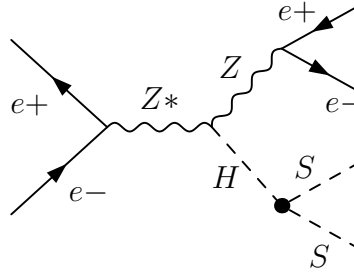


Figure 3.7: Feynman diagram for associate production of the S pair. Although this channel is subdominant at hadron colliders with respect to the WBF, it is still relevant for future lepton collider experiments at relatively low energies, such as ILC.

Associate production:

In the case of associate production, a Higgs is produced with a Z boson that subsequently decays to a pair of same-flavour oppositely-signed leptons as represented by the Feynman diagram of Fig. 3.7. Background contamination arises from channels $e^-e^+ \rightarrow \ell^-\ell^+\nu_\ell\bar{\nu}_\ell$, where the neutrinos appear as missing energy and thus have the same signature as the signal $e^-e^+ \rightarrow (Z \rightarrow \ell^+\ell^-)(h \rightarrow SS)$. A significant difference between the two is that the lepton pair from the signal process has a

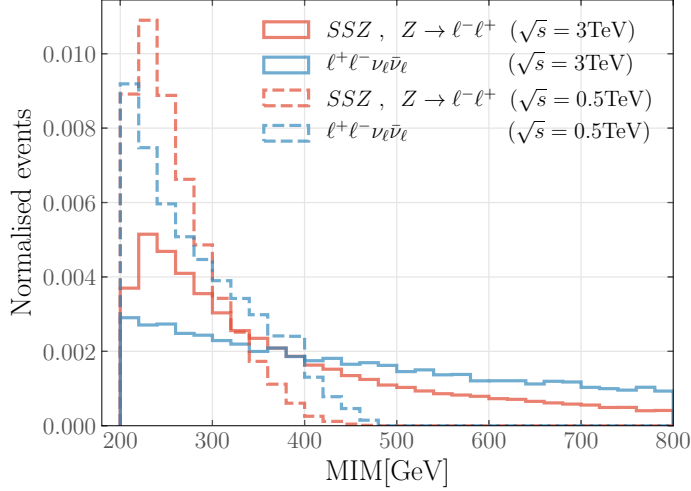


Figure 3.8: Associate production MIM distributions for an S particle with mass $m_S = 100$ GeV and a Higgs portal coupling $\lambda = 1$. Results for both 500 GeV ILC and 3 TeV CLIC are shown, where in the former case, associate production is more pertinent for the analysis than in the latter.

smaller pseudorapidity separation $\Delta\eta_{\ell\ell}$ and a restriction $\Delta\eta_{\ell\ell} < 1.3$ is required to discriminate the background. An important quantity with discriminative power is the missing invariant mass (MIM)

$$\text{MIM} = \sqrt{\not{p}_\mu \not{p}^\mu} \geq 200 \text{ GeV}, \quad (3.5)$$

where $\not{p} = (\sqrt{s}, \vec{0}) - p_{\ell^-} - p_{\ell^+}$ and Fig. 3.8 shows the MIM signal and background distributions for

Cuts	$SSZ, Z \rightarrow \ell^+\ell^-$ [fb]	$\ell^+\ell^-\nu_\ell\bar{\nu}_\ell$ [fb]
Generation	0.0236	669.68
$\Delta\eta_{\ell\ell} < 1.3$	0.0194	139.64
$\cancel{E}_T > 150$ GeV	0.0113	13.786
MIM > 200 GeV	0.0113	2.8209
$M_{\ell\ell} < 120$ GeV	0.0113	2.3947

Table 3.3: Cross sections before and after the applied cuts for the pair production of SS along with a Z through a virtual Higgs. The values are for $\sqrt{s} = 500$ GeV with model parameters set to $m_S = 100$ GeV and $\lambda = 1$.

$m_S = 100$ GeV, $\lambda = 1$ at ILC and CLIC energies. Furthermore, the search region is constrained by a cut on the missing energy, $\cancel{E}_T > 150$ GeV and the lepton invariant mass $M_{\ell\ell} > 200$ GeV. The effect of the applied cuts on the generated events can be seen in Tab. 3.3.

Weak boson fusion: Weak boson fusion is more significant than associated production at \sqrt{s} energies larger than 500 GeV. The signal has a signature similar to the associated production, but only electrons and positrons can appear in the final state. To distinguish the signal events from contamination arising from associate production, a cut is applied on the electron-positron pair invariant mass. For 3 TeV CLIC the value used is $M_{ee} > 2200$ GeV while for 500 GeV ILC, this is relaxed to $M_{ee} > 120$ GeV. The same quantities as in the associate production are appropriate for signal-background discrimination. In particular, a cut is imposed on the pseudorapidity separation between the two leptons $\Delta\eta_{ee} > 6$ ($\Delta\eta_{ee} > 2.0$) for CLIC (ILC). For the rest of the observables, the same cuts are applied for both of the collider concepts. Missing transverse energy must satisfy $\cancel{E}_T > 80$ GeV and the missing invariant mass $MIM > 200$ GeV, otherwise, the event is vetoed. The cut flow is shown in Tab. 3.4, where the events are generated with a requirement that the sum of neutrino's momenta must satisfy $\cancel{E}_T^\nu > 70$ GeV and that $M_{ee} > 1500$ GeV in order to improve the statistics. Fig. 3.9 shows the signal and background distributions for MIM as an example.

Cuts	SSe^-e^+ [fb]	$e^+e^-\nu_\ell\bar{\nu}_\ell$ [fb]
Generation	0.5364	43.86
MIM > 200 GeV	0.5364	9.257
$\Delta\eta_{ee} > 6$	0.4144	1.687
$\cancel{E}_T > 80$ GeV	0.2811	1.446
$M_{ee} > 2200$ GeV	0.2346	0.468

Table 3.4: The effect of the applied cuts on the cross sections for the S pair produced through WBF and background at 3 TeV CLIC. Parameters of the model are set to $m_S = 100$ GeV and $\lambda = 1$, while cuts $\cancel{E}_T^\nu > 70$ GeV and $M_{ee} > 1500$ GeV are enforced at generation level.

It should be noted that an alternative signature would be to use initial state radiation that is emitted from the two colliding electrons or the two W bosons fusing to produce the off-shell Higgs. This would allow using a final state that includes missing energy arising from the produced S pair in the signal case or from the neutrinos in the background processes. In this case, the background consists of processes resulting in $e^+e^- \rightarrow \gamma\nu_e\bar{\nu}_e$, however, after generating signal and

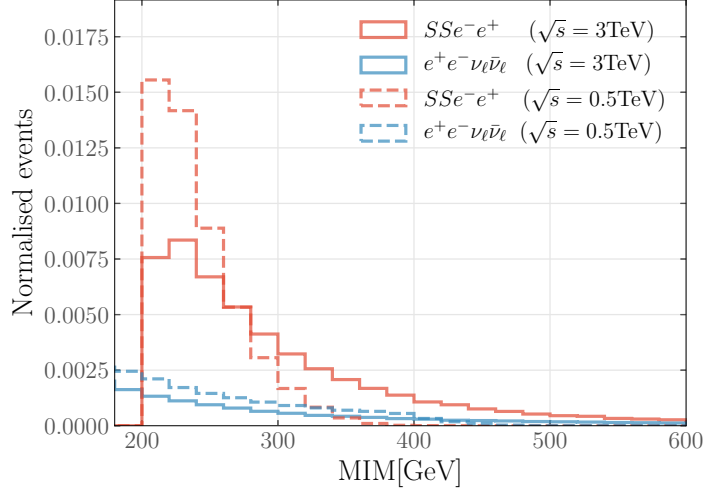


Figure 3.9: Distributions for MIM for signal with mass $m_S = 100$ GeV and $\lambda = 1$ at 500 GeV and 3 TeV lepton colliders produced through WBF, as well as the background contamination arising from the SM.

background events for this scenario, the significance is found to be $N_S/\sqrt{N_B} = 0.0082$. Here N_S denotes the number of signal events while N_B denotes the number of events for the background. This is much smaller than the case of WBF with an electron-positron pair or associate production with a lepton pair, and thus this final state is not further studied.

3.3 Indirect Sensitivity: Virtual S imprints

Precision observables measured at both lepton and hadron colliders can also receive virtual contributions from S that can lead to indirect effects. The discussion about such indirect measurements applies to both collider types.

The presence of an additional scalar induces modifications in the two-point functions between Higgs and Goldstone bosons. The Higgs potential of the SM Lagrangian (2.17) after expanding around the VEV includes the tadpole interactions

$$V(\Phi) \supset th \quad \text{where } t = v(\mu^2 - v^2\lambda_{\text{SM}}), \quad (3.6)$$

which can be minimised at tree level with the choice $t = 0$. However, this leads to tadpole diagrams

at higher orders that are typically removed with a counterterm (see Refs. [175, 176])

$$\delta t + \text{---} \textcircled{\bullet} = 0. \quad (3.7)$$

The consequence is that tadpole diagrams can be neglected in calculations, although δt will appear in other counterterm renormalisation constants such as the Goldstone mass renormalisation

$$\delta m_\pi^2 = -\frac{\delta t}{v} = -\frac{e}{2m_W s_W} \delta t. \quad (3.8)$$

which will be relevant in Sec. 3.3.4 when oblique corrections will be discussed. At one-loop, δt can be understood as corrections to the vacuum

$$\delta v = -\frac{\delta t}{m_h^2} \quad (3.9)$$

which indicates that in order to use the ‘correct’ VEV in the theory, tadpole contributions must be included when a Higgs boson leg is set to its VEV.

3.3.1 Higgs coupling modifications

The narrowness of the Higgs boson $\Gamma_h/m_h \simeq \mathcal{O}(10^{-5})$ allows the use of the Narrow Width Approximation (NWA)¹ when Higgs boson rates to decayed modes are reported. Signal strengths are defined in comparison to the SM expectation value through

$$\mu = \frac{\sigma(h) \times \text{BR}}{[\sigma(h) \times \text{BR}]_{\text{SM}}}, \quad (3.11)$$

where $\sigma(h)$ represents a Higgs production cross section and BR the branching ratio of a particular decay channel. For this particular Higgs portal model, when $m_S > m_h/2$, the Higgs boson signal strength receives modifications from the introduced S particle higher order loops without contributions from non-SM decay channels (see Refs. [170, 177, 178]).

Using the on-shell scheme, where the propagator has residue i , the wave function and mass

¹The Breit-Wigner distribution, obtained by squaring Eq. (2.52), can be approximated as

$$\left| \frac{i}{p^2 - m_{\text{pole}}^2 + im_{\text{pole}}\Gamma} \right|^2 \approx \frac{\pi}{m_{\text{pole}}\Gamma} \delta(p^2 - m_{\text{pole}}^2) \quad (3.10)$$

in the limit $\Gamma \ll m_{\text{pole}}$. This implies that the resonant particle can be treated as on-shell and the production process separates from the decay.

squared renormalisation constants can be computed as

$$\delta Z_H = -\frac{\lambda^2}{8\pi^2} \frac{2m_W s_W}{e} \operatorname{Re} \frac{\partial B_0(q^2, m_S^2, m_S^2)}{\partial q^2} \Big|_{q^2=m_h^2}, \quad (3.12)$$

and

$$\delta m_h^2 = \frac{\lambda^2}{8\pi^2} \frac{4m_W^2 s_W^2}{e^2} \operatorname{Re} B_0(m_h^2, m_S^2, m_S^2) + \frac{\lambda}{16\pi^2} \operatorname{Re} A_0(m_S^2), \quad (3.13)$$

respectively, where A_0 and B_0 are Passarino-Veltman [82] functions obtained after the reduction of tensor integrals in D -dimensional regularisation. These can be found in Ref. [175]. It should be noted that δZ_h is finite since the divergent pieces of the B_0 function are momentum-independent. The correction from S on a singly-produced Higgs or partial widths Γ_i reads as (see Ref. [177])

$$\frac{\sigma(h)}{[\sigma(h)]_{\text{SM}}} = \frac{\Gamma_i}{[\Gamma_i]_{\text{SM}}} = 1 + \delta Z_h \quad (3.14)$$

which implies that the signal strength simplifies to

$$\mu = \frac{\sigma(h) \times \text{BR}}{[\sigma(h) \times \text{BR}]_{\text{SM}}} = 1 + \delta Z_h. \quad (3.15)$$

3.3.2 Off-Shell Higgs boson probes

The off-shell measurement of $p(g)p(g) \rightarrow h \rightarrow ZZ \rightarrow 4$ leptons is of considerable interest since away from the Higgs resonance, Higgs contributions remain relevant due to the boson decaying to longitudinally polarised Z bosons with large destructive interference between $gg \rightarrow h \rightarrow ZZ$ and the scattering of $t\bar{t} \rightarrow ZZ$. The on-shell measurement of Eq. (3.11) can be correlated with the off-shell one in order to obtain a limit on the branching ratio of the Higgs decay to invisible states as shown in Refs. [179, 180]. The s -channel Higgs amplitude is modified by

$$\frac{\mathcal{M}}{\mathcal{M}_{\text{SM}}} - 1 = -\frac{\lambda^2 M_W^2 s_w^2}{8\pi^3 \alpha (s - m_h^2)} \times (B_0(s, m_S^2, m_S^2) - \operatorname{Re} B_0(m_h^2, m_S^2, m_S^2)). \quad (3.16)$$

The effect of the BSM physics can then be computed by modifying the VBFNLO [181] package.

The sensitivity of the channel is severely limited though, as shown from Fig. 3.10, even when extrapolated to 30/ab envisioned to be reached at the 100 TeV FCC-hh [150–152, 182]. Therefore constraints from this channel have not been calculated.

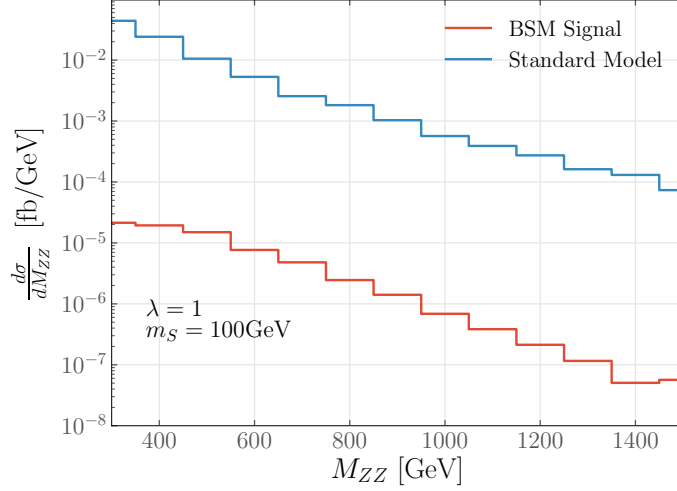


Figure 3.10: Differential cross sections for the channel $gg \rightarrow ZZ$ at 100 TeV FCC implying that corrections from S to the Higgs channel of $pp \rightarrow 4\ell$ are negligible.

3.3.3 Higgs Pair Production

Higgs pair production receives modifications from S -loops and since the trilinear Higgs vertex is obtained by setting one Higgs leg to the VEV, it will depend on the tadpole renormalisation constant δt . The dependence remains after the removal of tadpole diagrams with the choice

$$\delta t = -\frac{\lambda}{8\pi^2} \frac{2m_W s_W}{e} \text{Re} A_0(m_S^2). \quad (3.17)$$

At hadron colliders, the Higgs pair production will be driven mainly from $gg \rightarrow hh$, while for lepton colliders it will be through WBF $e^+e^- \rightarrow hh\nu_e\bar{\nu}_e$. The matrix element then reads

$$|\mathcal{M}|^2 = |\mathcal{M}_{\text{SM}}|^2 + 2\text{Re}(\mathcal{M}_{\text{SM}}\mathcal{M}_\lambda^*), \quad (3.18)$$

where the SM and next-to-leading contributions are given by \mathcal{M}_{SM} and \mathcal{M}_λ^* , respectively. This part follows Ref. [178] and calculation is performed by also modifying the VBFNLO [181] package.

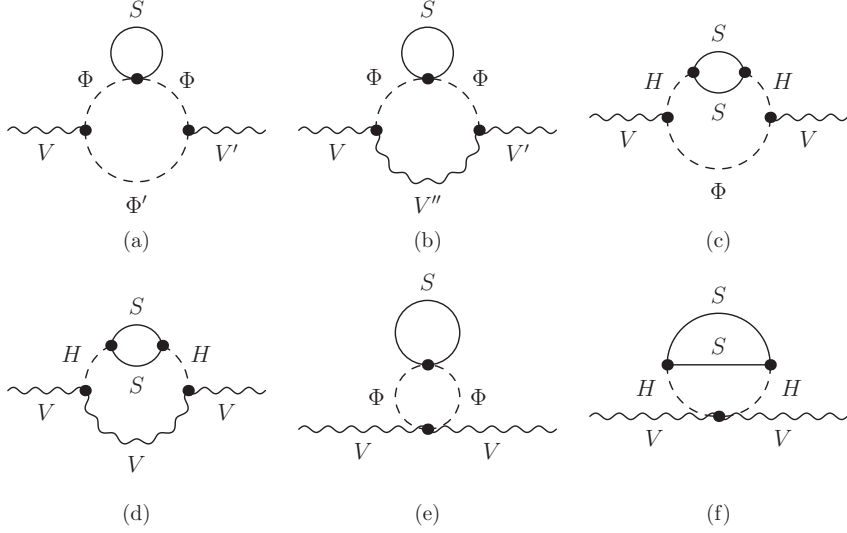


Figure 3.11: Representative Feynman diagrams for the polarisation functions of the boson V at two-loops. Such diagrams result in modifications of the Peskin-Takeuchi parameters S, T, U . Φ, Φ' indicate the possible Higgs and Goldstone boson insertions, while $V, V', V'' = W, Z, A$ are the allowed vector bosons.

3.3.4 Oblique Corrections

Contributions from new physics affecting the propagation of gauge bosons are often parameterised with the Peskin-Takeuchi S, T, U parameters [183] that are given in terms of polarization functions

$$\begin{aligned}
 \text{---} V^\mu(p) \text{---} \text{---} \text{---} \text{---} V^\nu(p) \text{---} &\sim \Pi_{VV'}^{\mu\nu}(p^2) = (p^2 - m_V^2)\delta_{VV'} + \Pi_{VV'}(p^2) \left(g^{\mu\nu} - \frac{p^\mu p^\nu}{p^2} \right) + B_{VV'}(p^2) \frac{p^\mu p^\nu}{p^2}, \\
 &\quad (3.19)
 \end{aligned}$$

where $\Pi_{VV'}$ and $B_{VV'}$ are the transverse and longitudinal parts, respectively. The oblique corrections are expressed using the transverse parts as (see also [184–191])

$$\begin{aligned}
 S &= \frac{4s_W^2 c_W^2}{\alpha} \left(\frac{\Pi_{ZZ}(m_Z^2) - \Pi_{ZZ}(0)}{m_Z^2} - \frac{c_W^2 - s_W^2}{c_W s_W} \frac{\Pi_{AZ}(m_Z^2) - \Pi_{AZ}(0)}{m_Z^2} - \frac{\Pi_{AA}(m_Z^2)}{m_Z^2} \right), \\
 T &= \frac{1}{\alpha} \left(\frac{\Pi_{WW}(0)}{m_W^2} - \frac{\Pi_{ZZ}(0)}{m_Z^2} - \frac{2s_W}{c_W} \frac{\Pi_{AZ}(0)}{m_Z^2} \right),
 \end{aligned}$$

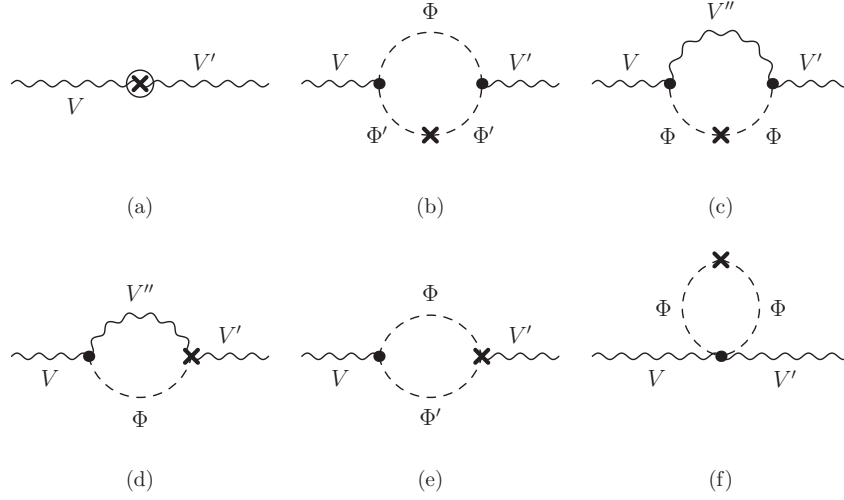


Figure 3.12: Example counterterm topologies required for renormalisation of two-loop polarisation function diagrams shown in Fig. 3.11. The first diagram indicates two-loop renormalisation constants that do not appear at one-loop level. Note that the $\Phi\Phi'V''$ vertex counterterms are suppressed.

$$\begin{aligned}
 U = & \frac{4s_W^2}{\alpha} \left(\frac{\Pi_{WW}(m_W^2) - \Pi_{WW}(0)}{m_W^2} - c_W^2 \frac{\Pi_{ZZ}(m_Z^2) - \Pi_{ZZ}(0)}{m_Z^2} - 2s_W c_W \frac{\Pi_{AZ}(m_Z^2) - \Pi_{AZ}(0)}{m_Z^2} \right. \\
 & \left. - s_W^2 \frac{\Pi_{AA}(m_Z^2)}{m_Z^2} \right). \tag{3.20}
 \end{aligned}$$

In the model of Eq. (3.1) the scalar does not acquire a VEV due to the unbroken \mathbb{Z}_2 and the only interaction is through the Higgs boson, which implies that contributions to the Peskin-Takeuchi parameters only arise at two-loop level. Example diagrams are shown in Fig. 3.11 while 3.12 shows the counterterms. It should be noted that due to the Ward identity, $\Pi_{AA}(0) = 0$, which has been exploited in Eq. (3.20). As a check, the insertions of the S scalar before renormalisation result to

$$\Pi_{AA}^0(0) = -\frac{\alpha(D-4)(D-2)}{256\pi^3 m_W^2} \lambda A_0(m_S^2) A_0(m_W^2), \tag{3.21}$$

where the Feynman gauge has been used. The scalar Passarino-Veltman A_0 function can be expanded for $D = 4 - \epsilon$

$$A_0(x) = x \left[\frac{2}{\epsilon} - \gamma_E - \log \frac{x}{4\pi\mu^2} + 1 + \frac{\epsilon}{4} \left((-\gamma_E - \log \frac{x}{\mu^2} + 1)^2 + 1 + \frac{\pi^2}{6} \right) \right], \quad (3.22)$$

which results to

$$\Pi_{AA}^0(0) = \frac{\alpha\lambda m_S^2}{32\pi^3} \left(\frac{1}{\epsilon} - \gamma_E + \log \left(\frac{m_S m_W}{4\pi\mu^2} \right) - \frac{1}{2} \right) + \mathcal{O}(\epsilon). \quad (3.23)$$

After on-shell renormalisation, this will cancel exactly because of the Goldstone contribution

$$\delta\Pi_{AA}(0) = -\frac{\alpha(D-4)(D-2)}{32\pi^2 m_W^2} \frac{e\delta t}{m_{WSW}} A_0(m_W^2). \quad (3.24)$$

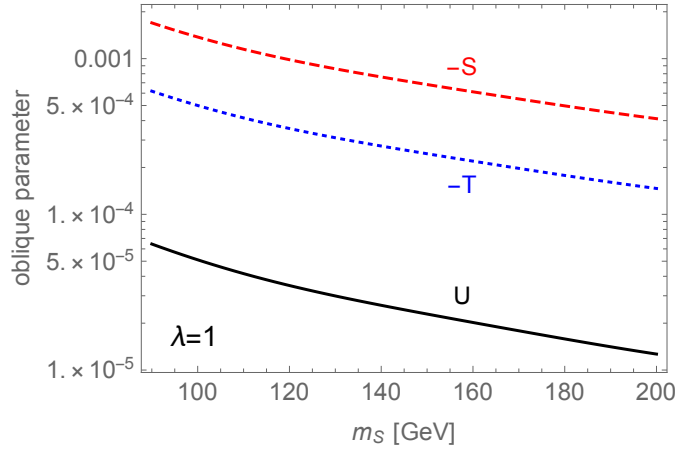


Figure 3.13: Values for the oblique parameters using $\lambda = 1$ at different masses.

The desired topologies and field insertions are obtained with FEYNARTS [192] and the oblique corrections are calculated using FEYNCALC [193, 194], LOOPTOOLS [76, 195] and TARCER [196] with analytical checks to verify that all UV-divergences are removed. Numerical results are then obtained using TSIL [197], which is based on Ref. [198] (see also [199]). The results are shown in Fig. 3.13, and it should be noted that U is suppressed compared to S, T by an order of magnitude. This is expected as the parameter U is sourced by effective operators of dimension-eight, instead of dimension-six that source S, T . The projections of GFITTER [200] with $U = 0$ will be employed for the LHC 300/fb and ILC/GigaZ fits.

3.4 Power meets Precision: Expected Collider Sensitivity

The aforementioned probes allow the discussion of the expected sensitivity of λ, m_S , but first, it is instructive to establish the allowed parameter region of λ , assuming perturbative unitarity is not violated. The discussion of Sec. 2.5.1 could be followed to set bounds on $Sh \rightarrow Sh$ scattering with the constraint on the zeroth partial wave (see also e.g. [201])

$$\text{Re } a_0(Sh \rightarrow Sh) \leq \frac{1}{2}, \quad (3.25)$$

but, in fact, the perturbativity constraint is weaker than constraints from stability considerations of Ref. [202].

In principle a $\lambda_S S^4$ term is allowed in the Lagrangian (3.1) which does not enter any of the calculations above. While the relevant coupling can not be measured due to its pure dark matter nature, it does have a significant role when considering phase transitions and stability. The field S could acquire a VEV w at some time in the history of the Universe and requiring the potential of the model $V(\Phi, S)$ to acquire the correct minimum from the Higgs doublet $V(v, 0) < V(0, w)$ yields bounds on λ_S in terms of m_S and λ . Avoiding negative runaway results in additional limits. These are discussed in detail in Ref. [202] provides the constraints in the λ - m_S plane by also imposing the additional requirement that λ_S remains perturbative. These regions excluded by stability, although not necessarily relevant, are used in the upcoming sections for completion.

3.4.1 Expected collider sensitivity for direct detection

Signal events are generated for several masses m_S between 75 GeV and 325 GeV using Higgs portal coupling $\lambda = 1$. Cross sections scale with λ^2 ; therefore, results for $\lambda \neq 1$ can be inferred by rescaling them. Subsequently, cross sections need to be rescaled with the integrated luminosity of each collider in order to obtain the final number of signal N_S and background events N_B . For hadron collisions at the 100 TeV FCC we assume luminosities of 3/ab and 30/ab. ILC, operating at 500 GeV, is foreseen to reach values of 2/ab at later stages of the experiment [203] and 3/ab for CLIC at collision energies of 3 TeV. For a total of N events, the signal and background relation $N_S = N - N_B$ has uncertainty $\sigma^2(N_S) = \sigma^2(N) + \sigma^2(N_B) \approx N$, when assuming that N is characterised by a Poissonian fluctuation and that $\sigma(N_B)$ is negligible. The latter is reasonable since the background is estimated with large Monte Carlo statistics. This

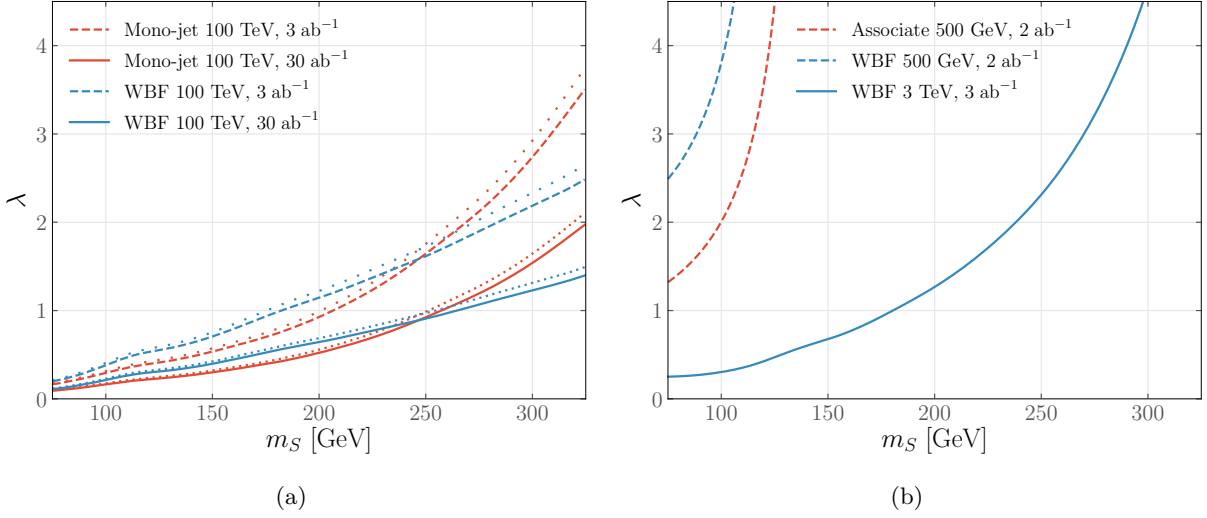


Figure 3.14: (a) 68% exclusion regions for FCC at integrated luminosities of 3 ab^{-1} and 30 ab^{-1} . 30% increment of the background for the 3 ab^{-1} and 30 ab^{-1} luminosities are shown as loosely dotted and dotted, respectively. (b) Exclusion regions at 68% for ILC at 2 ab^{-1} integrated luminosity and 3 TeV CLIC at 3 ab^{-1} .

gives the significance

$$\frac{N_S}{\sigma(N_S)} = \frac{N_S}{\sqrt{N_S + N_B}}, \quad (3.26)$$

which represents the number of standard deviations away from the signal's peak. By requiring $N_S/\sqrt{N_S + N_B} = 1$, one can obtain the 68% exclusion regions which are shown in Fig. 3.14 for FCC-hh and lepton colliders. In the former case, mono-jet and WBF processes are both competitive, although WBF delivers better sensitivity at masses larger than $m_S \sim 250$ GeV. Turning to lepton colliders, the associate production provides better results than WBF, but only at the energies of ILC. At higher energies, WBF is the only available mode.

3.4.2 Expected collider sensitivity for indirect detection

Errors for Higgs strength measurements in the presence of singlets have been supplied by Ref. [204] for LHC as

$$\text{LHC : } \mu = [0.96, 1.03]. \quad (3.27a)$$

For relatively low energy lepton colliders, the main constraints arise from the projection of $e^+e^- \rightarrow hZ$ and the fractional signal strength uncertainties are [205]

$$\text{ILC-250} : \frac{\delta\mu}{\mu} = 0.29\%, \quad (3.27b)$$

$$\text{CLIC-380} : \frac{\delta\mu}{\mu} = 0.44\%, \quad (3.27c)$$

$$\text{FCC-ee(240)} : \frac{\delta\mu}{\mu} = 0.2\%. \quad (3.27d)$$

Moving to a future hadron collider, based on Ref. [151] the uncertainties depending on the decay of the Higgs are anticipated as

$$\text{FCC-hh} : \frac{\delta\mu}{\mu} = 1.22 - 1.88\%. \quad (3.27e)$$

We show the results for these experiments in Fig. 3.15.

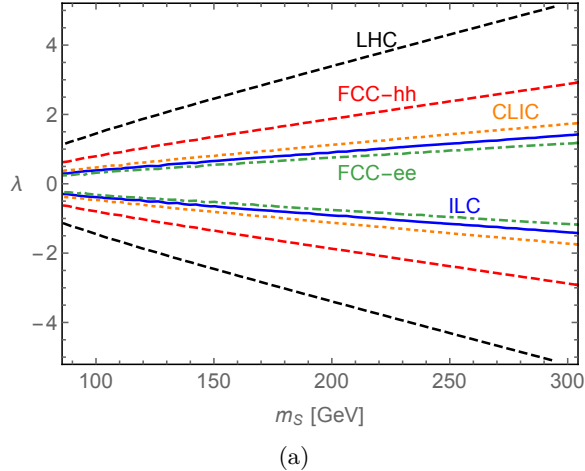


Figure 3.15: Limits from uncertainties quoted in Eqs. (3.27a)-(3.27e) for the parameter space of the Higgs portal model.

Moving to the Higgs self-coupling, CMS [207] quotes 68% and 95% confidence level intervals $\kappa_{\lambda_{\text{SM}}}^{68\%} = \lambda_{\text{SM}}^{68\%}/\lambda_{\text{SM}} = [0.35, 1.9]$ and $\kappa_{\lambda_{\text{SM}}}^{95\%} = \lambda_{\text{SM}}^{95\%}/\lambda_{\text{SM}} = [-0.18, 3.6]$, respectively, for the HL-LHC. The perturbative limits of hh scattering are slightly more than a factor of two away from these constraints. This indicates that even though the range of the self-coupling is perturbatively meaningful, the constraints are weak, which is because of the small di-Higgs production at the

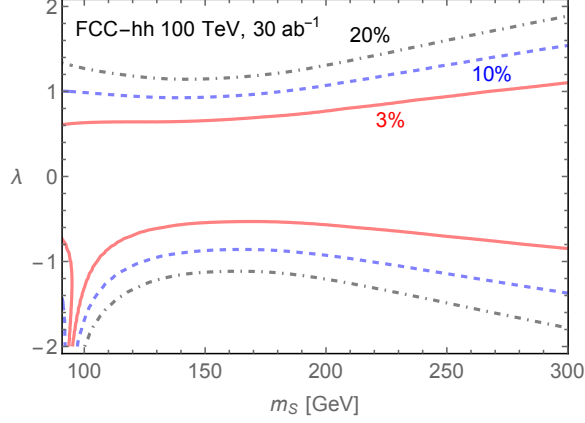


Figure 3.16: Sensitivity obtained from di-Higgs production at FCC-hh with an integrated luminosity of 30/ab. The different lines indicate the expected accuracies of κ_λ , and 3% corresponds to the 68% confidence level reported in Ref. [206]. Results for CLIC are shown in Fig. 3.18(b).

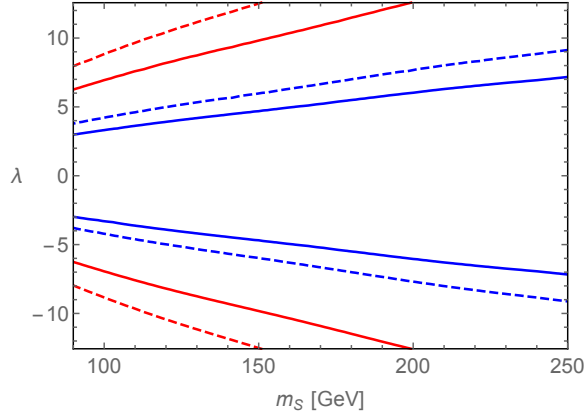


Figure 3.17: S, T constraints at 68% and 95% confidence levels are shown with solid and dashed lines, respectively. Red (blue) indicates the results for LHC 300/fb (ILC/GigaZ) obtained with the confidence intervals provided by GFITTER [200] for $U = 0$.

LHC. Increasing the production of a Higgs pair motivates the push for energies much higher than the LHC.

The FCC-hh with a centre-of-mass energy of 100 TeV is expected to deliver a precision up to 3 – 6%, depending on the capabilities of the machine and the detector [206, 208, 209]. Results shown in Fig. 3.16 are obtained following Ref. [178] by excluding S -induced corrections from points in the (λ, m_S) plane when they deviate more than the allowed modification expected from

κ_λ . However, due to the theoretical uncertainties lying around $\sim 10\%$ [210], reinterpretations are also shown Fig. 3.16 as they will affect the uncertainty of λ unless theoretical improvements are achieved. It should be noted that the WBF channel behaves in a qualitatively identical way at lepton colliders.

The last probe under consideration is the oblique parameters, where correlation matrices, central values and uncertainties are given in Ref. [200] as

$$\text{LHC} : \rho = \begin{pmatrix} 1 & 0.96 \\ 0.96 & 1 \end{pmatrix} \quad (\Delta S, \Delta T) = (0.086, 0.064), \quad (3.28)$$

$$\text{GigaZ} : \rho = \begin{pmatrix} 1 & 0.91 \\ 0.91 & 1 \end{pmatrix} \quad (\Delta S, \Delta T) = (0.018, 0.023). \quad (3.29)$$

By constructing the inverse of the covariance matrix using the correlation matrix and the uncertainties, one can obtain the relevant χ^2 and then the contours in the parameter space of the Higgs portal, shown in Fig. 3.17. Both the GigaZ and LHC constraints are not competitive with indirect constraints from on-shell Higgs measurements at Higgs factories such as ILC, CLIC and FCC-ee, even though GigaZ improves the sensitivity dramatically.

3.5 Discussion and Conclusions

In Fig. 3.18 we overview the expected sensitivity achievable by FCC-hh and CLIC for this particular singlet extension. For the indirect measurements, favourable constraints are obtained from di-Higgs production due to the sensitivity of $gg \rightarrow hh$ to deviations of the trilinear Higgs coupling. The Higgs signal strength delivers comparable constraints at lepton colliders such as CLIC, especially for relatively larger values of the scalar's mass. This is not the case for measurements through hadron collisions at FCC-hh.

The future lepton colliders are capable of enhancing the precision of the S , T and U parameters dramatically, which would render them the most precisely measured observables under consideration (see Ref. [211] for a theoretical discussion). However, since in our scalar extension scenario contributions to the oblique parameters only arise at two-loop order, the sensitivity is relatively poor compared to other suitable modes, and it is unlikely that they would compete unless sensitivity is increased by an order of magnitude.

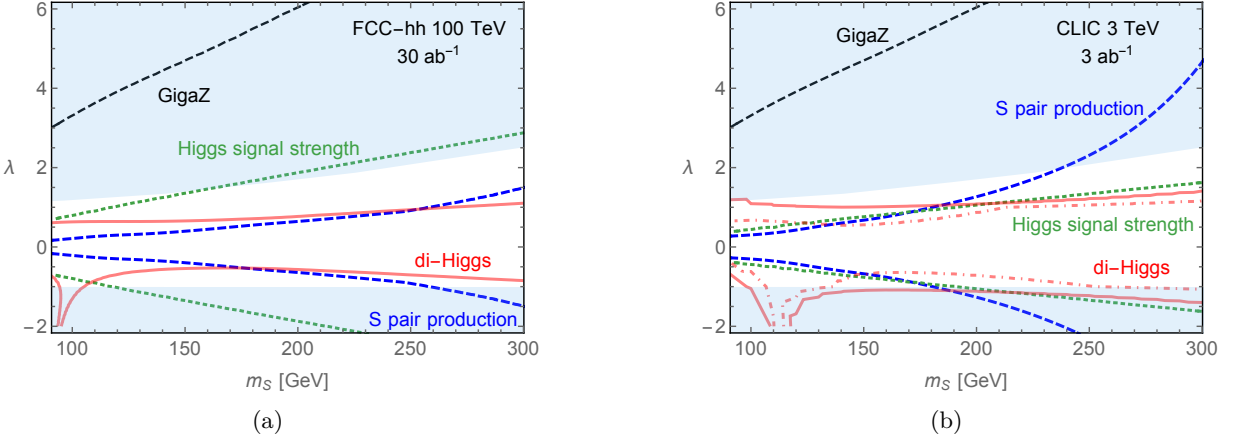


Figure 3.18: Best case sensitivities for (a) FCC-hh and (b) CLIC (3 TeV). The dashed blue line for S pair production refers to WBF, the green line denotes the expected constraints from Higgs signal strengths, and the GigaZ extrapolation of the sensitivity obtained from oblique corrections is shown as a black dashed line. Results from di-Higgs are reflected by the red lines and for 3 TeV CLIC both 5%- and 10%-level accuracies are included as dash-dotted and solid lines, respectively. The Higgs signal strength results are obtained with the 3 TeV value $\delta\mu/\mu = 0.39\%$ from Ref. [205]. Assuming no additional heavy states other than the singlet scalar, the stability constraints are shown as shaded regions [202].

For low masses, the direct searches for Higgs decaying to missing energy provide the best sensitivity, and are one of the most promising avenues for both CLIC and FCC-hh. Along with measurements of the Higgs trilinear coupling and the Higgs signal-strength for CLIC, they can constrain or possibly find evidence for the model under consideration and are complementary. It should also be noted that if the precision predicted by FCC-ee projections is achieved, then similar sensitivity can be achieved as with the combined direct searches and di-Higgs measurements at FCC-hh, as indicated by Fig. 3.15.

It is crucial to note, however, that the applicability of each analysis and its viability to reach such sensitivity does depend on the precision of each collider concept and on the control that can be accomplished over the relevant final states. The 3% accuracy for di-Higgs measurements at FCC-hh used in Fig. 3.18 does provide the best sensitivity at large masses and could be experimentally feasible to achieve (see Ref. [206]). However, this also heavily relies on reducing the uncertainty from the theory side. If this is not attainable and the accuracy is lowered to $\sim 10\%$ then the direct channels for missing energy become favourable, which are also impaired

by very small ratios of signal over background. This indicates that one would need to know the background at high accuracy in order to distinguish the signal. Data-driven techniques can result in improvements (see for example Refs. [212–214]). Nevertheless, both channels are complementary and can hint at the possible existence of a dark-matter scalar for a large mass range.

Lepton collider concepts also largely depend on the achievable accuracy. The di-Higgs production for an anticipated accuracy of around 5 – 10% (based on the extrapolations of [215, 216]) provides the optimal constraints at heavier masses compared to the alternative direct detection and signal strength measurements. However, more conservative estimates, such as 22% given in Ref. [217], render the self-coupling measurement unable to compete with the alternative modes. It should also be noted that the direct detection in lepton colliders does not suffer from the low signal-to-background ratio, which could be beneficial at lower masses.

The singlet extension model is by construction hard to constrain, with sensitivity largely dependent on the accuracy that can be achieved. FCC-hh and CLIC provide comparable constraints, although the former can be slightly better, assuming that systematic uncertainties are kept under control. The pattern that can be observed here is that for both scenarios, efficient extraction of information allowing to properly separate the background and improve the accuracy can be beneficial. This is especially the case for final states that are hard to efficiently detect especially in the presence of multi-jet backgrounds. This will be explored further in the next section in motivated scenarios, showing that using Machine Learning (ML) techniques can render previously inaccessible channels to become highly suitable for the detection of new physics.

Chapter 4

Asymmetric Cascade decays in models with rich scalar phenomenology

4.1 Introduction

Future colliders pushing the energy frontier to new heights will be crucial testing grounds for new physics models in the upcoming decades. Construction, design and assembly of such machines requires a substantial investment of manpower, time and funds; thus it would be apposite to ensure that the plethora of data collected by future (and present) experiments are fully exploited. The importance of efficiently separating signal from background in order to achieve high sensitivity in BSM studies has recently led to extensive use of ML techniques for various applications in particle physics (for an exhaustive collection of references, see Ref. [218]). For example, the decay of a Higgs to b -quarks $h \rightarrow b\bar{b}$ is known to be more demanding to identify than other decays (e.g. diphoton), but recent developments using ML (e.g. [219–223]) come to the rescue. Extending this to more complicated channels with multi-jet events can actually become highly relevant when Neural Networks (NNs) are used to efficiently utilise the information encoded in the event. As seen in the last Chapter, results from new collider concepts critically depend on this, and in this Chapter the benefit of using ML for event-based classification will be motivated.

With the Higgs sector being largely unexplored at the current luminosity of LHC, the possibility

of the existence of multiple heavy exotic scalar bosons that are coupled with SM particles remains viable, and their resonances could be produced through similar decay channels as the SM Higgs. In particular, gluon fusion could be a dominant production mode of such scalars, as long as there is a sizeable Yukawa coupling with the top quark. This would imply a relatively large decay branching ratio of the scalar to a $t\bar{t}$ pair if it is accessible kinematically, as shown in Fig. 4.1. While searching for an on-shell resonance in this mode could, in principle, enhance the discovery sensitivity, the channel suffers from a large interference with the continuum background $gg \rightarrow t\bar{t}$ arising from QCD, resulting in considerable distortion of the signal's peak [224–226] (see Fig. 4.2). This impacts the allowed parameter regions of UV completions to the SM that are commonly explored, such as the Two-Higgs Doublet Model (2HDM) (see Ref. [227] for a review). Although it is viable that this channel could still provide sensitivity¹, it would be advantageous also to study different processes. In cases where signal-background can decrease the $t\bar{t}$ peak, constructive signal-signal interference can enhance the signal of different channels (e.g. di-Higgs, see [231]) and restore sensitivity. However, as such processes can have substantially reduced sensitivities for the current luminosity of LHC, alternative signatures could also be considered with the potential to lead to new physics discoveries at the High Luminosity (HL) LHC.

Considering scenarios with richer scalar phenomenology, multi-Higgs production through cascade decays of a heavy scalar to a second neutral resonance and the SM Higgs becomes a viable option (see Fig. 4.1). Due to the busy final state of such a channel, though, sensitivity suffers unless one resorts to NNs for selecting the relevant signal region methodically. The motivated models are summarised in Sec. 4.2. Subsequently, the discovery potential of such signatures will be explored in Sec. 4.3, both in the context of the next-to-minimal Two-Higgs Doublet Model (N2HDM) [232] and through a model-independent scan. Finally, the effects from both signal and background interference in this channel are taken into consideration in Sec. 4.4.

¹Dedicated shape analyses taking interference into account could search peak-dip structures in the continuum background that arises from the presence of additional scalars [228–230]. Depending on the relative phases between signal and background, nearly pure dips could also appear, which would also help enhance sensitivity.

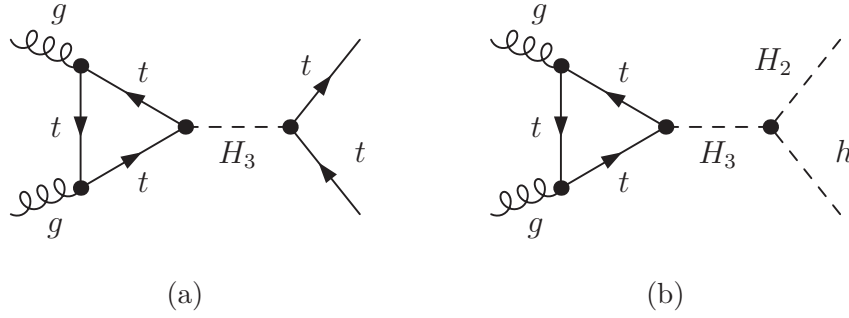


Figure 4.1: Gluon fusion diagrams for an H_3 resonance that decays to $H_3 \rightarrow t\bar{t}$ or $H_3 \rightarrow H_2 h$.

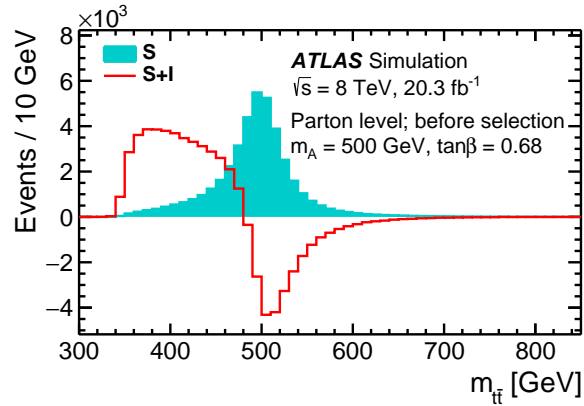


Figure 4.2: Signal only and destructive signal-background interference. The figure is from Ref. [233].

4.2 Models

For the purpose of this Chapter it is convenient to define a generic phenomenological Lagrangian that UV completions of the SM can be matched to so that both CP even and CP odd effects are

captured. The Lagrangian is given by

$$\begin{aligned}
\mathcal{L} = \mathcal{L}_{\text{SM}} + \sum_{i=2,3} \frac{H_i}{v} & \left[C_{H_i}^{\text{even}} \frac{g_s^2}{16\pi^2} G_{\mu\nu}^a G^{a\mu\nu} + C_{H_i}^{\text{odd}} \frac{g_s^2}{16\pi^2} G_{\mu\nu}^a \tilde{G}^{a\mu\nu} \right] \\
& - \frac{\lambda_{H_2hh}}{2} H_2 h^2 - \frac{\lambda_{H_3hh}}{2} H_3 h^2 - \lambda_{H_3H_2h} H_3 H_2 h \\
& - y_{H_3}^E \frac{m_t}{v} H_3 \bar{t}_L t_R - y_{H_2}^E \frac{m_t}{v} H_2 \bar{t}_L t_R + \text{h.c.} \\
& - iy_{H_3}^O \frac{m_t}{v} H_3 \bar{t}_L t_R - iy_{H_2}^O \frac{m_t}{v} H_2 \bar{t}_L t_R + \text{h.c.} ,
\end{aligned} \tag{4.1}$$

where the trilinear couplings λ_{ijk} for $i, j, k \in \{h, H_2, H_3\}$ introduce interactions between the scalar modes inducing the cascade decay. The dual field strength tensor of the gluon field is defined by $\tilde{G}_{\mu\nu}^a = \epsilon_{\mu\nu\sigma\rho} G^{a\sigma\rho}/2$. The interactions between $H_{2,3}$ and two gluons are matched at one-loop to capture the full top mass dependence given by the coefficients

$$C_{H_i}^{\text{even}} = \frac{3y_{H_i}^E m_t^2}{q^2} [2 - (q^2 - 4m_t^2)C_0(\tau)] , \tag{4.2}$$

$$C_{H_i}^{\text{odd}} = -4iy_{H_i}^O m_t^2 C_0(\tau) , \tag{4.3}$$

where $\tau = q^2/4m_t^2$ and q is the four momentum of the scalar leg. $C_0(\tau)$ is the scalar three-point function obtained after the Passarino-Veltman reduction [82] (see also [234]) of the triangle diagram of gluon fusion. In this case it can be simplified to [79, 235]

$$C_0(\tau) = \frac{1}{2q^2} f(\tau) , \tag{4.4}$$

where

$$f(\tau) = \begin{cases} \arcsin^2 \sqrt{\tau} & \text{for } \tau \leq 1 \\ \left[\log \left(\frac{1 + \sqrt{1 - \tau^{-1}}}{1 - \sqrt{1 - \tau^{-1}}} \right) - i\pi^2 \right]^2 & \text{for } \tau > 1 \end{cases} . \tag{4.5}$$

We additionally consider two motivated BSM scenarios that can be matched to the simplified Lagrangian and are introduced in the following sections.

4.2.1 N2HDM

The N2HDM is based on the CP conserving 2HDM that has two scalar doublets under $SU(2)_L$ (Φ_1 and Φ_2), extended by a real singlet field Φ_S that acquires a non-vanishing VEV [232]. It should be noted that if the singlet does not develop a VEV, the model provides a candidate for dark matter, similarly to the singlet extension of Eq. (3.1), but this will not be the case here. The scalar potential is

$$V = m_{11}^2 \Phi_1^\dagger \Phi_1 + m_{22}^2 \Phi_2^\dagger \Phi_2 - m_{12}^2 (\Phi_1^\dagger \Phi_2 + \text{h.c.}) + \frac{\lambda_1}{2} (\Phi_1^\dagger \Phi_1)^2 + \frac{\lambda_2}{2} (\Phi_2^\dagger \Phi_2)^2 \quad (4.6)$$

$$+ \frac{\lambda_3}{2} (\Phi_1^\dagger \Phi_1)(\Phi_2^\dagger \Phi_2) + \frac{\lambda_4}{2} (\Phi_1^\dagger \Phi_2)(\Phi_2^\dagger \Phi_1) + \frac{\lambda_5}{2} [(\Phi_1^\dagger \Phi_2)^2 + \text{h.c.}] \quad (4.7)$$

$$+ \frac{1}{2} m_S^2 \Phi_S^2 + \frac{\lambda_6}{8} \Phi_S^4 + \frac{\lambda_7}{2} (\Phi_1^\dagger \Phi_2) \Phi_S^2 + \frac{\lambda_8}{2} (\Phi_2^\dagger \Phi_1) \Phi_S^2, \quad (4.8)$$

where the last line is the introduction of further real scalar terms to the 2HDM. The following symmetries are imposed,

$$\mathbb{Z}_2 : \Phi_1 \rightarrow \Phi_1, \quad \Phi_2 \rightarrow -\Phi_2, \quad \Phi_S \rightarrow \Phi_S, \quad (4.9)$$

$$\mathbb{Z}'_2 : \Phi_1 \rightarrow \Phi_1, \quad \Phi_2 \rightarrow \Phi_2, \quad \Phi_S \rightarrow -\Phi_S, \quad (4.10)$$

where the first one is softly broken by the m_{12} term. Extending this symmetry to the fermion sector guarantees that flavour-changing neutral currents will not arise. This can result in various types of 2HDM, depending on how \mathbb{Z}_2 charges are assigned to the fermions, which will not be of relevance here. The \mathbb{Z}'_2 symmetry is spontaneously broken by the VEV v_S of Φ_S , inducing mixing among the distinct neutral particles. After electroweak SSB, the doublets can be expanded around their VEVs, becoming

$$\Phi_1 = \begin{pmatrix} \phi_1^+ \\ \frac{1}{\sqrt{2}}(v_1 + \rho_1 + i\eta_1) \end{pmatrix}, \quad \Phi_2 = \begin{pmatrix} \phi_2^+ \\ \frac{1}{\sqrt{2}}(v_2 + \rho_2 + i\eta_2) \end{pmatrix}, \quad (4.11)$$

where v_i , ϕ_i^+ , ρ_i , η_i are the VEV, complex charged, real neutral CP even and real neutral CP odd fields of Φ_i ($i = 1, 2$), respectively. The singlet scalar is parametrised by $\Phi_S = v_S + \rho_S$ and ρ_S is a real CP even field. Substituting the parametrisations of the doublets and the scalar in the Lagrangian, one obtains a 7×7 mass matrix that can be decomposed to 2×2 , 2×2 and 3×3 blocks for the charged Higgs, CP even and pseudoscalar states, respectively. As in the 2HDM,

the charged and CP odd matrices can be diagonalised by a rotation matrix

$$R_\beta = \begin{pmatrix} \cos \theta_\beta & \sin \theta_\beta \\ -\sin \theta_\beta & \cos \theta_\beta \end{pmatrix}, \quad (4.12)$$

where the angle θ_β is defined through the ratio $\tan \theta_\beta = v_2/v_1$ and the SM VEV $v \approx 246$ GeV is reproduced by $v_1^2 + v_2^2 = v^2$. The resulting states of the rotation are the Goldstone bosons π^\pm and π^0 that give mass to the W^\pm and Z bosons, with the addition of the charged Higgs H^\pm and a pseudoscalar A .

The CP even neutral sector is a 3×3 matrix M^2 , which can be diagonalised using an orthogonal matrix R , parametrised by three mixing angles α_i ($i = 1, 2, 3$) with eigenvalues

$$RM^2R^T = \text{diag}(m_{H_1}^2, m_{H_2}^2, m_{H_3}^2). \quad (4.13)$$

R rotates the states of the interaction basis (ρ_1, ρ_2, ρ_S) to the physical Higgs eigenbasis (H_1, H_2, H_3) , where by convention the SM Higgs is $h = H_1$ with mass $m_{H_1} = m_h = 125$ GeV and the masses of the exotic physical scalars are $m_{H_2} < m_{H_3}$. In total, N2HDM has 12 independent input parameters that can be chosen as ²

$$\alpha_{1,2,3}, \tan \theta_\beta, v, v_S, m_{H_{1,2,3}}, m_A, m_{H^\pm}, m_{12}^2. \quad (4.14)$$

4.2.2 Two-singlet extended SM

The two-singlet extended SM, where two real singlet scalars S_1, S_2 are introduced, is briefly reviewed in this section (for explorations in the literature involving this model, see Refs. [236–242]). This leads to signatures with CP even couplings [243] with the possibility of the appearance of a dark matter candidate (see for example [244, 245]). The potential of the model,

$$\begin{aligned} V(\Phi, S_1, S_2) = & -\mu_\Phi^2 \Phi^\dagger \Phi - \frac{1}{2} \mu_{S_1}^2 S_1^2 - \frac{1}{2} \mu_{S_2}^2 S_2^2 + \lambda_\Phi (\Phi^\dagger \Phi)^2 + \lambda_{S_1} S_1^4 + \lambda_{S_2} S_2^4 \\ & + \lambda_{\Phi S_1} \Phi^\dagger \Phi S_1^2 + \lambda_{\Phi S_2} \Phi^\dagger \Phi S_2^2 + \lambda_{S_1 S_2} S_1^2 S_2^2, \end{aligned} \quad (4.15)$$

²Requiring the VEVs to minimise the potential yields three minimisation conditions that reduce the independent parameters of the model. For a complete description of N2HDM, see [232].

can be obtained by introducing the two scalar degrees of freedom constrained with the discrete symmetries

$$\mathbb{Z}_2 : S_1 \rightarrow -S_1, S_2 \rightarrow S_2, \quad (4.16)$$

$$\mathbb{Z}'_2 : S_1 \rightarrow S_1, S_2 \rightarrow -S_2. \quad (4.17)$$

Here Φ denotes the SM Higgs doublet, which acquires a VEV v after SSB and gives rise to the usual Goldstone bosons ‘eaten’ by the W and Z boson fields, as well as a scalar field ϕ . The \mathbb{Z}_2 and \mathbb{Z}'_2 symmetries are also spontaneously broken by the two scalars that acquire non-zero VEVs when expanded to $S_1 = \phi_{S_1} + v_{S_1}$ and $S_2 = \phi_{S_2} + v_{S_2}$. The remaining scalar fields are mixed through the mass matrix that, after substituting the μ_{Φ, S_1, S_2} using the three constraints obtained by minimising the potential [242], becomes

$$M^2 = \begin{pmatrix} v^2 \lambda_{\Phi} & v v_{S_1} \lambda_{\Phi S_1} & v v_{S_2} \lambda_{\Phi S_2} \\ v v_{S_1} \lambda_{\Phi S_1} & 4 v_{S_1}^2 \lambda_{S_1} & 2 v_{S_1} v_{S_2} \lambda_{S_1 S_2} \\ v v_{S_2} \lambda_{\Phi S_2} & 2 v_{S_1} v_{S_2} \lambda_{S_1 S_2} & 4 v_{S_2}^2 \lambda_{S_2} \end{pmatrix}, \quad (4.18)$$

and can be diagonalised with

$$R = \begin{pmatrix} c_{\theta_1} c_{\theta_2} & s_{\theta_1} c_{\theta_2} & s_{\theta_2} \\ -s_{\theta_1} c_{\theta_3} - c_{\theta_1} s_{\theta_2} s_{\theta_3} & c_{\theta_1} c_{\theta_3} - s_{\theta_1} s_{\theta_2} s_{\theta_3} & c_{\theta_2} s_{\theta_3} \\ s_{\theta_1} s_{\theta_3} - c_{\theta_1} s_{\theta_2} c_{\theta_3} & -s_{\theta_1} s_{\theta_2} c_{\theta_3} - c_{\theta_1} s_{\theta_3} & c_{\theta_2} c_{\theta_3} \end{pmatrix}. \quad (4.19)$$

c_{θ_i} and s_{θ_i} denote $\cos \theta_i$ and $\sin \theta_i$, respectively and $\theta_i \in [-\pi/2, \pi/2]$ ($i = 1, 2, 3$). In the mass-diagonal basis, the three physical neutral scalars become

$$\begin{pmatrix} H_1 \\ H_2 \\ H_3 \end{pmatrix} = R \begin{pmatrix} \phi \\ \phi_{S_1} \\ \phi_{S_2} \end{pmatrix}, \quad (4.20)$$

and one can identify H_1 with the SM Higgs h . The parameters of the model are thus

$$\theta_{1,2,3}, v_{S_1}, v_{S_2}, m_{H_{2,3}}. \quad (4.21)$$

The couplings of the physical fields of the model are then obtained from

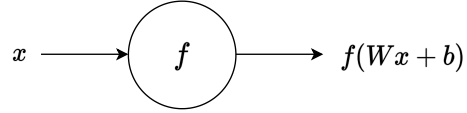
$$\begin{array}{c} H_j \\ \diagup \\ \bullet \\ \diagdown \\ H_i \quad H_k \end{array} = -i\lambda_{ijk} = iS_{ijk} \frac{\partial^3 \mathcal{L}}{\partial H_i \partial H_j \partial H_k}, \quad (4.22)$$

and can be mapped to the trilinear couplings of Eq. (4.1) up to combinatorial factors S_{ijk} due to conventions. The hierarchy $m_{H_3} \geq m_{H_2} \geq m_h$ along with the requirements $m_{H_3} \geq m_{H_2} + m_h$ and $m_{H_2} \geq m_t$ opens kinematically the possibility of multi-Higgs decays.

4.3 Sensitivity improvements through neural network memory

4.3.1 Remarks on Neural Networks with memory

Neural networks that endeavour to uncover hidden relationships in data using a series of interconnected nodes (or units) have been used widely in particle physics during the last few years (for a ‘living review’ see [218]). A node can be represented as



where f is an activation function, W is the weight matrix and b a bias vector. One of the most commonly used types of neural networks consists of fully connected nodes, forming a Dense Neural Network (DNN) as in Fig. 4.3. In supervised ML cases, weight values W are varied during training with gradient descent algorithms in order to (typically) reach the global minimum of the loss function L , which evaluates the ability of the network to predict the label of each data entry correctly. Simple cut-and-count analyses, even when using observables that can access kinematical correlations between the final states, result in rectangular signal regions of the kinematical observables measured at colliders which might systematically restrict the signal-to-background ratio. It is hence instrumental to consider advanced techniques involving NNs aiming to access additional information of such events directly, using only final state observables as available from detectors.

Although DNNs are useful tools in classification problems when adequately trained, it is often preferred to consider motivated alternatives that either perform better or can be trained more

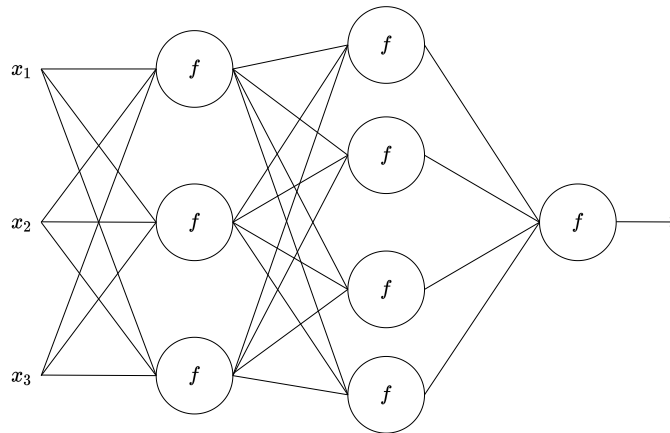


Figure 4.3: A Dense Neural Network.

easily. For example, Recurrent Neural Networks (RNNs) are designed to exploit information that appears in sequences of time-ordered events and have been used in the past for translation, music generation and sentiment classification. For one sequence, RNNs connect the current entry in the sequence to information learned from the previous entry, as shown schematically in Fig. 4.4. Multiple units can be used in each layer, and the input is split into ordered components (e.g. consecutive words within a sentence) before being passed to the layer. While the output for each component is passed to the next layer, it is also fed back to the same layer aiming to retain information from the previous components. Training is conducted similar to DNNs, however due to the codependence of weights on each other, RNNs often suffer from derivatives that either vanish (and the network does not learn) or become increasingly large (and a global minimum can not be found). RNNs also have a short-term memory, leaving out important information from the beginning of a long sequence. These issues have been resolved with more complicated architectures such as Long Short-Term Memory (LSTM) [246] and Gated Recurrent Units (GRU) [247] that regulate and retain information through different gates³.

LSTM networks have been used in the past for tagging heavy-flavoured and light-flavoured

³An LSTM includes an internal ‘cell state’ holding previous information. A ‘forget gate’ decides what information is kept from the cell state, while an ‘input gate’ updates it, and an ‘output gate’ combines information from the cell state and the current component of the sequence to produce the LSTM ‘hidden state’. The hidden and the cell states are then passed to the next layer and back to the same layer with the next entry of the sequence. GRUs are related, but they transfer information through the hidden state instead of a cell state. They incorporate a ‘reset gate’ choosing what past information to retain and an update gate that chooses what information from the current component should be added to the next hidden state.

jets using particle tracks and vertices [248, 249] and for tagging boosted tops [250] where they performed better than DNNs. In addition, RNNs were found to perform similar to Convolutional Neural Networks (CNNs) when attempting to classify up- and down-quark jets but with a smaller input representation, resulting in shorter training times and less memory usage [251]. This is of unquestionable importance, especially when high-end computing machines utilising Graphics Processing Units (GPUs) are limited. In Ref. [252] it was shown that entire events with jets could be embedded to an event-level sequence and used as an input for an RNN for classifying the event.

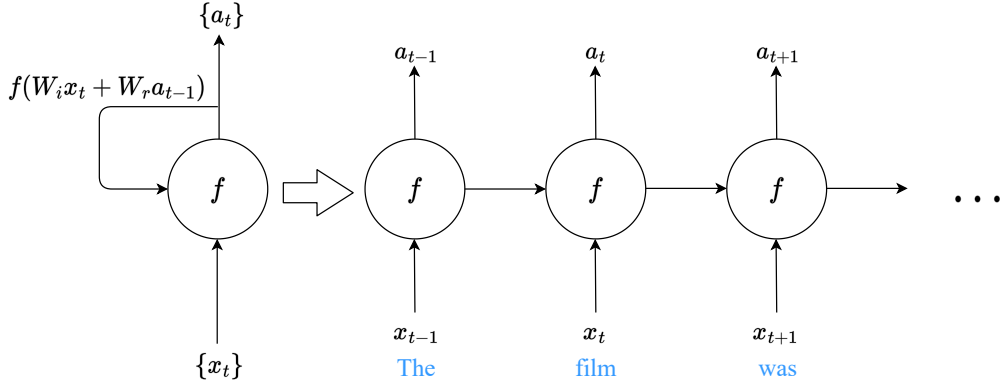


Figure 4.4: An RNN of a single unit and how it can be unfolded for each entry in the sequence. a_t denotes the node's output for the entry t in the sequence. Examples of input components are often words in a sentence.

4.3.2 Signature

The focus of this section will be in the specific parameter region where $m_{H_3} > m_{H_2} + m_h$ and $m_{H_2} > 2m_t$. Under these assumptions, the decay

$$H_3 \rightarrow (H_2 \rightarrow t\bar{t})(h \rightarrow b\bar{b}) \quad (4.23)$$

becomes kinematically accessible. The case where $t\bar{t}$ subsequently decays through W bosons to $b\bar{b}\ell^+\ell^-$ and neutrinos (appear as missing energy on the detector) is considered. Such signature is experimentally challenging due to the significant amount of missing energy when the resonances are heavy, as well as due to the fact that b -jet combinatorics are required to determine the source of each jet.

The process is contaminated by several SM background processes, dominated by $pp \rightarrow t\bar{t}b\bar{b}$, as it can be seen along with the other contributing processes in Tab. 4.1.

Process	Cross Section [fb]
$pp \rightarrow t\bar{t}b\bar{b}$	1215.050
$pp \rightarrow t\bar{t}(h \rightarrow b\bar{b})$	22.007
$pp \rightarrow t\bar{t}(Z \rightarrow b\bar{b})$	6.096
$pp \rightarrow bb\bar{b}\bar{b}W^+W^-$	2.561
$pp \rightarrow bb\bar{b}\bar{b}ZZ$	0.014

Table 4.1: SM contributions with identical final state as the signature of process (4.23) at the 13 TeV LHC. It should be noted that the rates of $t\bar{t}b\bar{b}$, $t\bar{t}h$ and $t\bar{t}Z$ have been scaled with K-factors 1.8 [253], 1.17 [105] and 1.2 [254], respectively. The selection criteria used are discussed in Sec. 4.3.3.

4.3.3 Event generation and selection

FEYNRULES [58, 59] is used to create a phenomenological model with interactions exported in the UFO [255] format which can be directly used by MADEVENT [94–96] and MADSPIN [256, 257] to generate and decay signal and background events. Showering of events is executed using PYTHIAS [167] producing HEPMC files [168]. By interfacing FASTJET [258, 259] through the reconstruction mode of MADANALYSIS [260–263], we cluster jets with the anti-kT algorithm [98] of radius 0.4.

All jets are required to have a transverse momentum of $p_T(j) > 20$ GeV and absolute pseudo-rapidity $|\eta(j)| < 4.5$. Exactly four b -tagged jets are required in the central part of the detector (i.e. $|\eta(b)| < 2.5$) that are selected with an efficiency $\epsilon = 0.8$ and contributions from mistagged light quarks are neglected. The final state must also include exactly two isolated⁴ leptons to be considered, that satisfy $p_T(\ell) > 5$ GeV and are also in the detector’s central part. Any event without two leptons and four b -jets satisfying the above constraints is vetoed. Additionally, we define the missing transverse momentum as the opposite of the sum of four-momenta components perpendicular to the beam of all jets and leptons. The magnitude of the missing transverse momentum is the missing transverse energy \cancel{E}_T .

⁴In this Chapter, a lepton is considered isolated if the total p_T of jets within the cone radius $R = \sqrt{(\Delta\eta)^2 + (\Delta\phi)^2} \leq 0.3$ is less than 20% of the transverse momentum of the lepton.

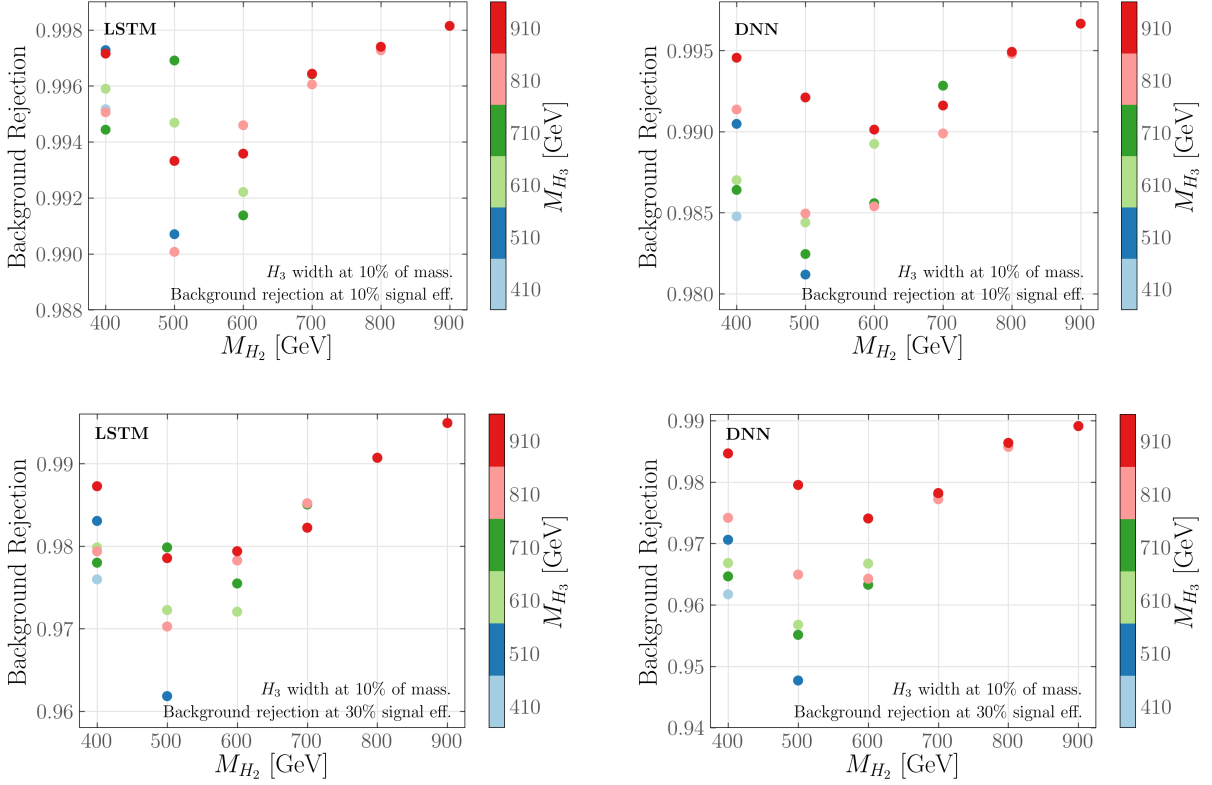


Figure 4.5: Background rejection values for different $M_{H_{2,3}}$ values for the LSTM and dense networks. These rejections are calculated at signal efficiencies of 10% and 30%, and the width of H_3 is always fixed to 10% of its mass. Using a width of 30% of M_{H_3} produces comparable results. This is anticipated since, while the width of the heavy resonance will influence the normalisation rate, cross section is not a feature used as input in the network. Therefore the efficiency of the network is unaffected by rescaling the total rate and sensitive only to kinematical features of the final states.

Our data contain seven four-momenta for missing transverse momentum, leptons and b -tagged jets that appear in the final state, in this particular order. When particles are of the same type, the order is determined by p_T , and the four momenta are in the (p_T, ϕ, η, E) basis, where ϕ is the azimuthal angle and E is the energy of the particle. Both the signal and background data samples consist of 69000 events unless otherwise specified. The background event numbers are such as expected by the cross sections of Tab. 4.1 at a fixed integrated luminosity of 500/fb.

4.3.4 Network Architectures

NNs are implemented using the KERAS [264] implementation included in the TENSORFLOW [265] framework. Events are always split into 81%, 9% and 10% for training, validation and testing, respectively. Weights in the LSTM/GRU units are initialised with Glorot uniform initialisers [266], and in order to avoid overfitting, a dropout of 0.1 is used between layers. By varying the number of units and layers, it has been decided that one LSTM/GRU layer of 45 units performs best and is used in all the following network runs. The aforementioned hyperparameters generally deliver good classification performance and avoid overfitting in all cases. Similarly, a DNN is implemented using two fully-connected layers of 80 nodes with ReLU [267] activation functions between the layers. The output layer in both cases is a linear layer activated with a softmax [268] function that outputs the probabilities for ‘signal’ and ‘background’.⁵

Optimisation of both types of networks is achieved with the Adam [269] algorithm by minimising the categorical cross-entropy loss function implemented in KERAS with a learning rate of 0.001. Networks are trained for 100 epochs unless the loss does not decrease for ten consecutive epochs, where training stops early (in all our runs, we never reach 100 epochs, which indicates that for the current hyperparameters, the results can not improve further by longer runs).

4.3.5 Model-independent performance tests

It is essential to evaluate whether LSTM/GRU networks gain any information compared to a DNN before turning to an actual benchmark scenario of N2HDM. We, therefore, first fix couplings of the phenomenological Lagrangian in such a way that decay widths of H_3 are either at 10% or 30% of its mass, and H_2 decays solely to $t\bar{t}$. A scan is conducted in the range $410 \text{ GeV} < M_{H_{2,3}} < 950 \text{ GeV}$, and both LSTM and DNN networks are trained on reduced samples of 10000 events before splitting. Background rejections are evaluated and are shown in Fig. 4.5 using Monte Carlo truth particles without realistic selection criteria and before showering or particle reconstruction. Despite the smaller number of events, both models have large background rejections, with LSTM performing slightly better. These results indicate the usability of such networks for cascade decay analyses. However, distortion of kinematical observables from showering and reconstruction requires the use of the full data sample for more realistic results. When showered and reconstructed events are considered with the aforesaid selection criteria, sensitivity projections evaluated as the final signal cross section σ_S required to achieve $N_S/\sqrt{N_B} = 2$, where N_S , N_B are signal and background

⁵Although one-hot encoded categorical labels are used, using a sigmoid activation function with binary labels yields similar results. In this case, a binary cross-entropy needs to be used as a loss function.

number of events expected at HL-LHC, are shown in Fig. 4.6⁶. Due to the considerable reduction of background contamination at heavier mass parameters, sensitivity increases and the possibility to probe smaller cross sections opens.

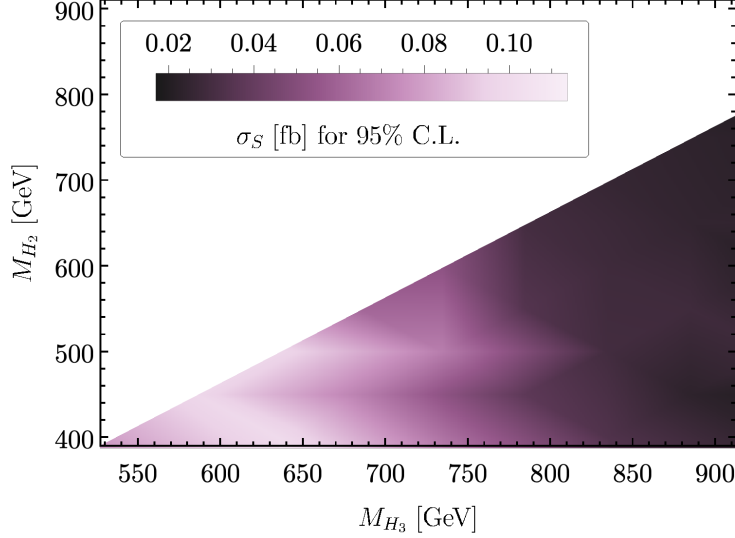


Figure 4.6: Final signal cross sections after all selection criteria required to achieve $N_S/\sqrt{N_B} = 2$ (95% CL) in the $M_{H_3} - M_{H_2}$ plane. For this scan the requirement $M_{H_3} > M_{H_2} + 125$ GeV is imposed and branching ratios are fixed to $\text{BR}(H_3 \rightarrow H_2 h) = 0.5$ and $\text{BR}(H_2 \rightarrow t\bar{t}) = 1$.

4.3.6 Sensitivity for a benchmark N2HDM point

Given that the LSTM delivers substantial exclusion power, one can examine the application of the network to the motivated N2HDM scenario. A scan is performed over the parameter space of the model using SCANNERS [232, 237, 241, 270, 271], searching for cases with large branching ratios relevant to the signature of (4.23). In particular, it is required that $\text{BR}(H_3 \rightarrow H_2 h)$, $\text{BR}(H_2 \rightarrow t\bar{t})$ and $\text{BR}(A \rightarrow t\bar{t})$ are all larger than 0.4. The networks are trained on a benchmark point that has $M_{H_3} = 722$ GeV, $M_{H_2} = 480$ GeV with widths $\Gamma_{H_3} = 45$ GeV and $\Gamma_{H_2} = 4.9$ GeV, branching ratios $\text{BR}(H_3 \rightarrow H_2 h) = 0.52$, $\text{BR}(H_2 \rightarrow t\bar{t}) = 0.84$ and yields a cross section of $3.43/\text{fb}$ ⁷.

⁶The determination of the ideal background rejection for each point is discussed in the following section (Sec. 4.3.6).

⁷This value is before selection of reconstructed events with our criteria. For this part, the full-top mass dependence is not implemented, and instead, we match to the infinite top mass limit and subsequently reweight to the LHC Higgs Cross Section Working Group values [272] at a scale of $M_{H_3}/2$ to include finite top effects and QCD corrections. This is not feasible for studies of interference though that require the full top mass dependence.

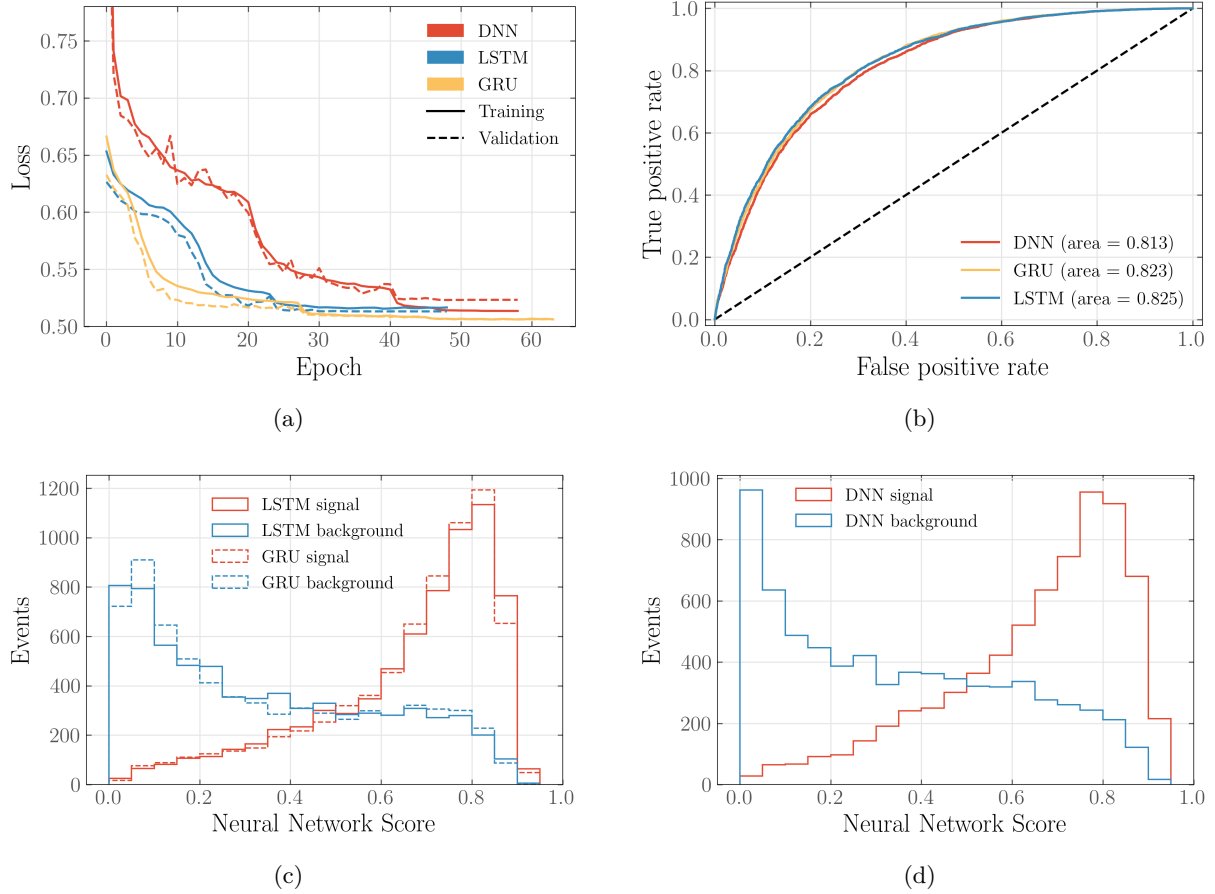


Figure 4.7: The loss function during training is shown for all networks in 4.7(a). 4.7(b) shows the ROC curves used to identify an optimal RNN (DNN) score cut-off, with the score also shown in 4.7(c) (4.7(d)).

Fig. 4.7 shows the performance of networks for the N2HDM benchmark point. None of the models seems to suffer from overfitting, as indicated by the loss curves obtained during training, and Receiver Operator Characteristic (ROC) curves indicate the discriminative power of the networks. Histograms displaying the probability of each class (‘signal’ or ‘background’) also confirm that all three can efficiently identify events arising from N2HDM physics. LSTM/GRU show slightly better performance, and their loss functions converge faster, indicating that kinematic information is more efficiently utilised by RNNs to learn the structure of the cascade decay. The DNN using the same kinematic information requires more epochs to reach a relatively similar performance

and is more unstable when varying its hyperparameters, getting easily stuck at local minima far from the global.

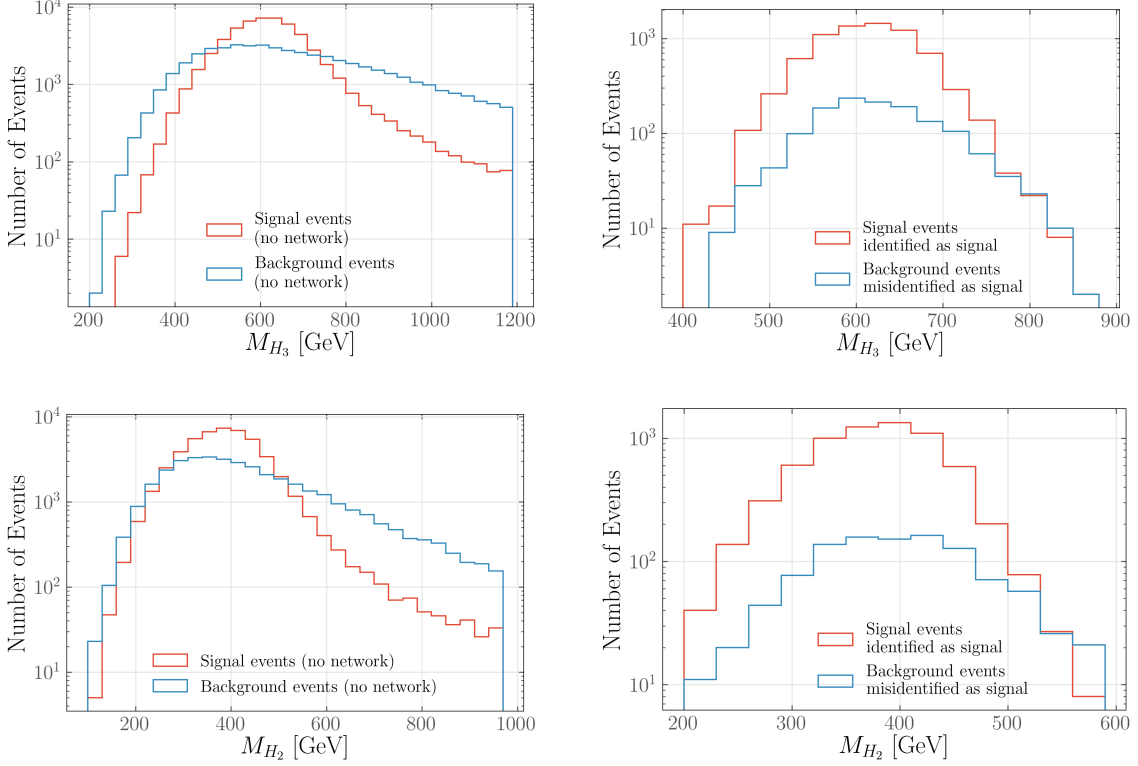


Figure 4.8: Example histograms for the reconstructed mass $M_{H_{3,2}}$ before (after) running the network selection are shown on the left (right) for the generated events. Masses were set to $M_{H_3} = 722$ GeV, $M_{H_2} = 480$ GeV and widths were set to 45 GeV and 4.9 GeV for H_3 and H_2 , respectively.

Using the LSTM, events are selected by determining a NN score threshold that yields a large cross section ratio σ_S/σ_B . Despite the omission of systematic uncertainties that may affect the background number of events, their impact is minimal when a large σ_S/σ_B is identified. The signal and background number of events with a NN score higher than the threshold are then evaluated as N_S and N_B , respectively, at an integrated luminosity of 3/ab, and we define the significance as $N_S/\sqrt{N_B}$. A significance of 5.3 (4.1) is obtained with LSTM (DNN) at $N_S/N_B \simeq 0.09$ ($N_S/N_B \simeq 0.08$), indicating that an LSTM⁸ architecture would be essential for discovery, while a

⁸GRU provides comparable quantities.

DNN would only be able to provide evidence of new physics at the HL-LHC.

Essentially discrimination of the signal from contaminating processes is driven by the ability to isolate resonant peaks from the final states, despite the heavy distortion arising from the missing energy. M_{H_3} is reconstructed by adding the four-momenta of the missing transverse momentum, the leptons and the b -tagged jets that appear in the final state, while M_{H_2} is constructed with the same quantities but without the two b -jets that have an invariant mass close to the SM Higgs, 125 ± 10 GeV. Fig. 4.8 displays these resonant structures before and after we run the network. The distorted peaks are visible before the network, and their region is appropriately identified with the network removing the rest of the events.

For comparison with simple approaches, a cut-and-count analysis is also conducted for comparison purposes. The kinematical observable space is restricted by applying transverse momentum cuts on the four b -tagged jets and the leptons,

- $p_T(b_1) > 100$ GeV,
- $p_T(b_2) > 80$ GeV,
- $p_T(b_3) > 65$ GeV,
- $p_T(b_4) > 50$ GeV,
- $p_T(\ell_1) > 30$ GeV,
- $p_T(\ell_2) > 10$ GeV,

as well as a missing energy cut of $\cancel{E}_T > 30$ GeV. The event is vetoed if no SM Higgs-compatible pair of b -jets is identified with invariant mass in the range of 125 ± 10 GeV.⁹ The four momentum of the Higgs is then reconstructed, and the search region is constrained by requiring that it must have a transverse momentum $p_T(h) > 120$ GeV. A final cut is applied on the other pair of b -jets, requiring its invariant mass to be $m_{bb} > 80$ GeV. The analysis results in a significance of 2.1 at a ratio $N_S/N_B = 0.04$, indicating considerably poorer performance and increased susceptibility to background systematics. This is anticipated since a simple cut-and-count analysis cuts rectangular regions in the kinematical observable space, while a NN allows for more complicated shapes.

⁹If in one event, there are more than one candidate pairs, then the one with the smallest ΔR separation between the two constituents is identified as the pair resulting from the SM Higgs.

4.4 Interference effects in multi-Higgs cascade decays

While the use of NNs enables us to gain sensitivity from this channel with rich scalar interactions, it is of importance to identify any possible constructive or destructive interference that can occur. A destructive interference similar to what occurs in the top chain channel can render the channel impossible to probe, severely reducing the ability of the NN to select a signal region appropriately.

4.4.1 Signal-Background Interference

Aiming to investigate whether signal-background interference has the potential to reduce sensitivity, the generic Lagrangian (4.1) is implemented in FEYNRULES [58, 59]. The cross section for the process is given by

$$d\sigma_S \sim d\text{LIPS} |\mathcal{M}|^2, \quad (4.24)$$

where the matrix element \mathcal{M} is obtained by including all the diagrams resulting in the final state signature of two bottoms and two tops,

$$\mathcal{M} = \mathcal{M}_S^{\text{res}} + \mathcal{M}_S^{\text{non-res}} + \mathcal{M}_B. \quad (4.25)$$

\mathcal{M}_B denotes contributions from SM processes, while $\mathcal{M}_S^{\text{res}}$ is the resonant BSM signal topology shown in 4.9(a). $\mathcal{M}_S^{\text{non-res}}$ includes all non-resonant BSM topologies, as for example 4.9(b). The signal-background interference contributions $|\mathcal{M}|^2 \supset 2\text{Re}(\mathcal{M}_S^{\text{res}} \mathcal{M}_B^*)$ are then dominated by QCD contributions and such events are generated using MADEVENT [94–96]. The HELAS [273] routines suitable for the ggH_i vertex were modified to include the top-loop matching¹⁰.

For the rest of this section, bottom and top quarks are considered stable since the subsequent effects of decaying and showering do not affect the signal-background interference. The four momentum of H_2 (h) is calculated as the sum of the four momenta of the top (bottom) pair, which allows us to reconstruct the mass of H_3 . To keep the decays to these quarks similar to the SM the trilinear $\lambda_{H_3 H_2 h}$ coupling is fixed, as well as the Yukawa y_{H_3} ($y_{H_i}^{(E/O)} = 1$ corresponds to a CP even/odd SM-like Higgs). We keep the mass of $H_{2,3}$ close to the mass of its decay products by defining the decay thresholds $m_{\text{dec}} = 2m_t$ ($m_{\text{dec}} = m_{H_2} + m_h$) for H_2 (H_3) and consider widths at 10%, and 30% of their masses. A scan is performed over different $C_{H_3}^{\text{even}}$ and $C_{H_3}^{\text{odd}}$ values and we also consider the case where the SM-like decay of $H_2 \rightarrow t\bar{t}$ is due to $y_{H_2}^E$ only or due to $y_{H_2}^E$ and

¹⁰This have been cross-checked analytically and numerically with Refs. [274, 275].

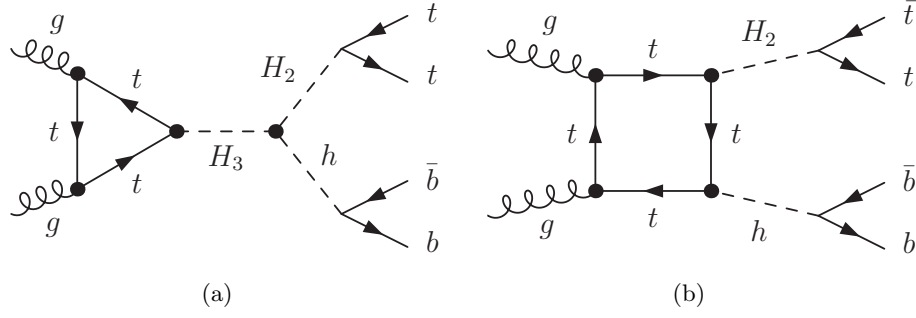


Figure 4.9: Triangle (a) and box (b) Feynman diagrams producing the H_2h state.

$y_{H_2}^O$ being at a 45° angle and unit length. Fig. 4.10 shows the impact of varying these parameters on the signal and signal-background differential distributions.

Due to the fact that the SM is mostly a CP even model, introducing a CP odd coefficient $C_{H_3}^{\text{odd}}$ will show small interference effects when probing the even invariant mass distribution. Studying the size of a CP odd parameter would require looking at alternative CP odd observables such as signed azimuthal angles, which is not of interest for this scenario but will be explored in Chapter 6. However, introducing a $C_{H_3}^{\text{even}}$ coefficient will lead to sizeable effects irrespective of how close the resonance mass is to the decay threshold in the region where such decays are significant. The effect of the width size is also significant, which is foreseen since the width is sensitive to the imaginary part of the H_3 two-point function¹¹.

To understand the impact of interference on the sensitivity of a channel, one needs to compare them with the signal-squared distributions shown. For the model-independent results of Figs 4.10(c) and 4.10(d), the peaks are distorted considerably from the SM-BSM interference, although a peak would still be visible at a slightly lower scale. It is, therefore, possible in such scenarios that one could recover sensitivity by taking the possible line shapes of the distributions into account,

¹¹Close to the resonance $s \sim m^2$ a Higgs s-channel diagram diverges but is regulated by the Dyson resummation of one-particle-irreducible self-energy diagrams at all orders. One obtains the propagator (see also Sec. 2.1.3)

$$D(s) = \frac{i}{s - m_0^2 + \Pi(s)}, \quad (4.26)$$

where $\Pi(s)$ are the one-particle-irreducible diagrams and m_0 is the bare mass of the Lagrangian. $\Pi(s)$ can be split into real and imaginary parts, with the real part absorbed in the renormalised mass m_R . The imaginary part can then be related to the Higgs width through unitarity using the optical theorem. The Breit-Wigner shape of the squared propagator is justified only for perturbative values of Γ_X/M_X . Larger values additionally become sensitive to how the imaginary part is included in the propagator (see [276–278]).

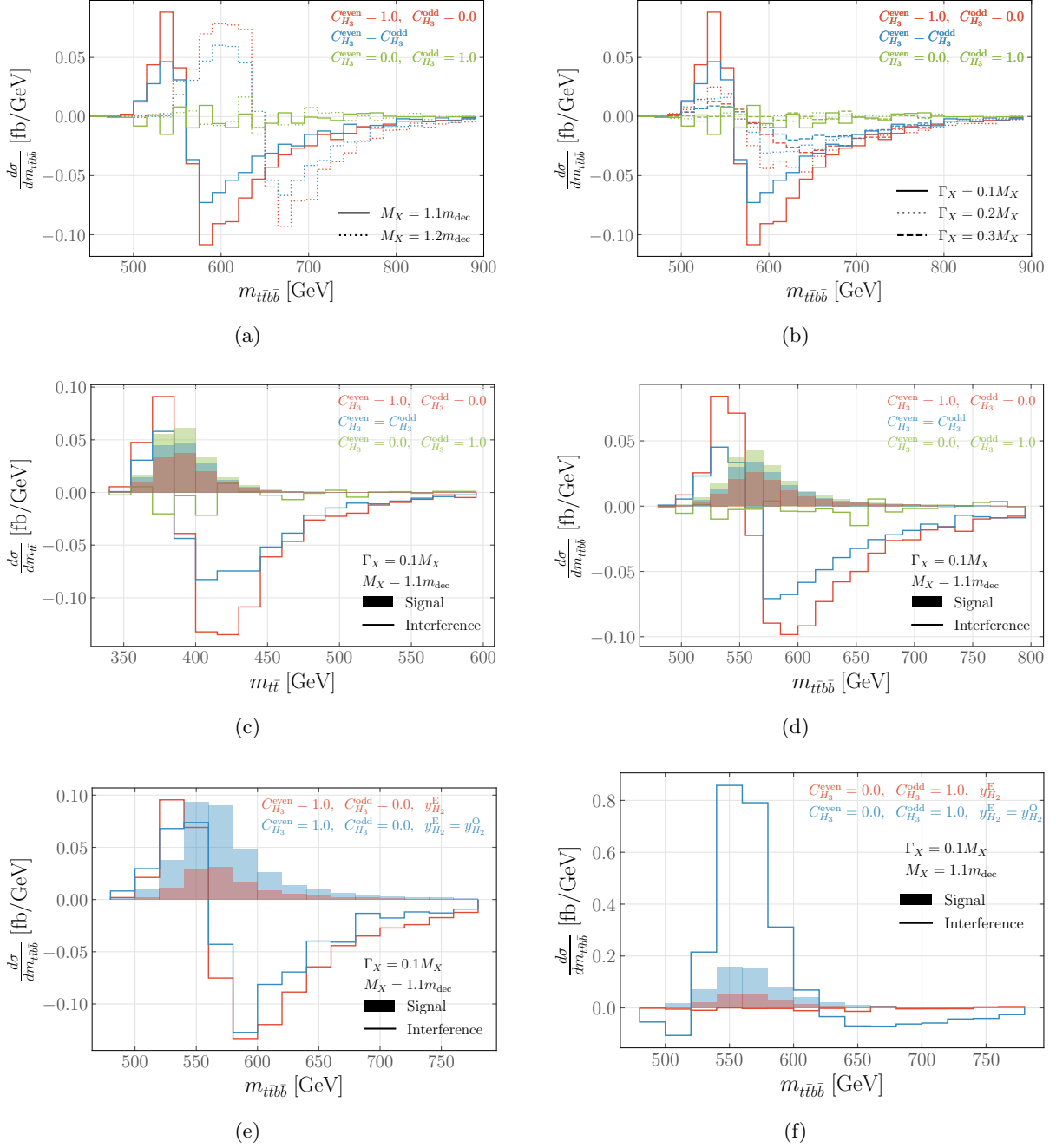


Figure 4.10: Effect of varying masses and widths for different ggH_i couplings is shown in 4.10(a) and 4.10(b), respectively. Figs. 4.10(c) and 4.10(d) compare interference and signal-squared contributions for $m_{t\bar{t}}$ and $m_{t\bar{t}b\bar{b}}$ while the effect of odd Yukawa couplings is shown in 4.10(e) and 4.10(f). It is highlighted that the plotted curves contribute to the differential cross section but only the sum of all contributions is physical (i.e. interference does not include the signal-squared terms and hence it can be negative).

as is done in the channel where a scalar decays to a top pair [233, 279].

It should also be noted that as shown in Figs. 4.10(e) and 4.10(f), the phase between the Yukawa couplings $y_{H_2}^{E,O}$ and the H_3 couplings $C_{H_3}^{\text{odd}}, C_{H_3}^{\text{even}}$ is also relevant. The decay of H_2 can alter the interference pattern from destructive to constructive depending on the CP phase of its Yukawa coupling. The inclusion of two CP odd couplings can lead to a dominant CP even contribution when squared and, it can reverse the destructive effect of signal-background interference, enhancing the peak of the invariant mass distribution (Fig. 4.10(f)). One can study the various interference shapes as in Ref. [230] to indirectly measure the different CP phases.

However, despite the generic characteristics seen here, interference is, in fact, model-dependent, as signal-signal interference could have a sizeable impact. It is hence informative to study this in the context of the two-singlet extended SM, in the next section.

4.4.2 Cascade interference in the two-singlet extended SM

A scan is executed over the parameter space of the two-singlet extended SM requiring an open $H_3 \rightarrow H_2 h \rightarrow t\bar{t}b\bar{b}$ channel. The mass of the lightest physical scalar resonance is fixed at 125 GeV, and the coupling modifications must remain close to the SM (within universal coupling modifications of $\kappa \gtrsim 0.9$). The theoretical constraints from perturbative unitarity derived in Ref. [280] are enforced as well as vacuum stability conditions [281, 282].

By computing the Peskin-Takeuchi observables [183, 188] it is found that the majority of scanned parameter points are allowed by the fit of Ref [200]. For the discussion of interference, we require $\sigma_{H_3} \times \text{BR}(H_3 \rightarrow H_2 h) \geq 4$ fb in order for the channel to be relevant and all cross sections are rescaled to include higher-order effects from the Higgs Cross Section Working group (Refs. [89, 105, 274]). By calculating the branching ratios of $H_{3,2}$ it has been found that they either decay through modes similar to the SM Higgs or through symmetric and asymmetric decays to scalars, with three-body decays being negligible and hence not considered. Cross sections with these requirements are maximised when the mass of H_3 is close to the sum of masses of its decay products, resulting in a large $H_3 \rightarrow H_2 h$ branching ratio.

Signal-signal interference can arise through several non-resonant diagrams such as the $gg \rightarrow H_2 h$ box topology shown in Fig. 4.9(b) or s -channel diagrams with H_2 or h at the propagator. In addition to the asymmetric cascade decay signature, the additional channels $pp \rightarrow H_{2,3} \rightarrow t\bar{t}$ and $pp \rightarrow H_{2,3}$ are also studied. We use results obtained from FEYNARTS [192], FORMCALC [76] and LOOPTOOLS [76] along with a modified version of VBFNLO [283] in order to evaluate the cross

section with and without interference effects close to the resonance mass m_{H_i} . The reconstructed mass of the resonance $m_{H_i}^{\text{reco}}$ ($i = 1, 2, 3$) is calculated from its decay products depending on the channel and cross section is measured only when $m_{H_i}^{\text{reco}} \in [m_{H_i} - 0.15m_{H_i}, m_{H_i} + 0.15m_{H_i}]$. Limiting the scan parameters to cases of large asymmetric decay results in smaller cross sections in the $H_3 \rightarrow t\bar{t}$ channel. The lower rate also results in a substantial reduction of the peak when combined with signal-signal interference, as shown in Fig. 4.11. However, the potential for discovery of BSM physics is anyway small for such points on the parameter space. The experimental investigation of new physics through Higgs-to-Higgs decays in this model, which was already suggested by Ref. [280] is also further encouraged by this work. For the cases where cross section rates are relatively large in symmetric multi-Higgs decays, signal-signal interference effects are not a limiting factor decreasing the discovery potential, in agreement with Ref. [231].

Focusing on asymmetric decays, we study both the signal-background and signal-signal interference with their impact on the signal cross section close to the resonance's mass shown in Figs. 4.12(a) and 4.12(b), respectively. As in symmetric decays, the signal-signal interference does not severely affect the channel (when compared with $H_3 \rightarrow t\bar{t}$), although the impact can be larger than signal-background contributions. The latter is small due to the size of the widths with respect to the mass¹² while signal-signal interference can be sizeable due to the rich scalar phenomenology of the model. The size of both contributions, however, depends on the cross section; the effects become more pronounced for points in the parameter space that have smaller cross sections, but in these regions, asymmetric decays would anyway not produce much sensitivity. However, the fact that H_2 decays to tops makes the channel hard to discriminate from the background due to the challenging b combinatorics in the final state and the large missing energy. Although this can be addressed with NNs, as previously discussed, sensitivity would still be suppressed at the LHC. This motivates the extrapolation our results for a future hadron collider (FCC-hh) operating at $\sqrt{s} = 100$ TeV in Fig. 4.13. As for the LHC scenario, the interference effect is insignificant, and a future hadron collider will be able to provide additional information regarding these signatures without being limited by interference.

¹²Smaller width implies a wider signal peak but at the same mass. From Fig. 4.10(b) one sees that the dip structure that would interfere destructively is shifted towards higher energies away from the actual mass. Therefore since we only measure cross sections close to the mass, this would not be a limiting factor for such search.

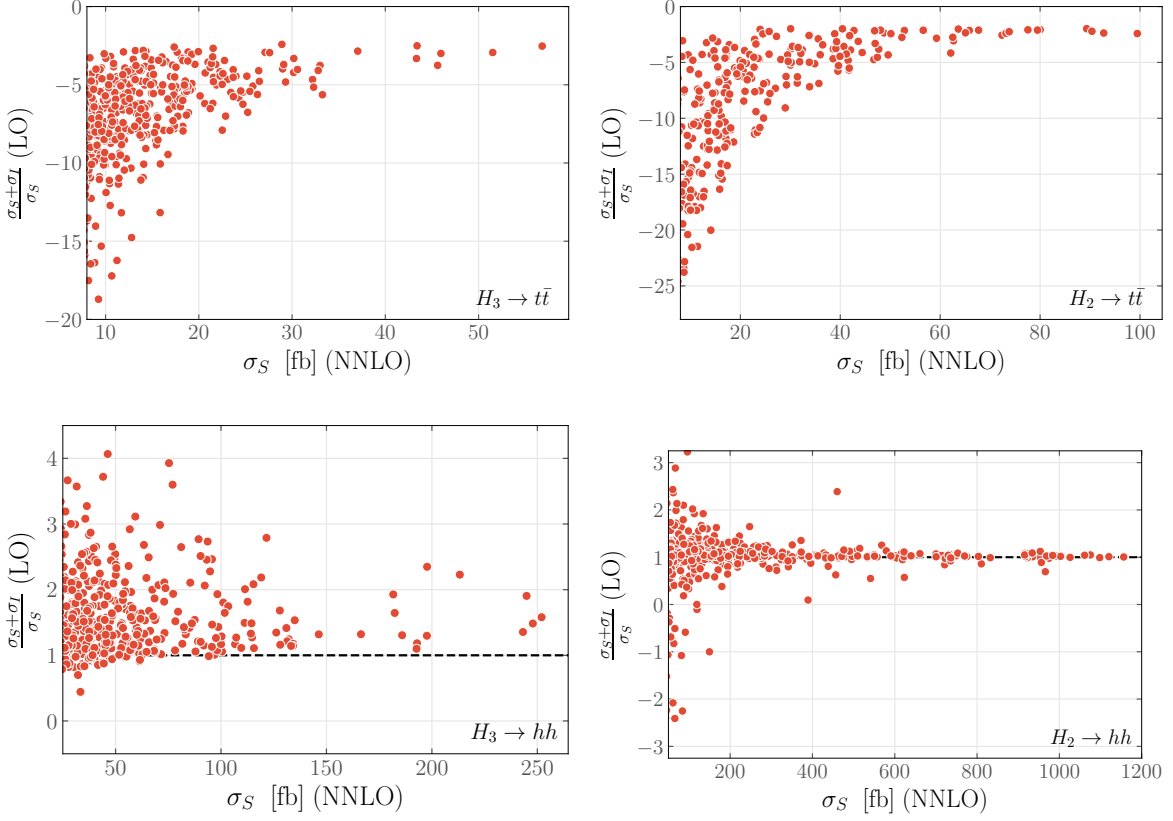


Figure 4.11: The effect of signal-signal interference as a ratio of the cross section close to the scalar’s mass with interference divided by the cross section without interference for the channels $H_i \rightarrow t\bar{t}, hh$ at 13 TeV. It is particularly important that such effects are included for the decay to $t\bar{t}$.

4.4.3 Conclusions

Due to considerable distortion of resonant peaks in the best motivated $pp \rightarrow H_i \rightarrow t\bar{t}$ final state arising from interference with QCD, it would be beneficial to also consider alternative channels with robust final states to ensure that a potential discovery is not obstructed. An example that could potentially lead to increased sensitivities in models with exotic scalar heavy resonances is multi-Higgs production through asymmetric cascade decays. The complex combinatorics arising in the final state and the sizeable distortion appearing from the considerable missing energy render simple analyses unable to extract information efficiently from kinematics. However, turning to NNs that deliver substantial discriminative power between the BSM signal and the

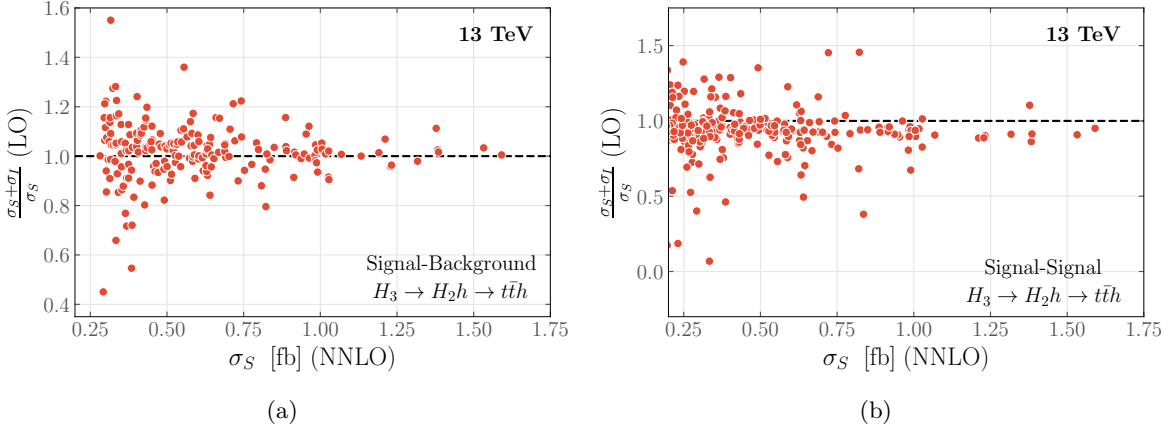


Figure 4.12: Effects from including signal-background (signal-signal) interference for the asymmetric cascade decay $H_3 \rightarrow H_2 h \rightarrow t\bar{t}h$ at 13 TeV are shown on the left (right).

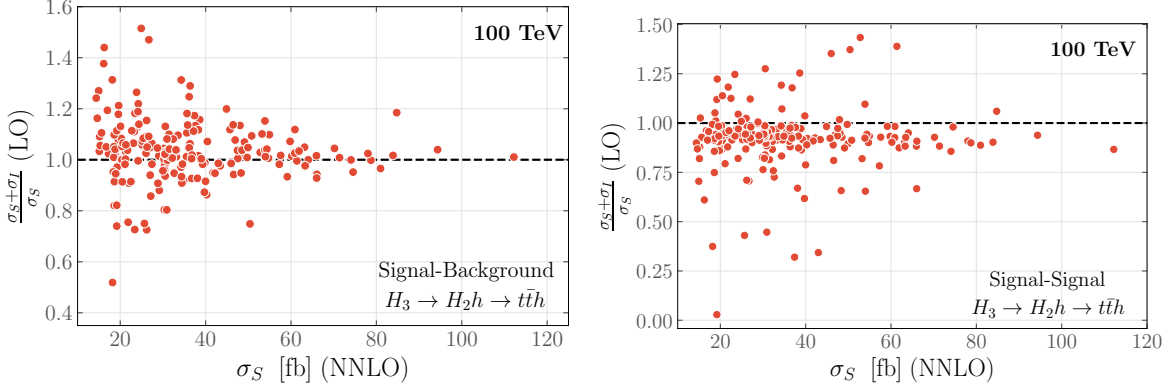


Figure 4.13: Figures show the importance of signal-background (left) and signal-signal (right) interference for the FCC-hh operating at energies of 100 TeV.

SM background can cure this issue.

To this end, the possibility of exploiting the ‘memory’ of past information that final states hold by using two types of RNNs has been explored, along with a comparison against a DNN and simple cut-and-count analysis. Results indicate that the DNN in all the trials performed slightly worse for the considered data while additionally suffering from slower convergence and more difficult optimisation of hyperparameters. The DNN still outperforms simple cut-and-count analyses but falls short of the significance required to claim discovery in the case of a benchmark point of the

N2HDM. In contrast, RNN architectures would be able to provide the required significance at the HL-LHC.

Furthermore, quantum effects such as interference can severely alter the predicted signal of new physics. While dedicated line shape searches can supply additional information, it is also essential to turn to different multi-Higgs channels that might provide greater sensitivity when the $H_i \rightarrow t\bar{t}$ has reduced rates. It is therefore also shown that the CP odd and CP even couplings can affect the expected distributions differently and could possibly result in constructive interference. In general, for a model-independent scan of possible parameters, the peak structures are still present.

Studying the effects in the context of two-singlet extended SM, where sensitivity to $t\bar{t}$ is further suppressed by signal-signal interference, we observe that both symmetric and asymmetric cascade decays have peak structures that remain largely intact. The $H_3 \rightarrow H_2 h$ channel becomes sensitive to signal-signal interference due to the rich scalar interactions that are present, which enables studying the new physics scenario further. It is anticipated that multi-Higgs decays will be promising signatures for future new physics searches at HL-LHC and FCC.

Additional models with multiple scalars could be explored in order to identify whether the asymmetric cascade decay indeed remains a promising avenue. The studies presented so far for the scalar extensions of the SM are inherently model-dependent analyses. However, BSM studies do not necessarily need to rely on a single model but can instead investigate new physics in model-independent searches through Effective Field Theories (EFTs), which in turn can be matched to specific models to reinterpret EFT results. While in this Chapter a phenomenological Lagrangian is used where models with additional scalars could be mapped to, this can be generalised to arbitrary models and processes through the language of EFTs, as discussed in Sec. 2.6. The following Chapters shift away from concrete models and explore new physics through the SMEFT framework.

Chapter 5

Improving constraints on Wilson Coefficients with Graph Neural Networks

5.1 Introduction

Reinterpreting experimental results as constraints of specific UV models is not an effortless task. BSM theories differ in the degrees of freedom, often leading to dramatically distinctive phenomenology, requiring the careful study of promising channels and evaluation of sensitivity. In addition, mapping such results to other dissimilar models can be a tedious and cumbersome process. Instead, identifying a common language in which results can be acquired in a model-independent fashion can be extremely useful. This is achieved through EFTs, which will be the centre of attention for the remaining of the thesis.

Due to the large number of effective interactions that can contribute to a relevant scenario (see Sec. 2.7.1), the sensitivity of a specific analysis targeting a single channel can be relatively limited¹. Additionally, constraints on the WCs can be severely impacted by systematic uncertainties. The allowed range of a WC then often lies in the non-perturbative regime when it is understood as a constraint on parameters of a UV completion after matching.

¹See for example Refs [284–287] for fits using SMEFT.

In order to improve the phenomenological sensitivity to BSM models, there are two possible avenues to pursue. Firstly, decreasing the statistical and systematic uncertainties from experiments as well as theoretical uncertainties will yield more restrictive limits for WCs unless there is a disagreement with the SM. Furthermore, the lower limits on direct evidence of new heavy mass particles will be increased in the future and hence the lower limit of the UV scale Λ will also improve as it depends on the coverage of the LHC and it is limited by the centre-of-mass energy.

The second conceivable avenue is to resort to a more comprehensive extraction of information from the available experimental data through machine learning (ML), remaining in the same mindset as the previous Chapter. In traditional cut-and-count analyses, cuts are imposed on collider observables such as the transverse momentum, angles and (pseudo)rapidities. However, the rectangular selection of a signal region does not necessarily fully capture the exclusion potential that can be achieved, as already shown in the previous Chapter. Cuts also often select only specific directions in the WC parameter space.

The aim of this Chapter is to showcase how the bounds on WCs can be improved through the latter avenue, focusing solely on the top sector [286–293]. Choosing the top pair production $pp \rightarrow t\bar{t}$ with the tops decaying semileptonically delivers a clean channel with decreased statistical uncertainties that allows the exploration of several ML-improved EFT strategies (see also Ref. [294]). Graph Neural Networks (GNNs) with Edge Convolution [295–298] will be used in order to exploit the structure of the data, where the intermediate final state particles will be represented as ‘nodes’, and the calculated ‘edges’ will capture the correlations between them in a physics-inspired setup. GNNs have received increased attention in the particle physics community recently [299–310].

Firstly, in Sec 5.2, the relevant EFT operators for this channel will be reviewed along with details for simulating and analysing the $t\bar{t}$ production. Sec. 5.3 focuses on the baseline cuts (guided from the CMS analysis of [311]) and the setup of the Neural Network. The performance improvements are given in Sec. 5.4 with a summary in 5.5.

5.2 Effective interactions for top pair production with leptonic decays

Having restricted the Lagrangian (2.65) to only dimension-six operators, the differential distribution of Eq. (2.66) can be also truncated at order Λ^{-2} , neglecting EFT-squared terms.

Distribution	Observable	Binning
$\frac{1}{\sigma} \frac{d\sigma}{d y_t^h }$	$ y_t^h $	[0.0, 0.2, 0.4, 0.7, 1.0, 1.3, 1.6, 2.5]
$\frac{1}{\sigma} \frac{d\sigma}{d y_t^l }$	$ y_t^l $	[0.0, 0.2, 0.4, 0.7, 1.0, 1.3, 1.6, 2.5]
$\frac{1}{\sigma} \frac{d\sigma}{d y_{t\bar{t}} }$	$ y_{t\bar{t}} $	[0.0, 0.2, 0.4, 0.6, 0.9, 1.3, 2.3]
$\frac{1}{\sigma} \frac{d\sigma}{dp_{\perp}^{t,h}}$	$p_{\perp}^{t,h}$	[0, 45, 90, 135, 180, 225, 270, 315, 400, 800] GeV
$\frac{1}{\sigma} \frac{d\sigma}{dp_{\perp}^{t,l}}$	$p_{\perp}^{t,l}$	[0, 45, 90, 135, 180, 225, 270, 315, 400, 800] GeV
$\frac{1}{\sigma} \frac{d\sigma}{dm_{t\bar{t}}}$	$m_{t\bar{t}}$	[300, 375, 450, 530, 625, 740, 850, 1100, 2000] GeV
$\frac{1}{\sigma} \frac{d\sigma}{d y_{t\bar{t}} d m_{t\bar{t}} }$	$ y_{t\bar{t}} $	[0.0, 0.2, 0.4, 0.6, 0.9, 1.3, 2.3]
	$m_{t\bar{t}}$	[300, 375, 450, 625, 850, 2000] GeV
$\frac{1}{\sigma} \frac{d\sigma}{dp_{\perp}^{t,h}d y_t^h }$	$p_{\perp}^{t,h}$	[0, 45, 90, 135, 180, 225, 270, 315, 400, 800] GeV
	$ y_t^h $	[0.0, 0.5, 1.0, 1.5, 2.5]

Table 5.1: Distributions used for the fit in this Chapter, from Ref. [311].

While this is theoretically consistent, one should keep in mind that it is also a conservative approach as contributions from Λ^{-4} operators will show a dramatic momentum transfer and will be, hence, easier to constrain. An improvement on the WC constraints in the linear case is thus expected to generalise to higher order terms in the cross section expansion.

5.2.1 Analysis Setup and Fit Methodology

The implementation of the SMEFT Lagrangian of SMEFTSim [312, 313] is used, with Feynman Rules for the effective operators calculated with FeynRules [59]. They are exported in the UFO [255] format in order to generate event samples with MadGraph5 [96] at leading order (LO). Although higher order terms are crucial for consistency between measured data and the SM hypothesis, they are omitted here as they will not impact the qualitative results. Samples are generated for (see also Fig. 5.1)

$$pp \rightarrow t\bar{t} \rightarrow \ell b\bar{b}jj + \cancel{E}_T. \quad (5.1)$$

at $\sqrt{s} = 13$ TeV and they are subsequently showered with Pythia8 [167] before being processed with Rivet [169, 314]. The analysis is inspired by CMS [311] which investigates (correlated) differential measurement results with representative data binning as given in Tab. 5.1.

Statistical inference for this section follows Refs. [287, 288]. A χ^2 is constructed using the SM as mock reference data as

$$\chi^2(\{\frac{C_k}{\Lambda^2}\}) = \sum_{\text{obs.}} \sum_{i,j} (b_{\text{SM+d6}}^i - b_{\text{SM}}^i) V_{ij}^{-1} (b_{\text{SM+d6}}^j - b_{\text{SM}}^j), \quad (5.2)$$

summing over observables and all their bins. b_{SM}^i is the number of events in bin i as predicted by the SM, while $b_{\text{SM+d6}}^i = b_{\text{SM+d6}}^i(\{C_k/\Lambda^2\})$ includes dimension-six contributions from interference and depends on the WCs. The covariance matrix V_{ij}^{-1} depends on bin-to-bin correlations given by experiments and the statistical uncertainties². Confidence Levels (CL) can be then defined using the χ^2 probability density function of n degrees of freedom $p_n(x)$ and are given by

$$1 - \text{CL} \geq \int_{\chi^2}^{\infty} dx p_n(x), \quad (5.3)$$

$$\chi^2 = \chi^2\left(\left\{\frac{C_k}{\Lambda^2}\right\}\right). \quad (5.4)$$

The degrees of freedom are equal to the number of measurements (i.e. total number of bins considered) minus the fitted WCs.

In order to avoid assumptions regarding correlations, a maximum sensitivity, minimum correlation assumption is used regarding the differential distributions used as input, following TOPFITTER [287, 315–318], which is detailed in greater extent in Ref. [4].

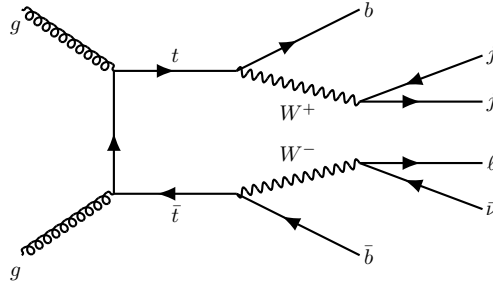


Figure 5.1: Feynman diagram that can receive corrections from dimension-six operators for the considered process.

²Although the covariance matrix can include the systematic uncertainties, these are not included. Any improvement achieved with the use of ML will also be observed when systematics are included. Additionally, these are not available at 3/ab, which is the luminosity considered.

Bounds on WCs for all the contributing effective interactions will be given in the ‘bar’ notation

$$\bar{C}_i = C_i \frac{v^2}{\Lambda^2}, \quad (5.5)$$

where v is the electroweak vacuum expectation value as in the SM.

The phase space region is often restricted in traditional analyses using rectangular cuts selected in a way that the background contribution from SM processes is minimised, increasing the sensitivity to new physics interactions. Due to their rectangular nature, the signal selection through cuts is often inferior compared to non-rectangular regions selected methodically using state-of-the-art machine learning classifiers, as seen in Chapter 4. An efficient event-by-event classification that successfully categorises the events as either SMEFT-induced interference or pure SM events could lead to major improvements on the constraints of WCs. In this section, classification will be performed on graph representations of the events using GNNs that will be discussed in detail in the following section.

5.3 Graph representation of events

There are many ways that detectable final states can be embedded in a graph structure characterised by the nodes, edges and the associated features. It is possible to associate a node with each final state and assign its observables as node features with edges connecting all nodes in a fully-connected setup. However, in this Chapter a physics-motivated approach is used where graphs are created similar to the decay chain of the process (5.1). The event samples are processed before the embedding requiring at least two non b -tagged jets with a transverse momentum $p_T(j) > 20$ GeV and a pseudorapidity $|\eta| < 5$. In the central part of the detector, i.e. $|\eta| < 2.5$, there must exist at least two b -jets and one lepton ℓ , otherwise, the event is vetoed. A requirement of a transverse momentum $p_T(b) > 20$ GeV is also imposed on the b -jets.

With this initial selection of events, graphs can be constructed with the final states but also with the reconstructed objects. In particular:

(i) *Nodes*: The Missing Transverse Momentum (MTM) can be defined as the imbalance of momentum in the transverse plane, i.e. $-p_T(\text{visible})$, and a corresponding node is added. Subsequently, for every lepton that passed the p_T requirement, the four momentum of the parent W boson is loosely reconstructed as the sum of the four momentum of the lepton and the MTM. If the invariant mass of the reconstructed momentum lies in the [65, 95] GeV range, nodes ℓ

and W_1 are added for the lepton and the boson, respectively. In the scenario where more than one combination of lepton and MTM is attainable that results in a viable invariant mass for the W , the one closest to the known mass of the W is chosen. Additionally a node is added for the b -jet b_1 with the smallest separation $\Delta R = \sqrt{\Delta\eta^2 + \Delta\phi^2}$ from W_1 . If no combination is found yielding a compatible invariant mass, then nodes ℓ and b_1 are added only for the leading lepton and its closest b -jet. The top that decayed leptonically is then reconstructed as the sum of four momenta of ℓ , b_1 and MTM without any requirement on the invariant mass and a node is added. In a similar fashion a scan is conducted over combinations of jets trying to identify a dijet pair that results in an invariant mass $70 \text{ GeV} \leq m(jj) \leq 90 \text{ GeV}$, and if one is found we add nodes j_1 , j_2 and W_2 . In the opposite case, only nodes j_1 and j_2 are added. Then a node b_2 is added for the leading b -jet from the ones that remained. Considering the b_2 , j_1 and j_2 final states, the hadronically decaying top t_2 is reconstructed. Since, in certain events, additional jets are present that may contain discriminative power, a node is added for jets that are within $\Delta R < 0.8$ of any of the aforementioned nodes.

(ii) *Edges*: Connections between the nodes are added according to the decay chain. Firstly, the MTM and lepton are connected to W_1 , and then W_1 , b_1 are connected to the top t_1 . If W_1 has not been obtained, the final states are connected directly to t_1 . Similarly the jets j_1 and j_2 are connected to W_2 which is then connected to t_2 along with b_2 , in the presence of W_2 . Otherwise, connections between t_2 and j_1 , j_2 , b_2 are added. The remaining jets are connected to the closest object in terms of separation ΔR . An example is shown in Fig. 5.2. These edges are used to create the adjacency matrix of the graph.

(iii) *Node features*: For each node a feature vector $[p_T, \eta, \phi, E, m, \text{PID}]$ containing the transverse momentum, pseudorapidity, azimuthal angle, energy, invariant mass and particle identification number (in accordance with PDG [319]) is added.

5.3.1 Graph Neural Networks with Edge Convolution

Despite the multitude of applications for Convolutional Neural Networks (CNNs), they are limited to grid-shaped data like images. This poses issues when considering non-Euclidean data, such as final states in the detector. Recently the convolution operation has been generalised to operate on graph structures overcoming the previous limitations and allowing the deployment of GNNs [320]. For supervised learning where labels exist for the data, this was formalised as Message Passing Neural Networks (MPNNs) in Ref. [297] that will be discussed initially before moving to edge

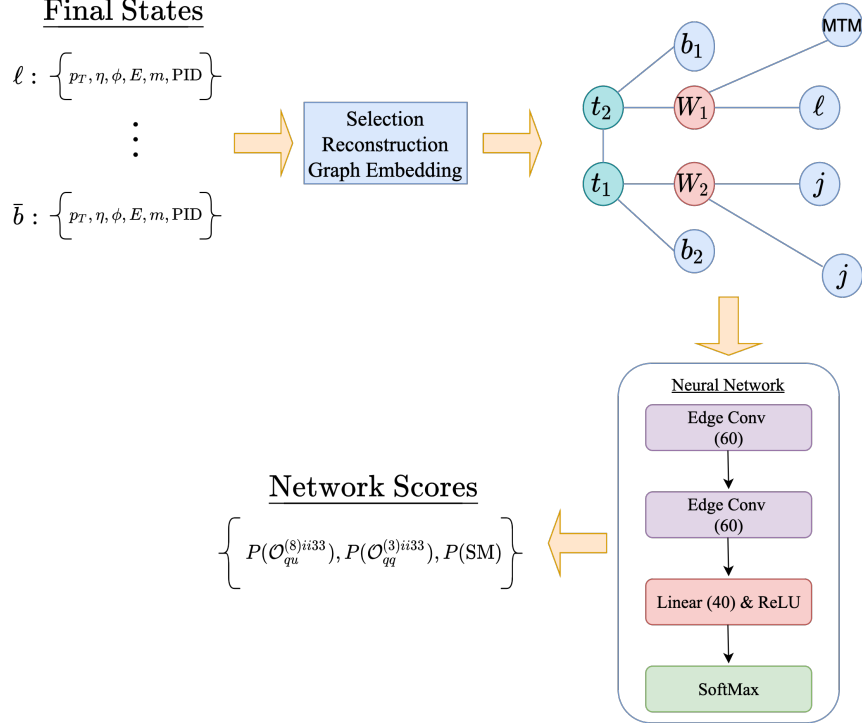


Figure 5.2: Diagram indicating the workflow. An event with final states passes through selection and reconstruction before being embedded in a graph structure. A representative diagram is shown for a created graph. The W bosons indicated with red may be missing if the W mass is not reconstructed, and then the final states will be connected directly to the top quarks. The event is then fed into the network of the indicated architecture, which supplies the scores for each class.

convolution (EdgeConv) networks that are used in this Chapter. Let i and j denote two adjacent nodes with edge $\vec{e}_{ij}^{(l)}$ where the vector implies a directed graph. Using a mathematical operation \vec{M} , a message $\vec{m}_{ij}^{(l)}$ is computed between the nodes with

$$\vec{m}_{ij}^{(l)} = \vec{M}^{(l)}(\vec{x}_i^{(l)}, \vec{x}_j^{(l)}, \vec{e}_{ij}^{(l)}). \quad (5.6)$$

where $x_i^{(l)}$ are the features of node i at time-step l . We use a linear activation function for the message function. The message passing phase is completed when messages for all adjacent nodes

have been calculated in a layer. The nodes are then updated with an aggregation function

$$\vec{x}_i^{(l+1)} = \vec{A}(\vec{x}_i^{(l)}, \{\vec{m}_{ij}^{(l)} | j \in \mathcal{N}(i)\}), \quad (5.7)$$

where $\mathcal{N}(i)$ represents the (neighbouring) nodes connected to node i and \vec{A} is a function. Commonly ‘max’, ‘sum’ or ‘mean’ are used as aggregation functions. The updated features are then the input for the next layer. When classification of graphs is desired, then a graph readout operation \square is applied in the final features $x_i^{(L)}$ where L denotes the last layer. Then one obtains a vector

$$\vec{X} = \square(\vec{x}_i^{(L)} | i \in G), \quad (5.8)$$

where G denotes the input graph. The resulting vector \vec{X} is of fixed size even though each graph can have a different number of nodes or edges, and the result can feed other usual layers in NNs. A graph can also be bi-directed, which is the type used in this Chapter.

For EdgeConv networks, the message passing function is edge convolution, defined as

$$\vec{x}_i^{(l+1)} = \frac{1}{|\mathcal{N}(i)|} \sum_{j \in \mathcal{N}(i)} \text{RELU} \left(\Theta(\vec{x}_j^{(l)} - \vec{x}_i^{(l)}) + \Phi(\vec{x}_i^{(l)}) \right), \quad (5.9)$$

where Θ and Φ are linear layers mapping the inputs to vectors of identical dimension. Aggregation is performed by taking the mean, and we use two layers $L = 2$ with the mean as the graph readout operation. EdgeConv does not require edge features and calculates them from the node features exploiting possible correlations.

5.3.2 Network Architecture and Training

To implement the GNN, the DEEP GRAPH LIBRARY [321] is used to construct the graphs, perform the message passing with edge convolution and execute the graph readout. PYTORCH [322] is used as the back-end for constructing a multi-class NN able to classify between each EFT interaction sourcing each event and the SM. For each class, a total of 70000 events are used, with 80% of events separated for training. The remaining 20% is split equally for validation and testing. Networks with EdgeConv layers followed by hidden linear layers with RELU activation functions are considered. By applying the softmax function on the output layer, probabilities for each class are obtained. Training is conducted by minimising the categorical cross-entropy loss function using a learning rate of 0.001 for the Adam optimiser [269] that decayed by a factor of 0.1 if the

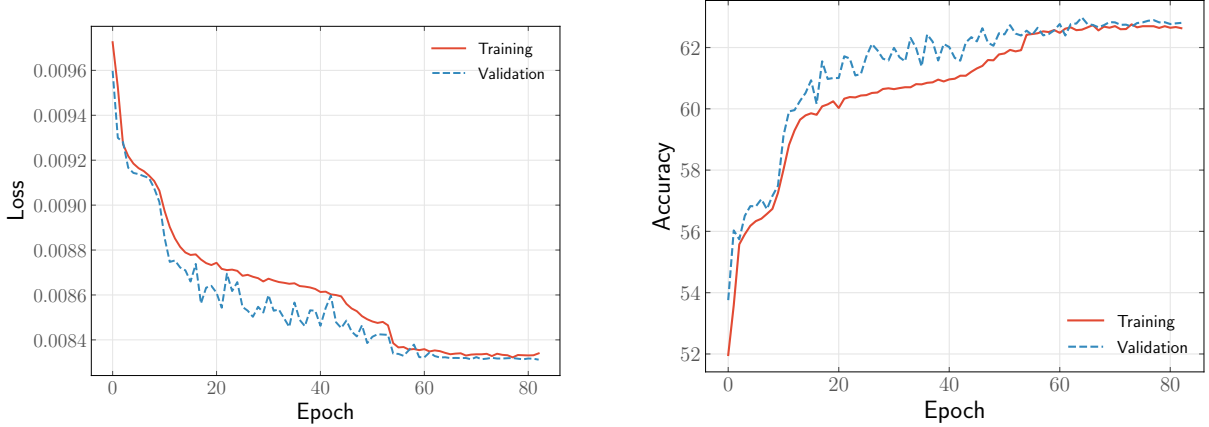


Figure 5.3: Loss and accuracy curves that show convergence for the minimal setup of Sec. 5.4.1 with only three classes. The choice of network architecture avoids overtraining, and this is generalised to the complete setup with all operators of Sec. 5.4.2.

loss function has not decreased for three consecutive epochs. Each considered network model was trained for a total of 100 epochs with batches of 100 events. An early stopping condition is imposed to stop the network when the loss does not decrease for ten epochs. Many models of alternative architectures were trained on the data samples in order to identify the optimal setup. For this setup, it has been concluded that two EdgeConv layers with 60 nodes and one hidden linear layer of 40 nodes performed best. It is worth highlighting that overtraining has been observed for deeper networks by checking loss and accuracy curves during training and validation. Examples for our setup are shown in Fig. 5.3. The relatively shallow network indicates that physics can be captured with only a few physical properties.

5.4 GNN-improved Wilson coefficient constraints

5.4.1 A minimal example

In order to explore the applicability of the network to the effective description, the simpler scenario of only two effective interactions (resulting in a total of three classes) is considered first. Each event is then assigned a probability of arising from an EFT or the SM class (see Fig. 5.2). Although not necessarily physically motivated, this more straightforward setup allows to study ways to use the network’s output to improve the constraints on the WCs, before generalising the discussion to all the relevant WCs for the considered channel in Sec. 5.4.2.

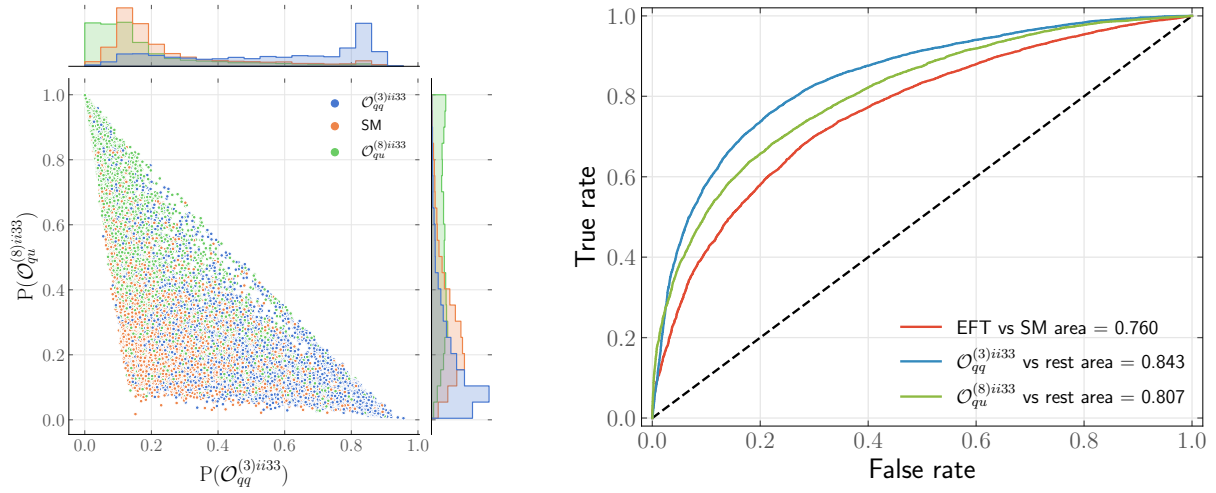


Figure 5.4: Distribution of generated events according to the SMEFT network scores is shown on the left while ROC curves are on the right. The latter are calculated in a one-vs-rest scheme for each class.

The WC space is thus restricted to the effective operators

$$\begin{aligned}\mathcal{O}_{qu}^{(8)ii33} &= (\bar{Q}_i \gamma_\mu t^a Q_i) (\bar{u}_3 \gamma^\mu t^a u_3), \\ \mathcal{O}_{qq}^{(3)ii33} &= (\bar{Q}_i \gamma_\mu \tau^I Q_i) (\bar{Q}_3 \gamma^\mu \tau^I Q_3).\end{aligned}\tag{5.10}$$

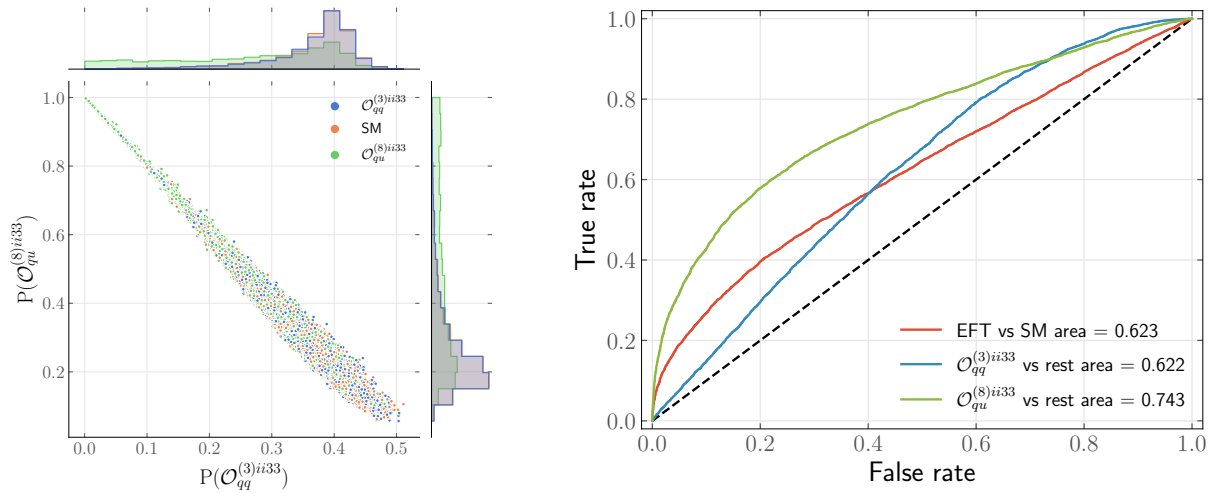


Figure 5.5: Same as Fig. 5.4 but for fully connected graphs.

With only three classes, classification becomes a seriously easier task, and the network can exploit correlations between momenta, azimuthal angles and rapidities of final states, as well as the graph structures of the events, in order to categorise them appropriately.

Fig. 5.4 (left) shows the probabilities calculated from the GNN for each individual event in the $P(\mathcal{O}_{qq}^{3(ii33)})$ - $P(\mathcal{O}_{qu}^{3(ii33)})$ plane. Events sourced by the presence of $\mathcal{O}_{qu}^{8(ii33)}$ are located on the upper left, while events from $\mathcal{O}_{qq}^{3(ii33)}$ lie in the bottom right as anticipated. The purely-SM events are located in a region where both probabilities of the EFT operators are low while $P(\text{SM})$ is higher. The figure indicates the efficient discrimination of three separate classes from the network and how the events can be split into different regions allowing us to select optimal signal regions with cuts on the probabilities. Performance is also assessed with ROC curves shown on the right of Fig. 5.4, calculated in a one-vs rest scheme where the labels are binarised for each WC. Marking all events from EFT insertions as signal and the SM as background allows us to also obtain an EFT vs SM curve, where the total EFT probability is the sum of $P(\mathcal{O}_{qq}^{3(ii33)})$ and $P(\mathcal{O}_{qu}^{3(ii33)})$.

For comparison, Fig. 5.5 shows the performance achieved with the same architecture but using fully connected graphs instead. The substantially poorer performance indicates the critical ability for distinguishing operators and background achieved by the physics-inspired approach. While performance could improve for the fully connected case when using deeper architectures, it would still be disadvantageous due to the increased computing time needed to embed the events, train the network and run it, which also implies a greater amount of resources.

Constraints on WCs can be then acquired by performing a χ^2 , similar to Ref. [287]. We use the leading b -jet transverse momentum distribution $p_T(b_1)$ with events extrapolated at an integrated luminosity of 3/ab foreseen to be achieved at the High-Luminosity (HL) LHC. It should be noted that improvements in bounds of WCs should be independent of the luminosity, though. Fig. 5.7 (left), shows the exclusion contours for the WCs when only the selection cuts are used with black.

In order to show the power of using the GNN for classification, we cut on the datasets above some threshold on the EFT probabilities and then perform the χ^2 on the $p_T(b_1)$ distribution. As expected, cutting on the probabilities $P(\mathcal{O}_{qq}^{3(ii33)})$ results in significantly tighter bounds in the direction of $C_{qq}^{3(ii33)}$, but poorer in the $C_{qu}^{3(ii33)}$ direction and vice-versa, indicating that contamination from the SM background or the other EFT operator is critically reduced. These are shown in red and blue on the left of Fig. 5.7. Binning is chosen in such a way that avoids depleting the bins from SM events that would result in unrealistic bounds.

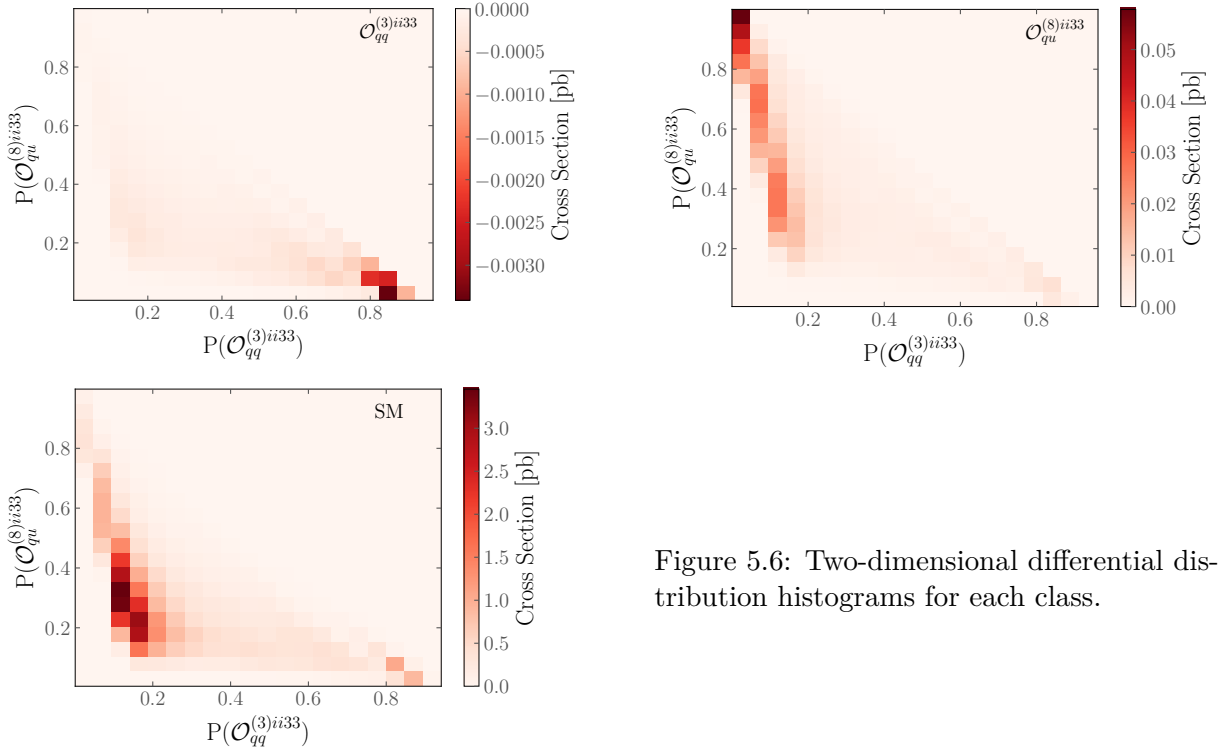


Figure 5.6: Two-dimensional differential distribution histograms for each class.

However, these cuts are expectedly not optimal as constraints in the direction of the uncut operator are worse than the full dataset. In order to obtain improved combined bounds and resolve this issue, it is helpful to define the P(BSM) probability summing the EFT probabilities, i.e.

$$P(\text{BSM}) = P(\mathcal{O}_{qu}^{(8)ii33}) + P(\mathcal{O}_{qq}^{(3)ii33}) , \quad (5.11)$$

which results in the optimal bound with superior results when compared to the full dataset case.

Exploring alternative ways, one possibility is to use directly the 2D histograms of the probabilities calculated by the network to formulate bounds instead of the $p_T(b_1)$ distribution. Representative histograms are shown in Fig. 5.6 for each class. Generally, the classification of d classes can be converted to a $d - 1$ histogram of probabilities due to the normalisation of probabilities which condenses the phenomenological information available in the events. For $\mathcal{O}_{qu}^{(8)ii33}$ and $\mathcal{O}_{qq}^{(3)ii33}$ the flattened 2D histograms can be used to construct a χ^2 in a similar manner with the one-dimensional $p_T(b_1)$ distribution, which results in the constraints shown on the right of

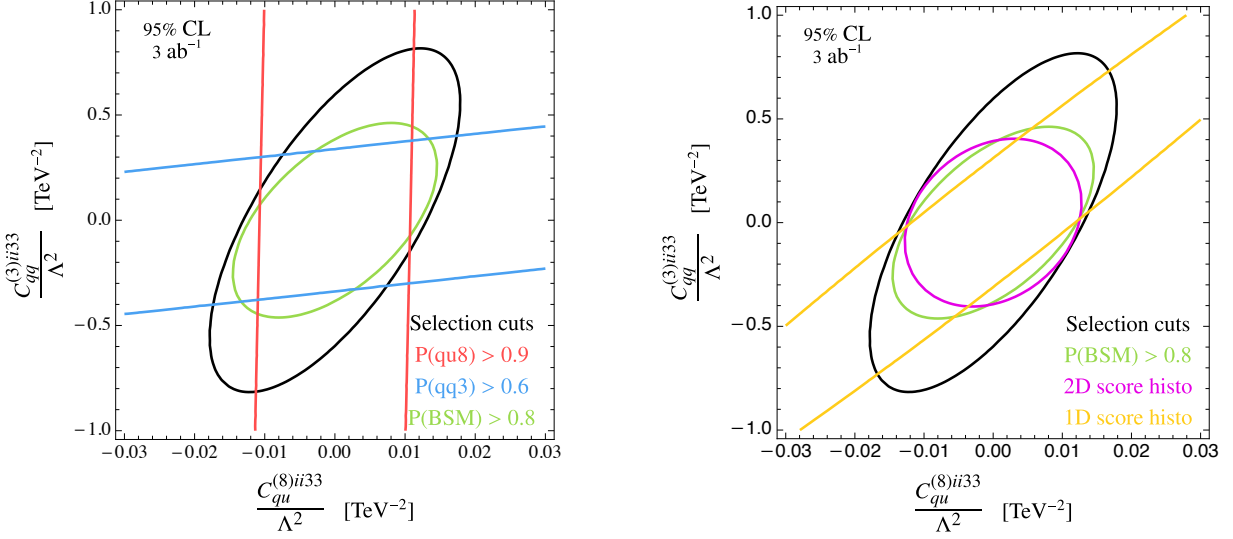


Figure 5.7: Exclusion contours on WCs at the 95% CL from the constructed χ^2 . The baseline results with the network selection of Sec. 5.2 are shown in black. On the left, contours are obtained by imposing cuts on the NN scores at optimal values and performing the analysis using $p_T(b_1)$ distributions. On the right, the result with the NN score is again shown in comparison with the contour from the analysis on the 2D score histograms (without cuts on the NN score). The contours from the analysis with the 1D BSM score histogram are also shown.

Fig. 5.7. This approach also provides tighter bounds compared to the $p_T(b_1)$ analysis with only selection cuts. However, the method is only suitable for a small subset of relevant interactions as it is quite difficult to generalise when many operators are present. A multi-dimensional histogram would require large amounts of statistics to avoid depleting bins from SM events. In addition, this approach is subject to the choice of binning, while cuts on the BSM score just depend on the threshold choice, which is considerably easier to obtain.

In principle the one-dimensional P(BSM) could also be used to calculate a χ^2 in order to get bounds shown in Fig. 5.7. This would avoid the need to identify an optimal BSM score. However, the projection of the two-dimensional output to a one-dimensional score results in loss of information, and only limited sensitivity can be achieved, showing that this method is inferior to the rest.

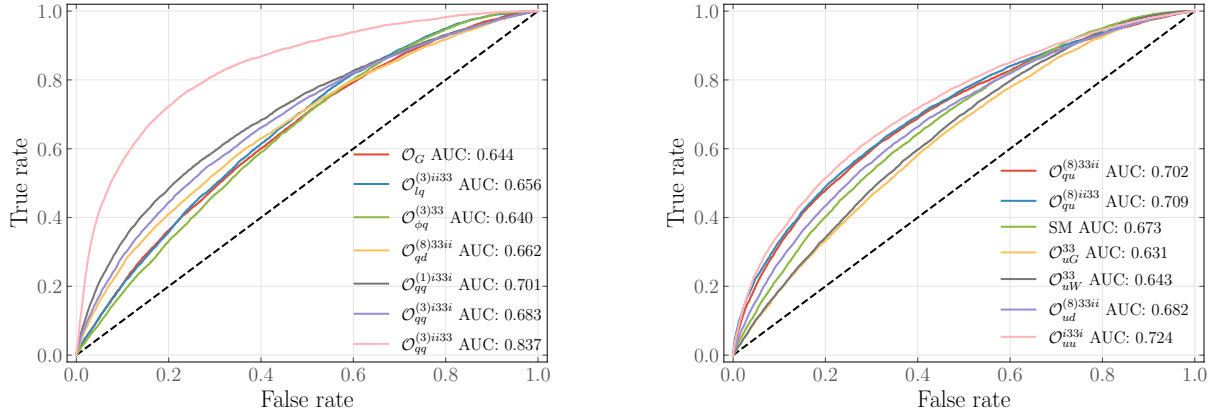


Figure 5.8: ROC curves for multi-class classification performed on all the thirteen SMEFT operators and the SM.

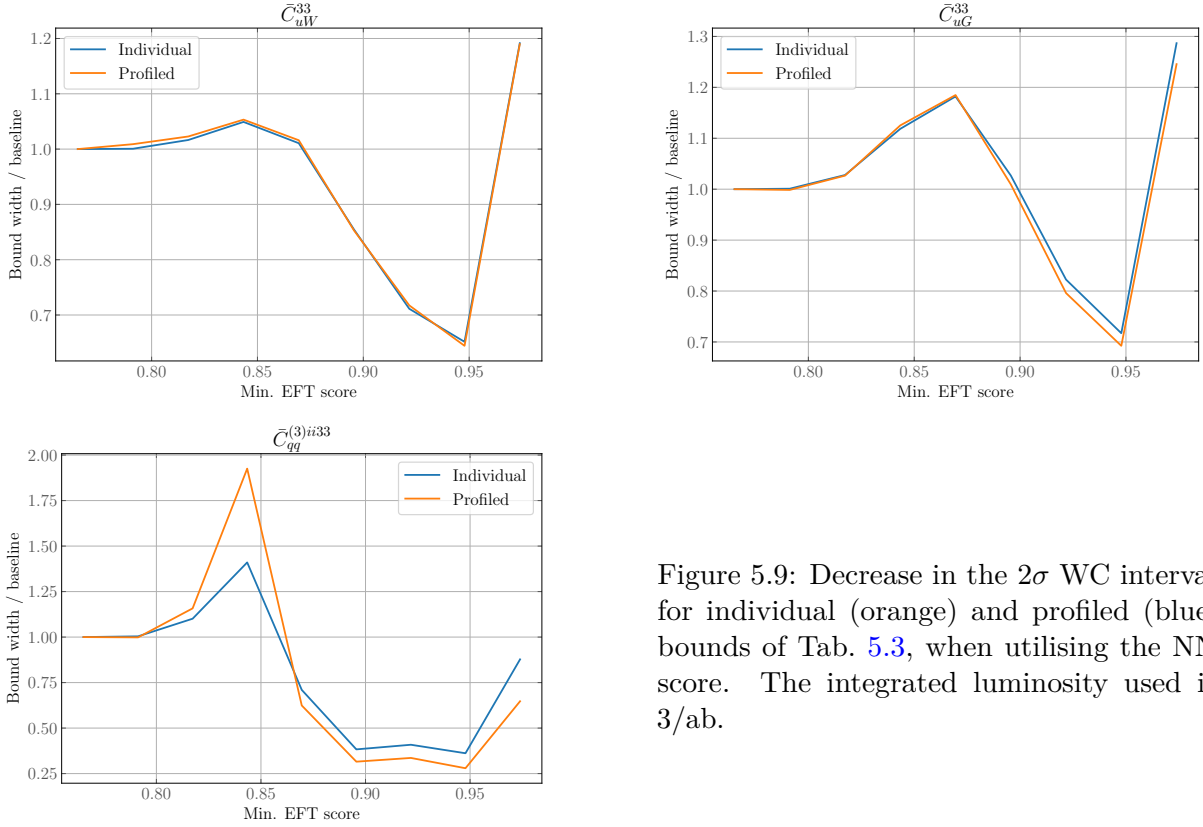


Figure 5.9: Decrease in the 2σ WC interval for individual (orange) and profiled (blue) bounds of Tab. 5.3, when utilising the NN score. The integrated luminosity used is $3/\text{ab}$.

5.4.2 Fit constraints with GNN selections

The setup is generalised to perform a multi-class classification of the thirteen effective operators relevant for the process (5.1) and the SM. The hyperparameters of the network are scanned to identify the optimal case; however, increasing the number of layer nodes delivers no significant increase in performance at the cost of longer training times. On the contrary, adding more layers to the architecture quickly shows signs of overtraining. Therefore the network setup is kept the same as the two-operator scenario. The ROC curves are shown in Fig. 5.8 calculated as before with one-vs-rest binarising. It is evident from the ROC curves that the performance is decreased compared to the two-operator case due to the higher complexity of the problem at hand. Still, it provides a critical distinction between the classes.

	2.3 fb ⁻¹		3 ab ⁻¹	
	Individual	Profiled	Individual	Profiled
\bar{C}_G	(-0.0543, 0.0535)	(-0.1785, 0.1776)	(-0.0015, 0.0015)	(-0.0047, 0.0047)
$\bar{C}_{\varphi q}^{(3)33}$	(-0.0317, 0.0326)	(-0.0806, 0.0758)	(-0.0009, 0.0009)	(-0.0022, 0.0022)
\bar{C}_{uG}^{33}	(-0.0253, 0.0247)	(-0.0622, 0.0655)	(-0.0007, 0.0007)	(-0.0017, 0.0017)
\bar{C}_{uW}^{33}	(-0.0234, 0.0228)	(-0.0544, 0.0580)	(-0.0006, 0.0006)	(-0.0015, 0.0016)
$\bar{C}_{qd}^{(8)33ii}$	(-0.1543, 0.1558)	(-0.3789, 0.3698)	(-0.0043, 0.0043)	(-0.0104, 0.0104)
$\bar{C}_{qq}^{(1)ii33i}$	(-0.0202, 0.0204)	(-0.0495, 0.0484)	(-0.0006, 0.0006)	(-0.0014, 0.0014)
$\bar{C}_{qq}^{(3)ii33i}$	(-0.0101, 0.0102)	(-0.0247, 0.0241)	(-0.0003, 0.0003)	(-0.0007, 0.0007)
$\bar{C}_{qq}^{(3)ii33}$	(-3.2964, 3.3259)	–	(-0.0917, 0.0917)	(-0.3045, 0.3046)
$\bar{C}_{qu}^{(8)33ii}$	(-0.0867, 0.0875)	(-0.2127, 0.2079)	(-0.0024, 0.0024)	(-0.0058, 0.0058)
$\bar{C}_{qu}^{(8)ii33}$	(-0.0577, 0.0583)	(-0.1416, 0.1383)	(-0.0016, 0.0016)	(-0.0039, 0.0039)
$\bar{C}_{ud}^{(8)33ii}$	(-0.1598, 0.1613)	(-0.3923, 0.3824)	(-0.0044, 0.0044)	(-0.0107, 0.0107)
\bar{C}_{uu}^{i33i}	(-0.0225, 0.0228)	(-0.0553, 0.0540)	(-0.0006, 0.0006)	(-0.0015, 0.0015)
$\bar{C}_{lq}^{(3)ii33}$	–	–	(-0.3289, 0.3288)	(-1.8493, 1.8930)

Table 5.2: 2σ bounds on WCs with the baseline analysis for different luminosities.

For comparisons we quote the baseline sensitivity in Tab. 5.2 with bounds obtained as discussed in Sec. 5.2. Individual constraints consider only one operator with the rest of the WCs fixed to

	2.3 fb ⁻¹		3 ab ⁻¹	
	Individual	Profiled	Individual	Profiled
\bar{C}_G	0.07%	14.12%	0.07%	11.09%
$\bar{C}_{\varphi q}^{(3)33}$	33.74%	34.19%	33.73%	33.48%
\bar{C}_{uG}^{33}	28.29%	32.18%	28.28%	30.74%
\bar{C}_{uW}^{33}	34.86%	35.35%	34.85%	35.53%
$\bar{C}_{qd}^{(8)33ii}$	4.71%	4.68%	4.71%	4.76%
$\bar{C}_{qq}^{(1)i33i}$	3.50%	3.45%	3.50%	4.73%
$\bar{C}_{qq}^{(3)i33i}$	4.35%	4.28%	4.35%	5.00%
$\bar{C}_{qq}^{(3)ii33}$	63.83%	–	63.83%	71.91%
$\bar{C}_{qu}^{(8)33ii}$	3.45%	3.51%	3.45%	3.48%
$\bar{C}_{qu}^{(8)ii33}$	3.74%	3.72%	3.74%	3.77%
$\bar{C}_{ud}^{(8)33ii}$	4.62%	4.46%	4.62%	4.79%
\bar{C}_{uu}^{i33i}	3.38%	3.35%	3.38%	1.95%
$\bar{C}_{lq}^{(3)ii33}$	–	–	10.57%	35.52%

Table 5.3: Optimal improvements on the 2σ constraints by using a cut on the NN score.

zero. However, this does not capture the impact of other interactions on the bounds of a WC, and it is, therefore, useful to profile over the remaining coefficients by fixing them to the value that minimises the χ^2 function. When an analysis is sensitive to the inclusion of additional effective operators, this will result in a drop in sensitivity. Cuts on the dataset are then performed for different thresholds on the EFT score (the sum of probabilities for each EFT operator), with representative examples shown in Fig 5.9. Stricter bounds are achieved with the network cut since the background contamination from the SM is efficiently removed, and events sourced from EFT operators remain. It should be noted that improvements on profiled bounds can sometimes be greater than individual ones. This occurs when the cut on the network score selects a region where the impact on the bounds of a particular operator by the presence of additional interactions is reduced. Nonetheless, it is not the aim of this Chapter to compare the robustness of one class against variations of others; thus, they will not be addressed further.

In general, the achievable improvements range between 5% and 60% as shown in Tab. 5.3

depending on the operator under consideration. Setting strict thresholds on the network score manages to select a BSM-sensitive region, efficiently separating the SM background, before eventually losing statistical control when the cut on the score approaches unity. A sizeable improvement is obtained for momentum-enhanced operators such as \bar{C}_{uG}^{33} . For non-resonant contributions to the decays of the tops i.e. operators \mathcal{O}_{uW}^{33} , $\mathcal{O}_{\phi q}^{(3)33}$ and $\mathcal{O}_{lq}^{(3)ii33}$, the network again manages to supply efficient discrimination. The poorest improvement is on the constraints of the \bar{C}_G direction, but it is relatively under control from the baseline selection, and sensitivity can be further enhanced by dedicated analyses exploiting the multi-jet production [323, 324]).

5.5 Conclusions

Despite the absence of new physics evidence at the LHC, EFT can enable pinpointing the direction that should be followed in the future by identifying modifications of expected SM interactions. The use of motivated differential distributions can give constraints on the WCs of EFTs such as SMEFT; however, employing NN techniques in an attempt to exploit as much information possible from correlations in the data can further enhance the achievable sensitivity of both current experiments and future collider concepts.

The choice of GNNs is mainly motivated for particle physics as we can choose the graph structure appropriately to reflect the channel modified by the additional interactions. Focus in this Chapter is on the $t\bar{t}$ state decaying semileptonically as this is a channel where viable new physics interactions might arise and can be tagged due to the unique final state. More importantly, depending on a critically large number of Wilson Coefficients, the parameter space is rendered an appropriate playground for employing multi-class classification. Considerable improvements are achievable, especially for coefficients that simple differential distribution analyses are not particularly sensitive to, demonstrating that ML excels in efficiently selecting an appropriate signal region leading to improved sensitivity.

It should be highlighted, however, that the analysis here is entirely based on Monte Carlo data, without including the theoretical and experimental uncertainties that appear when comparing Monte Carlo predictions with data from actual experiments. It is possible, though, to treat them through adversarial networks where results are obtained independent of unknown values of nuisance parameters [325, 326]. Treating theoretical and experimental uncertainties as such parameters to get classification scores independent of them was shown to be achievable in Refs. [327] and [328], respectively.

In addition to the impact of uncertainties, one should keep in mind that, as indicated by profiling, sensitivity can undergo a dramatic reduction in the presence of additional operators. While in the top-sector no tension with the SM was identified for the particular channel considered, it would be advantageous to explore SMEFT in a different setting where tension with the SM exists, which will enable an instrumental understanding of how to reinterpret the results for particular physics problems. The WC that acquires a non-zero best fit value can then be used to identify additional processes that can be used to scrutinise such excess. The following two Chapters concentrate on this, exploring CP violation in the Higgs-gauge sector first and, subsequently, the anomalous magnetic moment.

Chapter 6

CP violation in gauge-Higgs interactions

6.1 Introduction

The model-independence of the EFT framework explored previously comes with the drawback of substantial sensitivity suppression due to the large number of new interactions, resulting in weaker constraints on the relevant WCs. While improvements are achievable when uncertainties can be reduced or a more efficient extraction of information from data using NNs is possible, it is also desirable to consider a theoretically motivated approach to reduce the number of relevant operators. Instead of considering the full SMEFT, one could start from a top-down approach and use the interactions and particles within different UV scenarios to anticipate the hierarchy of various EFT operators. With certain operators appearing only at higher orders within the UV scenarios, it is possible to reduce the parameter space of applicable couplings. This idea will be explored in the context of CP violation in the gauge-Higgs sector motivated by the ATLAS study of Ref. [329].

As discussed in Sec. 2.6, the dominance of matter over antimatter in the Universe remains an open question in particle physics since the SM CP violation through the CKM matrix can not explain baryogenesis [113]. Recent experimental searches for a CP odd top Yukawa coupling were also not showing any such hints [330, 331], which motivates the search for CP violation arising in other sectors from new physics. While many BSM theories introduce CP odd effects, it is possible

to consider model-independent scenarios through EFTs [138] in the context of the Lagrangian of Eq. (2.65).

In a recent study of the associated production of a Z boson with two jets by the ATLAS collaboration [329], results are interpreted within the EFT framework by considering the CP violating operators

$$\mathcal{O}_{\widetilde{W}} = \epsilon^{abc} \widetilde{W}_{\mu\nu}^a W^{b\nu\rho} W^{c\rho\mu}, \quad (6.1)$$

$$\mathcal{O}_{\phi\widetilde{W}B} = (\Phi^\dagger \tau^a \Phi) \widetilde{W}_{\mu\nu}^a B^{\mu\nu}, \quad (6.2)$$

expressed in the Warsaw basis [139], where W and B refer to the field strength tensors of the gauge bosons of $SU(2)_L$ and $U(1)_Y$, respectively. The wide tilde denotes the dual field strength tensor for $X = W, B$ defined by

$$\widetilde{X}_{\mu\nu} = \frac{1}{2} \epsilon_{\mu\nu\sigma\rho} X^{\sigma\rho}. \quad (6.3)$$

Φ and τ^a are the SM Higgs doublet and the Pauli matrices, as in the SM. The matrix elements entering the differential cross section distributions obtain linear contributions from dimension-six interference terms

$$|\mathcal{M}|^2 = |\mathcal{M}_{\text{SM}}|^2 + 2 \text{Re} \left[\mathcal{M}_{\text{SM}} \mathcal{M}_{\text{d6}}^* (C_{\widetilde{W}}, C_{\phi\widetilde{W}B}) \right]. \quad (6.4)$$

ATLAS studied the signed azimuthal angle difference $\Delta\phi_{jj}$ of the two jets, as ordered by rapidity, appearing in $Z + jj$ providing the 95% confidence level constraints on the WCs as

$$C_{\widetilde{W}} \frac{\text{TeV}^2}{\Lambda^2} \in [-0.11, 0.14], \quad C_{\phi\widetilde{W}B} \frac{\text{TeV}^2}{\Lambda^2} \in [0.23, 2.34]. \quad (6.5)$$

It should be highlighted that $\Delta\phi_{jj}$ is sensitive to parity transformation, and as a CP odd observable, it does not depend on CP even operators of the EFT. Therefore, the inclusion of the CP even term $|\mathcal{M}_{\text{d6}}|^2$ would also not modify the constraints.¹ The fiducial cross section measured by ATLAS at 37.4 fb is in agreement (within errors) with the SM prediction of 39.5 fb [283, 332, 333] which as a CP even observable is not deformed by the additional operators.

As the constraint excludes the SM, it could be a clue of new physics and should be further investigated to tension or support the results using additional channels, especially since analyses

¹This was indeed showcased by ATLAS [329] by performing the analysis with and without the pure dimension-six terms.

of asymmetries in distribution shapes, as done by Ref. [329], are often limited by systematics. It would also be interesting to consider the effect of further operators in a model-independent fashion since there exist blind directions that should be taken into account in global analyses. In total, the CP violating effects related only to the electroweak sector can be captured by the dimension-6 operators of (6.1) and additionally [139]

$$\mathcal{O}_{\phi\widetilde{W}} = \Phi^\dagger \Phi \widetilde{W}_{\mu\nu}^a W^{a\mu\nu} \quad (6.6)$$

$$\mathcal{O}_{\phi\widetilde{B}} = \Phi^\dagger \Phi \widetilde{B}_{\mu\nu}^a B^{a\mu\nu}. \quad (6.7)$$

The focus of the work presented in this Chapter is, therefore, threefold. Firstly, the ability of the diboson production at the LHC to help scrutinise the deviations from the SM is demonstrated in Sec. 6.2.1. Secondly, it is motivated that the operator $\mathcal{O}_{\widetilde{W}}$ does not arise in certain concrete UV scenarios and can be excluded from the analysis. Finally, a minimal fit of CP violation combining diboson channels with WBF Higgs production, setting $C_{\widetilde{W}} = 0$ is performed, assessing the exclusion contours for the LHC at 3/ab.

6.2 Scrutinizing CP violating $\mathcal{O}_{\phi\widetilde{W}B}$ operator with diboson data

6.2.1 Analysis of the CP sensitive $\Delta\phi$ distribution

The statistical analysis is conducted using the signed azimuthal angle $\Delta\phi_{ij} = \phi_i - \phi_j$ where i, j are particles depending on the process and ordered depending on their rapidity $y_i > y_j$. For each process, the observables' differential distribution is sensitive to CP violation and can be obtained by adding the linear terms arising from the dimension-six operators

$$\frac{d\sigma(\{C_k/\Lambda^2\})}{d\Delta\phi_{ij}} = \frac{d\sigma_{\text{SM}}}{d\Delta\phi_{ij}} + \sum_k \frac{C_k}{\Lambda^2} \frac{d\sigma_k}{d\Delta\phi_{ij}}, \quad (6.8)$$

where $k \in \{\widetilde{W}, \phi\widetilde{W}B, \phi\widetilde{W}, \phi\widetilde{B}\}$, in line with Eq. (2.66). The cross sections σ_k do not depend on C_k but contain the interference effects from the additional operators \mathcal{O}_k . It is, therefore, possible to generate events at a fixed parameter point in the WC space (say $C_{\phi\widetilde{W}B} = 1$ with the rest fixed to zero) to capture only the effects of one operator and then rescale σ_k to get the effect of a different WC value and then combine contributions through Eq. (6.8). A χ^2 can then be

calculated with

$$\chi^2 \left(\frac{C_{\widetilde{W}}}{\Lambda^2}, \frac{C_{\phi\widetilde{W}B}}{\Lambda^2}, \frac{C_{\phi\widetilde{W}}}{\Lambda^2}, \frac{C_{\phi\widetilde{B}}}{\Lambda^2} \right) = \sum_{i \in \text{bins}} \frac{(b_{\text{SM+d6}}^i - b_{\text{SM}}^i)^2}{(\sqrt{b_{\text{SM}}^i})^2}, \quad (6.9)$$

where b_{SM}^i is the number of events in bin i as predicted by the SM with the BSM contributions turned off, while here

$$b_{\text{SM+d6}}^i = b_{\text{SM+d6}}^i \left(\frac{C_{\widetilde{W}}}{\Lambda^2}, \frac{C_{\phi\widetilde{W}B}}{\Lambda^2}, \frac{C_{\phi\widetilde{W}}}{\Lambda^2}, \frac{C_{\phi\widetilde{B}}}{\Lambda^2} \right). \quad (6.10)$$

Only statistical fluctuations $\sqrt{b_{\text{SM}}^i}$ are included as uncertainties since cancellations between the contribution of the symmetric SM, and antisymmetric SMEFT operators remove systematic uncertainties when summed.² Using the definition for confidence level intervals of Eq. (5.3), one can then obtain contours in two-dimensional planes by either taking slices in the WC parameter space or by profiling, where contours are obtained at values of WCs that minimise the χ^2 . As in the last Chapter, the latter is helpful in understanding how the contours' limits depend quantitatively on the particular coefficients.

6.2.2 Diboson analyses

The first considered process is diboson production at the current LHC luminosity that, due to the abundance of data, can already tension the constraints in (6.5). The channels $W\gamma \rightarrow \ell\nu\gamma$, $W^+W^- \rightarrow \ell^+\nu_\ell\ell^-\bar{\nu}_\ell$ and $WZ \rightarrow \ell\nu\ell^+\ell^-$ are sensitive to modifications of the gauge boson self-couplings. Using a CP sensitive observable, one can capture the effect of $\mathcal{O}_{\widetilde{W}}$ and $\mathcal{O}_{\phi\widetilde{W}B}$, while $\mathcal{O}_{\phi\widetilde{W}}$ and $\mathcal{O}_{\phi\widetilde{B}}$ do not appear due to conservation of momentum³.

Unless otherwise stated, FEYNRULES [58, 59] is used to extend the SM with the additional SMEFT operators exporting the Feynman rules as UFO [255] files that can be imported in MADGRAPH [96] for event generation using MADEVENT [94–96]. Events are stored in the LHEF format [334], and the analysis is executed on MC-truth events with the exception of $W\gamma$.

²Systematic uncertainties could, in principle, be included using Eq. (5.2) where the covariance matrix V could be constructed as $V_{ij} = (\epsilon_{\text{rel.stat}}^2 + \epsilon_{\text{rel.syst}}^2) b_{\text{SM}}^i b_{\text{SM}}^j$. $\epsilon_{\text{rel.stat}}$ and $\epsilon_{\text{rel.syst}}$ denote the relative statistical and relative systematic uncertainties for each process.

³The vertices with the operator $\mathcal{O}_{\phi\widetilde{W}}$ has a Feynman rule proportional to $iev^2 C_{\phi\widetilde{W}} \epsilon_{\mu\nu\rho\sigma} (p_1^\sigma + p_2^\sigma + p_3^\sigma)$ where p_i ($i = 1, 2, 3$) are the momenta of the legs. By conservation of momentum, the sum of them vanishes, and the situation is similar for $C_{\phi\widetilde{B}}$.

$W\gamma \rightarrow \ell\nu\gamma$:

The decay of the W boson to electrons and muons is considered separately, applying the cuts of CMS [335]. Events with up to one jet are included with matching and merging performed using PYTHIA8 [167]. FASTJET [258, 259] is interfaced through the reconstruction mode of MADANALYSIS [260–263] in order to cluster jets with the radius 0.4 anti-kT algorithm [98]. One isolated electron must appear in the central region of the detector with pseudorapidity $|\eta(e)| < 2.5$ that also has a transverse momentum of $p_T(e) > 30$ GeV. For the muon decay sample one muon must exist satisfying $|\eta(\mu)| < 2.4$ and $p_T(\mu) > 26$ GeV. If there are more than one lepton with $p_T > 20$ GeV the event is vetoed and at least one isolated photon with separation $\Delta R(\gamma, \ell) > 0.5$ is required to exist. The search region is further constrained by requiring $|\eta(\gamma)| < 2.5$, $p_T(\gamma) > 25$ GeV. A light lepton or a photon is considered isolated in this part when the sum of the transverse momenta of jets within the cone $\Delta R < 0.4$ is smaller than 50% of $p_T(i)$, where $i \in \{e, \mu, \gamma\}$. Neutrinos in the final state from the W decay lead to missing energy which is required to satisfy $\cancel{E}_T > 40$ GeV.

CMS [335] measured $N_{\text{CMS}}^e = 96000$ and $N_{\text{CMS}}^\mu = 164400$ events at an integrated luminosity of 137.1/fb within the search region defined by the cuts. Using the CMS results, event rates for the electron (muon) samples are normalised with $R^e = N_{\text{CMS}}^e/N_{\text{MC}}^e$ ($R^\mu = N_{\text{CMS}}^\mu/N_{\text{MC}}^\mu$), where $N_{\text{MC}}^{e,\mu}$ are the Monte-Carlo generated events for the SM. The signed azimuthal angle distribution for the photon and the lepton $\Delta\phi_{\gamma\ell}$ is calculated for the purpose of our analysis. Although two peaks characterise the distribution at LO, when a hard jet is emitted at higher orders, the picture is significantly distorted, impacting the channel’s sensitivity, as shown in Fig. 6.1. Regions with null radiation are anticipated in $W\gamma$ production due to the gauge structure of the vertex [336–339], but it is known that additional jet emissions involving a quark have no radiation zero [340–342]. An extra cut of $p_T(j) > 30$ GeV is thus enforced since it was found to improve the sensitivity to the WCs.

$W^+W^- \rightarrow \ell^+\nu_\ell\ell^-\bar{\nu}_\ell$: Following the ATLAS analysis in Ref. [343], the W^+W^- channel is probed with subsequent decays to the $e\nu_e\mu\nu_\mu$ final state, to study the $\Delta\phi_{e\mu}$ differential distribution. The cross section rate is normalised to the fiducial cross section given by ATLAS ($\sigma_{\text{fid}} = 379.1$ fb) and also rescaled to include various combinations of light leptons appearing in the final state. Exactly one electron and one muon are required satisfying $|\eta(\ell)| < 2.5$ and $p_T(\ell) > 27$ GeV without any other light lepton with $p_T > 10$ GeV. The two leptons must have no jet within a separation of $\Delta R < 0.4$ and are used to reconstruct the invariant mass and the transverse momentum of

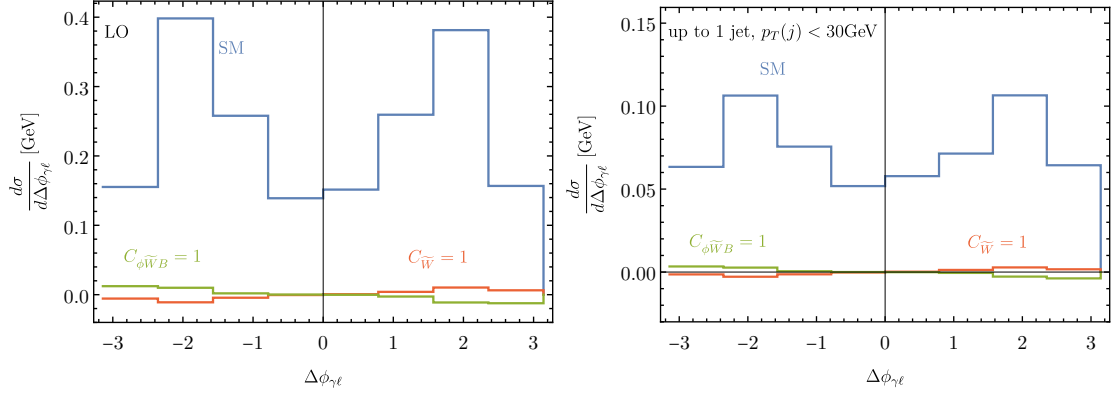


Figure 6.1: The $\Delta\phi_{\gamma\ell}$ distribution has two well-separated peaks at LO (left) but this behaviour changes when an extra jet is emitted (right).

the dilepton state. By restricting the search region to $m_{e\mu} > 55$ GeV and $p_T(e\mu) > 30$ GeV background contamination arising from Drell-Yan and $h \rightarrow W^+W^-$ channels is removed. Finally, an event with missing energy that does not comply with $\cancel{E}_T > 20$ GeV is vetoed.

$WZ \rightarrow \ell\nu\ell^+\ell^-$: Turning to the final diboson channel, WZ can be probed through the decays to $\ell\nu\ell^+\ell^-$. The characteristic of a same-flavour opposite-charge pair of leptons is necessary in the reconstruction of the four-momentum of the Z , which is used for our analysis of the signed azimuthal angle difference of the Z with the remaining lepton, $\Delta\phi_{\ell Z}$. Following CMS closely for the selection and cuts, the rate of the process is normalised to the calculated fiducial cross section of $\sigma_{\text{fid}} = 258$ fb [344]. Three leptons are required for selected events, without jets in the $\Delta R < 0.4$ cone and $|\eta(\ell)| < 2.5$, $p_T(\ell) > 5$ GeV. To identify the pair originating from the Z boson, the invariant dilepton mass is required to lie in the range [61 GeV, 121 GeV] and imposing a cut on the remaining lepton $p_T(\ell) > 20$ GeV which should be induced by W .

6.2.3 Diboson Results

The χ^2 is calculated for each process and 95% confidence levels (see Fig. 6.2(a)) are acquired after scanning for different Wilson coefficients using Eq. (5.3). For an integrated luminosity of 139/fb, the contour region and best-fit point that were evaluated by ATLAS [329] are included⁴. It can be seen that additional sensitivity can be obtained for $C_{\phi\widetilde{W}B}$, mainly driven by the $W\gamma$

⁴These are obtained by constructing a χ^2 and tuning a covariance matrix using details in [329].

production⁵. The measurement of $Z + 2j$ constrains substantially better the $\mathcal{O}_{\widetilde{W}}$ direction instead of $\mathcal{O}_{\phi\widetilde{W}B}$, which is due to the t -channel momentum transfer in WBF and because the Z boson has a larger overlap with the W^3 field compared to the photon. This additionally explains why the production of $W\gamma$ is more sensitive to the $\mathcal{O}_{\phi\widetilde{W}B}$ operator.

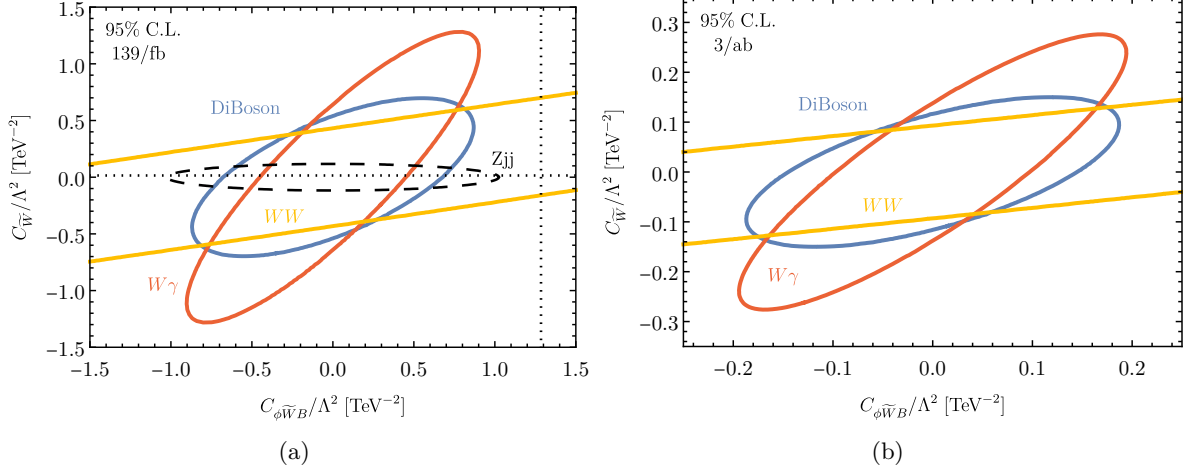


Figure 6.2: 95% CL contours for different diboson processes at 139/fb are shown on the left, including the Zjj contour⁶. On the left the best fit lines from the observations of Ref. [329] are included. On the right, the plot is reproduced for 3/ab.

The contours are also extrapolated to an integrated luminosity of 3/ab, to obtain the expected exclusion region for HL-LHC, and the results are shown in Fig. 6.2(b). It should be reiterated that $C_{\phi\widetilde{W}}$ and $C_{\phi\widetilde{B}}$ do not contribute to the χ^2 of the diboson processes.

6.3 Scenarios with low energy CP violation

In order to motivate theoretically that some operators can be excluded from the fits, it is essential to explore the hierarchy of the relevant operators as it arises from UV scenarios. Considering a simple extension of the SM with one heavy fermion Ψ firstly, the additional Lagrangian terms

⁵Results shown here are not as exclusive as our results in Ref. [5] due to the fact that no experimental information was available at the time and hard-jet emission was not included.

⁶The Zjj contour is obtained by reproducing the 95% individual expected confidence intervals, centred at zero, given in [329] using their provided data.

can be written as

$$\mathcal{L}_\Psi = \bar{\Psi} (i\mathcal{D} - M_\Psi) \Psi - \{ \bar{\Psi} Y_\Psi \Psi \Phi + \text{h.c.} \}, \quad (6.11)$$

where the quantum numbers under the SM symmetry group define the covariant derivative \mathcal{D} . The Lagrangian manifests interactions of Ψ with the rest of the SM fermions f (both leptons and quarks) through Yukawa interactions and also the Higgs field Φ . In order to obtain CP violating operators after integrating out the heavy fermion field, an odd number of γ_5 matrices must appear in the spin traces in numerators of loop diagrams. This would generate the Levi-Civita tensor $\epsilon_{\mu\nu\rho\sigma}$ through relations such as

$$2i\sigma_{\rho\sigma}\gamma_5 = \epsilon_{\mu\nu\rho\sigma}\sigma^{\mu\nu}, \quad (6.12)$$

where $\sigma_{\mu\nu} = \frac{i}{2} [\gamma_\mu, \gamma_\nu]$ is the Lorentz generator for fields of half-integer spins. This would induce the relevant operators with the dual of the field strength tensors that violate CP. However, even if explicit CP violation is imposed in the Yukawa interactions, there will only be an even number of γ_5 matrices in spin traces, which would lead to effective operators of the (X^3) or ($\phi^2 X^2$) classes, that conserve CP symmetry. These classes refer to the dimension-six operators in the Warsaw basis [139] given Sec. 2.7.1. X^3 ($\phi^2 X^2$) represents operators with three field strength tensors (two Higgs doublets and two field strength tensors). Hence, there is no way that the CP violating operators can be induced through this SM extension.

Moving to an alternative extension with two heavy vector-like leptons (VLL) Ψ_1 and Ψ_2 , the Lagrangian terms

$$\mathcal{L}_{2\Psi} = \bar{\Psi}_1 (i\mathcal{D} - M_{\Psi_1}) \Psi_1 + \bar{\Psi}_2 (i\mathcal{D} - M_{\Psi_2}) \Psi_2 - \{ \bar{\Psi}_1 Y_\Psi V \Psi_2 + \text{h.c.} \}, \quad (6.13)$$

can be included on top of the SM. $V = \Phi (a \mathbb{1}_4 + b \gamma_5)$ includes both CP even and odd interactions with a, b representing the even and odd couplings, respectively. For simplicity, both will be regarded as real, although in principle, they could be complex. When loop diagrams are considered that have an even number of γ_5 vertices, again, no CP violating operators will be induced. However, now it is possible to have an odd number of γ_5 vertices as shown in Fig. 6.3, which allows the generation of the Levi-Civita tensor through Eq. (6.12). The following section will discuss minimal setups where the vector-like fermions are an isospin-doublet and an isospin-triplet. It should be noted that heavy scalar extensions can not be used to induce $\mathcal{O}_{\widetilde{W}}$, again due to the absence of a γ_5

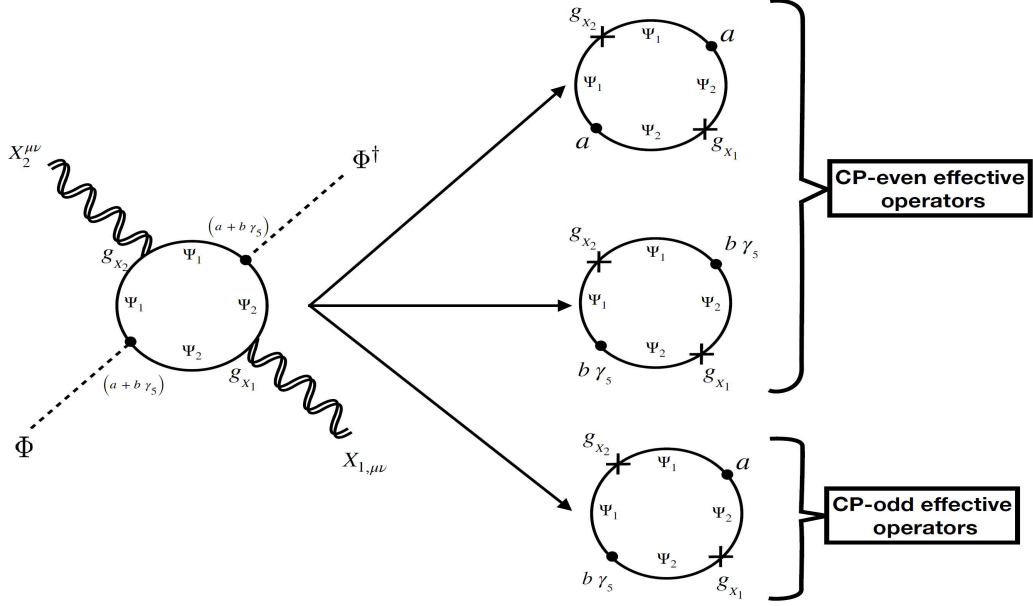


Figure 6.3: Field strengths are represented by X ($= B, W, G$). Assuming $X_1 = X_2$, the relevant dimension-six operators are $\mathcal{O}_{\phi W}$, $\mathcal{O}_{\phi B}$, $\mathcal{O}_{\phi G}$, $\mathcal{O}_{\phi \widetilde{W}}$, $\mathcal{O}_{\phi \widetilde{B}}$ and $\mathcal{O}_{\phi \widetilde{G}}$, while if $X_1 \neq X_2$, the relevant operators are $\mathcal{O}_{\phi WB}$ and $\mathcal{O}_{\phi \widetilde{W}B}$. Whether the diagram constructed by the field insertions results in a CP even or CP odd operator depends on the number of γ_5 matrices in the vertices; an even (odd) number of γ_5 s results in a CP even (odd) diagram.

matrix that can induce the Levi-Civita structure constant (see the appendices of Ref. [6]).

6.3.1 Doublet-Triplet VLL

To investigate a particular example, two heavy vector-like leptons χ_2 and χ_3 with relations under the SM gauge group

$$(\chi_2)_{L,R} : (\mathbf{1}, \mathbf{2}, 1/2), \quad (\chi_3)_{L,R} : (\mathbf{1}, \mathbf{3}, 1), \quad (6.14)$$

will be considered. These fields have masses m_{χ_2} and m_{χ_3} and interact with the Higgs Φ through Yukawa interactions inducing CP violating operators. The Lagrangian includes terms

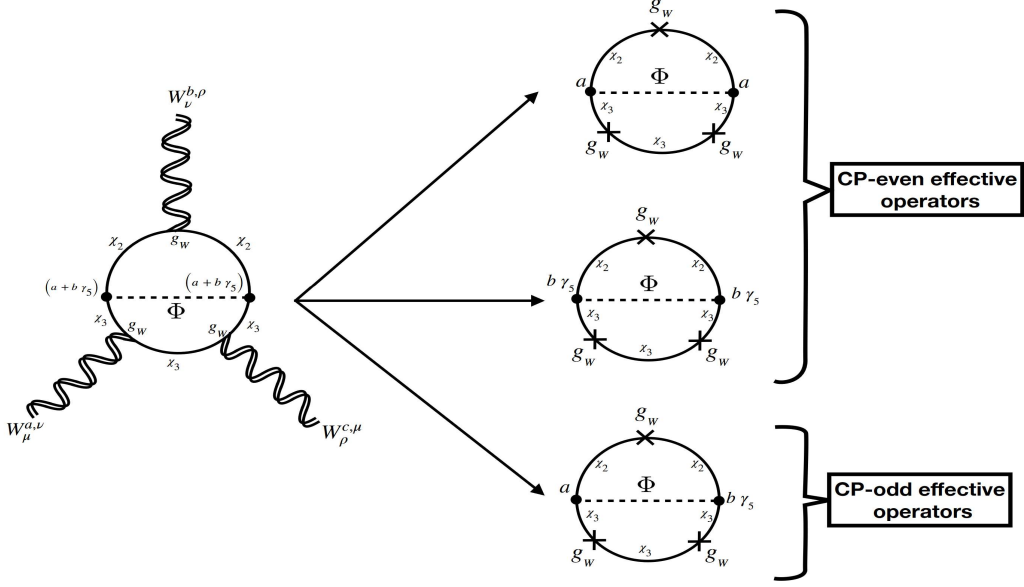


Figure 6.4: Diagrams to produce the operators \mathcal{O}_W and $\mathcal{O}_{\widetilde{W}}$ after integrating out the heavy VLL (see Eq. (6.15)). While the \mathcal{O}_W operator can be produced at one-loop, the CP violating $\mathcal{O}_{\widetilde{W}}$ can only be generated at two-loop processes. CP even and odd couplings in the diagram correspond to $a = \alpha_\chi$ and $b = \beta_\chi$ for the model of Eq. (6.18).

$$\mathcal{L}_{\text{DT}} \supset \bar{\chi}_2 (i\not{D}_{\chi_2} - m_{\chi_2}) \chi_2 + \bar{\chi}_3 (i\not{D}_{\chi_3} - m_{\chi_3}) \chi_3 - \left\{ \Phi^T \bar{\chi}_3^I \tau^I (y_{\chi_L} \mathbb{P}_L + y_{\chi_R} \mathbb{P}_R) i\tau_2 \chi_2 + \text{h.c.} \right\}, \quad (6.15)$$

where $I \in \{1, 2, 3\}$ is the isospin index. τ denotes the Pauli matrices, while \mathbb{P}_L and \mathbb{P}_R denote the left and right chiral projectors, respectively.

The BSM states can be integrated out and matched to an effective Lagrangian

$$\mathcal{L}_{\text{EFT}} = \mathcal{L}_{\text{SM}} + \frac{1}{16\pi^2 m^2} \sum_i \mathcal{C}_i \mathcal{O}_i, \quad (6.16)$$

where \mathcal{O} are SMEFT operators in the X^3 and $\phi^2 X^2$ classes. The cut-off scale of the theory is

Table 6.1: Operators of the X^3 and $\phi^2 X^2$ classes, along with their matched WCs obtained by integrating out the heavy VLL of Eq. (6.15). For simpler expressions, the WCs (\mathcal{C}_i) do not include the $(16\pi^2 m^2)^{-1}$ factor.

Operators	Operator Structures	Wilson coefficients (\mathcal{C}_i)
$\mathcal{O}_{\phi\tilde{B}}$	$(\Phi^\dagger\Phi)\tilde{B}_{\mu\nu}B^{\mu\nu}$	$-4g_Y^2\text{Im}\left[y_{\chi_L}y_{\chi_R}^*\right]$
$\mathcal{O}_{\phi\tilde{W}}$	$(\Phi^\dagger\Phi)\tilde{W}_{\mu\nu}{}^IW^{I,\mu\nu}$	$-g_W^2\text{Im}\left[y_{\chi_L}y_{\chi_R}^*\right]$
$\mathcal{O}_{\phi\tilde{W}B}$	$\frac{1}{2}(\Phi^\dagger\tau^I\Phi)\tilde{W}_{\mu\nu}{}^IB^{\mu\nu}$	$-\frac{10}{3}g_Wg_Y\text{Im}\left[y_{\chi_L}y_{\chi_R}^*\right]$
$\mathcal{O}_{\phi B}$	$(\Phi^\dagger\Phi)B_{\mu\nu}B^{\mu\nu}$	$\frac{1}{60}g_Y^2\left[19 \alpha_\chi ^2+15 \beta_\chi ^2\right]$
$\mathcal{O}_{\phi W}$	$(\Phi^\dagger\Phi)W_{\mu\nu}{}^IW^{I,\mu\nu}$	$\frac{1}{6}g_W^2\left[\alpha_\chi ^2+ \beta_\chi ^2\right]$
$\mathcal{O}_{\phi WB}$	$\frac{1}{2}(\Phi^\dagger\tau^I\Phi)W_{\mu\nu}{}^IB^{\mu\nu}$	$\frac{2}{15}g_Wg_Y\left[6 \alpha_\chi ^2+5 \beta_\chi ^2\right]$
\mathcal{O}_W	$\epsilon^{IJK}W_\mu^{I\nu}W_\nu^{J\rho}W_\rho^{K\mu}$	$\frac{7}{180}g_W^3$

Table 6.2: Dimension-eight CP violating operators of the $\phi^4 X^2$ class and their WCs. The operator structures are from Ref. [345].

Operators	Operator Structures	Wilson coefficients (\mathcal{C}_i) $\times (16\pi^2 m^4)^{-1}$
$\mathcal{O}_{B^2\phi^4}^{(2)}$	$(\Phi^\dagger\Phi)^2\tilde{B}_{\mu\nu}B^{\mu\nu}$	$-\frac{5}{3}g_Y^2\left[\alpha_\chi ^2-2 \beta_\chi ^2\right]\text{Im}\left[y_{\chi_L}y_{\chi_R}^*\right]$
$\mathcal{O}_{W^2\phi^4}^{(2)}$	$(\Phi^\dagger\Phi)^2\tilde{W}_{\mu\nu}{}^IW^{I,\mu\nu}$	$-\frac{1}{10}g_W^2\left[2 \alpha_\chi ^2-5 \beta_\chi ^2\right]\text{Im}\left[y_{\chi_L}y_{\chi_R}^*\right]$
$\mathcal{O}_{WB\phi^4}^{(2)}$	$\frac{1}{2}(\Phi^\dagger\Phi)(\Phi^\dagger\tau^I\Phi)\tilde{W}^{I,\mu\nu}B_{\mu\nu}$	$-\frac{16}{15}g_Wg_Y\left[\alpha_\chi ^2-5 \beta_\chi ^2\right]\text{Im}\left[y_{\chi_L}y_{\chi_R}^*\right]$

the mass $m = m_{\chi_2} = m_{\chi_3}$, and operators of the set

$$\{\mathcal{O}_W, \mathcal{O}_{\phi W}, \mathcal{O}_{\phi B}, \mathcal{O}_{\phi WB}\} \cup \{\mathcal{O}_{\phi\tilde{W}}, \mathcal{O}_{\phi\tilde{B}}, \mathcal{O}_{\phi\tilde{W}B}\}. \quad (6.17)$$

are induced after the matching procedure at one-loop level. Integrating out the heavy states is accomplished with the functional methods of Ref. [346] which allows for calculating the WCs. The methods were conveniently implemented in the CODEX [347] package, which allows matching the Wilson coefficients in an automated and efficient way and is used here. The relevant WCs are

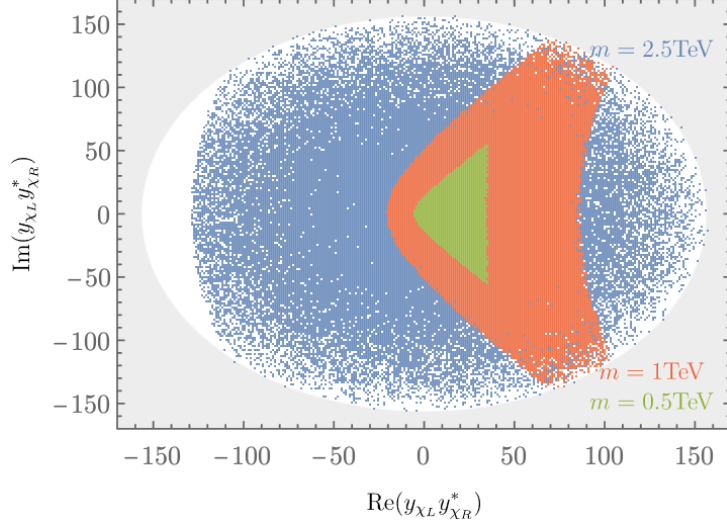


Figure 6.5: Scan over points in the $\text{Re}(y_{\chi_L} y_{\chi_R}^*)$ - $\text{Im}(y_{\chi_L} y_{\chi_R}^*)$ plane for three distinct VLL masses by sampling random values of y_{χ_L} and y_{χ_R} . The absolute values of the ratios in Tab. 6.3 are required to remain less than unity in order to indicate the regions where the leading contributions are sourced by dimension-six operators. The region shaded with gray indicates $|y_{\chi_{L,R}}| > 4\pi$.

Table 6.3: Ratio of dimension-eight and -six WCs.

$\frac{\mathcal{C}_{B^2\phi^4}^{(2)}}{\mathcal{C}_{\phi\bar{B}}} = \frac{\langle\Phi^\dagger\Phi\rangle}{m^2} \times \frac{(-\frac{5}{3} [\alpha_\chi ^2 - 2 \beta_\chi ^2])}{-4} \Big _{\langle\Phi^\dagger\Phi\rangle = \frac{v^2}{2}} = \frac{v^2}{2m^2} \times \frac{5 [\alpha_\chi ^2 - 2 \beta_\chi ^2]}{12}$
$\frac{\mathcal{C}_{W^2\phi^4}^{(2)}}{\mathcal{C}_{\phi\bar{W}}} = \frac{\langle\Phi^\dagger\Phi\rangle}{m^2} \times \frac{(-\frac{1}{10} [2 \alpha_\chi ^2 - 5 \beta_\chi ^2])}{-1} \Big _{\langle\Phi^\dagger\Phi\rangle = \frac{v^2}{2}} = \frac{v^2}{2m^2} \times \frac{[2 \alpha_\chi ^2 - 5 \beta_\chi ^2]}{10}$
$\frac{\mathcal{C}_{WB\phi^4}^{(2)}}{\mathcal{C}_{\phi\bar{W}B}} = \frac{\langle\Phi^\dagger\Phi\rangle}{m^2} \times \frac{(-\frac{16}{15} [\alpha_\chi ^2 - 5 \beta_\chi ^2])}{-\frac{10}{3}} \Big _{\langle\Phi^\dagger\Phi\rangle = \frac{v^2}{2}} = \frac{v^2}{2m^2} \times \frac{8 [\alpha_\chi ^2 - 5 \beta_\chi ^2]}{25}$

tabulated in Tab. 6.1 after the redefinitions

$$\alpha_\chi = \frac{y_{\chi_R} + y_{\chi_L}}{2}, \quad \text{and} \quad \beta_\chi = \frac{y_{\chi_R} - y_{\chi_L}}{2}. \quad (6.18)$$

It is necessary to take the left (y_{χ_L}) and right (y_{χ_R}) chiral couplings to be distinct in order to induce the operators that violate CP since the WCs are related to their difference.

Having motivated that the $\mathcal{O}_{\widetilde{W}}$ operator does not arise at one-loop, one needs to go to higher orders to generate it. This is shown schematically in Fig. 6.4 where the dimension-six $\mathcal{O}_{\widetilde{W}}$ is generated at two-loops. It is possible, though, to induce higher dimension operators at one-loop as, for example, operators of the dimension-eight $\phi^2 X^3$ class after fixing the scalar legs to the VEV. Three such operators violate CP and are shown in Tab. 6.2. It is necessary to identify regions where these higher orders are suppressed in order to show when it is possible to exclude these. The ratio of their contributions when compared to dimension-six after the SM Higgs acquires the VEV v is shown in Tab. 6.3 and in Fig. 6.5 a scan is performed over y_{χ_L} and y_{χ_R} . For a heavy VLL with mass $m \gtrsim 2.7$ TeV and perturbative values of couplings, dimension-six operators dominate, while for smaller masses, this depends on the value of $\text{Re}(y_{\chi_L} y_{\chi_R}^*)$. It should be noted that only the perturbativity of the couplings determines the validity of the dimension-six approach when the masses are large.

6.4 Minimal Fit of CP violation

Having seen that $C_{\widetilde{W}}$ only appears through matching at two-loops in certain realistic extensions of the SM that produce CP violation, the dominant effects of CP violation related to electroweak interactions should be captured only by $\mathcal{O}_{\phi\widetilde{W}B}$, $\mathcal{O}_{\phi\widetilde{W}}$ and $\mathcal{O}_{\phi\widetilde{B}}$. These operators would alter the $\Delta\phi_{ij}$ distributions in electroweak Higgs channels such as WBF [104, 348–351] which will be the focus of this section, aiming to identify a minimal set of observables that can collectively constrain all the other interactions. The WBF channel has reduced background contamination compared to gluon fusion and is characterised by two back-to-back jets and a rapidity gap [352–355]. The statistical techniques described in Sec. 6.2.1 are also used to obtain contours for WBF.

6.4.1 WBF selection and cuts

In general, the Higgs decays dominantly to a b -quark pair; however, it is known that due to the difficult combinatorics involved in the final state, it often yields a decreased sensitivity compared to other decay channels [356, 357]. It is therefore often essential to turn to other decay modes such as $h \rightarrow 4\ell$ [358] or $h \rightarrow \tau\tau$ [359–361] and in this section focus is on the latter. Events are generated at the MC-truth level with the same toolchain as before with a total decay width of the 125 GeV Higgs set to $\Gamma_H = 4.2$ MeV.

For selecting events, there should be two or more jets with transverse momentum $p_T > 25$ GeV and separated in rapidity by $\Delta y_{jj} > 2.8$. The search region is further restricted by imposing a

cut on the invariant mass $m_{jj} > 800$ GeV.

Samples are generated with the Higgs decayed to taus, $pp \rightarrow (h \rightarrow \tau\bar{\tau})jj$ and without decaying the Higgs (i.e. $pp \rightarrow hjj$) using the jet cuts described above. For the former sample, exactly two leptons tagged as taus with separation between them of $\Delta R > 0.4$ are additionally required. The event is vetoed unless both taus satisfy $p_T(\tau) > 40$ GeV and the pair has an invariant mass of 125 ± 10 GeV. The tagged taus are assumed to decay purely hadronically with a branching ratio of $\text{BR}(\tau \rightarrow \text{hadrons}) = 0.65$ and a tagging efficiency of 0.85. The Higgs identification efficiency can then be defined as the ratio of cross sections

$$\epsilon_h = \frac{\sigma(pp \rightarrow (h \rightarrow \tau\bar{\tau})jj)}{\sigma(pp \rightarrow hjj)}, \quad (6.19)$$

which is calculated at $\epsilon_h = 1.03\%$ ⁷.

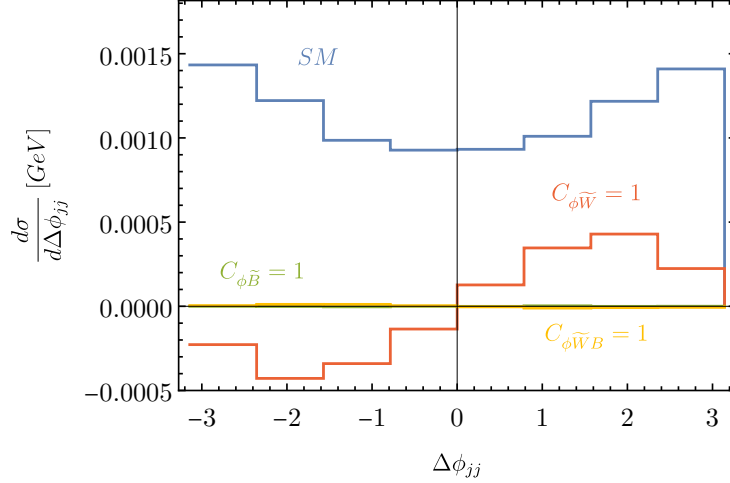


Figure 6.6: Example histogram for the WBF process showing the SM contribution and the effect of introducing further operators.

6.4.2 Combined WBF & Diboson Results

The $\Delta\phi_{jj}$ distribution for different WC values can be obtained (see for example Fig. 6.6), and the exclusion contours at a luminosity of 3/ab are shown in Fig. 6.7. Diboson and WBF manage to effectively constrain the $C_{\phi\widetilde{W}B}$ and $C_{\phi\widetilde{W}}$ coefficients, respectively, while $C_{\phi\widetilde{B}}$ is considerably

⁷This includes the branching ratio of the Higgs to tau leptons along with the effect of cuts and tagging efficiencies of taus.

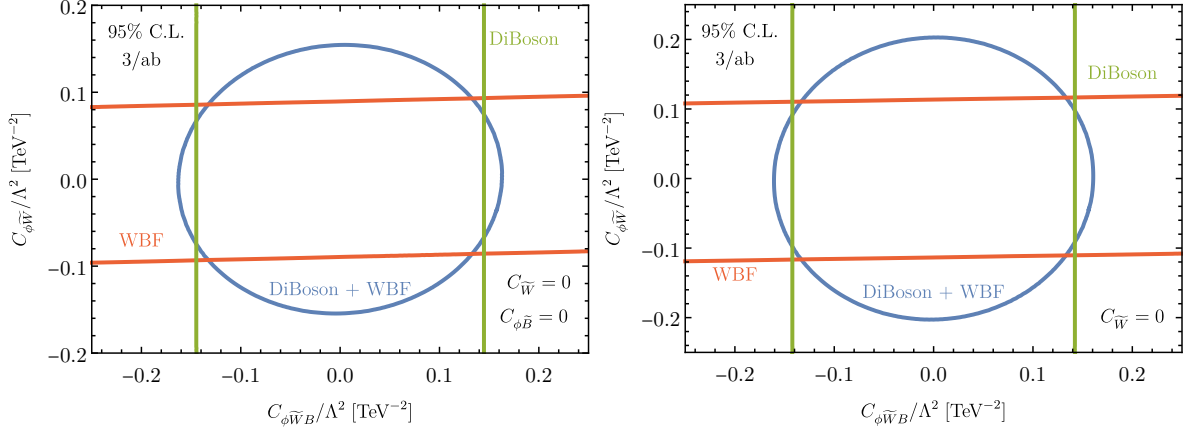


Figure 6.7: Contours for the combined WBF and diboson analyses at 3/ab. On the left, $C_{\widetilde{W}}$ and $C_{\phi\widetilde{B}}$ are fixed to zero, while on the right, only $C_{\widetilde{W}} = 0$ is fixed, and profiling is performed over $C_{\phi\widetilde{B}}$.

harder to exclude. By profiling over $C_{\phi\widetilde{B}}$ it can be seen that the analysis is not too limited by this WC. However, the inclusion of more electroweak Higgs channels such as $h \rightarrow ZZ \rightarrow 4\ell$ and $h \rightarrow \gamma\gamma$ critically enhances the sensitivity providing bounds on all relevant operators as shown by Ref. [362]. Nevertheless, the Higgs channels combined with the diboson data can provide an inclusive picture regarding CP violation. In concrete UV models, $C_{\phi\widetilde{W}}$ and $C_{\phi\widetilde{W}B}$ are correlated with $C_{\phi\widetilde{B}}$ because of the gauge representation and obtaining bounds on the former will suffice to constrain the model's parameter space.

A notable assumption of this analysis is that higher order deformations are insignificant compared to the dimension-six operators, as no contributions from dimension-eight were included in this analysis. This drawback is addressed by the comparison of dimension-six and -eight through matching calculations of BSM scenarios in Sec 6.3. For a heavy VLL, the constraints obtained are for WC values that the suppression of dimension-eight is indeed a reasonable assumption. For $m = 1$ TeV which is outside the coverage of the LHC (see for example Ref. [363]), the points of Fig. 6.5 would correspond to WCs of values $|C_{\phi\widetilde{B}}| \lesssim 0.4$, $|C_{\phi\widetilde{W}}| \lesssim 0.4$ and $|C_{\phi\widetilde{W}B}| \lesssim 0.6$.

6.5 Conclusions

While the SM provides sources of CP violation, these are insufficient to explain baryogenesis, implying that additional sources must arise from new physics. Searches of CP violation in various

channels are thus an integral part of the high-energy experimental programme and also for phenomenological studies. The gauge-Higgs sector might indicate CP violation as hinted by ATLAS [329]. On the one hand, it was shown that diboson analyses and particularly the critical $W\gamma$ channel, could scrutinise the excess due to the sensitivity in the $\mathcal{O}_{\phi\widetilde{W}B}$ direction. This will allow further understanding of whether the excess is merely a statistical fluctuation or actual evidence of CP violation arising from new physics.

On the other hand, alternative ways can be explored to reduce the relevant number of CP violating operators, enabling the possibility of a minimal fit for CP violation. Matching EFT to UV models will lead to hierarchical WC structures dependent on the symmetries and particles included. Following a top-down approach, dimension-six interactions are studied through one-loop matching. Conclusions show that in most concrete scenarios, the $\mathcal{O}_{\widetilde{W}}$ operator is either absent or two-loop suppressed. With heavy scalar extensions unable to generate the operator, one needs at least two heavy vector-like fermions to induce the triple field strength operator from the CP violating Yukawa couplings. Hence, it is possible to quantify the size of CP violation from electroweak physics by combining diboson and Higgs analyses. Omitting the $\mathcal{O}_{\widetilde{W}}$ operator is critical to constrain the rest of the dimension-six operators efficiently.

Remaining in a similar mindset, the next Chapter focuses on a different excess, the muon's anomalous magnetic moment, attempting to investigate how it can be scrutinised by additional processes at colliders.

Chapter 7

Implications of the muon anomalous magnetic moment for the LHC and MUonE

7.1 Introduction

The last shortcoming of the SM under consideration is the anomaly arising from the muon's magnetic moment, as measured by Fermilab/BNL (see Eq. (2.59)). With $F_{\mu\nu}$ denoting the Faraday tensor, anomalous magnetic moments can arise from the dimension-six operator $\bar{f}_L \sigma^{\mu\nu} f_R F_{\mu\nu}$ (and its Hermitian conjugate), indicating the direct sensitivity of Δa_μ to new interactions introduced by renormalisable field theories, while not playing a significant role in probing their defining parameters. This is part of the reason why the Δa_μ has received tremendous interest from the BSM community due to its ability to precisely constrain the structure of concrete SM extensions (for a review, see [364]).

Similarly to the previous Chapter, however, it is possible to interpret the measurement in terms of EFTs, particularly the SMEFT framework. There has been a series of such explorations [365–368] during the last few years by the community. This can have a crucial role in understanding the new physics behind Δa_μ , similar to how the 4-Fermi theory was historically necessary for the correct perception of the weak scale. Measuring the muon lifetime allowed constraining the cut-off of the low-energy theory, which gives rise to an upper limit on a fundamental mass scale (i.e. the

W mass). In the SM, the UV completing degrees of freedom of Fermi's model can be given in units of its cut-off as

$$\frac{m}{\Lambda} = \sqrt{G_F m_W^2} \simeq 0.27 \ll 1, \quad (7.1)$$

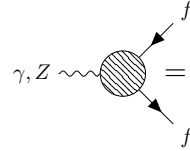
indicating that new physics can appear at relatively low scales compared to the cut-off. Motivated by this, one can anticipate that a similar situation can apply when considering Δa_μ in an effective theory for energy scales above the muon mass. Ref. [366] showed that by combining unitarity constraints and scale evolution, the new physics scale could be pushed to large values, considerably larger than what could be probed by next-generation colliders. In other words, perturbative unitarity violation leads to a No-Lose theorem corresponding to the anomalous magnetic moment far beyond the experiments' reach. Therefore, one can raise the question of whether a_μ can just fix one parameter in SMEFT without any significant implications for new physics. In Ref. [367], Δa_μ was obtained in SMEFT with higher order corrections through evolving $g - 2$ from Low Energy Effective Theory (LEFT), including flavour-violating operators, acquiring results consistent with Ref. [365].

The anomalous magnetic moment is revisited in this Chapter, calculating it in SMEFT at one-loop (based on the results of Refs. [145, 369]), with the aim to correlate a_μ with future measurements¹ of HL-LHC and MUonE [375], a future experiment attempting to specifically measure the contributions to a_μ from hadronic effects. In Sec. 7.2 the calculation of a_μ in SMEFT is described. The impact of higher orders at various scales is discussed in Sec. 7.2.1 and the possibility that Δa_μ arises due to radiative corrections from dimension-six operators in Sec. 7.2.2. Subsequently, Sec. 7.3 focuses on scrutinising the result with decays of the Z boson, the $h \rightarrow \mu\mu\gamma$ channel at HL-LHC and the MUonE experiment, before concluding in Sec. 7.4.

7.2 Δa_μ in SMEFT

Due to the Lorentz and gauge symmetries, the vertex for a vector boson coupled to a fermion such as the muon can be parameterised as

¹ a_μ has also been correlated with additional modes in new physics models, e.g. Refs. [370–374].



$$= -ieQ_f \bar{u}(p') \left[\gamma^\mu F_1(k^2) + i \frac{\sigma^{\mu\nu} k_\nu}{2m_f} F_2(k^2) + \frac{\sigma^{\mu\nu} k_\nu}{2m_f} \gamma_5 F_3(k^2) \right] u(p), \quad (7.2)$$

where the momentum of the vector boson is denoted by $k = p' - p$ and, as before, $\sigma_{\mu\nu} = i[\gamma_\mu, \gamma_\nu]/2$ are the Lorentz generators. Using a renormalisation condition $F_1(0) = 1$, the F_1 form factor at zero momentum transfer with on-shell fermion legs renormalises the electric charge e , while the second form factor defines the anomalous magnetic moment of the muon through $a_\mu = F_2(0)$. The parity-violating F_3 is related to the electric dipole moment. In principle, the anapole contribution of the form $F_4(k^2 \gamma^\mu - k^\mu \not{k}) \gamma^5$ appears in the brackets, which, nonetheless, is only relevant for virtual photons. More importantly, this contribution is unphysical (see Ref. [376]) and is therefore neglected for the rest of this Chapter.

The SMEFT Lagrangian truncated at dimension-six, is modelled by the SMEFTFR [145, 369] package in the Warsaw basis [139], with Feynman rules for the pertinent effective interactions acquired with the use of FEYNRULES [58, 59]. By interfacing the model with FEYNARTS [192] it is feasible to enumerate relevant diagrams for particular amplitudes and subsequently calculate them at one-loop order with FORMCALC [76]. As usual, reduced Passarino-Veltman functions [82] (see also Ref. [377]), appear in the calculations which can be evaluated analytically using PACKAGEX [378]. In order to obtain the form factors of Eq. (7.2) from FORMCALC amplitudes, the Gordon identities (see for example Ref. [379])

$$\bar{u}(p_1)(p_1 + p_2)^\mu u(p_2) = 2m_f \bar{u}(p_1) \gamma^\mu u(p_2) + i \bar{u}(p_1) \sigma^{\mu\nu} (p_2 - p_1)_\nu u(p_2), \quad (7.3)$$

$$\bar{u}(p_1)(p_1 + p_2)^\mu \gamma^5 u(p_2) = i \bar{u}(p_1) \sigma^{\mu\nu} (p_2 - p_1)_\nu \gamma^5 u(p_2), \quad (7.4)$$

can be used with the spinors on-shell. Evaluating the anomalous magnetic moment for the case of QED, contributions appear only at one-loop, and the a_μ reduces to the well-known result $a_\mu = \alpha/(2\pi)$ which was first calculated by Schwinger [380].

Just like in QED, there is no tree level contribution for the SM theory as well. In contrast, such contributions are induced when one considers SMEFT due to the operators (see Refs. [141,

146])

$$\begin{aligned}\mathcal{O}_{eB}^{f_1 f_2} &= (\bar{L}_{f_1} \sigma^{\mu\nu} \ell_{f_2}) \Phi B_{\mu\nu} , \\ \mathcal{O}_{eW}^{f_1 f_2} &= (\bar{L}_{f_1} \sigma^{\mu\nu} \ell_{f_2}) \tau^I \Phi W_{\mu\nu}^I ,\end{aligned}\tag{7.5}$$

constructed by the left- (L) and right-handed (ℓ) lepton fields and the field strength tensors $B_{\mu\nu}$ and $W_{\mu\nu}^I$ of the $U(1)$ and $SU(2)$ gauge groups respectively. The same notation as before is used, where Pauli matrices are written as τ^I and Φ represents the Higgs doublet field. Assuming minimum flavour violation, only diagonal entries of the operators are considered, and henceforth, the flavour indices will be suppressed.

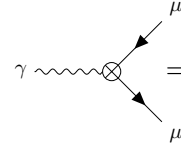
The two dimension-six operators induce the contribution to the anomalous magnetic moment given by

$$\Delta a_\mu^{\text{tree}} = \frac{\sqrt{2} v m_\mu}{e \Lambda^2} \left[c_W (C_{eB} + C_{eB}^*) - s_W (C_{eW} + C_{eW}^*) \right].\tag{7.6}$$

If one assumes that the WCs C_{eW} and C_{eB} are purely real, the contribution to the F_3 form factor (and thus the electric dipole moment) is removed, conserving parity in the theory. These assumptions lead to a modification of only a_μ , along with minor corrections that arise from electroweak contributions.

In the SM, no UV divergence relevant to the F_2 or the F_3 form factors arises, and only F_1 is used to define the renormalised electric charge in the Thomson limit. However, the additional SMEFT operators induce further divergences [146–148] and require the inclusion of extra renormalisation constants in order to extend the calculation to one-loop. The tree level contributions of Eq. (7.6) induce the additional counterterms δC_{eB} and δC_{eW} that allow the removal of divergences. Taking into consideration the UV divergent parts of both the $\gamma\mu\mu$ and $Z\mu\mu$ vertices (alongside the renormalisation of $Z - \gamma$ mixing), dimensional regularisation can be used in $d = 4 - 2\epsilon$ dimensions to subtract them in the $\overline{\text{MS}}$ scheme.

The introduction of the SM counterterms in the Lagrangian and δC_{eB} , δC_{eW} induces counterterm amplitudes and, using the Gordon identities (7.3), the factors related to different Lorentz structures can be projected out as before. This introduces the counterterm vertex



$$= -ieQ_\mu \bar{u}(p') \left[i \frac{\sigma^{\mu\nu} k_\nu}{2m_f} \delta F_2 + \frac{\sigma^{\mu\nu} k_\nu}{2m_f} \gamma_5 (i \delta F_3) \right] u(p), \quad (7.7)$$

where the factors δF_2 (δF_3) renormalise the Lorentz structure corresponding to the form factor F_2 (F_3). A factor of i multiplying δF_3 is included just for convenience, and as in the SM, F_1 is renormalised such that it corresponds to the correct electric charge²; thus, relevant divergences are not taken into consideration. δF_2 and δF_3 can be re-expressed in terms of SM couplings and renormalisation constants (see Ref. [175]), as well as the introduced δC_{eB} and δC_{eW} counterterms of the \mathcal{O}_{eB} and \mathcal{O}_{eW} interactions, as

$$\delta F_{2,3} = \frac{m_\mu}{\sqrt{2}e\Lambda^2} \left[C_{eB} K_1 \pm C_{eB}^* K_1' + C_{eW} K_2 \pm C_{eW}^* K_2' + 2c_W v (\delta C_{eB} \pm \delta C_{eB}^*) \right. \\ \left. - 2s_W v (\delta C_{eW} \pm \delta C_{eW}^*) \right], \quad (7.8)$$

$$K_1 = 2c_W \delta v + c_W v (\delta Z_{AA} + \delta Z_L^{\mu\mu,*} + \delta Z_R^{\mu\mu}) + v (2\delta c_W - s_W \delta Z_{ZA}),$$

$$K_2 = -2s_W \delta v - s_W v (\delta Z_{AA} + \delta Z_L^{\mu\mu,*} + \delta Z_R^{\mu\mu}) - v (2\delta s_W + c_W \delta Z_{ZA}).$$

The primed counterterms correspond to $\delta Z_L^{\mu\mu,*} \rightarrow \delta Z_L^{\mu\mu}$ and $\delta Z_R^{\mu\mu} \rightarrow \delta Z_R^{\mu\mu,*}$. The SM counterterms are calculated as in Ref. [175], while the choice of scheme for the VEV renormalisation can lead to differences. The Higgs potential in SMEFT is given as in the SM by Eq. (3.6) and is minimised through the choice $t = 0$. This induces tadpole diagrams that capture the shift away from the classical Higgs field value due to higher orders and are removed by introducing the counterterm of Eq. (3.9). The VEV is expressed as a function of the electromagnetic coupling, the Weinberg angle and the W mass, identifying

$$\frac{\delta v}{v} = \frac{\delta M_W^2}{2M_W^2} + \frac{\delta s_W}{s_W} - \delta Z_e. \quad (7.9)$$

with δM_W^2 , δs_W and δZ_e denoting the counterterms of M_W^2 , s_W and e in the same conventions as [175]. It should be noted that other schemes such as the Fleischer-Jegerlehner scheme [381]

²It should be noted that the electric charge is also shifted due to the $C_{\phi WB}$, but this operator will not be under consideration.

WC ($/\Lambda^2$)	Fermilab/BNL allowed [$1/\text{TeV}^2$]	SM allowed [$1/\text{TeV}^2$]
C_{eB}	$[8.21 \times 10^{-6}, 1.33 \times 10^{-5}]$	$[-1.84 \times 10^{-6}, 1.84 \times 10^{-6}]$
C_{eW}	$[-1.41 \times 10^{-5}, -2.27 \times 10^{-5}]$	$[3.15 \times 10^{-6}, -3.15 \times 10^{-6}]$
C_W	$[14.00, 22.60]$	$[-3.14, 3.14]$
$C_{\phi B}$	$[0.36, 0.58]$	$[-0.08, 0.08]$
$C_{\phi W}$	$[1.06, 1.71]$	$[-0.24, 0.24]$
$C_{\phi e}$	$[7.92, 12.80]$	$[-1.77, 1.77]$
$C_{\phi l}^{(1)}$	$[-8.27, -13.40]$	$[1.85, -1.85]$
$C_{\phi l}^{(3)}$	$[-8.27, -13.40]$	$[1.85, -1.85]$
C_{le}	$[-1.69, -2.72]$	$[0.38, -0.38]$

Table 7.1: Intervals on WCs (units of TeV^{-2}) for Δa_μ lying within the Fermilab/BNL measurement and for remaining within the errors of the SM prediction given in Ref. [136], using $\mu = m_\mu$. Only bounds with values $\lesssim 4\pi/\text{TeV}^2$ are shown.

(which shifts the bare vacuum expectation value by $\Delta v = -\delta t/m_H^2$; see also Refs. [176, 382]) can result in large corrections from the tadpole diagrams in renormalised quantities [383–385]. This leaves only δC_{eB} , δC_{eW} and their conjugated quantities unevaluated.

Due to the presence of two independent dimension-six operators giving contributions to the anomalous magnetic moment, the calculation is also repeated for the $Z\mu\mu$ vertex using similar counterterm expressions. Requiring that the UV divergences appearing in the F_2 and F_3 form factors for the $\gamma\mu\mu$ vertex and the corresponding ones for $Z\mu\mu$ are cancelled identically in the $\overline{\text{MS}}$ scheme enables the determination of δC_{eB} and δC_{eW} .³ Hence, only finite terms remain in the final expressions.

³Let $F_{2,3}^Z$ denote the form factors with the same Lorentz structures as $F_{2,3}$ but for the $Z\mu\mu$ vertex. The counterterms in the Lagrangian additionally give rise to $\delta F_{2,3}^Z$ similarly to the $\gamma\mu\mu$ vertex, with the only differences arising from the rotation of B_μ and W_μ^3 to Z_μ and A_μ . $\delta F_{2,3}^Z$ depends on the same counterterms as $\delta F_{2,3}$. By treating δC_{eB}^* and δC_{eW}^* as distinct variables and solving simultaneously the system

$$\begin{aligned} F_{2,3} \Big|_{\text{UV}} + \delta F_{2,3} &= 0, \\ F_{2,3}^Z \Big|_{\text{UV}} + \delta F_{2,3}^Z &= 0, \end{aligned}$$

the expressions for δC_{eB} , δC_{eW} , δC_{eB}^* and δC_{eW}^* are obtained and, as a check, it is verified that indeed δC_{eB}^* and δC_{eW}^* are the corresponding conjugated variables as expected.

The discussion of the anomalous magnetic moment in this Chapter neglects semileptonic operators of the four-fermion classes $(\bar{L}R)(\bar{R}L)$ and $(\bar{L}R)(\bar{L}R)$, which is often enforced through imposing flavour symmetries (e.g. [284, 291] for similar assumptions in the top-sector). The general case without such flavour restriction is provided by Ref. [367] and it should be noted that the semileptonic \mathcal{O}_{lequ} operators could contribute to the anomalous magnetic moment when included. Their effects have been studied extensively in the context of leptoquarks [371, 386, 387] that can generate the structure of the operator [388].

As the aim is to identify operators with significant corrections that can produce a deviation in the SM anomalous magnetic moment and push it to large values closer to the Fermilab result, it is convenient to impose certain additional assumptions on the operators that are included in the calculation. The focus is on CP conserving operators providing an explanation to the muon $g - 2$ with real WCs (this also eliminates the electric dipole moment, which requires parity-violating, imaginary WCs). Furthermore, the two operators related to oblique corrections through

$$S = \frac{16\pi v^2}{g_1 g_2} \frac{C_{\phi WB}}{\Lambda^2}, \quad T = -2\pi v^2 \left(\frac{1}{g_1^2} + \frac{1}{g_2^2} \right) \frac{C_{\phi D}}{\Lambda^2}, \quad (7.10)$$

are also not included as they can be efficiently constrained or even regarded as input to the theory. Using a renormalisation scale of $\mu = m_\mu$ as the scale suitable for the measurement of the anomalous magnetic moment, the constraints by reinterpretation of the Fermilab result are tabulated in Tab. 7.1. As evident from the table, only a handful of these are meaningful in the sense of perturbative expansion. The results are cross-checked with Ref. [367] that calculated the anomalous magnetic moment from RGE considerations, using their quoted scales, and we find good agreement given the different approaches.

7.2.1 UV divergent operators: a_μ as input parameter

Out of the contributing operators within the assumptions, only C_{eB} , C_{eW} , $C_{\phi B}$ and $C_{\phi W}$ give rise to divergent parts in the F_2 and F_3 form factors, and thus their contributions depend on the dimensional regularisation scale. While $C_{\phi B}$ and $C_{\phi W}$ can be constrained in a perturbatively meaningful way from the Fermilab measurement, their bounds from other modes at the LHC, mainly Simplified Template Cross Sections and Higgs signal strength measurements, are significantly more restrictive (see for example, Refs. [284, 285]). This does not leave much potential to explain the deviation of the anomalous magnetic moment from the SM through these interactions. On the other hand, C_{eB} and C_{eW} are constrained with very high precision by Fermilab and are

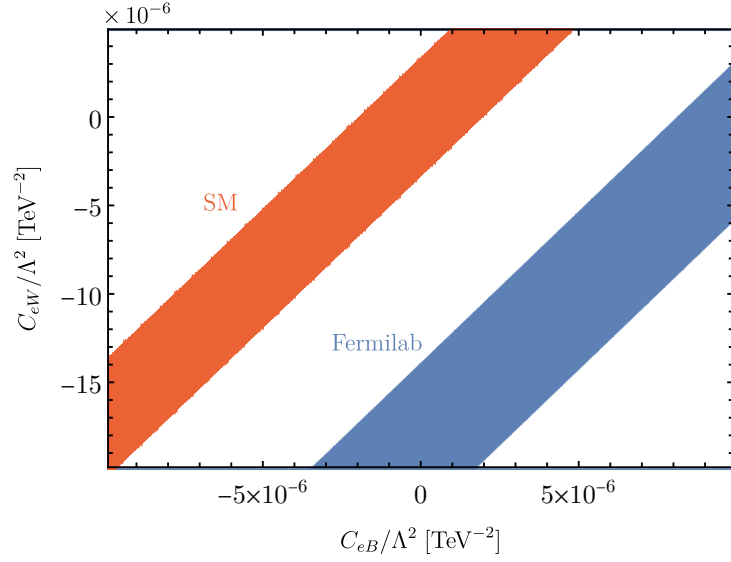


Figure 7.1: Contours for consistency with Fermilab/BNL in the C_{eW} - C_{eB} plane with $\mu = m_\mu$. The remaining WCs are fixed to zero.

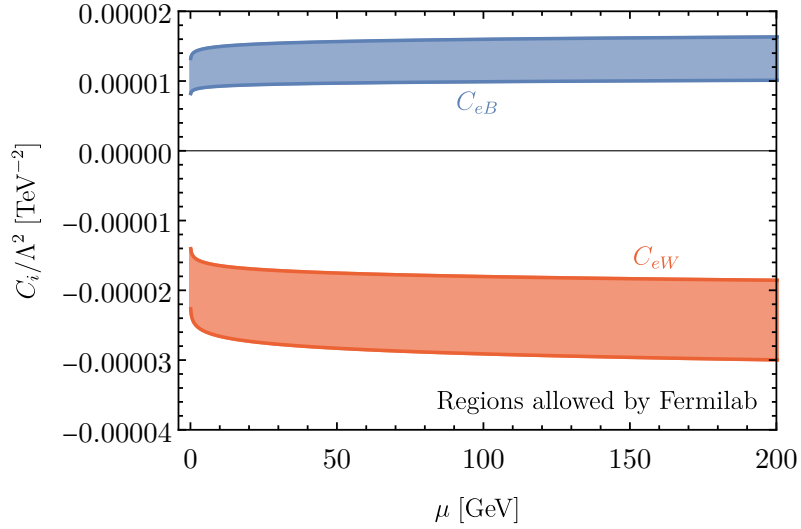


Figure 7.2: Individual intervals allowed by Fermilab/BNL for C_{eB} , C_{eW} as the dimensional regularisation scale μ is varied.

two of the few operators that can provide a viable explanation for the muon $g - 2$ when new physics is manifested at energies around the TeV scale. The allowed contours by the presence of

both operators are shown in Fig. 7.1, and these operators are hard to constrain as shown in the later sections.

Due to the dependence of these two operators on the (unphysical) renormalisation scale μ , the allowed interval for each WC can be considered individually as a function of μ . At $\Lambda = 1$ TeV, this is shown in Fig. 7.2 indicating the shift of the tree level allowed interval from the presence of higher orders at different values of μ .

In order to compare the 1-loop contribution to a_μ with the tree level, the choice of the muon mass is used as μ . The dipole operators can be rotated with

$$\begin{aligned} C_{e\gamma} &= c_W C_{eB} - s_W C_{eW} , \\ C_{eZ} &= s_W C_{eB} + c_W C_{eW} , \end{aligned} \quad (7.11)$$

in order to have $C_{e\gamma}$ as the only contributing WC in the muon $g - 2$ at the tree level. By using $C_{e\gamma}$ along with one further dimension-six operator, it is possible to assess how sizeable the K-factor can be when a_μ is taken to be an input value within the interval given by the Fermilab. The K-factor is defined as the ratio of $C_{e\gamma}$ at NLO that is needed for reproducing a value of Δa_μ , divided by the value $C_{e\gamma}$ when only tree-level contributions are considered. If only $C_{e\gamma}$ is

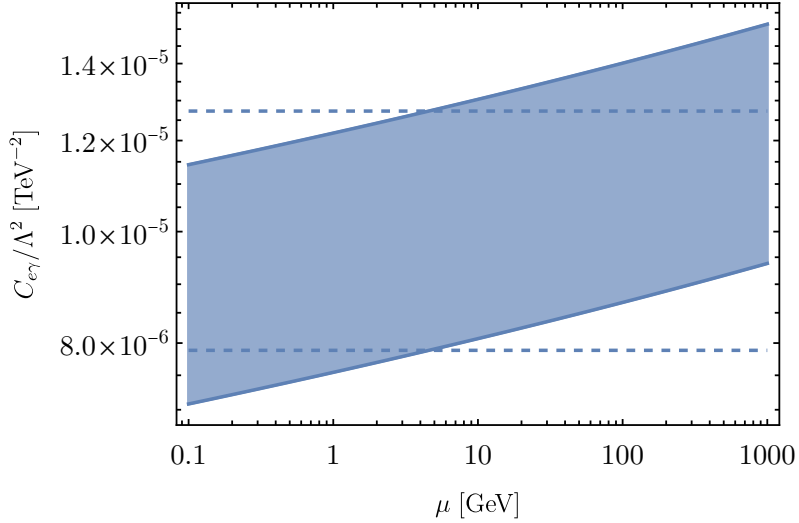


Figure 7.3: The filled interval denotes the individual bound on $C_{e\gamma}$ for consistency with the Fermilab/BNL measurement, including one-loop corrections, as a function of μ . The dashed lines indicate the corresponding interval for only tree level contributions.

considered individually, then the K-factor lies at ~ 0.9 for $\mu = m_\mu$. This increases logarithmically to ~ 1.2 at $\mu \rightarrow \Lambda = 1$ TeV and the dependence of $C_{e\gamma}$ on μ is shown in Fig. 7.3. Nevertheless, in the presence of further SMEFT interactions, the sizeable $g - 2$ can be reproduced without large radiative corrections. As an example, by sampling values of Δa_μ and C_{eZ} , it is shown in Fig. 7.4 that even if C_{eZ} is taken to be of order 10^{-4} the one-loop corrections can be rendered small.

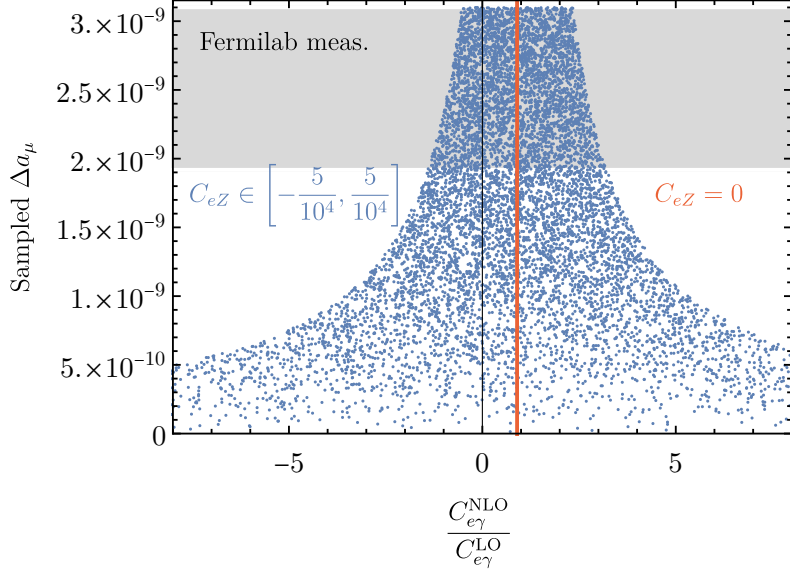


Figure 7.4: Plot showing the shift of the $C_{e\gamma}$ K-factor from the additional presence of C_{eZ} , with the scale fixed at $\mu = m_\mu$. The one-loop corrections can be rendered negligible with small values of C_{eZ} .

A similar procedure can be repeated for all the other contributing SMEFT operators, and the minimum possible K-factor of $C_{e\gamma}$ required for consistency between Δa_μ and the Fermilab measurement can be obtained at different values of the additional WC. This is shown in Fig. 7.5 and indicates how sizeable a second dimension-six operator has to be to cancel the one-loop induced $C_{e\gamma}$ contribution, such that only the tree level remains considerable. The figures show that for most operators, the dipole operator radiative correction will remain substantial unless the additional WC is relatively large. The three exceptions are C_{le} , $C_{\phi W}$ and $C_{\phi B}$ that can induce cancellations rendering the one-loop negligible without approaching the non-perturbative limit.

Regardless of the scheme and scale dependence of a_μ , the main result is that the bounds on the

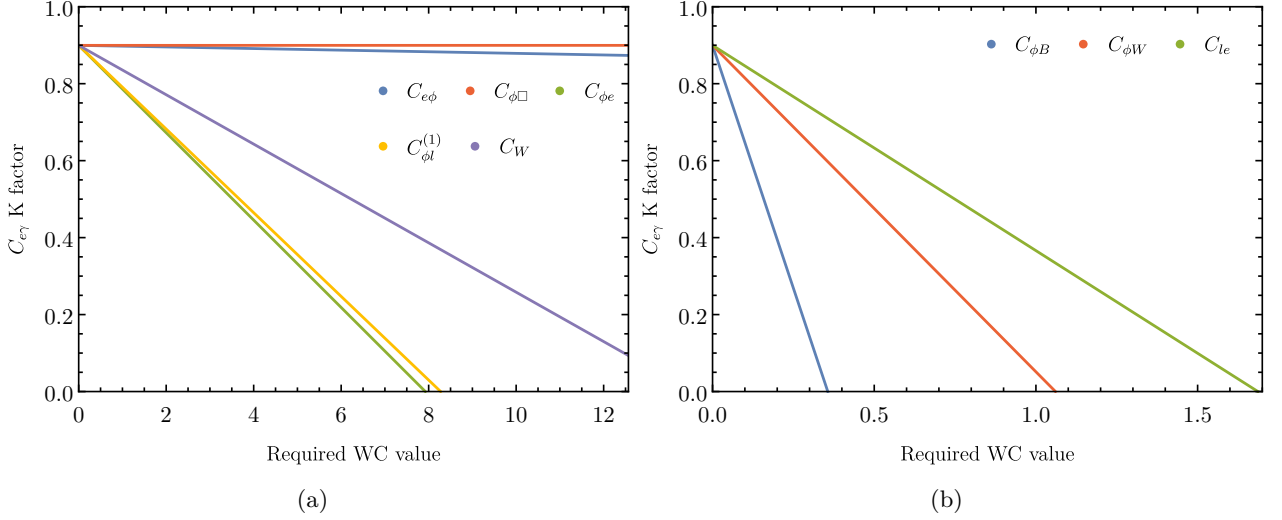


Figure 7.5: Plots showing the minimum possible K-factor for $C_{e\gamma}$ (at $\mu = m_\mu$), keeping the anomalous magnetic moment in agreement with Fermilab/BNL for different values of the additional WC.

dipole operators are significantly constrained raising the question whether other channels could reach a similar precision, which is discussed in Sec. 7.3.

7.2.2 a_μ as a radiative SMEFT effect

The deviation of the muon's anomalous magnetic moment from the SM value can also be interpreted in terms of dimension-six operators that contribute radiatively without inducing UV divergences. Considering each operator individually, $C_{\phi\Box}$, $C_{e\phi}$ and C_W are unable to lift the $g - 2$ to large enough values unless the absolute value of the WC exceeds $4\pi/\text{TeV}^2$. This limit would correspond to a WC value of order one at the electroweak scale of 246 GeV. From the rest of the operators, Electroweak Precision Observables (EWPO) can efficiently constrain $C_{\phi l}^{(1)}$, $C_{\phi l}^{(3)}$ and $C_{\phi e}$ without leaving room to reproduce Δa_μ and keeping consistency. Therefore the only remaining operator that is currently unconstrained and can be of relevance in the muon $g - 2$ explanation is the four-lepton C_{le} operator. This was also concluded in Refs. [365, 367] including the flavour-violating parts of the operator. In the future, lepton colliders will be able to deliver bounds as indicated by Refs. [389, 390].

7.3 Tensioning the dipole operators

As the dipole operators C_{eB} and C_{eW} are poorly constrained in general, several avenues are explored in this section which can potentially provide bounds either with current experimental uncertainties or in the future. In particular, the $Z \rightarrow \mu\mu$ decay is considered, and anticipated to be sensitive to C_{eZ} as well as interactions between the Higgs and muons. While the sensitivity of the $\mu\mu\gamma$ and $\mu\mu Z$ vertices arises when the Higgs doublet is set to its VEV, interactions in the Higgs sector such as the Higgs decay or the $\mu\mu h$ signal strength, are also sensitive and can be linked to the anomalous magnetic moment. The $h \rightarrow \mu\mu\gamma$ process also receives contributions from the dipole operators but with a lower statistical yield. However, this can be remedied by the excellent control of muons and photons at the LHC. Considering further future experiments, the MUonE experiment aiming to measure the hadronic contributions to a_μ in an extremely precise environment can deliver bounds on SMEFT operators. The above channels are considered in the upcoming sections.

7.3.1 Z decay

The Z boson and the photon in the physical basis are obtained through the rotation of the orthogonal fields B_μ and W_μ^3 , which also implies the appearance of C_{eB} and C_{eW} in the $Z\mu\mu$ vertex. Truncating the perturbative expansion at dimension-six only, the relevant part is only the linear contribution caused by the interference of BSM physics with the tree or virtual SM amplitudes. Virtual SMEFT contributions are neglected for this discussion as they do not enhance the relatively poor bounds calculated through this avenue.

Using M_{d6} to denote the tree level SMEFT amplitude and $\mathcal{M}_{SM}^{\text{tree}}$ ($\mathcal{M}_{SM}^{\text{virt}}$) for the tree (one-loop) SM amplitude, it is possible to express the deviation of the $Z \rightarrow \mu\mu$ partial width from the SM

WC ($/\Lambda^2$)	68% C.L bound
$C_{\phi e}$	$[-0.019, 0.019]$
$C_{\phi l}^{(1)}$	$[-0.016, 0.016]$
$C_{\phi l}^{(3)}$	$[-0.016, 0.016]$

Table 7.2: 68% bounds on WCs in units of TeV^{-2} from the Z boson decay. Perturbatively meaningful constraints for the dipole operators could not be obtained.

value with

$$\delta\Gamma_{Z\rightarrow\mu\mu} = \frac{|\vec{p}_1|}{48\pi m_Z^2} \left[2\mathcal{M}_{\text{d6}}^*(\mathcal{M}_{SM}^{\text{tree}} + \mathcal{M}_{SM}^{\text{virt}}) \right], \quad (7.12)$$

after averaging over initial polarisations of the gauge boson and performing the phase space integration. The suitable scale for the one-loop SM diagrams is the Z mass, which is used for the dimensional regularisation scale, $\mu = m_Z$.

According to the Particle Data Group (PDG) [319] the uncertainty on the decay width of $Z \rightarrow \mu\mu$ is 0.18 MeV which can be used to construct a χ^2 of one degree of freedom. Then allowed bounds can be calculated at various confidence levels for each contributing WC using Eq. (5.3). For 68% CL the constraints are shown in Tab. 7.2. However, the dipole operators remain essentially unconstrained as it is not feasible to extract perturbatively meaningful bounds (the absolute value of the WCs divided by Λ^2 can exceed $4\pi/\text{TeV}^2$). The only operators that can be constrained by $Z \rightarrow \mu\mu$ are those of the class $\psi^2\phi^2D$. Similarly to bounds from EWPO, it is again evident that $C_{\phi e}$, $C_{\phi l}^{(1)}$ and $C_{\phi l}^{(2)}$ can not provide a sufficient push to lift the anomalous magnetic moment to the interval expected by Fermilab without losing consistency with other measurements.

7.3.2 $gg \rightarrow h \rightarrow \mu\mu\gamma$ channel

Moving to the Higgs sector, the $h \rightarrow \mu\mu$ decay supplies an avenue for probing the dipole operators. In Ref. [391] this decay was calculated including one-loop effects from dimension-six operators (more details on the calculation are also given in Ref. [385]) and is utilised in this section to investigate whether the $h\mu\mu$ signal strength can provide strong constraints on C_{eW} and C_{eB} . Using their results, the signal strength can be written numerically as

$$\mu = 1 + \frac{\text{TeV}^2}{\Lambda^2} (0.67C_{eW} - 0.19C_{eB}), \quad (7.13)$$

where $\mu = m_h = 125$ GeV. As before, the 68% CL bounds on the WCs can be again acquired by a chi-squared $\chi^2 = (\mu - 1.19)^2/0.35^2$ constructed from the PDG value of the signal strength [319]. At a UV scale of $\Lambda = 1$ TeV, the allowed intervals are $C_{eB} \in [-2.8, 0.8]$ and $C_{eW} \in [0.24, 0.81]$, with sensitivity being still orders of magnitude less than what can be achieved by the anomalous magnetic moment.

Aside from motivated Higgs decays at one-loop, additional s -channel processes with a propagating Higgs depend on the C_{eW} and C_{eB} interactions at tree level and could possibly deliver further tension on the bounds from the muon $g - 2$. These operators appear in the diagram of Fig. 7.6

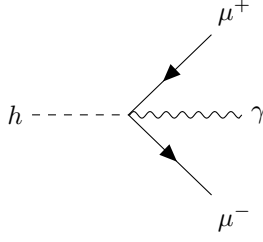


Figure 7.6: Vertex generated by the presence of the operators in Eq. (7.5) and contributing to the decay of the Higgs.

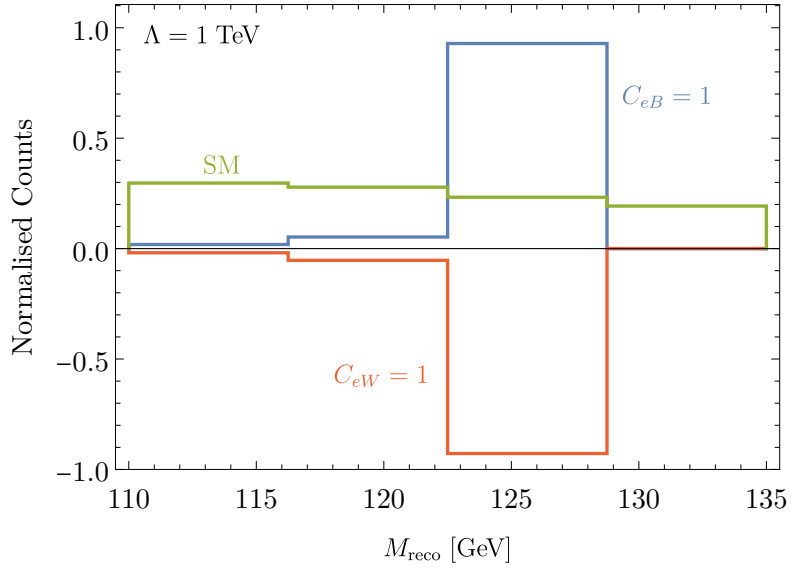


Figure 7.7: Normalised histogram for the reconstructed Higgs mass M_{reco} indicating the different shapes between the pure SM contributions and the interference with effective interactions.

which results in a final state of a hard photon and a muon pair. Since such a process can be produced at the LHC mainly by gluon fusion, the $gg \rightarrow h \rightarrow \mu^+ \mu^- \gamma$ channel is investigated to assess the sensitivity that can be obtained. An analysis inspired by bump-hunting close to the Higgs mass peak is beneficial in this case, as the background processes that arise from the SM will not maintain the same resonant structure characteristics.

For this investigation the SMEFTSIM [312, 313] implementation of the SMEFT interactions is used which incorporates the effective ggh interaction, allowing the modelling of gluon fusion. The

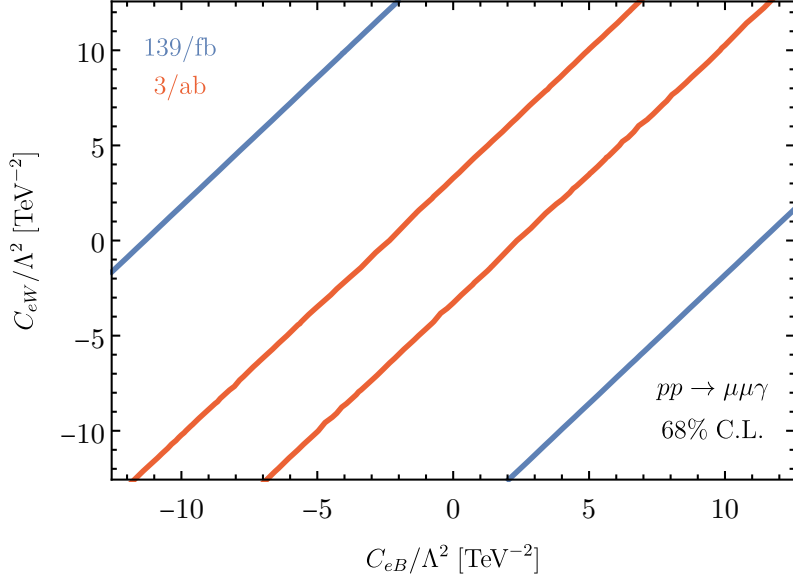


Figure 7.8: Exclusion intervals in the C_{eW} - C_{eB} plane obtained from the $h \rightarrow \mu\mu\gamma$ process.

software chain consists of using the UFO [255] model in MADEVENT [94–96] to generate events. Cuts are imposed on the final state by requiring at least two isolated leptons tagged as muons with transverse momentum $p_T(\mu) > 15$ GeV and pseudorapidity $|\eta(\mu)| < 2.5$ such that they lie in the central part of the detector. Isolation is imposed by summing the transverse momenta of the jets within a separation of $\Delta R = \sqrt{\Delta\phi^2 + \Delta\eta^2} < 0.4$ and requiring that it is less than 50% of the muon’s p_T . At least one photon must be identified in the final state satisfying $p_T(\gamma) > 15$ GeV and $|\eta(\gamma) < 2.5|$. Subsequently, the reconstructed Higgs mass M_{reco} is obtained as the invariant mass of the four momenta sum of the three final states and must lie within $110 \leq M_{\text{reco}} \leq 135$ (in GeV); otherwise, the event is vetoed. This final cut selects a signal region close to the resonant mass of the Higgs, centred at 125 GeV.

The differential cross sections are expressed as before with Eq. (2.66), including only pure-SM interactions and interference between SM and dimension-six operators. Any term suppressed by Λ^{-4} is neglected in this analysis, and an example histogram of the reconstructed Higgs mass is shown in Fig. 7.7. For integrated luminosities of 139/fb and 3/ab, the bounds are shown in Fig. 7.8, acquired by constructing a chi-squared weighted by the SM statistical uncertainty. As evident from the figures, the sensitivity that this process can achieve is once again critically limited compared to the reinterpreted results of the muon $g - 2$.

7.3.3 MUonE

In this Chapter, the motivation was to examine the deviation of the $g-2$ measurement from the SM given by Eq. (2.59) from the BSM perspective and consider the possibility that it arises from new physics. However, it is still likely that this deviation is, in fact, overestimated and could be much less significant if the sizeable hadronic contributions from the SM are actually able to resolve the tension. While these are theoretically calculated with lattice QCD techniques [134, 392–399] there is still currently some disagreement in the community. The MUonE is an alternative experimental approach proposed in order to resolve this by performing a highly accurate measurement of the hadronic contributions. Using the elastic $\mu e \rightarrow \mu e$ scattering (see Fig. 7.9), measurements of the differential cross section $d\sigma/dt$ can be taken, where t is the (negative) four-momentum transfer squared. This allows the measurement of the hadronic contributions to the fine structure constant that can then be related to the relevant $g-2$ contributions. MUonE is designed to operate using a 150 GeV muon beam from CERN to scatter off atomic electrons and is foreseen to reach an integrated luminosity of $L = 1.5 \times 10^7/\text{nb}$ [375]. Tree-level SM diagrams from the electroweak interaction are predicted to result in a cross section of ~ 250 b.

Any deviation from this cross section can be attributed to higher orders from QCD. However, this is not the only possibility, as new physics can lead to contributions affecting the measurements (for example, see Ref. [400]), rendering MUonE a setup that can explore BSM contributions as well. If a heavy new physics particle exists, it will have suppressed impact due to its mass unless it couples to the SM fields with a large coupling in the perturbative sense. Due to the centre-of-mass energy of the experiment, it is most sensitive to relatively light masses coupled directly to the two leptons at tree level.⁴ Nevertheless, in this section, tree level contributions from SMEFT interactions are considered, remaining in the model-independent framework and keeping the minimal flavour violation assumptions discussed before.

Using Eq. (2.66) the $d\sigma/dt$ differential distribution can be expressed linearly in terms of dimension-six coefficients, neglecting Λ^{-4} contributions. Then the unpolarised $d\sigma/dt$ for $\mu^-e^- \rightarrow \mu^-e^-$ can be calculated for the SM with and without the interference from SMEFT operators through

$$\frac{d\sigma}{dt} = \frac{1}{64\pi s |\vec{p}_1|^2} (|\mathcal{M}_{\text{SM}}|^2 + 2\mathcal{M}_{\text{SM}}^* \mathcal{M}_{\text{d6}}) , \quad (7.14)$$

⁴Examples are models with a light scalar or a light gauge boson coupled directly to the electron and the muon at tree level. Models with leptoquarks or heavy right-handed neutrinos are also able to explain the Fermilab measurement but have contributions only at one-loop level. This is detailed in Ref. [400].

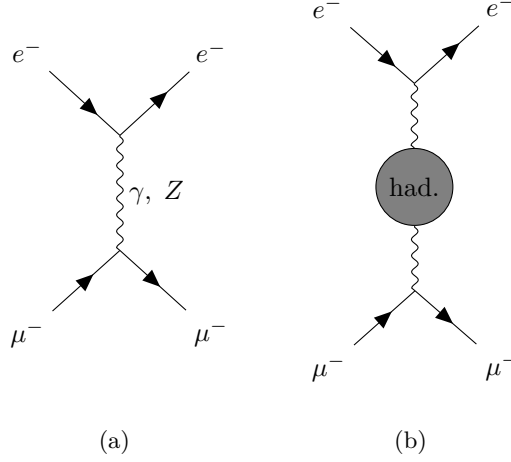


Figure 7.9: Electroweak (a) and hadronic (b) diagrams for different SM t -channel processes contributing to the differential cross section measured by the MUonE experiment.

where \vec{p}_1 is the three-momentum of one of the outgoing particles in the centre-of-mass frame. An example histogram is shown in Fig. 7.10. Following the same statistical methods as previously, the binned $\chi^2 = \sum_i (\delta N_i)^2 / \sigma_i^2$ is constructed, where δN_i denotes the deviation in event counts for bin i from the SM expectation N_i^{SM} . The combination of statistical and systematic uncertainties is denoted as $\sigma_i = \sqrt{\sigma_{\text{stat},i} + \sigma_{\text{syst},i}}$. The target systematic uncertainty anticipated to be achieved by MUonE is $\sigma_{\text{syst},i} = 10^{-5} N_i^{\text{SM}}$ [375] (see also Ref. [400]) and $\sigma_{\text{stat},i} = \sqrt{N_i^{\text{SM}}}$ is used for statistical uncertainties.

The relevant bounds are shown in Tab. 7.3. It should be noted that the WCs $C_{\phi e}$, $C_{\phi l}^{(1)}$ and $C_{\phi l}^{(3)}$ appear in the vertices but meaningful bounds can not be provided as they exceed $4\pi/\text{TeV}^2$. The results show that aside from the Fermilab/BNL experiment, MUonE delivers the most stringent constraints on the dipole operators out of the considered avenues. Unfortunately, the situation is similar: the obtained limits are orders of magnitude worse than the ones from the anomalous magnetic moment.

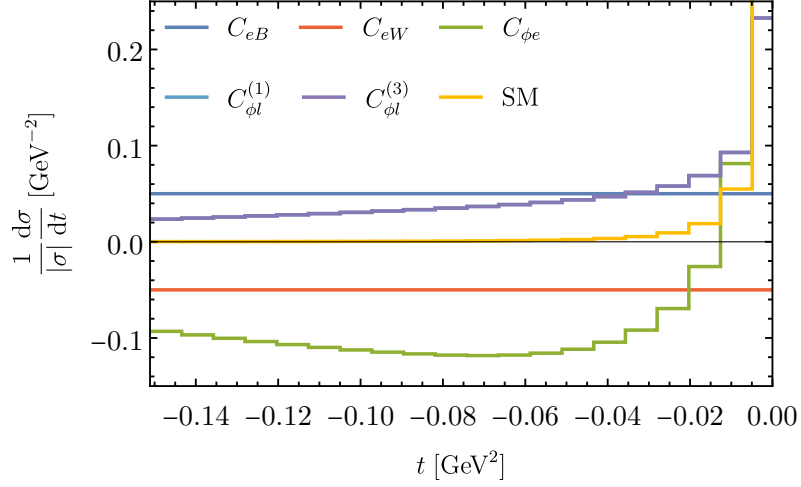


Figure 7.10: Contributions to the $d\sigma/dt$ differential distribution from Λ^{-2} terms when different WCs contribute and for the SM. The dimension-six contributions arise from interference with the SM and only a single WC is included for each case with its value set to +1. The histograms are normalised such that the area under the curve corresponds to ± 1 depending on whether the interference is positive or negative. For the SM, the bin adjacent to zero is ~ 0.9 . Additionally, $C_{\phi\ell}^{(1)}$ and $C_{\phi\ell}^{(3)}$ overlap.

WC ($/\Lambda^2$)	68% CL [$1/\text{TeV}^2$]
C_{eB}	$[-0.21, 0.21]$
C_{eW}	$[-0.39, 0.39]$

Table 7.3: 68% CL individual intervals on WCs from MUonE. When reexpressed, these correspond to $|C_{e\gamma}| \leq 0.18$ and $|C_{eZ}| < 12.75$, and MUonE can not obtain perturbatively meaningful constraints for operators of the $\psi^2\phi^2D$ class.

7.4 Conclusions

The one-loop calculation of the anomalous magnetic moment in SMEFT indicates that significant contributions arise from the dipole operators C_{eW} and C_{eB} , in line with generic results for concrete UV models where new heavy states have to be relatively strongly coupled to the muon. The presence of additional operators can lead to cancellations at the one-loop level only when the WCs are sizeable, with the exceptions of $C_{\phi B}$, $C_{\phi W}$ and C_{le} . Individual considerations of operators one by one can only solve the muon $g - 2$ anomaly when the dipole operators or C_{le} are included, in

line with previous results of Refs. [365, 367]. Therefore, the probable new physics at high-energy scales that can explain the Fermilab/BNL measurements are severely limited.

Assuming that the new physics couples directly to the muon, several avenues are explored in order to assess the effect of the dipole operators and evaluate whether they can be scrutinised by reaching a precision comparable to the Fermilab/BNL measurement. Sensitivity from the Z -decay is minimal with no potential to deliver sensible bounds on C_{eB} and C_{eW} , although it does constrain $C_{\phi e}$, $C_{\phi l}^{(1)}$ and $C_{\phi l}^{(3)}$. The Higgs sector can also provide sensitivity as the dipole operators are constructed from the Higgs doublet, which motivates looking at the $h\mu\mu$ signal strength. However, as the dipole operators enter only through loops, an alternative avenue is the $h \rightarrow \mu\mu\gamma$ at the LHC, where, despite its limited statistical yield, there is good control of the final state. This renders it an ideal channel to acquire bounds on the C_{eB} and C_{eW} operators as they appear at tree level. Nonetheless, even at the HL-LHC luminosity of 3/ab, results are far from comparable to the bounds from the a_μ measurement.

Lastly, the MUonE, designed to specifically measure the hadronic contributions from QCD to the muon $g - 2$, can also be used to obtain bounds on the dipole operators when its results are reinterpreted in terms of SMEFT interactions. Indeed, this setup is the most competitive compared to the aforementioned avenues, but once again, without any prospect of competing with the extreme precision of the Fermilab/BNL measurement.

Chapter 8

Conclusions

In this thesis, the Standard Model of particle physics was introduced as the current best description of high-energy physics in Chapter 2. For the new physics practitioner, the SM resolves issues of perturbative unitarity that occur without the presence of the Higgs, without the prospect of identifying a No-Lose theorem and a clear way forward for experiments. It is, therefore, necessary to take the SM's particular shortcomings at face value and explore the possible solutions that can be modelled.

Chapter 3 explored a particularly straightforward solution to the dark matter problem, extending the SM by a heavy scalar coupled only to the Higgs and providing a dark matter candidate. Despite the simplicity of the model, a thorough examination of different particular direct and indirect modes was required in order to identify the best suitable channels for several future experimental proposals. This reveals the distinct strengths of each particular experiment, indicating the sensitivity reach that can be achieved and the attainable constraints on the model's parameter space.

Identification of important channels is a vital ingredient in providing efficient constraints on BSM scenarios, especially with certain channels suffering from destructive interference between new physics diagrams and the SM. Exploring this in motivated scenarios in Chapter 4, cascade decays were identified as a channel able to provide sensitivity. To achieve this, however, the challenging final state had to be adequately discriminated from the SM background contamination, and it was shown that Neural Networks could be instrumental in selecting the most appropriate signal region of the phase space. Such decays can even be further enhanced by constructive signal-background

interference without being limited by signal-signal interference.

As indicated by Chapters 3 and 4, working with specific models is not an effortless task. One often prefers to consider model-independent reinterpretations of the experimental results in terms of bounds on SMEFT Wilson Coefficients in order to pinpoint processes where new physics with heavy degrees of freedom might enter. The applicability of this approach relies on how efficient the constraints can be, and in Chapter 5 Graph Neural Networks showed to improve the bounds in semileptonic top pair decays when the final states are embedded in physics-inspired graphs.

In cases where an excess is indeed found from experiments, with bounds on Wilson Coefficients disfavouring the SM, it is crucial to then explore ways to scrutinise the results. Chapter 6 focused on one such excess on the CP violating $C_{\phi\widetilde{W}B}$ operator by ATLAS, observed in the electroweak Zjj production, which could be scrutinised by diboson processes. In motivated scenarios where the $C_{\widetilde{W}}$ operator can be neglected, Higgs data measurements such as WBF production with decays to tau particles proved to be integral in constraining the WC parameter space in a minimal fit of CP violation in the electroweak sector.

Remaining in the same line of thought, Chapter 7 took the anomalous magnetic moment measurement of Fermilab/BNL at face value in an attempt to also scrutinise the relevant dipole operators. However, this proved to be a significantly arduous task as neither $h \rightarrow \mu\mu\gamma$ at LHC nor the most promising MUonE $e^-\mu^- \rightarrow e^-\mu^-$ elastic scattering can deliver constraints with the prospect of competing with the extreme precision of the Fermilab/BNL measurement of the muon $g - 2$.

Indeed finding the answer to “What is beyond the Standard Model?” is by no means an easy task. Just like the developments that led to the establishment of the Standard Model as the currently best description of nature, a definitive answer to this question can take years and most likely, the deficiencies will be resolved one by one and step by step. Nevertheless, the playground of new physics provides the unique opportunity to develop, adjust and adopt new models or methods in an attempt to push our understanding forward, with a glimpse of the tremendous efforts of the community demonstrated in this thesis. With the hopes that such developments in the physics community will soon become fruitful, the moment when nature’s choice will be revealed is anticipated with excitement.

Bibliography

- [1] C. Englert, J. Jaeckel, M. Spannowsky, and P. Stylianou, *Power meets Precision to explore the Symmetric Higgs Portal*, *Phys. Lett. B* **806**, 135526 (2020), [arXiv:2002.07823 \[hep-ph\]](#).
- [2] C. Englert, M. Fairbairn, M. Spannowsky, P. Stylianou, and S. Varma, *Sensing Higgs boson cascade decays through memory*, *Phys. Rev. D* **102**, 095027 (2020), [arXiv:2008.08611 \[hep-ph\]](#).
- [3] O. Atkinson, C. Englert, and P. Stylianou, *On interference effects in top-philic decay chains*, *Phys. Lett. B* **821**, 136618 (2021), [arXiv:2012.07424 \[hep-ph\]](#).
- [4] O. Atkinson, A. Bhardwaj, S. Brown, C. Englert, D. J. Miller, and P. Stylianou, *Improved constraints on effective top quark interactions using edge convolution networks*, *JHEP* **04**, 137 (2022), [arXiv:2111.01838 \[hep-ph\]](#).
- [5] S. Das Bakshi, J. Chakraborty, C. Englert, M. Spannowsky, and P. Stylianou, *CP violation at ATLAS in effective field theory*, *Phys. Rev. D* **103**, 055008 (2021), [arXiv:2009.13394 \[hep-ph\]](#).
- [6] S. D. Bakshi, J. Chakraborty, C. Englert, M. Spannowsky, and P. Stylianou, *Landscaping CP-violating BSM scenarios*, *Nucl. Phys. B* **975**, 115676 (2022), [arXiv:2103.15861 \[hep-ph\]](#).
- [7] A. Bhardwaj, C. Englert, and P. Stylianou, *Implications of the muon anomalous magnetic moment for the LHC and MUonE*, (2022), [arXiv:2206.14640 \[hep-ph\]](#).
- [8] G. Aad *et al.* (ATLAS), *Observation of a new particle in the search for the Standard Model Higgs boson with the ATLAS detector at the LHC*, *Phys. Lett. B* **716**, 1 (2012), [arXiv:1207.7214 \[hep-ex\]](#).

- [9] S. Chatrchyan *et al.* (CMS), *Observation of a New Boson at a Mass of 125 GeV with the CMS Experiment at the LHC*, *Phys. Lett. B* **716**, 30 (2012), [arXiv:1207.7235 \[hep-ex\]](#).
- [10] W. A. Bardeen, H. Fritzsch, and M. Gell-Mann, *Light cone current algebra, π^0 decay, and e^+e^- annihilation*, in *Topical Meeting on the Outlook for Broken Conformal Symmetry in Elementary Particle Physics* (1972) [arXiv:hep-ph/0211388](#).
- [11] S. Weinberg, *Nonabelian Gauge Theories of the Strong Interactions*, *Phys. Rev. Lett.* **31**, 494 (1973).
- [12] H. Fritzsch, M. Gell-Mann, and H. Leutwyler, *Advantages of the Color Octet Gluon Picture*, *Phys. Lett. B* **47**, 365 (1973).
- [13] S. L. Glashow, *Partial Symmetries of Weak Interactions*, *Nucl. Phys.* **22**, 579 (1961).
- [14] S. Weinberg, *A Model of Leptons*, *Phys. Rev. Lett.* **19**, 1264 (1967).
- [15] A. Salam, *Weak and Electromagnetic Interactions*, *Conf. Proc. C* **680519**, 367 (1968).
- [16] E. P. Wigner, *On Unitary Representations of the Inhomogeneous Lorentz Group*, *Annals Math.* **40**, 149 (1939).
- [17] G. 't Hooft, *Renormalizable Lagrangians for Massive Yang-Mills Fields*, *Nucl. Phys. B* **35**, 167 (1971).
- [18] E. Kraus, *Renormalization of the Electroweak Standard Model to All Orders*, *Annals Phys.* **262**, 155 (1998), [arXiv:hep-th/9709154](#).
- [19] C. Kopper and V. F. Muller, *Renormalization of Spontaneously Broken $SU(2)$ Yang-Mills Theory with Flow Equations*, *Rev. Math. Phys.* **21**, 781 (2009), [arXiv:0902.2486 \[math-ph\]](#).
- [20] M. Bohm, A. Denner, and H. Joos, *Gauge theories of the strong and electroweak interaction* (2001).
- [21] M. D. Schwartz, *Quantum Field Theory and the Standard Model* (Cambridge University Press, 2014).
- [22] M. E. Peskin and D. V. Schroeder, *An Introduction to quantum field theory* (Addison-Wesley, Reading, USA, 1995).
- [23] C.-N. Yang and R. L. Mills, *Conservation of Isotopic Spin and Isotopic Gauge Invariance*, *Phys. Rev.* **96**, 191 (1954).

- [24] G. Zweig, *An $SU(3)$ model for strong interaction symmetry and its breaking. Version 2*, in *DEVELOPMENTS IN THE QUARK THEORY OF HADRONS. VOL. 1. 1964 - 1978*, edited by D. B. Lichtenberg and S. P. Rosen (1964) pp. 22–101.
- [25] M. Gell-Mann, *A Schematic Model of Baryons and Mesons*, *Phys. Lett.* **8**, 214 (1964).
- [26] M. Y. Han and Y. Nambu, *Three Triplet Model with Double $SU(3)$ Symmetry*, *Phys. Rev.* **139**, B1006 (1965).
- [27] C. Athanassopoulos *et al.* (LSND), *Evidence for $\nu(\mu) \rightarrow \nu(e)$ neutrino oscillations from LSND*, *Phys. Rev. Lett.* **81**, 1774 (1998), [arXiv:nucl-ex/9709006](#).
- [28] Y. Fukuda *et al.* (Super-Kamiokande), *Evidence for oscillation of atmospheric neutrinos*, *Phys. Rev. Lett.* **81**, 1562 (1998), [arXiv:hep-ex/9807003](#).
- [29] A. Aguilar-Arevalo *et al.* (LSND), *Evidence for neutrino oscillations from the observation of $\bar{\nu}_e$ appearance in a $\bar{\nu}_\mu$ beam*, *Phys. Rev. D* **64**, 112007 (2001), [arXiv:hep-ex/0104049](#).
- [30] T. Araki *et al.* (KamLAND), *Measurement of neutrino oscillation with KamLAND: Evidence of spectral distortion*, *Phys. Rev. Lett.* **94**, 081801 (2005), [arXiv:hep-ex/0406035](#).
- [31] Y. Ashie *et al.* (Super-Kamiokande), *Evidence for an oscillatory signature in atmospheric neutrino oscillation*, *Phys. Rev. Lett.* **93**, 101801 (2004), [arXiv:hep-ex/0404034](#).
- [32] M. H. Ahn *et al.* (K2K), *Measurement of Neutrino Oscillation by the K2K Experiment*, *Phys. Rev. D* **74**, 072003 (2006), [arXiv:hep-ex/0606032](#).
- [33] K. Abe *et al.* (Super-Kamiokande), *Solar neutrino results in Super-Kamiokande-III*, *Phys. Rev. D* **83**, 052010 (2011), [arXiv:1010.0118 \[hep-ex\]](#).
- [34] K. Abe *et al.* (T2K), *Observation of Electron Neutrino Appearance in a Muon Neutrino Beam*, *Phys. Rev. Lett.* **112**, 061802 (2014), [arXiv:1311.4750 \[hep-ex\]](#).
- [35] K. Abe *et al.* (T2K), *Measurements of neutrino oscillation in appearance and disappearance channels by the T2K experiment with 6.6×10^{20} protons on target*, *Phys. Rev. D* **91**, 072010 (2015), [arXiv:1502.01550 \[hep-ex\]](#).
- [36] F. Englert and R. Brout, *Broken Symmetry and the Mass of Gauge Vector Mesons*, *Phys. Rev. Lett.* **13**, 321 (1964).

- [37] P. W. Higgs, *Broken Symmetries and the Masses of Gauge Bosons*, [Phys. Rev. Lett. **13**, 508 \(1964\)](#).
- [38] G. S. Guralnik, C. R. Hagen, and T. W. B. Kibble, *Global Conservation Laws and Massless Particles*, [Phys. Rev. Lett. **13**, 585 \(1964\)](#).
- [39] T. W. B. Kibble, *Symmetry breaking in nonAbelian gauge theories*, [Phys. Rev. **155**, 1554 \(1967\)](#).
- [40] J. Bernstein, *Spontaneous symmetry breaking, gauge theories, the higgs mechanism and all that*, [Rev. Mod. Phys. **46**, 7 \(1974\)](#), [Erratum: Rev.Mod.Phys. 47, 259–259 (1975), Erratum: Rev.Mod.Phys. 46, 855–855 (1974)].
- [41] S. R. Coleman and E. J. Weinberg, *Radiative Corrections as the Origin of Spontaneous Symmetry Breaking*, [Phys. Rev. D **7**, 1888 \(1973\)](#).
- [42] N. Cabibbo, L. Maiani, G. Parisi, and R. Petronzio, *Bounds on the Fermions and Higgs Boson Masses in Grand Unified Theories*, [Nucl. Phys. B **158**, 295 \(1979\)](#).
- [43] P. Q. Hung, *Vacuum Instability and New Constraints on Fermion Masses*, [Phys. Rev. Lett. **42**, 873 \(1979\)](#).
- [44] M. Lindner, *Implications of Triviality for the Standard Model*, [Z. Phys. C **31**, 295 \(1986\)](#).
- [45] G. Degrandi, S. Di Vita, J. Elias-Miro, J. R. Espinosa, G. F. Giudice, G. Isidori, and A. Strumia, *Higgs mass and vacuum stability in the Standard Model at NNLO*, [JHEP **08**, 098 \(2012\)](#), [arXiv:1205.6497 \[hep-ph\]](#).
- [46] F. Devoto, S. Devoto, L. Di Luzio, and G. Ridolfi, *False vacuum decay: an introductory review*, (2022), [10.1088/1361-6471/ac7f24](#), [arXiv:2205.03140 \[hep-ph\]](#).
- [47] H. Yukawa, *On the Interaction of Elementary Particles I*, [Proc. Phys. Math. Soc. Jap. **17**, 48 \(1935\)](#).
- [48] T. Nakano and K. Nishijima, *Charge Independence for V-particles*, [Prog. Theor. Phys. **10**, 581 \(1953\)](#).
- [49] M. Gell-Mann, *The interpretation of the new particles as displaced charge multiplets*, [Nuovo Cim. **4**, 848 \(1956\)](#).

- [50] G. Arnison *et al.* (UA1), *Experimental Observation of Isolated Large Transverse Energy Electrons with Associated Missing Energy at $\sqrt{s} = 540$ GeV*, *Phys. Lett. B* **122**, 103 (1983).
- [51] G. Arnison *et al.* (UA1), *Experimental Observation of Lepton Pairs of Invariant Mass Around 95-GeV/c**2 at the CERN SPS Collider*, *Phys. Lett. B* **126**, 398 (1983).
- [52] M. Banner *et al.* (UA2), *Observation of Single Isolated Electrons of High Transverse Momentum in Events with Missing Transverse Energy at the CERN anti-p p Collider*, *Phys. Lett. B* **122**, 476 (1983).
- [53] P. Bagnaia *et al.* (UA2), *Evidence for $Z^0 \rightarrow e^+e^-$ at the CERN $\bar{p}p$ Collider*, *Phys. Lett. B* **129**, 130 (1983).
- [54] N. Cabibbo, *Unitary Symmetry and Leptonic Decays*, *Phys. Rev. Lett.* **10**, 531 (1963).
- [55] M. Kobayashi and T. Maskawa, *CP Violation in the Renormalizable Theory of Weak Interaction*, *Prog. Theor. Phys.* **49**, 652 (1973).
- [56] H. Lehmann, K. Symanzik, and W. Zimmermann, *On the formulation of quantized field theories*, *Nuovo Cim.* **1**, 205 (1955).
- [57] L. D. Faddeev and V. N. Popov, *Feynman Diagrams for the Yang-Mills Field*, *Phys. Lett. B* **25**, 29 (1967).
- [58] N. D. Christensen and C. Duhr, *FeynRules - Feynman rules made easy*, *Comput. Phys. Commun.* **180**, 1614 (2009), [arXiv:0806.4194 \[hep-ph\]](#).
- [59] A. Alloul, N. D. Christensen, C. Degrande, C. Duhr, and B. Fuks, *FeynRules 2.0 - A complete toolbox for tree-level phenomenology*, *Comput. Phys. Commun.* **185**, 2250 (2014), [arXiv:1310.1921 \[hep-ph\]](#).
- [60] F. Staub, *SARAH 4 : A tool for (not only SUSY) model builders*, *Comput. Phys. Commun.* **185**, 1773 (2014), [arXiv:1309.7223 \[hep-ph\]](#).
- [61] R. P. Feynman, *Space - time approach to quantum electrodynamics*, *Phys. Rev.* **76**, 769 (1949).
- [62] G. 't Hooft and M. J. G. Veltman, *Regularization and Renormalization of Gauge Fields*, *Nucl. Phys. B* **44**, 189 (1972).

- [63] M. Jacob and G. C. Wick, *On the General Theory of Collisions for Particles with Spin*, [Annals Phys. **7**, 404 \(1959\)](#).
- [64] E. Fermi, *An attempt of a theory of beta radiation. 1.* [Z. Phys. **88**, 161 \(1934\)](#).
- [65] R. P. Feynman and M. Gell-Mann, *Theory of Fermi interaction*, [Phys. Rev. **109**, 193 \(1958\)](#).
- [66] E. C. G. Sudarshan and R. e. Marshak, *Chirality invariance and the universal Fermi interaction*, [Phys. Rev. **109**, 1860 \(1958\)](#).
- [67] J. S. Schwinger, *A Theory of the Fundamental Interactions*, [Annals Phys. **2**, 407 \(1957\)](#).
- [68] T. D. Lee and C.-N. Yang, *Possible Nonlocal Effects in μ Decay*, [Phys. Rev. **108**, 1611 \(1957\)](#).
- [69] S. A. Bludman, *On the universal Fermi interaction*, [Nuovo Cim. **9**, 433 \(1958\)](#).
- [70] J. Leite Lopes, *A model of the universal fermi interaction*, [Nucl. Phys. **8**, 234 \(1958\)](#).
- [71] S. Abachi *et al.* (D0), *Observation of the top quark*, [Phys. Rev. Lett. **74**, 2632 \(1995\)](#), [arXiv:hep-ex/9503003](#).
- [72] F. Abe *et al.* (CDF), *Observation of top quark production in $\bar{p}p$ collisions*, [Phys. Rev. Lett. **74**, 2626 \(1995\)](#), [arXiv:hep-ex/9503002](#).
- [73] A. Wulzer, *Behind the Standard Model*, in *2015 European School of High-Energy Physics* (2019) [arXiv:1901.01017 \[hep-ph\]](#).
- [74] C. Itzykson and J. B. Zuber, *Quantum Field Theory*, International Series In Pure and Applied Physics (McGraw-Hill, New York, 1980).
- [75] L. Di Luzio, J. F. Kamenik, and M. Nardecchia, *Implications of perturbative unitarity for scalar di-boson resonance searches at LHC*, [Eur. Phys. J. C **77**, 30 \(2017\)](#), [arXiv:1604.05746 \[hep-ph\]](#).
- [76] T. Hahn and M. Perez-Victoria, *Automatized one loop calculations in four-dimensions and D-dimensions*, [Comput. Phys. Commun. **118**, 153 \(1999\)](#), [arXiv:hep-ph/9807565](#).
- [77] B. W. Lee, C. Quigg, and H. B. Thacker, *Weak Interactions at Very High-Energies: The Role of the Higgs Boson Mass*, [Phys. Rev. D **16**, 1519 \(1977\)](#).
- [78] G. Breit and E. Wigner, *Capture of Slow Neutrons*, [Phys. Rev. **49**, 519 \(1936\)](#).

- [79] A. Djouadi, *The Anatomy of electro-weak symmetry breaking. I: The Higgs boson in the standard model*, [Phys. Rept. **457**, 1 \(2008\)](#), [arXiv:hep-ph/0503172](#).
- [80] T. G. Rizzo, *Decays of Heavy Higgs Bosons*, [Phys. Rev. D **22**, 722 \(1980\)](#).
- [81] W.-Y. Keung and W. J. Marciano, *HIGGS SCALAR DECAYS: $H \rightarrow W^{+-} X$* , [Phys. Rev. D **30**, 248 \(1984\)](#).
- [82] G. Passarino and M. J. G. Veltman, *One Loop Corrections for $e^+ e^-$ Annihilation Into $\mu^+ \mu^-$ in the Weinberg Model*, [Nucl. Phys. B **160**, 151 \(1979\)](#).
- [83] M. A. Shifman, A. I. Vainshtein, M. B. Voloshin, and V. I. Zakharov, *Low-Energy Theorems for Higgs Boson Couplings to Photons*, [Sov. J. Nucl. Phys. **30**, 711 \(1979\)](#).
- [84] M. Gavela, G. Girardi, C. Malleville, and P. Sorba, *A non-linear r gauge condition for the electroweak $su(2) \times u(1)$ model*, [Nuclear Physics B **193**, 257 \(1981\)](#).
- [85] G. Aad *et al.* (ATLAS), *Measurement of Higgs boson decay into b -quarks in associated production with a top-quark pair in pp collisions at $\sqrt{s} = 13$ TeV with the ATLAS detector*, [JHEP **06**, 097 \(2022\)](#), [arXiv:2111.06712 \[hep-ex\]](#).
- [86] G. Aad *et al.* (ATLAS), *Measurements of Higgs boson production cross-sections in the $H \rightarrow \tau^+ \tau^-$ decay channel in pp collisions at $\sqrt{s} = 13$ TeV with the ATLAS detector*, (2022), [arXiv:2201.08269 \[hep-ex\]](#).
- [87] *Measurements of Higgs boson production in the decay channel with a pair of τ leptons in proton-proton collisions at $\sqrt{s} = 13$ TeV*, (2022), [arXiv:2204.12957 \[hep-ex\]](#).
- [88] A. M. Sirunyan *et al.* (CMS), *Evidence for the Higgs boson decay to a bottom quark–antiquark pair*, [Phys. Lett. B **780**, 501 \(2018\)](#), [arXiv:1709.07497 \[hep-ex\]](#).
- [89] J. R. Andersen *et al.* (LHC Higgs Cross Section Working Group), *Handbook of LHC Higgs Cross Sections: 3. Higgs Properties*, (2013), [10.5170/CERN-2013-004](#), [arXiv:1307.1347 \[hep-ph\]](#).
- [90] A. Denner, S. Heinemeyer, I. Puljak, D. Rebuffi, and M. Spira, *Standard Model Higgs-Boson Branching Ratios with Uncertainties*, [Eur. Phys. J. C **71**, 1753 \(2011\)](#), [arXiv:1107.5909 \[hep-ph\]](#).
- [91] J. C. Collins, D. E. Soper, and G. F. Sterman, *Factorization of Hard Processes in QCD*, [Adv. Ser. Direct. High Energy Phys. **5**, 1 \(1989\)](#), [arXiv:hep-ph/0409313](#).

- [92] T. Plehn, *Lectures on LHC Physics*, *Lect. Notes Phys.* **844**, 1 (2012), [arXiv:0910.4182 \[hep-ph\]](#).
- [93] J. J. Ethier and E. R. Nocera, *Parton Distributions in Nucleons and Nuclei*, *Ann. Rev. Nucl. Part. Sci.* **70**, 43 (2020), [arXiv:2001.07722 \[hep-ph\]](#).
- [94] J. Alwall, M. Herquet, F. Maltoni, O. Mattelaer, and T. Stelzer, *MadGraph 5 : Going Beyond*, *JHEP* **06**, 128 (2011), [arXiv:1106.0522 \[hep-ph\]](#).
- [95] P. de Aquino, W. Link, F. Maltoni, O. Mattelaer, and T. Stelzer, *ALOHA: Automatic Libraries Of Helicity Amplitudes for Feynman Diagram Computations*, *Comput. Phys. Commun.* **183**, 2254 (2012), [arXiv:1108.2041 \[hep-ph\]](#).
- [96] J. Alwall, R. Frederix, S. Frixione, V. Hirschi, F. Maltoni, O. Mattelaer, H. S. Shao, T. Stelzer, P. Torrielli, and M. Zaro, *The automated computation of tree-level and next-to-leading order differential cross sections, and their matching to parton shower simulations*, *JHEP* **07**, 079 (2014), [arXiv:1405.0301 \[hep-ph\]](#).
- [97] B. A. Kniehl and M. Spira, *Low-energy theorems in Higgs physics*, *Z. Phys. C* **69**, 77 (1995), [arXiv:hep-ph/9505225](#).
- [98] M. Cacciari, G. P. Salam, and G. Soyez, *The anti- k_t jet clustering algorithm*, *JHEP* **04**, 063 (2008), [arXiv:0802.1189 \[hep-ph\]](#).
- [99] G. P. Salam, *Towards Jetography*, *Eur. Phys. J. C* **67**, 637 (2010), [arXiv:0906.1833 \[hep-ph\]](#).
- [100] D. L. Rainwater and D. Zeppenfeld, *Searching for $H \rightarrow \gamma\gamma$ in weak boson fusion at the LHC*, *JHEP* **12**, 005 (1997), [arXiv:hep-ph/9712271](#).
- [101] D. L. Rainwater, D. Zeppenfeld, and K. Hagiwara, *Searching for $H \rightarrow \tau^+\tau^-$ in weak boson fusion at the CERN LHC*, *Phys. Rev. D* **59**, 014037 (1998), [arXiv:hep-ph/9808468](#).
- [102] D. L. Rainwater and D. Zeppenfeld, *Observing $H \rightarrow W^*W^* \rightarrow e^\pm\mu^\mp \not{p}_T$ in weak boson fusion with dual forward jet tagging at the CERN LHC*, *Phys. Rev. D* **60**, 113004 (1999), [Erratum: *Phys.Rev.D* 61, 099901 (2000)], [arXiv:hep-ph/9906218](#).
- [103] D. L. Rainwater, *Intermediate mass Higgs searches in weak boson fusion*, Other thesis (1999), [arXiv:hep-ph/9908378](#).
- [104] T. Plehn, D. L. Rainwater, and D. Zeppenfeld, *Determining the Structure of Higgs Couplings at the LHC*, *Phys. Rev. Lett.* **88**, 051801 (2002), [arXiv:hep-ph/0105325](#).

- [105] D. de Florian *et al.* (LHC Higgs Cross Section Working Group), *Handbook of LHC Higgs Cross Sections: 4. Deciphering the Nature of the Higgs Sector*, **2/2017** (2016), [10.23731/CYRM-2017-002](https://arxiv.org/abs/1610.07922), [arXiv:1610.07922](https://arxiv.org/abs/1610.07922) [hep-ph].
- [106] J. M. Butterworth, A. R. Davison, M. Rubin, and G. P. Salam, *Jet substructure as a new Higgs search channel at the LHC*, *AIP Conf. Proc.* **1078**, 189 (2009), [arXiv:0809.2530](https://arxiv.org/abs/0809.2530) [hep-ph].
- [107] J. Mellenthin (ATLAS), *Observation of the $t\bar{t}H$ production*, *J. Phys. Conf. Ser.* **1390**, 012042 (2019).
- [108] M. C. Gonzalez-Garcia and M. Maltoni, *Phenomenology with Massive Neutrinos*, *Phys. Rept.* **460**, 1 (2008), [arXiv:0704.1800](https://arxiv.org/abs/0704.1800) [hep-ph].
- [109] S. De Curtis, L. Delle Rose, S. Moretti, and K. Yagyu, *Supersymmetry versus Compositeness: 2HDMs tell the story*, *Phys. Lett. B* **786**, 189 (2018), [arXiv:1803.01865](https://arxiv.org/abs/1803.01865) [hep-ph].
- [110] P. Salucci, *The distribution of dark matter in galaxies*, *Astron. Astrophys. Rev.* **27**, 2 (2019), [arXiv:1811.08843](https://arxiv.org/abs/1811.08843) [astro-ph.GA].
- [111] J. D. Simon, *The faintest dwarf galaxies*, *Annual Review of Astronomy and Astrophysics* **57**, 375 (2019).
- [112] S. W. Allen, A. E. Evrard, and A. B. Mantz, *Cosmological parameters from observations of galaxy clusters*, *Annual Review of Astronomy and Astrophysics* **49**, 409 (2011).
- [113] A. D. Sakharov, *Violation of CP Invariance, C asymmetry, and baryon asymmetry of the universe*, *Pisma Zh. Eksp. Teor. Fiz.* **5**, 32 (1967).
- [114] B. Abi *et al.* (Muon g-2), *Measurement of the Positive Muon Anomalous Magnetic Moment to 0.46 ppm*, *Phys. Rev. Lett.* **126**, 141801 (2021), [arXiv:2104.03281](https://arxiv.org/abs/2104.03281) [hep-ex].
- [115] G. W. Bennett *et al.* (Muon g-2), *Measurement of the negative muon anomalous magnetic moment to 0.7 ppm*, *Phys. Rev. Lett.* **92**, 161802 (2004), [arXiv:hep-ex/0401008](https://arxiv.org/abs/hep-ex/0401008).
- [116] T. Aoyama, M. Hayakawa, T. Kinoshita, and M. Nio, *Complete Tenth-Order QED Contribution to the Muon g-2*, *Phys. Rev. Lett.* **109**, 111808 (2012), [arXiv:1205.5370](https://arxiv.org/abs/1205.5370) [hep-ph].
- [117] T. Aoyama, T. Kinoshita, and M. Nio, *Theory of the Anomalous Magnetic Moment of the Electron*, *Atoms* **7**, 28 (2019).

- [118] A. Czarnecki, W. J. Marciano, and A. Vainshtein, *Refinements in electroweak contributions to the muon anomalous magnetic moment*, *Phys. Rev. D* **67**, 073006 (2003), [Erratum: *Phys.Rev.D* 73, 119901 (2006)], [arXiv:hep-ph/0212229](#).
- [119] C. Gnendiger, D. Stöckinger, and H. Stöckinger-Kim, *The electroweak contributions to $(g - 2)_\mu$ after the Higgs boson mass measurement*, *Phys. Rev. D* **88**, 053005 (2013), [arXiv:1306.5546 \[hep-ph\]](#).
- [120] M. Davier, A. Hoecker, B. Malaescu, and Z. Zhang, *Reevaluation of the hadronic vacuum polarisation contributions to the Standard Model predictions of the muon $g - 2$ and $\alpha(m_Z^2)$ using newest hadronic cross-section data*, *Eur. Phys. J. C* **77**, 827 (2017), [arXiv:1706.09436 \[hep-ph\]](#).
- [121] A. Keshavarzi, D. Nomura, and T. Teubner, *Muon $g - 2$ and $\alpha(M_Z^2)$: a new data-based analysis*, *Phys. Rev. D* **97**, 114025 (2018), [arXiv:1802.02995 \[hep-ph\]](#).
- [122] G. Colangelo, M. Hoferichter, and P. Stoffer, *Two-pion contribution to hadronic vacuum polarization*, *JHEP* **02**, 006 (2019), [arXiv:1810.00007 \[hep-ph\]](#).
- [123] M. Hoferichter, B.-L. Hoid, and B. Kubis, *Three-pion contribution to hadronic vacuum polarization*, *JHEP* **08**, 137 (2019), [arXiv:1907.01556 \[hep-ph\]](#).
- [124] M. Davier, A. Hoecker, B. Malaescu, and Z. Zhang, *A new evaluation of the hadronic vacuum polarisation contributions to the muon anomalous magnetic moment and to $\alpha(\mathbf{m}_Z^2)$* , *Eur. Phys. J. C* **80**, 241 (2020), [Erratum: *Eur.Phys.J.C* 80, 410 (2020)], [arXiv:1908.00921 \[hep-ph\]](#).
- [125] A. Keshavarzi, D. Nomura, and T. Teubner, *$g - 2$ of charged leptons, $\alpha(M_Z^2)$, and the hyperfine splitting of muonium*, *Phys. Rev. D* **101**, 014029 (2020), [arXiv:1911.00367 \[hep-ph\]](#).
- [126] A. Kurz, T. Liu, P. Marquard, and M. Steinhauser, *Hadronic contribution to the muon anomalous magnetic moment to next-to-next-to-leading order*, *Phys. Lett. B* **734**, 144 (2014), [arXiv:1403.6400 \[hep-ph\]](#).
- [127] K. Melnikov and A. Vainshtein, *Hadronic light-by-light scattering contribution to the muon anomalous magnetic moment revisited*, *Phys. Rev. D* **70**, 113006 (2004), [arXiv:hep-ph/0312226](#).

- [128] P. Masjuan and P. Sanchez-Puertas, *Pseudoscalar-pole contribution to the $(g_\mu - 2)$: a rational approach*, *Phys. Rev. D* **95**, 054026 (2017), [arXiv:1701.05829 \[hep-ph\]](#).
- [129] G. Colangelo, M. Hoferichter, M. Procura, and P. Stoffer, *Dispersion relation for hadronic light-by-light scattering: two-pion contributions*, *JHEP* **04**, 161 (2017), [arXiv:1702.07347 \[hep-ph\]](#).
- [130] M. Hoferichter, B.-L. Hoid, B. Kubis, S. Leupold, and S. P. Schneider, *Dispersion relation for hadronic light-by-light scattering: pion pole*, *JHEP* **10**, 141 (2018), [arXiv:1808.04823 \[hep-ph\]](#).
- [131] A. Gérardin, H. B. Meyer, and A. Nyffeler, *Lattice calculation of the pion transition form factor with $N_f = 2 + 1$ Wilson quarks*, *Phys. Rev. D* **100**, 034520 (2019), [arXiv:1903.09471 \[hep-lat\]](#).
- [132] J. Bijnens, N. Hermansson-Truedsson, and A. Rodríguez-Sánchez, *Short-distance constraints for the HLbL contribution to the muon anomalous magnetic moment*, *Phys. Lett. B* **798**, 134994 (2019), [arXiv:1908.03331 \[hep-ph\]](#).
- [133] G. Colangelo, F. Hagelstein, M. Hoferichter, L. Laub, and P. Stoffer, *Longitudinal short-distance constraints for the hadronic light-by-light contribution to $(g - 2)_\mu$ with large- N_c Regge models*, *JHEP* **03**, 101 (2020), [arXiv:1910.13432 \[hep-ph\]](#).
- [134] T. Blum, N. Christ, M. Hayakawa, T. Izubuchi, L. Jin, C. Jung, and C. Lehner, *Hadronic Light-by-Light Scattering Contribution to the Muon Anomalous Magnetic Moment from Lattice QCD*, *Phys. Rev. Lett.* **124**, 132002 (2020), [arXiv:1911.08123 \[hep-lat\]](#).
- [135] G. Colangelo, M. Hoferichter, A. Nyffeler, M. Passera, and P. Stoffer, *Remarks on higher-order hadronic corrections to the muon $g-2$* , *Phys. Lett. B* **735**, 90 (2014), [arXiv:1403.7512 \[hep-ph\]](#).
- [136] T. Aoyama *et al.*, *The anomalous magnetic moment of the muon in the Standard Model*, *Phys. Rept.* **887**, 1 (2020), [arXiv:2006.04822 \[hep-ph\]](#).
- [137] K. G. Wilson, *Renormalization group and critical phenomena. 1. Renormalization group and the Kadanoff scaling picture*, *Phys. Rev. B* **4**, 3174 (1971).
- [138] S. Weinberg, *Phenomenological Lagrangians*, *Physica A* **96**, 327 (1979).

- [139] B. Grzadkowski, M. Iskrzynski, M. Misiak, and J. Rosiek, *Dimension-Six Terms in the Standard Model Lagrangian*, *JHEP* **10**, 085 (2010), [arXiv:1008.4884 \[hep-ph\]](#).
- [140] S. Weinberg, *Baryon and Lepton Nonconserving Processes*, *Phys. Rev. Lett.* **43**, 1566 (1979).
- [141] W. Buchmuller and D. Wyler, *Effective Lagrangian Analysis of New Interactions and Flavor Conservation*, *Nucl. Phys. B* **268**, 621 (1986).
- [142] C. J. C. Burges and H. J. Schnitzer, *Virtual Effects of Excited Quarks as Probes of a Possible New Hadronic Mass Scale*, *Nucl. Phys. B* **228**, 464 (1983).
- [143] C. N. Leung, S. T. Love, and S. Rao, *Low-Energy Manifestations of a New Interaction Scale: Operator Analysis*, *Z. Phys. C* **31**, 433 (1986).
- [144] K. Hagiwara, R. D. Peccei, D. Zeppenfeld, and K. Hikasa, *Probing the Weak Boson Sector in $e^+ e^- \rightarrow W^+ W^-$* , *Nucl. Phys. B* **282**, 253 (1987).
- [145] A. Dedes, W. Materkowska, M. Paraskevas, J. Rosiek, and K. Suxho, *Feynman rules for the Standard Model Effective Field Theory in R -gauges*, *JHEP* **06**, 143 (2017), [arXiv:1704.03888 \[hep-ph\]](#).
- [146] R. Alonso, E. E. Jenkins, A. V. Manohar, and M. Trott, *Renormalization Group Evolution of the Standard Model Dimension Six Operators III: Gauge Coupling Dependence and Phenomenology*, *JHEP* **04**, 159 (2014), [arXiv:1312.2014 \[hep-ph\]](#).
- [147] E. E. Jenkins, A. V. Manohar, and M. Trott, *Renormalization Group Evolution of the Standard Model Dimension Six Operators II: Yukawa Dependence*, *JHEP* **01**, 035 (2014), [arXiv:1310.4838 \[hep-ph\]](#).
- [148] E. E. Jenkins, A. V. Manohar, and M. Trott, *Renormalization Group Evolution of the Standard Model Dimension Six Operators I: Formalism and lambda Dependence*, *JHEP* **10**, 087 (2013), [arXiv:1308.2627 \[hep-ph\]](#).
- [149] I. Brivio and M. Trott, *The Standard Model as an Effective Field Theory*, *Phys. Rept.* **793**, 1 (2019), [arXiv:1706.08945 \[hep-ph\]](#).
- [150] A. Abada *et al.* (FCC), *FCC-ee: The Lepton Collider: Future Circular Collider Conceptual Design Report Volume 2*, *Eur. Phys. J. ST* **228**, 261 (2019).
- [151] A. Abada *et al.* (FCC), *FCC-hh: The Hadron Collider: Future Circular Collider Conceptual Design Report Volume 3*, *Eur. Phys. J. ST* **228**, 755 (2019).

- [152] A. Abada *et al.* (FCC), *FCC Physics Opportunities: Future Circular Collider Conceptual Design Report Volume 1*, [Eur. Phys. J. C **79**, 474 \(2019\)](#).
- [153] *A Multi-TeV Linear Collider Based on CLIC Technology: CLIC Conceptual Design Report*, (2012), [10.5170/CERN-2012-007](#).
- [154] J. Erler, S. Heinemeyer, W. Hollik, G. Weiglein, and P. M. Zerwas, *Physics impact of GigaZ*, [Phys. Lett. B **486**, 125 \(2000\)](#), [arXiv:hep-ph/0005024](#).
- [155] J. Erler and S. Heinemeyer, *GigaZ: High precision tests of the SM and the MSSM*, in *5th International Symposium on Radiative Corrections: Applications of Quantum Field Theory to Phenomenology* (2001) [arXiv:hep-ph/0102083](#).
- [156] *The International Linear Collider Technical Design Report - Volume 2: Physics*, (2013), [arXiv:1306.6352 \[hep-ph\]](#).
- [157] T. Binoth and J. J. van der Bij, *Influence of strongly coupled, hidden scalars on Higgs signals*, [Z. Phys. C **75**, 17 \(1997\)](#), [arXiv:hep-ph/9608245](#).
- [158] R. M. Schabinger and J. D. Wells, *A Minimal spontaneously broken hidden sector and its impact on Higgs boson physics at the large hadron collider*, [Phys. Rev. D **72**, 093007 \(2005\)](#), [arXiv:hep-ph/0509209](#).
- [159] B. Patt and F. Wilczek, *Higgs-field portal into hidden sectors*, (2006), [arXiv:hep-ph/0605188](#).
- [160] M. Ahlers, J. Jaeckel, J. Redondo, and A. Ringwald, *Probing Hidden Sector Photons through the Higgs Window*, [Phys. Rev. D **78**, 075005 \(2008\)](#), [arXiv:0807.4143 \[hep-ph\]](#).
- [161] B. Batell, M. Pospelov, and A. Ritz, *Probing a Secluded $U(1)$ at B-factories*, [Phys. Rev. D **79**, 115008 \(2009\)](#), [arXiv:0903.0363 \[hep-ph\]](#).
- [162] C. Englert, T. Plehn, D. Zerwas, and P. M. Zerwas, *Exploring the Higgs portal*, [Phys. Lett. B **703**, 298 \(2011\)](#), [arXiv:1106.3097 \[hep-ph\]](#).
- [163] V. Barger, P. Langacker, M. McCaskey, M. J. Ramsey-Musolf, and G. Shaughnessy, *LHC Phenomenology of an Extended Standard Model with a Real Scalar Singlet*, [Phys. Rev. D **77**, 035005 \(2008\)](#), [arXiv:0706.4311 \[hep-ph\]](#).
- [164] A. Djouadi, O. Lebedev, Y. Mambrini, and J. Quevillon, *Implications of LHC searches for Higgs-portal dark matter*, [Phys. Lett. B **709**, 65 \(2012\)](#), [arXiv:1112.3299 \[hep-ph\]](#).

- [165] A. Djouadi, A. Falkowski, Y. Mambrini, and J. Quevillon, *Direct Detection of Higgs-Portal Dark Matter at the LHC*, *Eur. Phys. J. C* **73**, 2455 (2013), [arXiv:1205.3169 \[hep-ph\]](#).
- [166] C. Degrande, *Automatic evaluation of UV and R2 terms for beyond the Standard Model Lagrangians: a proof-of-principle*, *Comput. Phys. Commun.* **197**, 239 (2015), [arXiv:1406.3030 \[hep-ph\]](#).
- [167] T. Sjöstrand, S. Ask, J. R. Christiansen, R. Corke, N. Desai, P. Ilten, S. Mrenna, S. Prestel, C. O. Rasmussen, and P. Z. Skands, *An introduction to PYTHIA 8.2*, *Comput. Phys. Commun.* **191**, 159 (2015), [arXiv:1410.3012 \[hep-ph\]](#).
- [168] M. Dobbs and J. B. Hansen, *The HepMC C++ Monte Carlo event record for High Energy Physics*, *Comput. Phys. Commun.* **134**, 41 (2001).
- [169] A. Buckley, J. Butterworth, D. Grellscheid, H. Hoeth, L. Lonnblad, J. Monk, H. Schulz, and F. Siegert, *Rivet user manual*, *Comput. Phys. Commun.* **184**, 2803 (2013), [arXiv:1003.0694 \[hep-ph\]](#).
- [170] N. Craig, H. K. Lou, M. McCullough, and A. Thalapillil, *The Higgs Portal Above Threshold*, *JHEP* **02**, 127 (2016), [arXiv:1412.0258 \[hep-ph\]](#).
- [171] M. Ruhdorfer, E. Salvioni, and A. Weiler, *A Global View of the Off-Shell Higgs Portal*, *SciPost Phys.* **8**, 027 (2020), [arXiv:1910.04170 \[hep-ph\]](#).
- [172] A. M. Sirunyan *et al.* (CMS), *Search for invisible decays of a Higgs boson produced through vector boson fusion in proton-proton collisions at $\sqrt{s} = 13$ TeV*, *Phys. Lett. B* **793**, 520 (2019), [arXiv:1809.05937 \[hep-ex\]](#).
- [173] M. L. Mangano *et al.*, *Physics at a 100 TeV pp Collider: Standard Model Processes*, (2016), [10.23731/CYRM-2017-003.1](#), [arXiv:1607.01831 \[hep-ph\]](#).
- [174] G. Aad *et al.* (ATLAS), *Search for new phenomena with the monojet and missing transverse momentum signature using the ATLAS detector in $\sqrt{s} = 7$ TeV proton-proton collisions*, *Phys. Lett. B* **705**, 294 (2011), [arXiv:1106.5327 \[hep-ex\]](#).
- [175] A. Denner, *Techniques for calculation of electroweak radiative corrections at the one loop level and results for W physics at LEP-200*, *Fortsch. Phys.* **41**, 307 (1993), [arXiv:0709.1075 \[hep-ph\]](#).

- [176] A. Denner and S. Dittmaier, *Electroweak Radiative Corrections for Collider Physics*, *Phys. Rept.* **864**, 1 (2020), [arXiv:1912.06823 \[hep-ph\]](#).
- [177] N. Craig, C. Englert, and M. McCullough, *New Probe of Naturalness*, *Phys. Rev. Lett.* **111**, 121803 (2013), [arXiv:1305.5251 \[hep-ph\]](#).
- [178] C. Englert and J. Jaeckel, *Probing the Symmetric Higgs Portal with Di-Higgs Boson Production*, *Phys. Rev. D* **100**, 095017 (2019), [arXiv:1908.10615 \[hep-ph\]](#).
- [179] F. Caola and K. Melnikov, *Constraining the Higgs boson width with ZZ production at the LHC*, *Phys. Rev. D* **88**, 054024 (2013), [arXiv:1307.4935 \[hep-ph\]](#).
- [180] C. Englert and M. Spannowsky, *Limitations and Opportunities of Off-Shell Coupling Measurements*, *Phys. Rev. D* **90**, 053003 (2014), [arXiv:1405.0285 \[hep-ph\]](#).
- [181] J. Baglio *et al.*, *VBFNLO: A Parton Level Monte Carlo for Processes with Electroweak Bosons – Manual for Version 2.7.0*, (2011), [arXiv:1107.4038 \[hep-ph\]](#).
- [182] A. Abada *et al.* (FCC), *HE-LHC: The High-Energy Large Hadron Collider: Future Circular Collider Conceptual Design Report Volume 4*, *Eur. Phys. J. ST* **228**, 1109 (2019).
- [183] M. E. Peskin and T. Takeuchi, *A New constraint on a strongly interacting Higgs sector*, *Phys. Rev. Lett.* **65**, 964 (1990).
- [184] M. Golden and L. Randall, *Radiative Corrections to Electroweak Parameters in Technicolor Theories*, *Nucl. Phys. B* **361**, 3 (1991).
- [185] B. Holdom and J. Terning, *Large corrections to electroweak parameters in technicolor theories*, *Phys. Lett. B* **247**, 88 (1990).
- [186] G. Altarelli and R. Barbieri, *Vacuum polarization effects of new physics on electroweak processes*, *Phys. Lett. B* **253**, 161 (1991).
- [187] B. Grinstein and M. B. Wise, *Operator analysis for precision electroweak physics*, *Phys. Lett. B* **265**, 326 (1991).
- [188] M. E. Peskin and T. Takeuchi, *Estimation of oblique electroweak corrections*, *Phys. Rev. D* **46**, 381 (1992).
- [189] G. Altarelli, R. Barbieri, and S. Jadach, *Toward a model independent analysis of electroweak data*, *Nucl. Phys. B* **369**, 3 (1992), [Erratum: *Nucl.Phys.B* 376, 444 (1992)].

- [190] C. P. Burgess, S. Godfrey, H. Konig, D. London, and I. Maksymyk, *A Global fit to extended oblique parameters*, *Phys. Lett. B* **326**, 276 (1994), [arXiv:hep-ph/9307337](#).
- [191] R. Barbieri, A. Pomarol, R. Rattazzi, and A. Strumia, *Electroweak symmetry breaking after LEP-1 and LEP-2*, *Nucl. Phys. B* **703**, 127 (2004), [arXiv:hep-ph/0405040](#).
- [192] T. Hahn, *Generating Feynman diagrams and amplitudes with FeynArts 3*, *Comput. Phys. Commun.* **140**, 418 (2001), [arXiv:hep-ph/0012260](#).
- [193] R. Mertig, M. Bohm, and A. Denner, *FEYN CALC: Computer algebraic calculation of Feynman amplitudes*, *Comput. Phys. Commun.* **64**, 345 (1991).
- [194] V. Shtabovenko, R. Mertig, and F. Orellana, *New Developments in FeynCalc 9.0*, *Comput. Phys. Commun.* **207**, 432 (2016), [arXiv:1601.01167 \[hep-ph\]](#).
- [195] T. Hahn, *Automatic loop calculations with FeynArts, FormCalc, and LoopTools*, *Nucl. Phys. B Proc. Suppl.* **89**, 231 (2000), [arXiv:hep-ph/0005029](#).
- [196] R. Mertig and R. Scharf, *TARCER: A Mathematica program for the reduction of two loop propagator integrals*, *Comput. Phys. Commun.* **111**, 265 (1998), [arXiv:hep-ph/9801383](#).
- [197] S. P. Martin and D. G. Robertson, *TSIL: A Program for the calculation of two-loop self-energy integrals*, *Comput. Phys. Commun.* **174**, 133 (2006), [arXiv:hep-ph/0501132](#).
- [198] O. V. Tarasov, *Generalized recurrence relations for two loop propagator integrals with arbitrary masses*, *Nucl. Phys. B* **502**, 455 (1997), [arXiv:hep-ph/9703319](#).
- [199] G. Weiglein, R. Scharf, and M. Bohm, *Reduction of general two loop selfenergies to standard scalar integrals*, *Nucl. Phys. B* **416**, 606 (1994), [arXiv:hep-ph/9310358](#).
- [200] M. Baak, J. Cúth, J. Haller, A. Hoecker, R. Kogler, K. Mönig, M. Schott, and J. Stelzer (Gfitter Group), *The global electroweak fit at NNLO and prospects for the LHC and ILC*, *Eur. Phys. J. C* **74**, 3046 (2014), [arXiv:1407.3792 \[hep-ph\]](#).
- [201] S. Dawson, C. Englert, and T. Plehn, *Higgs Physics: It ain't over till it's over*, *Phys. Rept.* **816**, 1 (2019), [arXiv:1808.01324 \[hep-ph\]](#).
- [202] D. Curtin, P. Meade, and C.-T. Yu, *Testing Electroweak Baryogenesis with Future Colliders*, *JHEP* **11**, 127 (2014), [arXiv:1409.0005 \[hep-ph\]](#).

- [203] H. Aihara *et al.* (ILC), *The International Linear Collider. A Global Project*, (2019), [arXiv:1901.09829 \[hep-ex\]](#).
- [204] M. Klute, R. Lafaye, T. Plehn, M. Rauch, and D. Zerwas, *Measuring Higgs Couplings at a Linear Collider*, [EPL **101**, 51001 \(2013\)](#), [arXiv:1301.1322 \[hep-ph\]](#).
- [205] J. de Blas *et al.*, *Higgs Boson Studies at Future Particle Colliders*, [JHEP **01**, 139 \(2020\)](#), [arXiv:1905.03764 \[hep-ph\]](#).
- [206] R. Contino *et al.*, *Physics at a 100 TeV pp collider: Higgs and EW symmetry breaking studies*, (2016), [10.23731/CYRM-2017-003.255](#), [arXiv:1606.09408 \[hep-ph\]](#).
- [207] *Prospects for HH measurements at the HL-LHC*, (2018).
- [208] S. Banerjee, C. Englert, M. L. Mangano, M. Selvaggi, and M. Spannowsky, *hh + jet production at 100 TeV*, [Eur. Phys. J. C **78**, 322 \(2018\)](#), [arXiv:1802.01607 \[hep-ph\]](#).
- [209] S. Banerjee, F. Krauss, and M. Spannowsky, *Revisiting the $t\bar{t}hh$ channel at the FCC-hh*, [Phys. Rev. D **100**, 073012 \(2019\)](#), [arXiv:1904.07886 \[hep-ph\]](#).
- [210] J. Alison *et al.*, *Higgs boson potential at colliders: Status and perspectives*, [Rev. Phys. **5**, 100045 \(2020\)](#), [arXiv:1910.00012 \[hep-ph\]](#).
- [211] L. Chen and A. Freitas, *Leading fermionic three-loop corrections to electroweak precision observables*, [JHEP **07**, 210 \(2020\)](#), [arXiv:2002.05845 \[hep-ph\]](#).
- [212] G. Aad *et al.* (ATLAS), *Search for the Standard Model Higgs boson decaying into $b\bar{b}$ produced in association with top quarks decaying hadronically in pp collisions at $\sqrt{s} = 8$ TeV with the ATLAS detector*, [JHEP **05**, 160 \(2016\)](#), [arXiv:1604.03812 \[hep-ex\]](#).
- [213] M. Aaboud *et al.* (ATLAS), *Measurements of $t\bar{t}$ differential cross-sections of highly boosted top quarks decaying to all-hadronic final states in pp collisions at $\sqrt{s} = 13$ TeV using the ATLAS detector*, [Phys. Rev. D **98**, 012003 \(2018\)](#), [arXiv:1801.02052 \[hep-ex\]](#).
- [214] *Measurements of top-quark pair single- and double-differential cross-sections in the all-hadronic channel in pp collisions at $\sqrt{s} = 13$ TeV using the ATLAS detector*, (2020).
- [215] T. K. Charles *et al.* (CLICdp, CLIC), *The Compact Linear Collider (CLIC) - 2018 Summary Report*, [2/2018 \(2018\)](#), [10.23731/CYRM-2018-002](#), [arXiv:1812.06018 \[physics.acc-ph\]](#).

- [216] J. de Blas *et al.* (CLIC), *The CLIC Potential for New Physics*, **3/2018** (2018), [10.23731/CYRM-2018-003](#), [arXiv:1812.02093 \[hep-ph\]](#).
- [217] H. Abramowicz *et al.*, *Higgs physics at the CLIC electron–positron linear collider*, *Eur. Phys. J. C* **77**, 475 (2017), [arXiv:1608.07538 \[hep-ex\]](#).
- [218] M. Feickert and B. Nachman, *A Living Review of Machine Learning for Particle Physics*, (2021), [arXiv:2102.02770 \[hep-ph\]](#).
- [219] K. Datta, A. Larkoski, and B. Nachman, *Automating the Construction of Jet Observables with Machine Learning*, *Phys. Rev. D* **100**, 095016 (2019), [arXiv:1902.07180 \[hep-ph\]](#).
- [220] J. Lin, M. Freytsis, I. Moulton, and B. Nachman, *Boosting $H \rightarrow b\bar{b}$ with Machine Learning*, *JHEP* **10**, 101 (2018), [arXiv:1807.10768 \[hep-ph\]](#).
- [221] E. A. Moreno, T. Q. Nguyen, J.-R. Vlimant, O. Cerri, H. B. Newman, A. Perival, M. Spiropulu, J. M. Duarte, and M. Pierini, *Interaction networks for the identification of boosted $H \rightarrow b\bar{b}$ decays*, *Phys. Rev. D* **102**, 012010 (2020), [arXiv:1909.12285 \[hep-ex\]](#).
- [222] C. K. Khosa and S. Marzani, *Higgs boson tagging with the Lund jet plane*, *Phys. Rev. D* **104**, 055043 (2021), [arXiv:2105.03989 \[hep-ph\]](#).
- [223] J. Guo, J. Li, T. Li, and R. Zhang, *Boosted Higgs boson jet reconstruction via a graph neural network*, *Phys. Rev. D* **103**, 116025 (2021), [arXiv:2010.05464 \[hep-ph\]](#).
- [224] K. J. F. Gaemers and F. Hoogeveen, *Higgs Production and Decay Into Heavy Flavors With the Gluon Fusion Mechanism*, *Phys. Lett. B* **146**, 347 (1984).
- [225] D. Dicus, A. Stange, and S. Willenbrock, *Higgs decay to top quarks at hadron colliders*, *Phys. Lett. B* **333**, 126 (1994), [arXiv:hep-ph/9404359](#).
- [226] W. Bernreuther, P. Galler, C. Mellein, Z. G. Si, and P. Uwer, *Production of heavy Higgs bosons and decay into top quarks at the LHC*, *Phys. Rev. D* **93**, 034032 (2016), [arXiv:1511.05584 \[hep-ph\]](#).
- [227] G. C. Branco, P. M. Ferreira, L. Lavoura, M. N. Rebelo, M. Sher, and J. P. Silva, *Theory and phenomenology of two-Higgs-doublet models*, *Phys. Rept.* **516**, 1 (2012), [arXiv:1106.0034 \[hep-ph\]](#).
- [228] S. Jung, J. Song, and Y. W. Yoon, *Dip or nothingness of a Higgs resonance from the*

- interference with a complex phase*, *Phys. Rev. D* **92**, 055009 (2015), [arXiv:1505.00291 \[hep-ph\]](#).
- [229] M. Carena and Z. Liu, *Challenges and opportunities for heavy scalar searches in the $t\bar{t}$ channel at the LHC*, *JHEP* **11**, 159 (2016), [arXiv:1608.07282 \[hep-ph\]](#).
- [230] A. Djouadi, J. Ellis, A. Popov, and J. Quevillon, *Interference effects in $t\bar{t}$ production at the LHC as a window on new physics*, *JHEP* **03**, 119 (2019), [arXiv:1901.03417 \[hep-ph\]](#).
- [231] P. Basler, S. Dawson, C. Englert, and M. Mühlleitner, *Di-Higgs boson peaks and top valleys: Interference effects in Higgs sector extensions*, *Phys. Rev. D* **101**, 015019 (2020), [arXiv:1909.09987 \[hep-ph\]](#).
- [232] M. Mühlleitner, M. O. P. Sampaio, R. Santos, and J. Wittbrodt, *The $N2HDM$ under Theoretical and Experimental Scrutiny*, *JHEP* **03**, 094 (2017), [arXiv:1612.01309 \[hep-ph\]](#).
- [233] M. Aaboud *et al.* (ATLAS), *Search for Heavy Higgs Bosons A/H Decaying to a Top Quark Pair in pp Collisions at $\sqrt{s} = 8$ TeV with the ATLAS Detector*, *Phys. Rev. Lett.* **119**, 191803 (2017), [arXiv:1707.06025 \[hep-ex\]](#).
- [234] A. Denner and S. Dittmaier, *Reduction schemes for one-loop tensor integrals*, *Nucl. Phys. B* **734**, 62 (2006), [arXiv:hep-ph/0509141](#).
- [235] T. Plehn, *Lectures on LHC Physics* (2015).
- [236] V. Barger, P. Langacker, M. McCaskey, M. Ramsey-Musolf, and G. Shaughnessy, *Complex Singlet Extension of the Standard Model*, *Phys. Rev. D* **79**, 015018 (2009), [arXiv:0811.0393 \[hep-ph\]](#).
- [237] R. Coimbra, M. O. P. Sampaio, and R. Santos, *ScannerS: Constraining the phase diagram of a complex scalar singlet at the LHC*, *Eur. Phys. J. C* **73**, 2428 (2013), [arXiv:1301.2599 \[hep-ph\]](#).
- [238] S. Y. Choi, C. Englert, and P. M. Zerwas, *Multiple Higgs-Portal and Gauge-Kinetic Mixings*, *Eur. Phys. J. C* **73**, 2643 (2013), [arXiv:1308.5784 \[hep-ph\]](#).
- [239] A. Ahriche, A. Arhrib, and S. Nasri, *Higgs Phenomenology in the Two-Singlet Model*, *JHEP* **02**, 042 (2014), [arXiv:1309.5615 \[hep-ph\]](#).
- [240] R. Costa, A. P. Morais, M. O. P. Sampaio, and R. Santos, *Two-loop stability of a complex singlet extended Standard Model*, *Phys. Rev. D* **92**, 025024 (2015), [arXiv:1411.4048 \[hep-ph\]](#).

- [241] R. Costa, M. Mühlleitner, M. O. P. Sampaio, and R. Santos, *Singlet Extensions of the Standard Model at LHC Run 2: Benchmarks and Comparison with the NMSSM*, *JHEP* **06**, 034 (2016), [arXiv:1512.05355 \[hep-ph\]](#).
- [242] P. M. Ferreira, *The vacuum structure of the Higgs complex singlet-doublet model*, *Phys. Rev. D* **94**, 096011 (2016), [arXiv:1607.06101 \[hep-ph\]](#).
- [243] I. P. Ivanov, *Building and testing models with extended Higgs sectors*, *Prog. Part. Nucl. Phys.* **95**, 160 (2017), [arXiv:1702.03776 \[hep-ph\]](#).
- [244] A. Ahriche, A. Arhrib, and S. Nasri, *Higgs Phenomenology in the Two-Singlet Model*, *JHEP* **02**, 042 (2014), [arXiv:1309.5615 \[hep-ph\]](#).
- [245] V. Barger, P. Langacker, M. McCaskey, M. Ramsey-Musolf, and G. Shaughnessy, *Complex Singlet Extension of the Standard Model*, *Phys. Rev. D* **79**, 015018 (2009), [arXiv:0811.0393 \[hep-ph\]](#).
- [246] S. Hochreiter and J. Schmidhuber, *Long Short-Term Memory*, *Neural Comput.* **9**, 1735 (1997).
- [247] K. Cho, B. van Merriënboer, C. Gulcehre, D. Bahdanau, F. Bougares, H. Schwenk, and Y. Bengio, *Learning phrase representations using RNN encoder–decoder for statistical machine translation*, in *Proceedings of the 2014 Conference on Empirical Methods in Natural Language Processing (EMNLP)* (Association for Computational Linguistics, Doha, Qatar, 2014) pp. 1724–1734.
- [248] D. Guest, J. Collado, P. Baldi, S.-C. Hsu, G. Urban, and D. Whiteson, *Jet Flavor Classification in High-Energy Physics with Deep Neural Networks*, *Phys. Rev. D* **94**, 112002 (2016), [arXiv:1607.08633 \[hep-ex\]](#).
- [249] *Identification of Jets Containing b-Hadrons with Recurrent Neural Networks at the ATLAS Experiment*, (2017).
- [250] S. Egan, W. Fedorko, A. Lister, J. Pearkes, and C. Gay, *Long Short-Term Memory (LSTM) networks with jet constituents for boosted top tagging at the LHC*, (2017), [arXiv:1711.09059 \[hep-ex\]](#).
- [251] K. Fraser and M. D. Schwartz, *Jet Charge and Machine Learning*, *JHEP* **10**, 093 (2018), [arXiv:1803.08066 \[hep-ph\]](#).

- [252] G. Louppe, K. Cho, C. Becot, and K. Cranmer, *QCD-Aware Recursive Neural Networks for Jet Physics*, *JHEP* **01**, 057 (2019), [arXiv:1702.00748 \[hep-ph\]](#).
- [253] A. Bredenstein, A. Denner, S. Dittmaier, and S. Pozzorini, *NLO QCD corrections to $pp \rightarrow t \text{ anti-}t b \text{ anti-}b + X$ at the LHC*, *Phys. Rev. Lett.* **103**, 012002 (2009), [arXiv:0905.0110 \[hep-ph\]](#).
- [254] *Addendum to the report on the physics at the HL-LHC, and perspectives for the HE-LHC: Collection of notes from ATLAS and CMS*, *CERN Yellow Rep. Monogr.* **7**, Addendum (2019), [arXiv:1902.10229 \[hep-ex\]](#).
- [255] C. Degrande, C. Duhr, B. Fuks, D. Grellscheid, O. Mattelaer, and T. Reiter, *UFO - The Universal FeynRules Output*, *Comput. Phys. Commun.* **183**, 1201 (2012), [arXiv:1108.2040 \[hep-ph\]](#).
- [256] S. Frixione, E. Laenen, P. Motylinski, and B. R. Webber, *Angular correlations of lepton pairs from vector boson and top quark decays in Monte Carlo simulations*, *JHEP* **04**, 081 (2007), [arXiv:hep-ph/0702198](#).
- [257] P. Artoisenet, R. Frederix, O. Mattelaer, and R. Rietkerk, *Automatic spin-entangled decays of heavy resonances in Monte Carlo simulations*, *JHEP* **03**, 015 (2013), [arXiv:1212.3460 \[hep-ph\]](#).
- [258] M. Cacciari, G. P. Salam, and G. Soyez, *FastJet User Manual*, *Eur. Phys. J. C* **72**, 1896 (2012), [arXiv:1111.6097 \[hep-ph\]](#).
- [259] M. Cacciari and G. P. Salam, *Dispelling the N^3 myth for the k_t jet-finder*, *Phys. Lett. B* **641**, 57 (2006), [arXiv:hep-ph/0512210](#).
- [260] E. Conte, B. Fuks, and G. Serret, *MadAnalysis 5, A User-Friendly Framework for Collider Phenomenology*, *Comput. Phys. Commun.* **184**, 222 (2013), [arXiv:1206.1599 \[hep-ph\]](#).
- [261] E. Conte, B. Dumont, B. Fuks, and C. Wymant, *Designing and recasting LHC analyses with MadAnalysis 5*, *Eur. Phys. J. C* **74**, 3103 (2014), [arXiv:1405.3982 \[hep-ph\]](#).
- [262] B. Dumont, B. Fuks, S. Kraml, S. Bein, G. Chalons, E. Conte, S. Kulkarni, D. Sengupta, and C. Wymant, *Toward a public analysis database for LHC new physics searches using MADANALYSIS 5*, *Eur. Phys. J. C* **75**, 56 (2015), [arXiv:1407.3278 \[hep-ph\]](#).

- [263] E. Conte and B. Fuks, *Confronting new physics theories to LHC data with MADANALYSIS 5*, *Int. J. Mod. Phys. A* **33**, 1830027 (2018), [arXiv:1808.00480 \[hep-ph\]](#).
- [264] F. Chollet *et al.*, *Keras*, <https://keras.io> (2015).
- [265] M. Abadi, A. Agarwal, P. Barham, E. Brevdo, Z. Chen, C. Citro, G. S. Corrado, A. Davis, J. Dean, M. Devin, S. Ghemawat, I. Goodfellow, A. Harp, G. Irving, M. Isard, Y. Jia, R. Jozefowicz, L. Kaiser, M. Kudlur, J. Levenberg, D. Mane, R. Monga, S. Moore, D. Murray, C. Olah, M. Schuster, J. Shlens, B. Steiner, I. Sutskever, K. Talwar, P. Tucker, V. Vanhoucke, V. Vasudevan, F. Viegas, O. Vinyals, P. Warden, M. Wattenberg, M. Wicke, Y. Yu, and X. Zheng, *Tensorflow: Large-scale machine learning on heterogeneous distributed systems*, (2016), [arXiv:1603.04467 \[cs.DC\]](#).
- [266] X. Glorot and Y. Bengio, *Understanding the difficulty of training deep feedforward neural networks*, in *Proceedings of the Thirteenth International Conference on Artificial Intelligence and Statistics*, Proceedings of Machine Learning Research, Vol. 9, edited by Y. W. Teh and M. Titterton (PMLR, Chia Laguna Resort, Sardinia, Italy, 2010) pp. 249–256.
- [267] V. Nair and G. E. Hinton, *Rectified linear units improve restricted boltzmann machines*, in *Proceedings of the 27th International Conference on International Conference on Machine Learning*, ICML'10 (Omnipress, USA, 2010) pp. 807–814.
- [268] J. S. Bridle, *Probabilistic interpretation of feedforward classification network outputs, with relationships to statistical pattern recognition*, in *Neurocomputing*, edited by F. F. Soulié and J. Héroult (Springer Berlin Heidelberg, Berlin, Heidelberg, 1990) pp. 227–236.
- [269] D. P. Kingma and J. Ba, *Adam: A method for stochastic optimization*, [CoRR abs/1412.6980](#) (2014), [arXiv:1412.6980](#).
- [270] P. M. Ferreira, R. Guedes, M. O. P. Sampaio, and R. Santos, *Wrong sign and symmetric limits and non-decoupling in 2HDMs*, *JHEP* **12**, 067 (2014), [arXiv:1409.6723 \[hep-ph\]](#).
- [271] M. Mühlleitner, M. O. P. Sampaio, R. Santos, and J. Wittbrodt, *ScannerS: Parameter Scans in Extended Scalar Sectors*, (2020), [arXiv:2007.02985 \[hep-ph\]](#).
- [272] S. Dittmaier *et al.* (LHC Higgs Cross Section Working Group), *Handbook of LHC Higgs Cross Sections: 1. Inclusive Observables*, (2011), [10.5170/CERN-2011-002](#), [arXiv:1101.0593 \[hep-ph\]](#).

- [273] H. Murayama, I. Watanabe, and K. Hagiwara, *HELAS: HELicity amplitude subroutines for Feynman diagram evaluations*, (1992).
- [274] M. Spira, *HIGLU: A program for the calculation of the total Higgs production cross-section at hadron colliders via gluon fusion including QCD corrections*, (1995), [arXiv:hep-ph/9510347](#).
- [275] C. Anastasiou, A. Brandhuber, P. Heslop, V. V. Khoze, B. Spence, and G. Travaglini, *Two-Loop Polygon Wilson Loops in $N=4$ SYM*, *JHEP* **05**, 115 (2009), [arXiv:0902.2245 \[hep-th\]](#).
- [276] M. H. Seymour, *The Higgs boson line shape and perturbative unitarity*, *Phys. Lett. B* **354**, 409 (1995), [arXiv:hep-ph/9505211](#).
- [277] S. Gorla, G. Passarino, and D. Rosco, *The Higgs Boson Lineshape*, *Nucl. Phys. B* **864**, 530 (2012), [arXiv:1112.5517 \[hep-ph\]](#).
- [278] C. Englert, I. Low, and M. Spannowsky, *On-shell interference effects in Higgs boson final states*, *Phys. Rev. D* **91**, 074029 (2015), [arXiv:1502.04678 \[hep-ph\]](#).
- [279] A. M. Sirunyan *et al.* (CMS), *Search for heavy Higgs bosons decaying to a top quark pair in proton-proton collisions at $\sqrt{s} = 13$ TeV*, *JHEP* **04**, 171 (2020), [arXiv:1908.01115 \[hep-ex\]](#).
- [280] T. Robens, T. Stefaniak, and J. Wittbrodt, *Two-real-scalar-singlet extension of the SM: LHC phenomenology and benchmark scenarios*, *Eur. Phys. J. C* **80**, 151 (2020), [arXiv:1908.08554 \[hep-ph\]](#).
- [281] K. Kannike, *Vacuum Stability Conditions From Copositivity Criteria*, *Eur. Phys. J. C* **72**, 2093 (2012), [arXiv:1205.3781 \[hep-ph\]](#).
- [282] B. Díaz Sáez, K. Möhling, and D. Stöckinger, *Two real scalar WIMP model in the assisted freeze-out scenario*, *JCAP* **10**, 027 (2021), [arXiv:2103.17064 \[hep-ph\]](#).
- [283] K. Arnold *et al.*, *VBFNLO: A Parton level Monte Carlo for processes with electroweak bosons*, *Comput. Phys. Commun.* **180**, 1661 (2009), [arXiv:0811.4559 \[hep-ph\]](#).
- [284] J. Ellis, M. Madigan, K. Mimasu, V. Sanz, and T. You, *Top, Higgs, Diboson and Electroweak Fit to the Standard Model Effective Field Theory*, *JHEP* **04**, 279 (2021), [arXiv:2012.02779 \[hep-ph\]](#).
- [285] Anisha, S. Das Bakshi, S. Banerjee, A. Biekötter, J. Chakraborty, S. Kumar Patra, and

- M. Spannowsky, *Effective limits on single scalar extensions in the light of recent LHC data*, (2021), [arXiv:2111.05876 \[hep-ph\]](#).
- [286] J. J. Ethier, G. Magni, F. Maltoni, L. Mantani, E. R. Nocera, J. Rojo, E. Slade, E. Vryonidou, and C. Zhang (SMEFiT), *Combined SMEFT interpretation of Higgs, diboson, and top quark data from the LHC*, *JHEP* **11**, 089 (2021), [arXiv:2105.00006 \[hep-ph\]](#).
- [287] A. Buckley, C. Englert, J. Ferrando, D. J. Miller, L. Moore, M. Russell, and C. D. White, *Constraining top quark effective theory in the LHC Run II era*, *JHEP* **04**, 015 (2016), [arXiv:1512.03360 \[hep-ph\]](#).
- [288] A. Buckley, C. Englert, J. Ferrando, D. J. Miller, L. Moore, M. Russell, and C. D. White, *Global fit of top quark effective theory to data*, *Phys. Rev. D* **92**, 091501 (2015), [arXiv:1506.08845 \[hep-ph\]](#).
- [289] M. Vos *et al.*, *Top physics at high-energy lepton colliders*, (2016), [arXiv:1604.08122 \[hep-ex\]](#).
- [290] N. Castro, J. Erdmann, C. Grunwald, K. Kröninger, and N.-A. Rosien, *EFTfitter—A tool for interpreting measurements in the context of effective field theories*, *Eur. Phys. J. C* **76**, 432 (2016), [arXiv:1605.05585 \[hep-ex\]](#).
- [291] D. Barducci *et al.*, *Interpreting top-quark LHC measurements in the standard-model effective field theory*, (2018), [arXiv:1802.07237 \[hep-ph\]](#).
- [292] N. P. Hartland, F. Maltoni, E. R. Nocera, J. Rojo, E. Slade, E. Vryonidou, and C. Zhang, *A Monte Carlo global analysis of the Standard Model Effective Field Theory: the top quark sector*, *JHEP* **04**, 100 (2019), [arXiv:1901.05965 \[hep-ph\]](#).
- [293] I. Brivio, S. Bruggisser, F. Maltoni, R. Moutafis, T. Plehn, E. Vryonidou, S. Westhoff, and C. Zhang, *O new physics, where art thou? A global search in the top sector*, *JHEP* **02**, 131 (2020), [arXiv:1910.03606 \[hep-ph\]](#).
- [294] J. D’Hondt, A. Mariotti, K. Mimasu, S. Moortgat, and C. Zhang, *Learning to pinpoint effective operators at the LHC: a study of the $t\bar{t}b\bar{b}$ signature*, *JHEP* **11**, 131 (2018), [arXiv:1807.02130 \[hep-ph\]](#).
- [295] J. Zhou, G. Cui, Z. Zhang, C. Yang, Z. Liu, L. Wang, C. Li, and M. Sun, *Graph neural networks: A review of methods and applications*, (2018), [arXiv:1812.08434 \[cs\]](#).
- [296] Z. Wu, S. Pan, F. Chen, G. Long, C. Zhang, and P. S. Yu, *A comprehensive survey on*

- graph neural networks*, *IEEE Transactions on Neural Networks and Learning Systems* **32**, 4 (2021), [arXiv:1901.00596 \[cs\]](#).
- [297] J. Gilmer, S. S. Schoenholz, P. F. Riley, O. Vinyals, and G. E. Dahl, *Neural message passing for quantum chemistry*, in *International Conference on Machine Learning* (PMLR, 2017) pp. 1263–1272, [arXiv:1704.01212 \[cs\]](#).
- [298] Y. Wang, Y. Sun, Z. Liu, S. E. Sarma, M. M. Bronstein, and J. M. Solomon, *Dynamic graph cnn for learning on point clouds*, *Acm Transactions On Graphics (tog)* **38**, 1 (2019), [arXiv:1801.07829 \[cs\]](#).
- [299] F. A. Dreyer and H. Qu, *Jet tagging in the Lund plane with graph networks*, *JHEP* **03**, 052 (2021), [arXiv:2012.08526 \[hep-ph\]](#).
- [300] A. Blance and M. Spannowsky, *Unsupervised Event Classification with Graphs on Classical and Photonic Quantum Computers*, (2021), [arXiv:2103.03897 \[hep-ph\]](#).
- [301] O. Atkinson, A. Bhardwaj, C. Englert, V. S. Ngairangbam, and M. Spannowsky, *Anomaly detection with convolutional Graph Neural Networks*, *JHEP* **08**, 080 (2021), [arXiv:2105.07988 \[hep-ph\]](#).
- [302] H. Qu and L. Gouskos, *ParticleNet: Jet Tagging via Particle Clouds*, *Phys. Rev. D* **101**, 056019 (2020), [arXiv:1902.08570 \[hep-ph\]](#).
- [303] T. Dorigo, M. Fumanelli, C. Maccani, M. Mojsavska, G. C. Strong, and B. Scarpa, *RanBox: Anomaly Detection in the Copula Space*, (2021), [arXiv:2106.05747 \[physics.data-an\]](#).
- [304] V. Mikuni and F. Canelli, *ABCNet: An attention-based method for particle tagging*, *Eur. Phys. J. Plus* **135**, 463 (2020), [arXiv:2001.05311 \[physics.data-an\]](#).
- [305] O. Knapp, O. Cerri, G. Dissertori, T. Q. Nguyen, M. Pierini, and J.-R. Vlimant, *Adversarially Learned Anomaly Detection on CMS Open Data: re-discovering the top quark*, *Eur. Phys. J. Plus* **136**, 236 (2021), [arXiv:2005.01598 \[hep-ex\]](#).
- [306] V. Mikuni and F. Canelli, *Unsupervised clustering for collider physics*, *Phys. Rev. D* **103**, 092007 (2021), [arXiv:2010.07106 \[physics.data-an\]](#).
- [307] G. Dezoort, S. Thais, I. Ojalvo, P. Elmer, V. Razavimaleki, J. Duarte, M. Atkinson, and M. Neubauer, *Charged particle tracking via edge-classifying interaction networks*, (2021), [arXiv:2103.16701 \[hep-ex\]](#).

- [308] M. Abdughani, J. Ren, L. Wu, and J. M. Yang, *Probing stop pair production at the LHC with graph neural networks*, [JHEP **08**, 055 \(2019\)](#), [arXiv:1807.09088 \[hep-ph\]](#).
- [309] .
- [310] X. Ju and B. Nachman, *Supervised Jet Clustering with Graph Neural Networks for Lorentz Boosted Bosons*, [Phys. Rev. D **102**, 075014 \(2020\)](#), [arXiv:2008.06064 \[hep-ph\]](#).
- [311] V. Khachatryan *et al.* (CMS), *Measurement of differential cross sections for top quark pair production using the lepton+jets final state in proton-proton collisions at 13 TeV*, [Phys. Rev. D **95**, 092001 \(2017\)](#), [arXiv:1610.04191 \[hep-ex\]](#).
- [312] I. Brivio, Y. Jiang, and M. Trott, *The SMEFTsim package, theory and tools*, [JHEP **12**, 070 \(2017\)](#), [arXiv:1709.06492 \[hep-ph\]](#).
- [313] I. Brivio, *SMEFTsim 3.0 — a practical guide*, [JHEP **04**, 073 \(2021\)](#), [arXiv:2012.11343 \[hep-ph\]](#).
- [314] C. Bierlich *et al.*, *Robust Independent Validation of Experiment and Theory: Rivet version 3*, [SciPost Phys. **8**, 026 \(2020\)](#), [arXiv:1912.05451 \[hep-ph\]](#).
- [315] S. Brown, A. Buckley, C. Englert, J. Ferrando, P. Galler, D. Miller, C. Wanotayaroj, N. Warrack, and C. White, *New results from TopFitter*, [PoS **ICHEP2020**, 322 \(2021\)](#).
- [316] A. Buckley, C. Englert, J. Ferrando, D. J. Miller, L. Moore, K. Nördstrom, M. Russell, and C. D. White, *Results from TopFitter*, [PoS **CKM2016**, 127 \(2016\)](#), [arXiv:1612.02294 \[hep-ph\]](#).
- [317] S. Brown, A. Buckley, C. Englert, J. Ferrando, P. Galler, D. J. Miller, L. Moore, M. Russell, C. White, and N. Warrack, *TopFitter: Fitting top-quark Wilson Coefficients to Run II data*, [PoS **ICHEP2018**, 293 \(2019\)](#), [arXiv:1901.03164 \[hep-ph\]](#).
- [318] L. Moore, C. Englert, J. Ferrando, d. J. Miller, M. Russell, and C. D. White, *TopFitter: A global fit of the top effective theory to data*, [PoS **TOP2015**, 065 \(2016\)](#).
- [319] P. A. Zyla *et al.* (Particle Data Group), *Review of Particle Physics*, [PTEP **2020**, 083C01 \(2020\)](#).
- [320] Y. Lecun, L. Bottou, Y. Bengio, and P. Haffner, *Gradient-based learning applied to document recognition*, [Proceedings of the IEEE **86**, 2278 \(1998\)](#).

- [321] M. Wang, D. Zheng, Z. Ye, Q. Gan, M. Li, X. Song, J. Zhou, C. Ma, L. Yu, Y. Gai, T. Xiao, T. He, G. Karypis, J. Li, and Z. Zhang, *Deep graph library: A graph-centric, highly-performant package for graph neural networks*, (2020), [arXiv:1909.01315 \[cs.LG\]](#).
- [322] A. Paszke, S. Gross, F. Massa, A. Lerer, J. Bradbury, G. Chanan, T. Killeen, Z. Lin, N. Gimelshein, L. Antiga, A. Desmaison, A. Köpf, E. Yang, Z. DeVito, M. Raison, A. Tejani, S. Chilamkurthy, B. Steiner, L. Fang, J. Bai, and S. Chintala, *Pytorch: An imperative style, high-performance deep learning library*, (2019), [arXiv:1912.01703 \[cs.LG\]](#).
- [323] H. K. Dreiner, A. Duff, and D. Zeppenfeld, *How well do we know the three gluon vertex?* *Phys. Lett. B* **282**, 441 (1992).
- [324] L. J. Dixon and Y. Shadmi, *Testing gluon selfinteractions in three jet events at hadron colliders*, *Nucl. Phys. B* **423**, 3 (1994), [Erratum: *Nucl.Phys.B* 452, 724–724 (1995)], [arXiv:hep-ph/9312363](#).
- [325] G. Louppe, M. Kagan, and K. Cranmer, *Learning to Pivot with Adversarial Networks*, (2016), [arXiv:1611.01046 \[stat.ML\]](#).
- [326] R. Kansal, J. Duarte, H. Su, B. Orzari, T. Tomei, M. Pierini, M. Touranakou, J.-R. Vlimant, and D. Gunopulos, *Particle Cloud Generation with Message Passing Generative Adversarial Networks*, (2021), [arXiv:2106.11535 \[cs.LG\]](#).
- [327] C. Englert, P. Galler, P. Harris, and M. Spannowsky, *Machine Learning Uncertainties with Adversarial Neural Networks*, *Eur. Phys. J. C* **79**, 4 (2019), [arXiv:1807.08763 \[hep-ph\]](#).
- [328] M. Bellagente, A. Butter, G. Kasieczka, T. Plehn, and R. Winterhalder, *How to GAN away Detector Effects*, *SciPost Phys.* **8**, 070 (2020), [arXiv:1912.00477 \[hep-ph\]](#).
- [329] G. Aad *et al.* (ATLAS), *Differential cross-section measurements for the electroweak production of dijets in association with a Z boson in proton–proton collisions at ATLAS*, *Eur. Phys. J. C* **81**, 163 (2021), [arXiv:2006.15458 \[hep-ex\]](#).
- [330] A. M. Sirunyan *et al.* (CMS), *Measurements of ttH Production and the CP Structure of the Yukawa Interaction between the Higgs Boson and Top Quark in the Diphoton Decay Channel*, *Phys. Rev. Lett.* **125**, 061801 (2020), [arXiv:2003.10866 \[hep-ex\]](#).
- [331] G. Aad *et al.* (ATLAS), *CP Properties of Higgs Boson Interactions with Top Quarks in*

- the $t\bar{t}H$ and tH Processes Using $H \rightarrow \gamma\gamma$ with the ATLAS Detector*, *Phys. Rev. Lett.* **125**, 061802 (2020), [arXiv:2004.04545 \[hep-ex\]](#).
- [332] J. Baglio *et al.*, *Release Note - VBFNLO 2.7.0*, (2014), [arXiv:1404.3940 \[hep-ph\]](#).
- [333] J. Bellm *et al.*, *Herwig 7.0/Herwig++ 3.0 release note*, *Eur. Phys. J. C* **76**, 196 (2016), [arXiv:1512.01178 \[hep-ph\]](#).
- [334] J. Alwall *et al.*, *A Standard format for Les Houches event files*, *Comput. Phys. Commun.* **176**, 300 (2007), [arXiv:hep-ph/0609017](#).
- [335] A. M. Sirunyan *et al.* (CMS), *Measurement of the $W\gamma$ Production Cross Section in Proton-Proton Collisions at $\sqrt{s}=13$ TeV and Constraints on Effective Field Theory Coefficients*, *Phys. Rev. Lett.* **126**, 252002 (2021), [arXiv:2102.02283 \[hep-ex\]](#).
- [336] M. A. Samuel, *AMPLITUDE ZEROS*, *Phys. Rev. D* **27**, 2724 (1983).
- [337] M. A. Samuel, A. Sen, G. S. Sylvester, and M. L. Laursen, *GENERAL CRITERIA FOR RADIATION AMPLITUDE ZEROS*, *Phys. Rev. D* **29**, 994 (1984).
- [338] S. J. Brodsky and R. W. Brown, *Zeros in Amplitudes: Gauge Theory and Radiation Interference*, *Phys. Rev. Lett.* **49**, 966 (1982).
- [339] R. W. Brown, K. L. Kowalski, and S. J. Brodsky, *Classical Radiation Zeros in Gauge Theory Amplitudes*, *Phys. Rev. D* **28**, 624 (1983), [Addendum: *Phys.Rev.D* 29, 2100–2104 (1984)].
- [340] F. K. Diakonos, O. Korakianitis, C. G. Papadopoulos, C. Philippides, and W. J. Stirling, *$W + \text{gamma} + \text{jet}$ production as a test of the electromagnetic couplings of W at LHC and SSC*, *Phys. Lett. B* **303**, 177 (1993), [arXiv:hep-ph/9301238](#).
- [341] U. Baur, T. Han, and J. Ohnemus, *QCD corrections to hadronic $W\gamma$ production with nonstandard $WW\gamma$ couplings*, *Phys. Rev. D* **48**, 5140 (1993), [arXiv:hep-ph/9305314](#).
- [342] F. Campanario, C. Englert, and M. Spannowsky, *Precise predictions for (non-standard) $W\gamma + \text{jet}$ production*, *Phys. Rev. D* **83**, 074009 (2011), [arXiv:1010.1291 \[hep-ph\]](#).
- [343] M. Aaboud *et al.* (ATLAS), *Measurement of fiducial and differential W^+W^- production cross-sections at $\sqrt{s} = 13$ TeV with the ATLAS detector*, *Eur. Phys. J. C* **79**, 884 (2019), [arXiv:1905.04242 \[hep-ex\]](#).

- [344] V. Khachatryan *et al.* (CMS), *Measurement of the WZ production cross section in pp collisions at $\sqrt{s} = 13$ TeV*, *Phys. Lett. B* **766**, 268 (2017), [arXiv:1607.06943 \[hep-ex\]](#).
- [345] C. W. Murphy, *Dimension-8 operators in the Standard Model Effective Field Theory*, *JHEP* **10**, 174 (2020), [arXiv:2005.00059 \[hep-ph\]](#).
- [346] A. Angelescu and P. Huang, *Integrating Out New Fermions at One Loop*, *JHEP* **01**, 049 (2021), [arXiv:2006.16532 \[hep-ph\]](#).
- [347] S. Das Bakshi, J. Chakraborty, and S. K. Patra, *CoDEx: Wilson coefficient calculator connecting SMEFT to UV theory*, *Eur. Phys. J. C* **79**, 21 (2019), [arXiv:1808.04403 \[hep-ph\]](#).
- [348] V. D. Barger, T. Han, T.-J. Li, and T. Plehn, *Measuring CP violating phases at a future linear collider*, *Phys. Lett. B* **475**, 342 (2000), [arXiv:hep-ph/9907425](#).
- [349] V. Hankele, G. Klamke, D. Zeppenfeld, and T. Figy, *Anomalous Higgs boson couplings in vector boson fusion at the CERN LHC*, *Phys. Rev. D* **74**, 095001 (2006), [arXiv:hep-ph/0609075](#).
- [350] C. Englert, D. Goncalves-Netto, K. Mawatari, and T. Plehn, *Higgs Quantum Numbers in Weak Boson Fusion*, *JHEP* **01**, 148 (2013), [arXiv:1212.0843 \[hep-ph\]](#).
- [351] C. Englert, M. Spannowsky, and M. Takeuchi, *Measuring Higgs CP and couplings with hadronic event shapes*, *JHEP* **06**, 108 (2012), [arXiv:1203.5788 \[hep-ph\]](#).
- [352] Y. L. Dokshitzer, S. I. Troian, and V. A. Khoze, *Collective QCD Effects in the Structure of Final Multi - Hadron States. (In Russian)*, *Sov. J. Nucl. Phys.* **46**, 712 (1987).
- [353] Y. L. Dokshitzer, V. A. Khoze, and T. Sjostrand, *Rapidity gaps in Higgs production*, *Phys. Lett. B* **274**, 116 (1992).
- [354] V. D. Barger, K.-m. Cheung, T. Han, and D. Zeppenfeld, *Single forward jet tagging and central jet vetoing to identify the leptonic WW decay mode of a heavy Higgs boson*, *Phys. Rev. D* **44**, 2701 (1991), [Erratum: *Phys.Rev.D* 48, 5444 (1993)].
- [355] J. D. Bjorken, *Rapidity gaps and jets as a new physics signature in very high-energy hadron hadron collisions*, *Phys. Rev. D* **47**, 101 (1993).
- [356] V. Khachatryan *et al.* (CMS), *Search for the standard model Higgs boson produced through vector boson fusion and decaying to $b\bar{b}$* , *Phys. Rev. D* **92**, 032008 (2015), [arXiv:1506.01010 \[hep-ex\]](#).

- [357] C. Englert, O. Mattelaer, and M. Spannowsky, *Measuring the Higgs-bottom coupling in weak boson fusion*, *Phys. Lett. B* **756**, 103 (2016), [arXiv:1512.03429 \[hep-ph\]](#).
- [358] S. Banerjee, R. S. Gupta, O. Ochoa-Valeriano, M. Spannowsky, and E. Venturini, *A fully differential SMEFT analysis of the golden channel using the method of moments*, *JHEP* **06**, 031 (2021), [arXiv:2012.11631 \[hep-ph\]](#).
- [359] S. Chatrchyan *et al.* (CMS), *Evidence for the 125 GeV Higgs boson decaying to a pair of τ leptons*, *JHEP* **05**, 104 (2014), [arXiv:1401.5041 \[hep-ex\]](#).
- [360] J. Y. Araz, S. Banerjee, R. S. Gupta, and M. Spannowsky, *Precision SMEFT bounds from the VBF Higgs at high transverse momentum*, *JHEP* **04**, 125 (2021), [arXiv:2011.03555 \[hep-ph\]](#).
- [361] M. J. Dolan, P. Harris, M. Jankowiak, and M. Spannowsky, *Constraining CP-violating Higgs Sectors at the LHC using gluon fusion*, *Phys. Rev. D* **90**, 073008 (2014), [arXiv:1406.3322 \[hep-ph\]](#).
- [362] F. U. Bernlochner, C. Englert, C. Hays, K. Lohwasser, H. Mildner, A. Pilkington, D. D. Price, and M. Spannowsky, *Angles on CP-violation in Higgs boson interactions*, *Phys. Lett. B* **790**, 372 (2019), [arXiv:1808.06577 \[hep-ph\]](#).
- [363] O. Buchmuller, M. J. Dolan, and C. McCabe, *Beyond Effective Field Theory for Dark Matter Searches at the LHC*, *JHEP* **01**, 025 (2014), [arXiv:1308.6799 \[hep-ph\]](#).
- [364] P. Athron, C. Balázs, D. H. J. Jacob, W. Kotlarski, D. Stöckinger, and H. Stöckinger-Kim, *New physics explanations of a in light of the FNAL muon $g - 2$ measurement*, *JHEP* **09**, 080 (2021), [arXiv:2104.03691 \[hep-ph\]](#).
- [365] A. Crivellin, S. Najjari, and J. Rosiek, *Lepton Flavor Violation in the Standard Model with general Dimension-Six Operators*, *JHEP* **04**, 167 (2014), [arXiv:1312.0634 \[hep-ph\]](#).
- [366] L. Allwicher, L. Di Luzio, M. Fedele, F. Mescia, and M. Nardecchia, *What is the scale of new physics behind the muon $g-2$?* *Phys. Rev. D* **104**, 055035 (2021), [arXiv:2105.13981 \[hep-ph\]](#).
- [367] J. Aebischer, W. Dekens, E. E. Jenkins, A. V. Manohar, D. Sengupta, and P. Stoffer, *Effective field theory interpretation of lepton magnetic and electric dipole moments*, *JHEP* **07**, 107 (2021), [arXiv:2102.08954 \[hep-ph\]](#).

- [368] V. Cirigliano, W. Dekens, J. de Vries, K. Fuyuto, E. Mereghetti, and R. Ruiz, *Leptonic anomalous magnetic moments in ν SMEFT*, *JHEP* **08**, 103 (2021), [arXiv:2105.11462 \[hep-ph\]](#).
- [369] A. Dedes, M. Paraskevas, J. Rosiek, K. Suxho, and L. Trifyllis, *SmeftFR – Feynman rules generator for the Standard Model Effective Field Theory*, *Comput. Phys. Commun.* **247**, 106931 (2020), [arXiv:1904.03204 \[hep-ph\]](#).
- [370] E. Coluccio Leskow, G. D’Ambrosio, A. Crivellin, and D. Müller, *$(g - 2)_\mu$, lepton flavor violation, and Z decays with leptoquarks: Correlations and future prospects*, *Phys. Rev. D* **95**, 055018 (2017), [arXiv:1612.06858 \[hep-ph\]](#).
- [371] A. Crivellin, D. Mueller, and F. Saturnino, *Correlating $h \rightarrow \mu + \mu^-$ to the Anomalous Magnetic Moment of the Muon via Leptoquarks*, *Phys. Rev. Lett.* **127**, 021801 (2021), [arXiv:2008.02643 \[hep-ph\]](#).
- [372] S. Fajfer, J. F. Kamenik, and M. Tamaro, *Interplay of New Physics effects in $(g - 2)$ and $h \rightarrow \ell^+ \ell^-$ — lessons from SMEFT*, *JHEP* **06**, 099 (2021), [arXiv:2103.10859 \[hep-ph\]](#).
- [373] A. Crivellin and M. Hoferichter, *Consequences of chirally enhanced explanations of $(g - 2)$ for $h \rightarrow \mu\mu$ and $Z \rightarrow \mu\mu$* , *JHEP* **07**, 135 (2021), [arXiv:2104.03202 \[hep-ph\]](#).
- [374] P. Paradisi, O. Sumensari, and A. Valenti, *The high-energy frontier of the muon $g-2$* , (2022), [arXiv:2203.06103 \[hep-ph\]](#).
- [375] G. Abbiendi *et al.*, *Measuring the leading hadronic contribution to the muon $g-2$ via μe scattering*, *Eur. Phys. J. C* **77**, 139 (2017), [arXiv:1609.08987 \[hep-ex\]](#).
- [376] M. J. Musolf and B. R. Holstein, *Observability of the anapole moment and neutrino charge radius*, *Phys. Rev. D* **43**, 2956 (1991).
- [377] A. Denner and S. Dittmaier, *Techniques for one-loop tensor integrals in many-particle processes*, *Nucl. Phys. B Proc. Suppl.* **157**, 53 (2006), [arXiv:hep-ph/0601085](#).
- [378] H. H. Patel, *Package-X: A Mathematica package for the analytic calculation of one-loop integrals*, *Comput. Phys. Commun.* **197**, 276 (2015), [arXiv:1503.01469 \[hep-ph\]](#).
- [379] T. Hahn and J. I. Illana, *Excursions into FeynArts and FormCalc*, *Nucl. Phys. B Proc. Suppl.* **160**, 101 (2006), [arXiv:hep-ph/0607049](#).

- [380] J. S. Schwinger, *On Quantum electrodynamics and the magnetic moment of the electron*, [Phys. Rev. **73**, 416 \(1948\)](#).
- [381] J. Fleischer and F. Jegerlehner, *Radiative Corrections to Higgs Decays in the Extended Weinberg-Salam Model*, [Phys. Rev. D **23**, 2001 \(1981\)](#).
- [382] V. Dūdėnas and M. Löschner, *Vacuum expectation value renormalization in the Standard Model and beyond*, [Phys. Rev. D **103**, 076010 \(2021\)](#), [arXiv:2010.15076 \[hep-ph\]](#).
- [383] W. Dekens and P. Stoffer, *Low-energy effective field theory below the electroweak scale: matching at one loop*, [JHEP **10**, 197 \(2019\)](#), [arXiv:1908.05295 \[hep-ph\]](#).
- [384] C. Hartmann and M. Trott, *On one-loop corrections in the standard model effective field theory; the $\Gamma(h \rightarrow \gamma\gamma)$ case*, [JHEP **07**, 151 \(2015\)](#), [arXiv:1505.02646 \[hep-ph\]](#).
- [385] J. M. Cullen, B. D. Pecjak, and D. J. Scott, *NLO corrections to $h \rightarrow b\bar{b}$ decay in SMEFT*, [JHEP **08**, 173 \(2019\)](#), [arXiv:1904.06358 \[hep-ph\]](#).
- [386] F. F. Freitas, J. a. Gonçalves, A. P. Morais, R. Pasechnik, and W. Porod, *On interplay between flavour anomalies and neutrino properties*, (2022), [arXiv:2206.01674 \[hep-ph\]](#).
- [387] S.-L. Chen, W.-w. Jiang, and Z.-K. Liu, *Combined explanations of B-physics anomalies, $(g-2)_{e,\mu}$ and neutrino masses by scalar leptoquarks*, (2022), [arXiv:2205.15794 \[hep-ph\]](#).
- [388] V. Gherardi, D. Marzocca, and E. Venturini, *Matching scalar leptoquarks to the SMEFT at one loop*, [JHEP **07**, 225 \(2020\)](#), [Erratum: JHEP 01, 006 (2021)], [arXiv:2003.12525 \[hep-ph\]](#).
- [389] A. O. Bouzas and F. Larios, *Two-to-Two Processes at an Electron-Muon Collider*, [Adv. High Energy Phys. **2022**, 3603613 \(2022\)](#), [arXiv:2109.02769 \[hep-ph\]](#).
- [390] J. de Blas, Y. Du, C. Grojean, J. Gu, V. Miralles, M. E. Peskin, J. Tian, M. Vos, and E. Vryonidou, *Global SMEFT Fits at Future Colliders*, in *2022 Snowmass Summer Study* (2022) [arXiv:2206.08326 \[hep-ph\]](#).
- [391] J. M. Cullen and B. D. Pecjak, *Higgs decay to fermion pairs at NLO in SMEFT*, [JHEP **11**, 079 \(2020\)](#), [arXiv:2007.15238 \[hep-ph\]](#).
- [392] S. Borsanyi *et al.* (Budapest-Marseille-Wuppertal), *Hadronic vacuum polarization contribution to the anomalous magnetic moments of leptons from first principles*, [Phys. Rev. Lett. **121**, 022002 \(2018\)](#), [arXiv:1711.04980 \[hep-lat\]](#).

- [393] T. Blum, P. A. Boyle, V. Gülpers, T. Izubuchi, L. Jin, C. Jung, A. Jüttner, C. Lehner, A. Portelli, and J. T. Tsang (RBC, UKQCD), *Calculation of the hadronic vacuum polarization contribution to the muon anomalous magnetic moment*, *Phys. Rev. Lett.* **121**, 022003 (2018), [arXiv:1801.07224 \[hep-lat\]](#).
- [394] C. T. H. Davies *et al.* (Fermilab Lattice, LATTICE-HPQCD, MILC), *Hadronic-vacuum-polarization contribution to the muon's anomalous magnetic moment from four-flavor lattice QCD*, *Phys. Rev. D* **101**, 034512 (2020), [arXiv:1902.04223 \[hep-lat\]](#).
- [395] A. Gérardin, M. Cè, G. von Hippel, B. Hörz, H. B. Meyer, D. Mohler, K. Ottnad, J. Wilhelm, and H. Wittig, *The leading hadronic contribution to $(g-2)_\mu$ from lattice QCD with $N_f = 2+1$ flavours of $O(a)$ improved Wilson quarks*, *Phys. Rev. D* **100**, 014510 (2019), [arXiv:1904.03120 \[hep-lat\]](#).
- [396] C. Aubin, T. Blum, C. Tu, M. Golterman, C. Jung, and S. Peris, *Light quark vacuum polarization at the physical point and contribution to the muon $g-2$* , *Phys. Rev. D* **101**, 014503 (2020), [arXiv:1905.09307 \[hep-lat\]](#).
- [397] S. Borsanyi *et al.*, *Leading hadronic contribution to the muon magnetic moment from lattice QCD*, *Nature* **593**, 51 (2021), [arXiv:2002.12347 \[hep-lat\]](#).
- [398] C. Lehner and A. S. Meyer, *Consistency of hadronic vacuum polarization between lattice QCD and the R -ratio*, *Phys. Rev. D* **101**, 074515 (2020), [arXiv:2003.04177 \[hep-lat\]](#).
- [399] M. Cè *et al.*, *Window observable for the hadronic vacuum polarization contribution to the muon $g-2$ from lattice QCD*, (2022), [arXiv:2206.06582 \[hep-lat\]](#).
- [400] P. S. B. Dev, W. Rodejohann, X.-J. Xu, and Y. Zhang, *MUonE sensitivity to new physics explanations of the muon anomalous magnetic moment*, *JHEP* **05**, 053 (2020), [arXiv:2002.04822 \[hep-ph\]](#).